Theoretical aspects of high amplitude pulsed ultrasound used in lithotripsy

Choi, Min Joo

Award date:
1992

Awarding institution:
University of Bath

THEORETICAL ASPECTS OF HIGH AMPLITUDE PULSED ULTRASOUND USED IN LITHOTRIPSY

submitted by Min Joo Choi

for the degree of PhD

of the University of Bath

1992

ProQuest LLC
789 East Eisenhower Parkway
P.O. Box 1346
Ann Arbor, MI 48106-1346

ACKNOWLEDGEMENTS

The study was carried out at the Medical Physics Department, St Thomas' Hospital, London with support from the Medical Research Council (Grant number: G8722353SA and G8902690SA). I am deeply indebted to Dr Andrew J. Coleman who has given systematic and challenging supervision on the project. Without his help it would not have been possible for the work to be completed.

I gratefully acknowledge the supervision of Dr V.F. Humphrey (School of Physics, University of Bath) as well as invaluable discussions and numerous correspondences with Dr D.R. Bacon (National Physical Laboratory), Dr C.L. Morfey (University of Southampton) and Dr A.C. Baker (University of Bath).

Also I would like to acknowledge the support given me by the staff of the Medical Physics Department at St Thomas' Hospital, in particular, John Saunders (Head of the Department), Richard Knott, Angela Tyson, Mike Whitlock, Tony Greener and Stephen Hughes.

Special thanks must be given to my wife (Jung Hae Choi) for her patience and sacrifice and my parents for their support. This work is offered for the glory of God.

ABSTRACT

The aim of this study is to examine theoretical models which allow predictions to be made concerning the exposure in water and tissue in the focused, high amplitude pulsed acoustic fields generated by clinical extracorporeal shock wave lithotripters. In particular, a novel one dimensional frequency domain model is developed in which nonlinear propagation, focusing, diffraction, attenuation, and dispersion effects are considered. This model specifically allows prediction of pulsed fields and in most practical applications is not constrained by the parabolic approximation. Special attention has been paid to the problems related to nonlinear effects which may alter the beam profile during propagation and to numerical stability of the model. The model gives good agreement with measurements from diagnostic transducers and reasonable predictions in lithotripsy fields. More precise comparison of predictions and measurements in lithotripsy fields awaits improvements in pressure measurement techniques and more precise characterizations of the acoustic sources.

Since acoustic cavitation has been found to play a crucial role in stone fragmentation and tissue damage resulting from exposure to lithotripsy fields, an analysis of the bubble response to the typical pressure waveform has been carried out. Theoretical predictions based on a single bubble model show reasonable agreement with measurements of

the temporal variation of cavitation activity following a shock pulse. The influence of cavitation on the measured exposure is also examined by an analysis of the effect of shock pulse propagation in a gas bubble-fluid mixture. This provides a theoretical basis for limiting the pulse repetition rate in clinical lithotripsy.

CONTENTS

LIST OF SYMBOLS AND ABBREVIATIONS

$\mathcal{A}$, $\mathcal{B}$	pressure constants used in Tait equation
$\mathbb{A}_n$, $\mathbb{B}_n$	real and imaginary parts of $\mathbb{\varnothing}_n$ ($=\mathbb{A}_n - j\mathbb{B}_n$)
a	aperture radius of a circular radiator
a_o, a_n	characteristic aperture radii of reference frequency and *n*th harmonic
$\tilde{a}_n(z)$	beam radius of *n*th harmonic along axis
$\tilde{a}$	arbitrary constant
$\alpha(n,i)$	element of **J** matrix
b	power index of attenuation coefficient
C	speed of sound at bubble wall
c	speed of small signal sound at the frequency *f*
c_o	speed of small signal sound
c_G	speed of sound in gas
c_L	speed of sound in liquid
$\tilde{c}$	complex speed of sound in a gas bubble-liquid
$\mathcal{C}_s$, $\mathcal{C}_i$	saturation and initial gas concentrations
$\mathcal{D}$	diffusion constant of gas in liquid
D_{-3dB}	-3dB focal depth
E_{pa}	error due to the parabolic approximation in predicting focal pressures at low amplitude
e	2.718281828
e	eccentricity of ellipse
F	focal distance
F_1, F_2	first and second foci of ellipse
$\mathbb{F}_n(z)$	normalized complex axial variation of *n*th harmonic at low amplitude
f	frequency
f_o	reference frequency
f_r	resonance frequency
Δf	incremental frequency
f_n	*n*th frequency ($=n\Delta f$)
G	pressure gain
G_{lin}	linear pressure gain
$\mathcal{G}$	universal gas constant (8.315J/mol K)

$g(t)$	normalized aperture waveform
H	enthalpy of liquid at the bubble interface
$\mathbb{H}_n$	local harmonic truncation error at *n*th harmonic
I_c	cavitation likelihood index for pulses
I_{spta}	spatial peak temporal average intensity
$\mathbf{J}$	N X N Jacobian matrix
j	$\sqrt{-1}$
$K(r,\tau)$	aperture shading function
$\mathbb{K}_n(r)$	aperture shading function of *n*th harmonic
k	wavenumber
k_n	wavenumber at f_n
L, d	scalar length
M, M_o	instantaneous and initial mole numbers of gas inside the bubble
m	power index in the Tait equation
n, n_c	harmonic number
N	truncation harmonic number
p	instantaneous acoustic pressure
$P(R)$	pressure at bubble wall
P_g	pressure of gas within bubble
P_o	static pressure of surrounding liquid
P_∞	pressure in liquid far from bubble
p_+, p_-	positive and negative peak pressures
p_{lin}	acoustic pressure predicted by linear theory
p_o	reference pressure
p_{o+}, p_{o-}	positive and negative aperture peak pressures
p_s	shock formation aperture pressure
q	parameter defined in Eq(6.2-4)
$Q(q)$	secondary parameter defined in Eq(6.2-4)
R, R_o	instantaneous and initial bubble radii
$\mathbb{R}$	Rayleigh distance
$\mathbb{R}_n$, $\mathbb{R}_o$	Rayleigh distances at f_n and f_o
R_{oi}	time varying equilibrium bubble radius
r	radial coordinate
S^i	stability interval
S^f	measure of stiffness
T_o	temperature in Kelvin
t	time variable

t_c, t_e	time constants
t_r	rise time of waveform
t_+, t_-	time durations of positive and negative cycle
t_a	time delay of wavefront at the aperture
t_d	time delay between primary and secondary shocks
t_q	predicted acoustic quiet time
$\bar{t}_q$	time period between the main two peaks in detected cavitation signal
$t_{5\%}$	time for 5% reduction in bubble radius
$t_{95\%}$	time for 95% reduction in bubble radius
U	dR/dt
x, y, z	coordinates in the cartesian system
α	attenuation coefficient
α_n, α_o	α at f_n and f_o
$\bar{\alpha}$, $\bar{\alpha}_n$	α and α_n for a gas bubble-liquid mixture
β	nonlinear parameter
ε_n	small quantity defined by Eq(4.2-3)
$\bar{\varepsilon}$	arbitrary small constant
ϵ	acoustic mach number
δ	dispersion coefficient
δ_n	the value of δ at f_n
$\bar{\delta}$, $\bar{\delta}_n$	δ and δ_n for a gas bubble-liquid mixture
Γ	nonlinear gain (p/p_{lin})
Γ_+, Γ_-	nonlinear gains for positive and negative peak pressures ($\Gamma_+=p_+/p_{lin+}$, $\Gamma_-=p_-/p_{lin-}$)
γ	specific heat ratio of gas
η	polytropic exponent of gas
κ	arbitrary power index
Λ_i	ith eigenvalue of matrix
λ	wavelength
μ, $\bar{\mu}$	coefficients of shear and bulk viscosity
$\varnothing_n$	nth complex coefficient of Fourier series
$\bar{\varnothing}_n$	complex conjugate of $\varnothing_n$ ($\bar{\varnothing}_n=A_n+jB_n$)
θ_o	aperture angle
ρ	time varying density
ρ_o	equilibrium density
σ	distance normalized to shock formation length
ϕ	surface tension

τ	retarded time ($=t-z/c_o$)
τ_d	retarded time delay at object point
υ	volume fraction of gas in liquid
Ω	variant of bubble motion at bubble wall
ξ	complex attenuation coefficient ($=\alpha-j\delta$)
ξ_n	ξ at f_n
$\bar{\xi}$, $\bar{\xi}_n$	ξ and ξ_n for a gas bubble-liquid mixture
ζ, ζ'	damping coefficients
$\Delta_\perp$	Laplacian in transverse coordinates

ESWL	Extracorporeal shock wave lithotripsy
EH	Electrohydraulic
EM	Electromagnetic
KZK	Khokhlov Zabolotskaya Kuznetsov
PE	Piezoelectric
PRP	pulse repetition period
PVDF	polyvinylidene difluoride
$\mathcal{I}m$	imaginary part of a complex number
$\mathcal{R}e$	real part of a complex number

CHAPTER 1. INTRODUCTION

The use of high amplitude pulsed ultrasonic fields in the treatment of urinary stone disease is now well established and the clinical procedure is known as extracorporeal shock wave lithotripsy (ESWL). These fields have been studied more recently for their application in tumour therapy and in modifying drug uptake in tissue (Russo et al 1987). This chapter briefly summarizes the current status of clinical ESWL and the physical characteristics of the high amplitude pulsed ultrasound used. The project aim and the structure of the thesis are then outlined.

1.1 Extracorporeal shock wave lithotripsy

Extracorporeal shock wave lithotripsy (ESWL) has, since the first successful treatment of a patient with urinary stone disease in 1980 (Chaussy et al 1980), become established as part of a growing armoury of non-invasive techniques for treating stone disease (Kirchberger 1991, Heinrich et al 1989, Chaussy 1988). ESWL involves focusing high amplitude pulsed ultrasound generated outside the body on to calculi at depth in human tissue so that they disintegrate (Davros et al 1991, Rotus 1987, Chaussy 1986). Stones are positioned at the focus of the sound field under X-ray or ultrasound guidance (Coleman et al 1987c). Stone debris,

following urinary stone treatment, passes down the urinary tract spontaneously, or, in the case of gall stones, is either spontaneously passed through the bile duct or chemically dissolved (Hofmann 1991, Delius et al 1988b, Neubrand 1986). In contrast to other methods, ESWL is non-invasive and on modern lithotripters, patients commonly require little or no anaesthesia.

In the treatment of urinary stone disease, ESWL competes with and compliments minimally invasive procedures including percutaneous surgery (Mays et al 1988, Webb et al 1986) and endoscopic methods (Eisenberger et al 1985) for extracting or crushing stones. It is used as a single therapy in about 70% of cases and in combination with other techniques in about 15% of cases (Kahnoski et al 1986, Schulze et al 1986). Together, these procedures have largely replaced the once dominant open surgical procedure for kidney stone removal which is now performed in less than 1% of cases.

Indications that ESWL might make surgery obsolete in biliary stone disease have not been fulfilled and ESWL is used in only about 20% of treatments in combination with chemolytic drugs in accelerating stone dissolution (Griffith and Gleeson 1990). Common bile duct stones, which make up about 5% of all biliary stones and for which surgical procedures still have a relatively high associated morbidity, are often beneficially treated using ESWL as are

the 5% of patients who are unfit for general anaesthesia or unwilling to undergo what is now a highly successful minimally invasive surgical procedure known as laparascopic cholysystectomy (Sauerbruch and Paumgartner 1991).

Progress in the safe application of ESWL in stone disease has been driven by increasing clinical experience rather than by any great advance in the understanding of the basic physical mechanisms causing stone fragmentation or side effects. Nevertheless, this novel medical use of high amplitude pulsed ultrasound fields has inspired a wide range of studies, many of which describe previously unreported biological effects.

1.2 Physical properties of lithotripsy fields

The properties which particularly characterize the acoustic fields employed in clinical lithotripters are high amplitudes, low pulse centre frequencies and low duty-cycles. A typical pressure waveform measured in water at the focus of a lithotripter (Dornier HM3) is shown in Fig 1.2-1 (Coleman et al 1987b). The waveform is characterized by an initial compressional half cycle having a rapidly rising leading edge which is followed by a more slowly varying rarefactional half cycle. The rapid rise time of the leading edge is characteristic of a shock wave and, while this term has a strictly technical definition

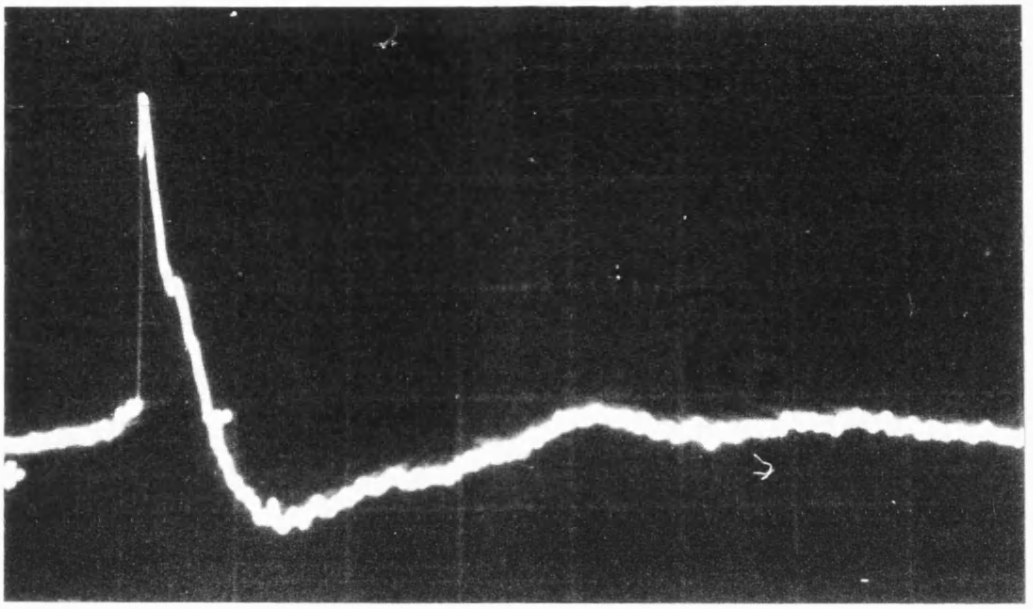

[Fig 1.2-1] A typical pressure waveform measured in water at the focus of a Dornier HM3 lithotripter (Coleman et al 1987b).

which is considered in chapter 5, it is common practice to refer to lithotripsy pulses as shock waves, a term used here to denote the high amplitude pulse generated by any lithotripter whether technically shocked or not.

The physical properties of the acoustic field used in ESWL are illustrated in Fig 1.2-2 and Fig 1.2-3 which show how usefully the ESWL field is distinguished from those used in medical diagnostic and physiotherapeutic applications (Coleman et al 1992b). The data used in these figures were obtained from a variety of sources (measured in water) including Duck and Martin (1991), Coleman and Saunders (1989), Hill and ter Haar (1989), Duck (1987), McHugh (1986) and Duck et al (1986, 1985).

A plot of spatial peak temporal average intensity (I_{spta} in W/m^2) against spatial peak compression (p_+ in MPa) is shown in Fig 1.2-2. Clinical ESWL equipment radiating into water clearly generates values of p_+, 20 to 100MPa, which are well above those employed in medical diagnostic and physiotherapeutic uses of ultrasound. However, the low duty cycle and short pulse duration give the lithotripsy field a characteristically low time averaged intensity with values often lower than those generated by diagnostic and physiotherapeutic ultrasonic machines. The horizontal line shown in Fig 1.2-2 represents the time averaged intensity below which it has been suggested (AIUM/NEMA 1989) that biological effects in tissue due to thermal mechanisms can

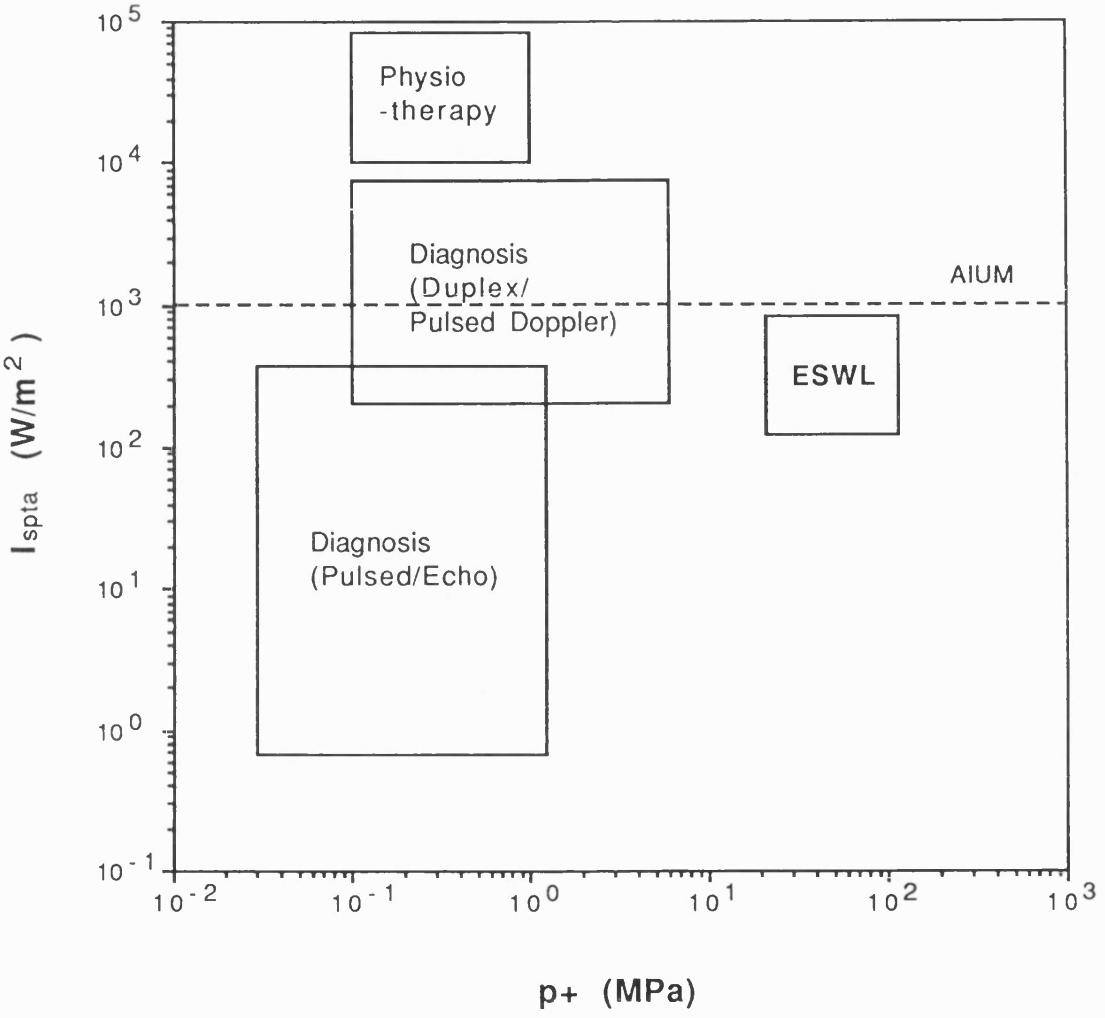

[Fig 1.2-2] A plot of the spatial peak temporal average intensity (I_{spta} in W/m^2) against the spatial peak pressure (p_+ in MPa) for different medical ultrasonic modalities. The horizontal dotted line indicates the level referred to in the AIUM/NEMA statement on the safety of medical ultrasound.

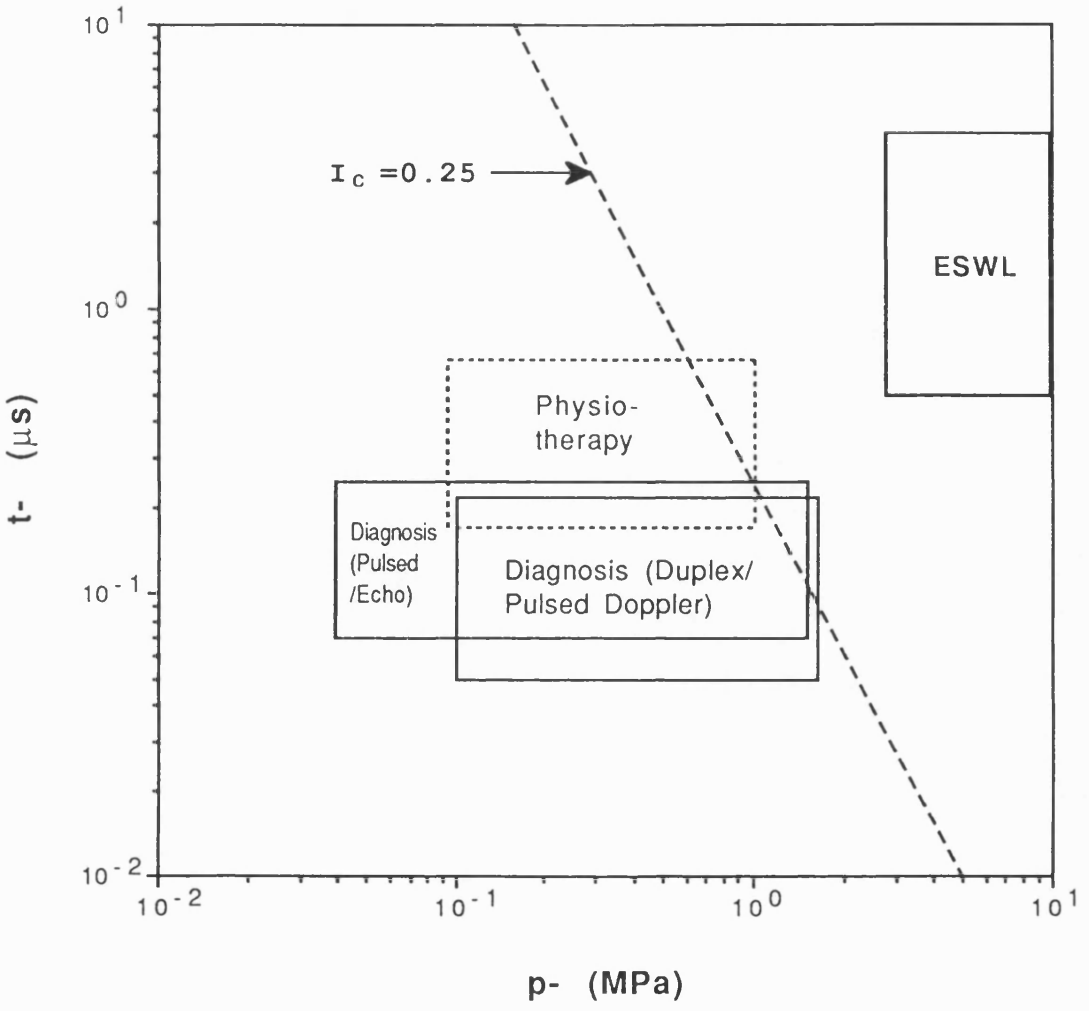

[Fig 1.2-3] A plot of the duration of the first negative half cycle (t- in μs) against the peak negative pressure (p- in MPa) for different medical ultrasonic modalities. Above the dotted diagonal line the cavitation likelihood index (I_c) is greater than 0.25 and cavitation is likely whereas below the line cavitation is unlikely. Physiotherapy ranges of p- and t- are shown (in dotted box) for completeness, although I_c refers only to a pulsed ultrasound.

be assumed to be absent. In general, therefore, at the clinically used duty cycles of 1 to 3Hz, lithotripters will produce no appreciable heating in exposed tissue despite the large amplitudes generated. Indeed Filipczynski and Piechocki (1990) estimated that even at 100Hz pulse repetition rates, two orders of magnitude higher than clinically used, the temperature rise will be less than 2°C for a typical 3000 shock wave exposure using a Dornier HM2 machine with p_+=80MPa measured in water.

Comparison of the peak negative pressure (p- in MPa) with the duration of the first negative half cycle of pulse (t- in μs) shown in Fig 1.2-3 illustrates another important distinction in the acoustic fields used in between ESWL and other pulsed ultrasonic medical applications. In the figure the physiotherapy shown in dotted box is for completeness, although continuous waves are used in it. Lithotripters are seen to generate the highest values of p- (up to 10 MPa) although the lower range overlaps with those in certain diagnostic procedures. The values of p- and t- determine the amount of mechanical work that can be performed on a pre-existing bubble in the negative phase of the acoustic cycle (Apfel and Holland 1991). Therefore these two parameters give some guide as to the likelihood of cavitation generation in fluids provided optimally sized bubble nuclei can be assumed to be present. Such a cavitation likelihood index (defined only for pulses), $I_c=(p-)^2t-$, has been suggested by Apfel and Holland (1991).

Experimental evidence suggests that for values of I_c more than 0.25 (for p- in MPa and t- in μs) cavitation is likely provided optimally sized nuclei can be assumed to be present in the exposed fluid (water or blood serum). Values of I_c = 0.25 are shown as a dotted diagonal line in Fig 1.2-3 indicating that cavitation is likely in the region above the line which includes some diagnostic equipment as well as all clinical lithotripters.

The high amplitude pulsed ultrasound field used in clinical lithotripsy, therefore, can be expected, under appropriate conditions, to generate nonlinear and cavitation effects in the absence of tissue heating. This combination of properties is unique to the field and makes them a useful tool not only in stone disease but also in the study of the non-thermal biological effects of ultrasound.

1.3 Aim and structure of the thesis

1.3.1 Aim of the thesis

The thesis aims to show that useful predictions related to the medical application of the high amplitude pulsed ultrasonic field are possible provided nonlinear effects including shock formation and acoustic cavitation are considered. The modeling of such a field has been considered in several studies but there is little published

information on practical modeling of the ESWL field. There are far less published studies which allow detailed predictions related to acoustic cavitation. It is the aim of this thesis to make a first attempt to solve these problems by utilizing relatively simple theoretical models.

The particular interest in the high amplitude pulsed ultrasound considered in the thesis is justified since it has been used in medical applications only recently and represents an extreme and potentially interesting example of nonlinear acoustic behaviour. It is expected that the detailed consideration of problems of the acoustic exposure from lithotripters will allow identification of the physical parameters of the acoustic fields that influence the degree of acoustic cavitation and the biological effects associated with cavitation. This study also serves to highlight deficiencies in hydrophone technology as well as in theoretical models for the specification of the *in situ* acoustic exposure in ESWL fields.

This study is intended to make it possible to specify tissue exposure from lithotripters, to identify the parameters related to biological effects, and to indicate ways of controlling the acoustic field for enhancing the treatment (eg, to minimize tissue damage in ESWL or to increase the damage in proposed tumour therapy applications). It is also intended that this study will contribute to wider applications of high amplitude pulsed

ultrasound fields.

1.3.2 Structure of the thesis

Chapter 1 defines the acoustic field to be considered in the thesis under the heading of high amplitude pulsed ultrasound. The measured parameters of ultrasonic fields commonly used in medicine are compared with those of the high amplitude pulsed ultrasonic fields used in clinical ESWL. The aim and structure of the thesis are then given.

Chapter 2 considers the experimentally and clinically observed properties of high amplitude pulsed ultrasound fields and some evidence of the mechanisms by which they interact with various media including tissue. Much of this evidence comes from experience with clinical lithotripsy although more limited evidence from tumour therapeutic uses is also considered.

Chapter 3 overviews the relevant theoretical models of finite amplitude wave propagation in diffractive fields and discusses the limitations of these models with respect to the prediction of lithotripsy fields.

In Chapter 4, a one dimensional frequency domain nonlinear propagation model is developed which can be appropriate to focused high amplitude pulsed fields generated by clinical lithotripters. Special attention is paid to the problems related to nonlinear effects which may alter the beam

profile during propagation and to stability of the numerical model including other possible sources of error. The model is validated by comparison made with existing models as well as published measurements.

In Chapter 5, the prediction of the temporal and spatial parameters of the field generated by an electrohydraulic type of lithotripter is made using the proposed propagation model. The effects of the source output setting on focal fields are also investigated and saturation effects are examined at high source output powers.

In Chapter 6, special consideration is given to the cavitation field produced by the rapidly pulsed high amplitude ultrasound where the prediction is not possible using the (single pulse) propagation model alone. A reasonable analysis of the cavitation field is achieved using the propagation model properly combined with existing bubble dynamic models.

Chapter 7 summarizes the proposed theoretical approach and achieved results. Suggestions for the extension of the theoretical approaches and further experimental works are also given.

The main original contributions of this study are contained in Chapter 4 to 7.

CHAPTER 2. HIGH AMPLITUDE PULSED ULTRASOUND: EXPERIMENTAL AND CLINICAL RESULTS

2.1 Introduction

The high amplitude pulsed ultrasonic fields generated by lithotripters have been employed in a wide range of studies on their biological effects. Many of these studies are directed at elucidating the mechanisms by which the high amplitude pulsed ultrasound interacts with tissue and stone. The literature on the physical aspects and biological effects of high amplitude pulsed ultrasound fields has been reviewed by Coleman et al (1992b), Griffith and Gleeson (1990), and Chaussy and Fuchs (1989).

This chapter summarizes the main experimental and clinical results of the lithotripsy field and its unique ability to generate acoustic cavitation in the absence of tissue heating making it a valuable tool in the study of the biological effects produced by cavitation. These studies highlight the need for the precise specification of *in situ* tissue exposure if further advances in the understanding of biological effects in the high amplitude pulsed ultrasound fields are to be made.

2.2 Acoustic cavitation

Acoustic cavitation has been defined as any observable activity involving pre-existing cavities or bubbles stimulated into motion by an acoustic field (Crum and Fowlkes 1986, Apfel 1981). This effect has been widely recognized as a possible mechanism by which the high amplitude pulsed ultrasound may induce biological effects (Riedlinger 1990, Delius et al 1989).

Theoretical work by Church (1989) using the Gilmore model predicts that a spherical bubble in water exposed to the lithotripsy field is first quickly compressed due to the positive pressure cycle, and then grows rapidly several hundred fold in size. This prolonged expansion phase lasts for a long time compared with the pulse duration, and during this time any gas in the fluid may diffuse into the bubble. The bubble may then collapse a second time and subsequently a number of times. This theoretical study indicates that the violence of this transient cavitation activity is sensitive in particular to the negative pressure which follows the initial compressive cycle in the pressure waveform.

The mechanisms by which cavitation may cause biological damage are usually cited as extremely high localized temperatures and pressure gradients, although the biological consequences of such factors are largely unknown. Church (1989) predicts pressures of the order of

10^5MPa and temperatures up to 10^5K at the moment of collapse within optimum sized bubbles in an aqueous medium at a typical ESWL field under the assumption of symmetrical bubble collapse. In practice, the bubble near a boundary, however, collapses asymmetrically and, in this case, the damage is associated with high speed liquid jets which impinge on the surface (Lauterborn and Bolle 1975, Plesset and Chapman 1971). Fig 2.2-1 shows a photograph of a bubble collapsing near a boundary and clearly indicates the presence of an impinging jet of liquid (Crum 1982).

Cavitation induced damage generated during ESWL in water has been variously observed as pitting of metal foils (Coleman et al 1987b) and membrane hydrophone electrodes (Coleman and Saunders 1989) including discrete regions (10 to 2000μm in diameter) of fogging in photographic emulsions (Geise et al 1990). Fig 2.2-2 shows the general view of a 0.02mm thick section of a aluminum foil in water exposed to the high amplitude pulsed ultrasound generated by a Dornier HM3 lithotripter. The deep impressions in the foil are caused by the extremely violent impact of a high speed liquid jets developed in asymmetrically collapsing cavitation bubbles.

Any bubbles that may occur in tissue will be inhibited in their capacity to expand by the surrounding tissues (Carstensen et al 1990) and it is probable that such gas bodies in tissue do not respond to acoustic fields in the

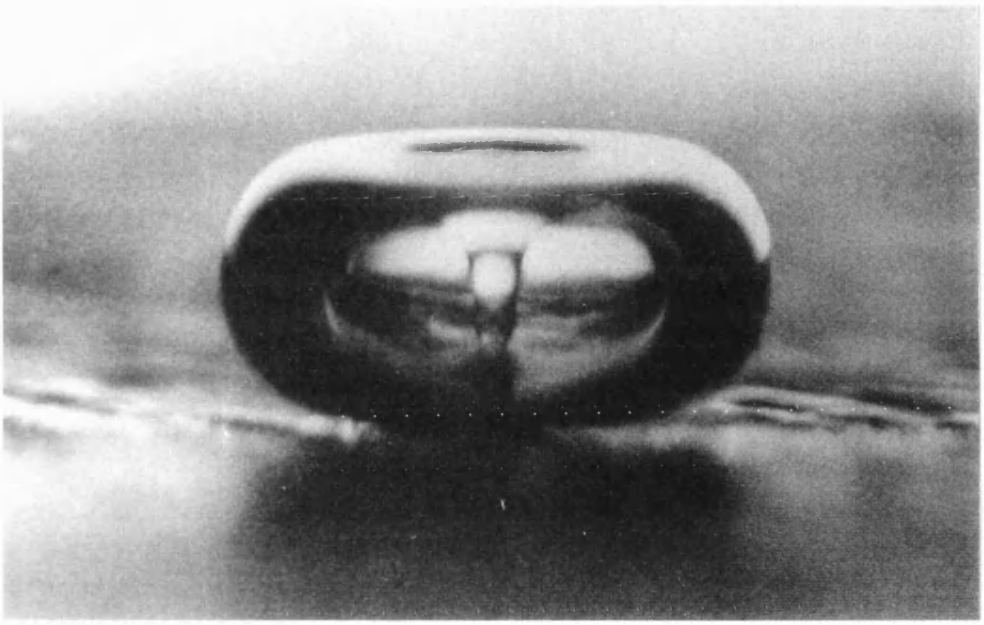

[Fig 2.2-1] Photograph of liquid jet formation during cavitation bubble collapse: the diameter of the bubble is about 2mm (Crum 1982).

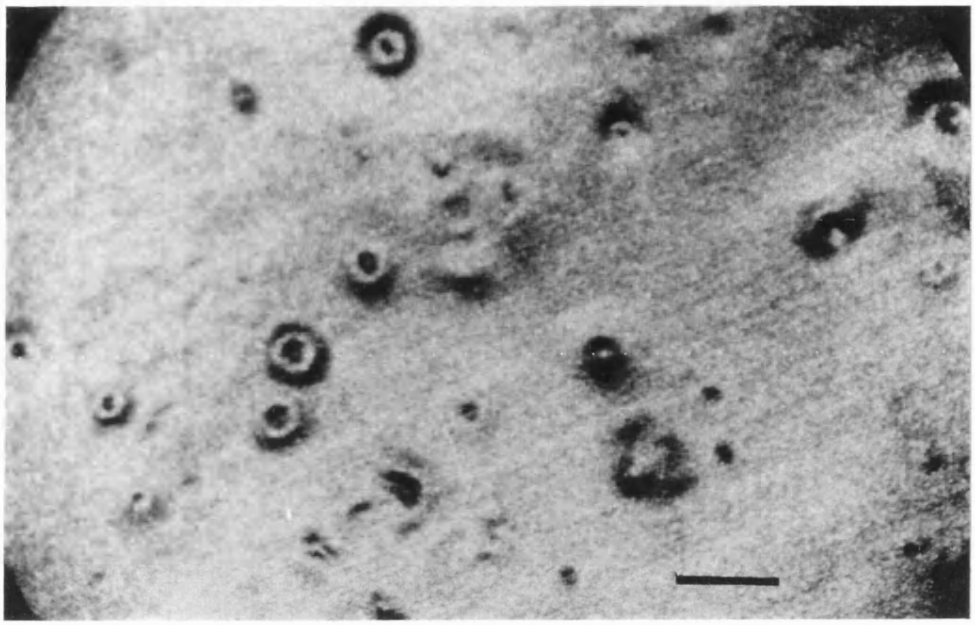

[Fig 2.2-2] Light micrograph of a 0.02mm thick section of aluminum foil following the exposure of high amplitude acoustic pulses generated from a Dornier HM3 lithotripter. The deep impressions shown in the foil are caused by the impact of a cavitation jet. The scale bar represents 1mm (Coleman et al 1987b).

manner described by such a model which assumes the presence of spherical bubbles in an infinite aqueous medium. Accordingly, cavitation induced effects in tissue may be qualitatively different from those predicted in water and the negative pressure, as a classical predictor of cavitation, should be reconsidered for the behaviour of gas bodies in tissue (Hartman et al 1990a). This has been displayed *in vitro* by embedding cells in gelatin resulting in considerably less cell damage than cells in suspension (Brümmer 1989a).

The presence of bubbles stabilized by diffusion influences considerably the compressibility of a medium. For an oscillating resonant bubble, the effective absorption scattering cross section is many times greater than for a liquid or solid particle of the same size (Anderson and Hampton 1980). The acoustic beam is therefore effectively scattered and little coherent signal is passed through a region of even mild cavitation. Reduction in stone damage, when cavitation activity is enhanced by increasing the oxygen content in the lithotripter water bath (Brümmer et al 1989ab), suggests the increased attenuation of shock waves that propagate to the focus in the cavitation field.

Cavitation activity in lithotripsy fields has been observed using a focused hydrophone, fast photomultiplier tube (Coleman et al 1992a), resonant bubble detector (William et al 1989), and fibre optic hydrophone (Granz et al 1989).

The cavitation signals from the different detectors show similarities in structure and timing and are shown in this thesis to be in reasonable agreement with the theoretical predictions based on single spherical bubble dynamics.

2.3 Stone fragmentation

While the precise mechanism of stone fragmentation induced by high amplitude acoustic pulses is not clearly known, direct and indirect mechanisms are identified from studies using stone substitute materials (Delius and Gambilher 1991, Holmer et al 1991, Kambe et al 1988, Whelan and Finlayson 1988). The direct effect results from propagation of the shock waves in the stone material and is attributed to spalling (Brümmer et al 1989a, Nasr 1986). The indirect effect, on the other hand, appears to be mediated by the fluid surrounding the stone and is attributed to acoustic cavitation (Sass et al 1991, Koch and Grüewald 1989, Delius et al 1988a). The direct and indirect effects do not exclude each other and, indeed, act in common, although the relative importance of these mechanisms appears to vary depending on the properties of stones (Vakil et al 1991) and exposure conditions (Whelan et al 1988).

Spalling results from the enhanced high tensile stress as a result of the internal reflection of high amplitude acoustic pulses, and, if this is important, acoustic

impedance would be a major determinant of stone destruction. Cracks may be induced in the brittle stone due to shear stresses resulting from the acoustic wave travelling inside the stone. The pressure waveform is expected to determine the pressure gradient in the stone and hence the fragment size produced. For instance, a short pulse width with rapid rise time would produce smaller fragments (Eisenmenger 1988, Hepp 1988).

Cavitation events mediating stone fragmentation are demonstrated in Fig 2.3-1. This figure represents high speed photograph images at 100μs intervals of a human gallstone suspended in water following exposure to a single acoustic pulse (p_+=64MPa) generated from an electromagnetic source (Sass et al 1991). Bubbles are seen to grow and collapse around the stone and a jet of stone debris is observed on the anterior surface of the stone. Bubble activity appears to commence immediately with the bubbles achieving maximum diameter within 100μs of the shock wave arrival and dying away some 500 to 600μs after the shock wave. The cavitation activity is also observed within the small split lines of the stone which are produced as a result of the direct effect of the high amplitude acoustic pulse when the surrounding fluid enters the small cracks. The cavitation event inside the stone may enhance stone fragmentation. The electron microscopy shown in Fig 2.3-2 reveals 20 μm to 70 μm diameter cavitation pits in fissures deep within the stone.

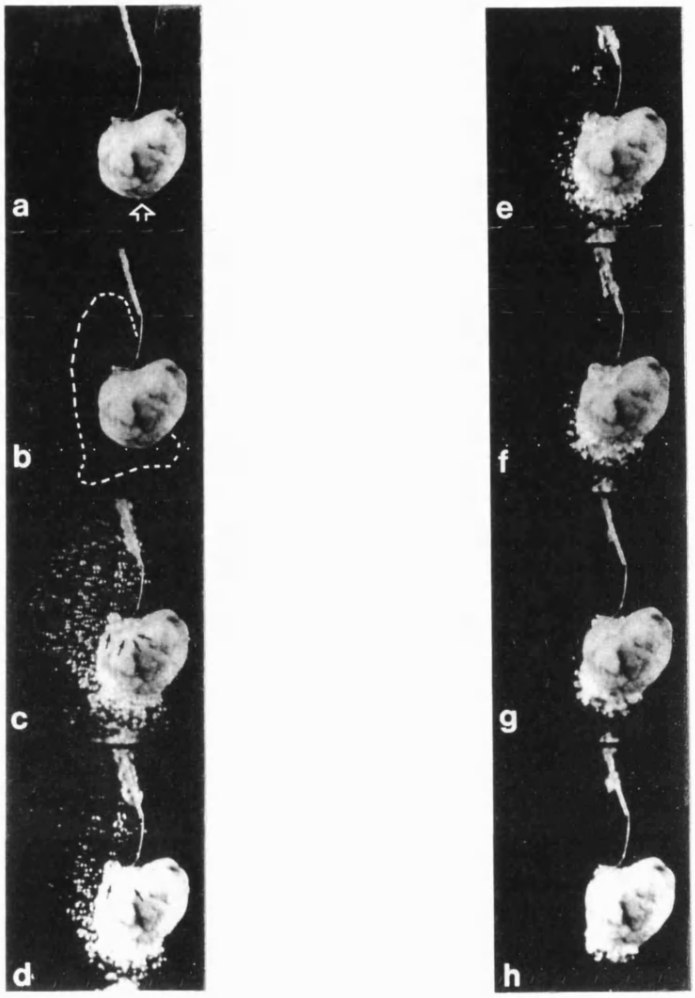

[Fig 2.3-1] High speed sequence of a human gallstone (1.3cm X 1.5cm X 0.9cm) hit by high amplitude pulsed ultrasound. The interval between frames is 100μs. (a) represents the stone 100μs prior to the acoustic exposure and (b)-(h) show cavitation activity for 600μs following the exposure. The arrow in (a) indicates the ultrasonic pulse orientation from below, and inside the marked area in (b) indicates a vague haze of small bubbles (not clearly shown in this picture) as a sign of growing cavitation (Sass et al 1991).

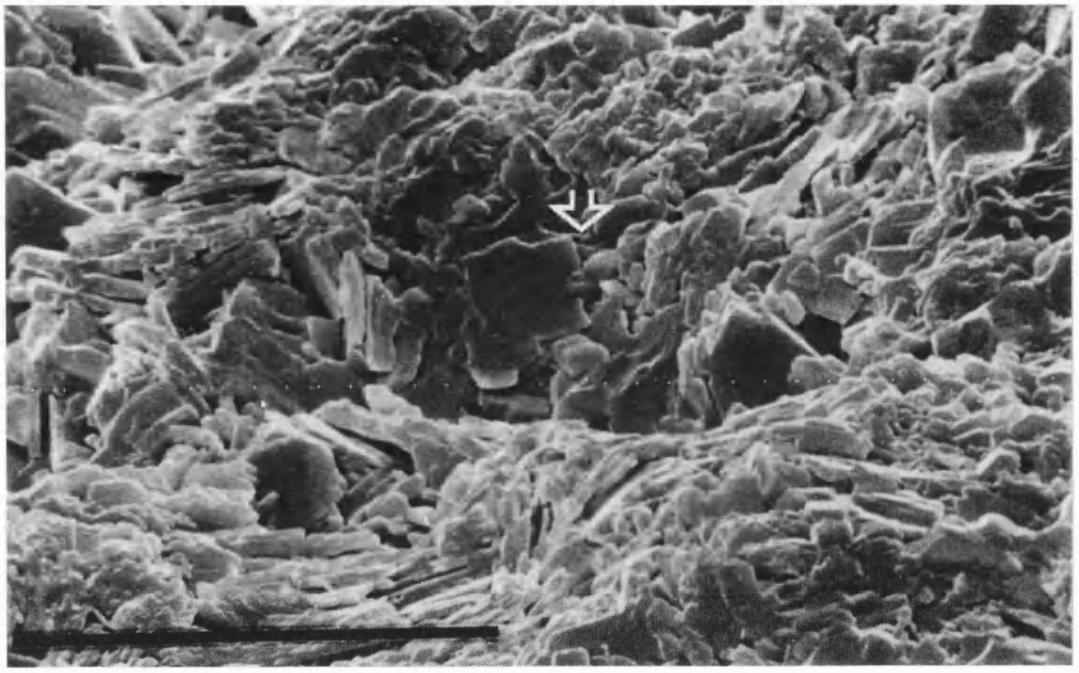

[Fig 2.3-2] Scanning electron micrograph of a human gallstone after fragmentation inside an intact human gallbladder filled with natural viscous bile. Microjet damage within a small cracked fissure which is caused by imploding cavitation bubbles is indicated by the arrow. The scale bar represents 50μm (Sass 1991).

An experimental observation that hyperbaric pressure suppresses gallstone destruction (Delius and Brendel 1989) supports the condition that cavitation can be regarded as a major mechanism of gallstone destruction. It has also been observed that the fragmentation of gallstones in a highly viscous fluid such as a glycerol was impeded (Delius et al 1988a) and the increased partial pressure of CO_2 in the fluid surrounding stones inhibits the fragmentation (Coleman et al 1991c). These suggest that the condition of the fluid is important, ie, the high viscosity increases the cavitation threshold and the increased gas tension reduces the violence of the bubble collapse. The successful clinical fragmentation of human urinary stones compared to biliary stones may therefore be the result of the high viscosity of bile relative to urine.

2.4 Biological effects: Clinical

The routine treatment, involving not more than 3000 shocks, does not seem to cause clinically significant injury, but there is major injury to most tissues at the large exposure of up to 6000 shocks (Wilbert et al 1990). Haemorrhaging in the kidney can be caused in routine treatment, but this side effect is considered to be minor and reversible. As indicated from *in vivo* experimental studies, lung tissue is most vulnerable to shock wave exposure and is always

excluded from the exposure during ESWL, in particular, during the treatment of the biliary stone disease (Hartman et al 1990b).

Clinically observed short term side effects following ESWL include haematuria, renal colic, perirenal and intrarenal haematomas, biliary colic, pancreatitis, arrythmias and skin bruising (Escartin et al 1989, Baumgartner et al 1987, Coleman et al 1987c, Newman 1987, Drach et al 1986, Chaussy 1986). Imaging techniques have shown morphological changes in kidneys following ESWL (Dyer et al 1990), such as diminished perfusions, perirenal fluid collection and oedema (Jocham 1987, Jenkins et al 1987). Changes in the urinary protein concentrations were measured and interpreted as indicating transient parenchymal trauma comparable to a renal contusion following ESWL (Knapp et al 1988).

Most of these side effects can be attributed to shock wave exposure, although some, including ureteric colic, obstruction and urosepsis are undoubtedly due to the passage of stone fragments. The short term complications are likely to be limited, reversible, and of no clinical significance. So far there is no evidence of suggested long term side effects such as a reduction in renal (ie, glomerular and tubular) function or increased incidence of hypertension (Lingeman et al 1988).

2.5 Biological effects: Experimental

2.5.1 *in vitro* studies

The disruption, reduced viability and proliferation of cells exposed to the high amplitude pulsed acoustic field, while held in a suspension in culture medium, has been widely demonstrated by techniques such as trypan blue exclusion (Smits et al 1991, Gambihler et al 1990), clonogenic assay (Laudon et al 1989, Oosterhof et al 1989) and flow cytometry (Brümmer et al 1989a, Russo et al 1986). All *in vitro* studies indicate that the shock wave induced cell damage depends on 'exposure' although this parameter cannot, as yet, be precisely specified.

Fig 2.5-1 shows the electron micrographs of L1210 mouse leukemia cells in suspension exposed to 500 shock waves generated by a Dornier XL1 lithotripter (Bräuner et al 1989). Figure a represents cells in control conditions and figures b to f illustrate cell fragmentation including the alteration of cell shape, swelling of mitochondria, vacuolization of the cytoplasm, perinuclear and cytoplasmic cisternae and ruptured cell membrane. These changes in cell morphology are commonly interpreted as indicating osmotic effects providing evidence of changes in cell membrane permeability (Brümmer et al 1989a, Oosterhof et al 1989).

The cell damage and cytotoxicity induced by high amplitude acoustic pulses are inhibited when cells are immobilized in

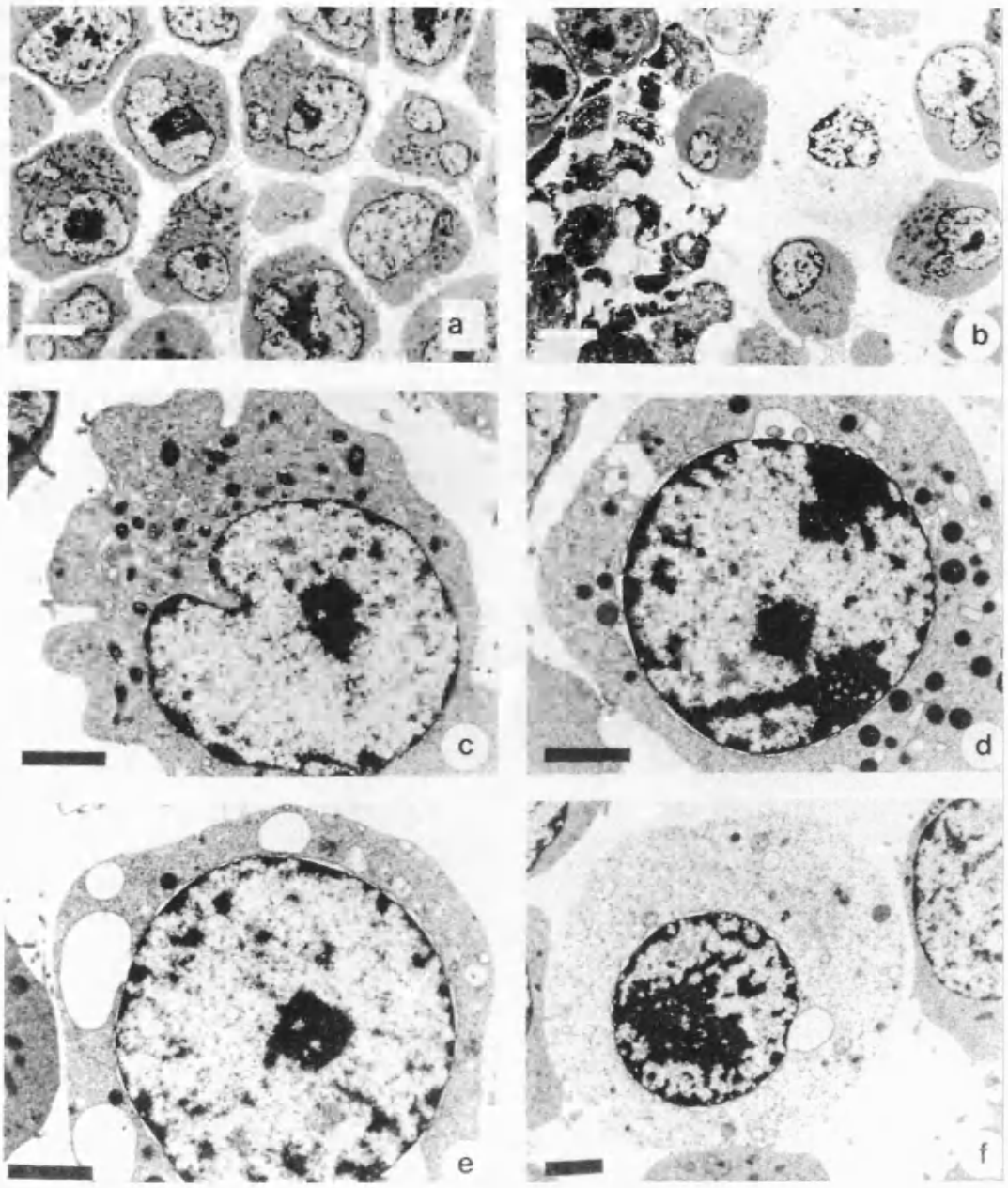

[Fig 2.5-1] Electron micrographs of L1210 mouse leukemia cells in suspension. (a) represents cells in control and (b)-(f) show cell suspensions treated with 500 high amplitude acoustic pulses from a Dornier XL1 lithotripter: (b) cell fragmentation, (c) alteration of cell shape (d) swollen mitochondria and vacuolisation of the cytoplasm, (e) large perinuclear and cytoplasmic cisternae, and (f) ruptured cell membrane (Bräuner et al 1989).

gelatin (Smits et al 1991, Brümmer et al 1989a) possibly due to a reduction in the amount or violence of cavitation activity in gelatin. Other experimental evidence suggesting that cavitation is an important mechanism of cell disruption is that, when placed in suspension under an increased static pressure, cells exposed to shock waves suffer from less disruption than those at atmospheric pressure (Gambihler et al 1990). As yet there is no clear evidence that shock waves have a direct effect on cells which is not mediated by intercellular fluids.

The possibility that shock waves can induce the enhancement of cytotoxicity of certain drugs has been widely examined in the literature. The drug is added to the cells typically 1 to 24 hours after the exposures of the orders of 2000 high amplitude acoustic pulses. The cytotoxic effect on cell growth, viability and attachment are reported to have been enhanced by drugs such as Vinblastin (Oosterhof et al 1989) and Cisplatin, Doxorubicin (Berens et al 1989) although in several studies there is insufficient evidence to verify a synergistic rather than simply additive effect.

2.5.2 *in vivo* studies

In vivo cellular damage including haemorrhages in the inner and outer renal capsule (Delius and Brendel 1989) and bleeding in the lungs (Delius et al 1987) occur preferentially in or at the vascular system where fluid interacts with high amplitude pulsed ultrasound. Vascular

damage induced by the shock wave exposure *in vivo* was observed in several studies (Goetz et al 1988) and this is recognized as an important approach to increasing therapeutic gain in cancer therapy.

Temporal suppression in the growth of tumors *in vivo* exposed to the high amplitude pulsed ultrasound fields have been reported (Oosterhof et al 1990, Randazzo et al 1988, Russo et al 1987). A growth delay can, not surprisingly, be induced if tumour cells are exposed to shock waves in suspension prior to injection into the animals (Russo et al 1986). A significant delay in tumor growth has been reported by the fractionation of the exposure with appropriate delay on the periphery of the tumour (Weiss et al 1990) and this suggests that tissue at the periphery of tumours is more susceptible to damage than the tumour tissue itself. Goetz et al (1988) has shown that, when exposed to as few as 100 shock waves on a Dornier XM1 lithotripter operated at 15KV, A-Mel-3 tumours in hamsters suffered from petechial haemorrhaging, macro molecular leakage, intravascular haemorrhages at the site of small venules as well as transient arterial vasoconstriction in tissue surrounding the tumour.

As indicated in *in vitro* studies, synergistic effects of shock waves with biological response modifiers (Oosterhof et al 1991), and chemotherapeutic drugs (Oosterhof et al 1990, Randazzo et al 1988) under *in vivo* conditions have

been reported in several studies. The cytotoxic drug, Cisplatin, injected just before exposure to 2000 shock waves from a Dornier XL-1 lithotripter operated at 20 KV causes a 13 day delay in AT-2 tumour growth and no observed increase in lung metastases compared with a growth delay of 1.5 days with shock waves alone and 7 days with Cisplatin alone although the combined treatment increased mortality from 9% with Cisplatin alone to 29% (Holmes et al 1990).

Extensive damage of pulmonary tissues was observed during ESWL treatment, in particular, for gallstone treatment in animal experiments (Hartman 1990b, Delius et al 1987). The lung tissue trauma is likely to be attributed to the acoustic impedance mismatch between air and pulmonary tissue, and the lung haemorrhage is probably a example of cavitation related processes (Delius and Brendel 1989).

Evidence that ESWL fields generate cavitation *in vivo* has been reported by Delius et al (1990) who detected signals associated with cavitation using a conventional real time B-scan ultrasound scanner when high amplitude acoustic pulses were administrated to liver tissues. Cavitation bubbles were detected first intravascularly and were flushed away with the blood flow, and later stationary changes were seen. The occurrence of cavitation and the focal nature of the tissue damage in the shock wave path suggests that cavitation might be involved in the generation of tissue damage.

Further experimental evidence suggesting that cavitation plays an important role in tissue damage was given by Delius and Brendel (1989). Renal tissue and haemolysis were increased when shock waves were applied with fast administration rates (15 to 100Hz), and the haemolysis was also increased after administration of pairs of shock waves with normal administration rate (1Hz). This is attributed to a tandem action of shock waves in tissue, ie, the tensile waves of the first shock wave generates bubbles that are hit by the positive pressure part of the following shock wave.

2.5.3 Summary

Shock waves produce haemorrhages in vascularized tissue and thrombi in blood vessels. In most tumours there is little effect but there is some evidence that highly vascularized tumour tissue or tissue at the periphery of tumours can be damaged to produce a growth delay. Increased echogenicity in vessels, both transient and long term, may suggest the presence of cavitation *in vivo* during the clinical exposure of the high amplitude pulsed ultrasound fields.

2.6 Exposure and dose parameters

The biological effects literature reviewed here highlights the lack of any reasonable dose parameter in lithotripsy. This is due both to the difficulty in measuring exposure parameters such as peak pressures and also a lack of understanding of the mechanisms by which shock waves generate the observed biological effects.

The dose is often specified in the literature by the product of the number of shock waves and electrical energy stored in the discharge capacitor prior to release of shock pulses, since this requires no technically difficult measurements. However this parameter is easily shown to be inadequate and the same total electrical energy can cause different amounts of biological damage depending on the exposure conditions (Gambihler et al 1990). For instance, viscosity, gas content or temperature of the cell suspension fluid influence cell lysis, since these are likely factors to influence the degree of cavitation implicated as a principle mechanism inducing biological effects. This suggests that some relevant aspect of cavitation, such as the acoustic emission or sonoluminescence associated with cavitation activity may eventually provide a reasonable dose parameter in ESWL. A convenient, preferably non-invasive measurement of these parameters may therefore provide an independent variable for examining dose response to biological effects and a link between *in vitro* and *in vivo* studies by removing some

of uncertainties introduced by exposure conditions.

The acoustic exposure, as opposed to dose, in ESWL has been measured within the past few years using hydrophone probes made of a piezoelectric polymer, polyvinylidene difluoride (PVDF). However these PVDF hydrophones were originally developed for the measurements of the acoustic output of diagnostic ultrasonic devices (Lewin and Schafer 1986) and have frequency and amplitude response limitations in ESWL fields. Measurement problems are critical in ESWL fields since the hydrophone is required to response linearly and needs to have a calibrated response over the wide range of frequencies (0.1-50MHz) and pressures (up to at least 100MPa), which, in practice, is not easy to achieve (Lewin and Schafer 1991). Sources of systematic uncertainty in a PVDF hydrophone measurements of p_+ in ESWL fields has been estimated to be 25% (Coleman et al 1987a) and, if random uncertainty is included, about 36% on an electrohydraulic type lithotripter. Theoretical works of Harris (1991) on typical ESWL pressure waveforms predicts that significant errors can occur in the measurement of the fields unless hydrophone bandwidths are much wider.

Under *in vivo* conditions the problems of measurement are considerably increased as a result of additional uncertainties in calibration and directional response problems. At present there are no reliable published

reports of *in situ* pressures generated during ESWL. This emphasizes both the need for a theoretical approach and the difficulties in verifying such an approach using existing measurements.

In summary the improvement of the ability to specify *in situ* acoustic exposure and better quantification of the relevant aspects of cavitation fields may be key issues to extend the present knowledge of biological effects of the high amplitude pulsed ultrasound fields and enhancement of clinical ESWL. Since these parameters are difficult to measure, a reasonable approach at present is to obtain the theoretical predictions based on nonlinear propagation models and bubble dynamic theories. While experimental evidence remains sparse there is some indication that this theoretical approach may yield useful results which can be used to improve the design of biological effect experiments with ESWL fields.

CHAPTER 3. OVERVIEW OF THEORETICAL APPROACHES OF FINITE AMPLITUDE ULTRASOUND IN DIFFRACTIVE FIELDS

3.1 Introduction

The study of nonlinear acoustics dates back to the 19th century (Beyer 1974) and, since then, has resulted in the derivation of a number of approximate nonlinear wave equations that describe the nonlinear propagation process. Although analytical solutions can be obtained for certain specific cases, it is not in general possible to obtain the solutions analytically that may be applicable to practical situations such as are required in this study of lithotripsy fields. For this reason much of the work over the last decade has concentrated on the use of numerical models to solve the nonlinear propagation process.

In this chapter, some of the theoretical models describing the propagation of finite amplitude ultrasound in focused fields and their numerical solutions are considered. In particular the current limitations of the models with respect to the prediction of lithotripter fields are discussed.

3.2 Nonlinear wave propagation

In finite amplitude propagation in real fluids, the acoustic wave distorts primarily because the pressure density relationship of the medium is nonlinear. If the wave travels a distance of many wavelengths before its profile is significantly distorted (weak shock condition), it may be sufficient to terminate the Taylor series expansion form of the pressure density relationship at the 2nd order term in the derivation of the governing wave equation. One typical example of such a 2nd order wave equation is the Burgers equation which describes the nonlinear distortion of a finite amplitude plane wave propagating through a thermoviscous fluid (Blackstock 1964). A simple form of Burgers equation for the acoustic pressure is

$$\frac{\partial p}{\partial z} = \frac{\beta}{c_o^3 \rho_o} p \frac{\partial p}{\partial \tau} + \frac{\zeta'}{2c_o^3 \rho_o} \frac{\partial^2 p}{\partial \tau^2} \qquad (3.2\text{-}1)$$

where $p(z,\tau)$, the instantaneous acoustic pressure at a distance z from the initial plane (z=0), has been abbreviated by dropping the term (z,τ), τ is the retarded time given by $t-z/c_o$ where t is a time variable, β and ρ_o are the nonlinear parameter and density of the medium respectively, and ζ' is the damping coefficient defined by $\bar{\mu}+4\mu/3$ where μ and $\bar{\mu}$ are respectively the shear and bulk viscosity coefficients.

The weak shock condition may be specified by the acoustic mach number defined by the ratio of the particle velocity to the phase velocity and the 2nd order approximation used in Eq(3.2-1) is valid for values of the acoustic mach number considerably less than unity, in particular, not bigger than 0.1 (Fenlon 1971). In water this condition is valid up to the pressure of about 225MPa which is considerably higher than pressures measured in medical ultrasound including lithotripsy applications. This maximum pressure will be raised if a higher order approximation than the 2nd order is involved in the derivation of the governing equation and an example of the 3rd order approximation is given by McLachlan (1935).

In a real acoustic source, diffraction takes place because of the finite aperture size and therefore the modeling of such a field is required to include the diffraction process in addition to nonlinear propagation. The combination of these effects has been treated by several techniques including decoupling, parabolic approximation, angular spectrum approach and axial approximation which are discussed below.

3.3 Decoupling

Sutin (1978) proposed an approximate analysis that accounts for the influence of both nonlinearity and diffraction by

decoupling the two phenomena in a focused field. This method employs nonlinear spherical wave theory in the prefocal region and linear diffraction theory within the focal region.

Because the two effects are not assumed to act simultaneously, the intricate side lobe structure of harmonic components in the focal region of many real sources cannot be accurately described with this model. Bacon (1984) has pointed out that Sutin's approach cannot be applied to situations where the focal gain is small, less than about 7, since it gives physically unreasonable results in such cases. Also it is not clear how this technique applies to pulsed fields. In lithotripsy fields, since both nonlinear effects and diffraction are very important around the beam focus, it is difficult to see how such an approach could be used.

3.4 Parabolic approximation

If the complex pressure varies slowly along the axial direction, the second order derivative of the complex field with respect to z can be ignored (parabolic approximation). The solution of the linear (or Helmholtz) wave equation then satisfies the following simplified integral (Novikov et al 1987, Lucas and Muir 1982):

$$(3.4\text{-}1) \qquad \frac{\partial p}{\partial z} = \frac{c_o}{2} \int \nabla_\perp^2 \, p \, d\tau$$

where $\nabla_\perp^2$ is the Laplacian operator in transverse coordinates.

Combining the Burgers equation Eq(3.2-1) with the parabolic integral Eq(3.4-1), a nonlinear parabolic wave equation can be obtained:

$$(3.4\text{-}2) \qquad \frac{\partial p}{\partial z} = \frac{\zeta'}{2 c_o^3 \rho_o} \frac{\partial^2 p}{\partial \tau^2} + \frac{\beta}{c_o^3 \rho_o} p \frac{\partial p}{\partial \tau} + \frac{c_o}{2} \int \nabla_\perp^2 p \, d\tau$$

This equation accounts consistently for the combined effects of nonlinearity, diffraction and absorption to an equal order (Tjøtta and Tjøtta 1981) and therefore describes propagation of a bounded acoustic wave with finite amplitude in a dissipative medium. This equation is often named as the Khokhlov Zabolotskaya Kuznetsov (KZK) equation after the names of inventors (Zabolotskaya and Khokhlov 1969, Kuznetsov 1970).

Since there is no complete analytical solution of the KZK equation, attention has been concentrated on the use of numerical approaches either in the time domain (Bakhvalov et al 1978) or in the frequency domain (Aanonsen 1983) and sometimes in both the domains. The frequency domain (or decomposition) approach simplifies the analysis of finding the monochromatic solutions. The construction of a pressure field for the full solution is achieved by superimposing

the calculated monochromatic solutions. The time domain approach is particularly attractive for short pulses where the solution approximates the impulse response of the source transducer but it is often not straightforward to introduce frequency dependent attenuation. While the attenuation term of the KZK equation (the first term on the right hand side of Eq(3.4-2)) applies to the medium where attenuation depends on the square of frequency and dispersion is negligible, this equation in the frequency domain can be easily modified for the prediction of fields in tissue where attenuation varies with frequency more closely to linear rather than the quadratic dependence and dispersion is not negligible (Wells 1977). As nonlinear effects become significant, the error due to harmonic truncation in the frequency domain approach becomes serious, while the sampling time in the time domain method is required to be small in order to properly resolve the shock front.

A promising numerical model has been developed in the frequency domain by Aanonsen (1983). The computation efficiency of this model has been improved for a focused field using the coordinate transformation introduced by Hart and Hamilton (1988). These numerical solutions of the KZK equation for moderately focused acoustic fields show excellent agreement with experiments for the cases of both continuous and pulsed waves (Baker 1989, Baker et al 1987). The frequency domain approach of the KZK equation has been

used in order to examine the lithotripsy field produced by a piezoelectric source and the computation results show several characteristic features associated with the experimental pulse propagation (Neighbors and Bjørnø 1988).

However the parabolic approximation used in the theoretical model requires the condition that diffraction over the distance of the order of a wavelength is small (weak diffraction condition). This condition effectively puts a limit on the aperture angle. The use of the parabolic approximation produces errors of not more than 10% in the far field for aperture angles less than 20° (Lucas and Muir 1983) and becomes less accurate as approaching the source (Hamilton et al 1985). The aperture angle for a piezoelectric type of lithotripters is greater than 40° (Appendix B3), so that the use of the KZK equation in such cases will be restricted.

3.5 Angular spectrum approach

The limitation of the KZK equation can be overcome using a diffraction term which does not require the parabolic approximation. Christopher et al (1990) have developed such a model in the form of a time stepping process where diffraction is characterized by the angular spectrum. The concept of the angular spectrum approach is the transform domain equivalent of Huygen's principle and the diffractive

field is represented as a superposition of plane waves propagating over a spectrum of angles.

In each step a new angular spectrum can be calculated using a Fast Fourier Transformation technique. In Christopher's approach, a Fast Hankel Transformation (Johnson 1987), instead of the Fast Fourier Transformation, is used for a particular case of radially symmetric field and this greatly improves the computing efficiency.

The nonlinear effect in each step is accounted for in either time domain or frequency domain approach to the Burgers equation. The time domain approach is preferred for higher amplitude and/or pulsed source while the frequency domain is typically chosen for low amplitude or continuous wave source. The basic idea of the time domain nonlinear operator is that the shock front is identified and consolidated, and the resulting shock front is propagated as a whole. The use of the time domain nonlinear algorithm allows Christopher's model to propagate previously intractable high intensity (pulsed) nonlinear fields.

Although Christopher's model does not suffer from the limitation due to the parabolic approximation, this model and those based on the KZK equation require considerable computing time even on a super computer. In particular, very high drive levels (or pulsed fields), which are typical in ESWL fields, require a large number of frequency

components in the numerical computation (note that the computing time is proportional to N^2 where N is the harmonic number retained in the calculation) and this causes the models to run much more slowly. For instance, Christopher's model has been examined in the field generated by the Dornier HM3 lithotripter with some success but a time domain pulsed waveform is derived for only a small number of harmonics (N=63). Since peak pressures are very sensitive to the exact form of shock front it seems unlikely that such a small number of harmonics can provide reasonable estimates of peak pressures.

3.6 Axial approximation

An axial approximation has been motivated from the observation that the information on axis is generally most valuable and can often lead to reasonable estimation on the off axis response as well as from the fact that the one dimensional model can be relatively easily implemented and involves considerably less computing time than three dimensional models.

Neglecting the influence of variations in the off-axis beam profile on the axial profile (axial approximation), ie, assuming that the shape of radial beam profiles does not change during the nonlinear wave propagation, the diffraction term of the KZK equation (the third term on the

right hand side of Eq(3.4-2)) may be replaced for axial propagation by $p(z,\tau)f'(z)/f(z)$ where $f(z)$ is a normalized pressure variation on axis at low amplitude and $f'(z)$ is the first derivative with respect to z (Bacon 1986). An alternative form of the one dimensional nonlinear model may be given by the Burgers equation if a geometric spreading function is incorporated to cover non-planar one dimensional waves (Blackstock 1969).

Bacon (1986, 1989) has developed such a model, based on the assumption that the beam profile is gaussian in form, that permits the KZK equation to be reduced to one dimension. Since the computing time has been significantly reduced compared to a full (three dimensional) model, the model has been reasonably implemented on a PC rather than a mainframe computer. The axial approximation used in Bacon's model has been shown to be in good agreement with measurements on a focused transducer. Comparison with a three dimensional model of the KZK equation suggests some relatively small discrepancies probably associated with difficulty in matching boundary conditions which are differently specified in the two models (Bacon and Baker 1989).

Although Bacon's model has been used with some success to describe the field at the focus of a piston transducer, the model is basically valid for a focused gaussian radiator of small aperture angle. The condition of the model that the beam width of each harmonic mode varies inversely with the

square root of harmonic number in nonlinear fields is less likely appropriate for pulsed fields (see Section 4.1.2). Accordingly Bacon's model may not be directly applicable to high amplitude pulsed fields of non-gaussian large aperture lithotripters in general.

The axial approximation will be violated, when nonlinear effects are significant and so the radial beam profile is altered. The one dimensional model may not be reliable when the propagation distance is more than twice that of the shock formation distance (Bacon 1984). A simple *ad hoc* technique to overcome the beam broadening problem was proposed by Bacon (1986), which involves the alteration of the phase to compensate for the beam broadening. The use of this approach in pulsed fields has not been examined. In general, the axial approximation can only be used in highly nonlinear pulsed fields if some off axis information is included from prior knowledge of the field.

3.7 Summary

The high amplitude pulsed focused field used in the clinical extracorporeal shock wave lithotripsy is characterized by significant diffraction coupled with nonlinear propagation. In order to calculate such a field, the combination of these effects has been treated by several formulations and numerical techniques, but few of

them are practically relevant to clinical lithotripsy fields.

Existing three dimensional models which consider all the relevant effects have been shown to predict accurately a nonlinear focusing field but they require a huge amount of computing time. Especially, when they are used for the high amplitude pulsed fields of lithotripsy, the computing time may be unmanageable. The axial approximation which can permit significant reduction in the computing efforts, therefore, seems attractive for obtaining quick predictions on reliable time domain waveforms produced by lithotripters of moderate accuracy. Such a model has been studied in this thesis.

CHAPTER 4. A PROPOSED MODEL FOR HIGH AMPLITUDE PULSE PROPAGATION IN A FOCUSED FIELD

4.1 Specification

The motivation for the approach used here is to provide a model which will predict the axial field of an axially symmetric plane or focused, continuous or pulsed source of low or high amplitude sound. To be generally applicable to real lithotripsy sources it is required that the model not be constrained by the parabolic approximation.

The proposed approach involves the use of computer models to numerically propagate the acoustic field step by step outward from the source aperture. At each propagation step the effects of nonlinearity, diffraction and attenuation have to be included and each of these factors is summarized below.

4.1.1 Summary of approach

A. The physical aperture of a broad band acoustic source will be represented by a set of piston sources of radius a_n, each emitting at a frequency f_n with a complex amplitude ϕ_n. The aperture radius of each virtual source may be given by

$$(4.1\text{-}1) \qquad a_n = a_o \left(\frac{f_n}{f_o} \right)^{-\kappa}$$

where a_o is the aperture radius corresponding to the reference frequency f_o, f_n represents the *n*th frequency component given by n times of an incremental frequency Δf, and κ is a parameter determined on the basis of measurements of waveforms across the source aperture ($0 \le \kappa < 1$), for example, $\kappa=0$ for a uniformly activated piston source where each virtual source has the same radius. The value of f_o can be set to the centre frequency for pulsed fields, while it is the fundamental frequency for continuous wave fields (ie, $f_o=\Delta f$). The parameter κ, as will be described later, provides a way of introducing some experimentally determined off axis information to the proposed one dimensional model.

B. The value of ϕ_n at the source aperture ($z=0$) is set as boundary conditions along with the value of κ and the shading function for each harmonic ($\mathbb{K}_n(r)$).

C. Each virtual source is assumed to generate a field which may be obtained by considering linear diffraction and the diffraction effect due to each virtual source in one incremental step (Δz) along the beam axis may be given by

$$(4.1\text{-}2) \qquad \phi_n(z+\Delta z) = \phi_n(z) + \left(\frac{\partial \mathbb{F}_n(z)/\partial z}{\mathbb{F}_n(z)} \phi_n(z) \right) \Delta z$$

where $\mathbb{F}_n(z)$ is the normalized complex axial variation with distance z of the *n*th frequency source at low amplitude

determined using linear diffraction theory.

D. Nonlinear effects are assumed in this model to act independently of diffraction. These effects alter the relative amplitude and phase of each harmonic in each step (Δz) and are calculated using Burgers equation given here in its frequency domain form:

$$(4.1\text{-}3) \quad \phi_n(z+\Delta z) = \phi_n(z) + \frac{j\beta\epsilon k_n \Delta z}{4}\left(\sum_{i=1}^{n-1}\phi_i\phi_{n-i} + 2\sum_{i=n+1}^{\infty}\phi_i\bar{\phi}_{i-n} + 2\phi_o\phi_n\right)$$

where $\bar{\phi}_n(z)$ is the complex conjugate of $\phi_n(z)$, $\phi_o(z)$ represents the DC component of the time domain waveform, β is the nonlinear parameter of medium, ϵ is the acoustic mach number, and k_n is the wavenumber at the frequency f_n. Note that $\phi_n(z)$ and $\bar{\phi}_n(z)$ in the bracket have been abbreviated by dropping '(z)'.

E. Attenuation and dispersion are included in each step (Δz) using:

$$(4.1\text{-}4) \quad \phi_n(z+\Delta z) = \phi_n(z) - \xi_n \phi_n(z)\,\Delta z$$

where ξ_n denotes the complex attenuation coefficient of the *n*th frequency component at low amplitude.

F. The full pressure field $p(z,\tau)$ produced by the source is then written in the time domain using the inverse Fourier

series:

$$(4.1\text{-}5) \quad p(z,\tau) = \frac{1}{2} p_o \left(\phi_o(z) + \sum_{n=1}^{\infty} \phi_n(z) \exp(j2\pi f_n \tau) + \sum_{n=1}^{\infty} \bar{\phi}_n(z) \exp(-j2\pi f_n \tau) \right)$$

where $\tau(=t-z/c_o)$ is the retarded time at the distance z on the axis from the source aperture.

4.1.2 Details of approach

A. Diffraction

For a focused field generated by a circular piston (with the focal distance of F and the aperture radius of a_n) radiating a signal of the frequency f_n, the normalized axial response $F_n(z)$ at low amplitude in a lossless medium can be obtained from the Rayleigh integral (Appendix A3) transformed into the frequency domain:

$$(4.1\text{-}6) \quad F_n(z) = jk_n \int_o^{a_n} r dr \frac{K_n(r)}{L(r;z)} \exp\left(-j2\pi f_n \tau_d(r;z)\right)$$

where r is a radial coordinate at the aperture, $K_n(r)$ is the shading function at the *n*th harmonic, $L(r;z) = \sqrt{r^2+z^2}$, $\tau_d(r;z) = L(r;z)/c_o - t_a(r) - z/c_o$ which represents the retarded time at the distance z, and $t_a(r) = (\sqrt{r^2+z^2}-F)/c_o$ which is the time delay across the aperture plane.

The shape of the shading function for harmonics is assumed

to remain the same, so $\mathbb{K}_n(r) = K(r_n)$ where $K(r)$ is the shading function at the reference frequency f_o and $r_n = ra_o/a_n$. If, in particular, $\kappa=0$ (ie, $a_o=a_n$), then $\mathbb{K}_n(r)=K(r)$ for all harmonics.

The gaussian field is of special interest because it greatly simplifies the mathematical representation of linear diffraction allowing an analytical solution if the parabolic approximation is used (Novikov et al 1987). Consider a circular focusing radiator at which the radial profile of each harmonic is assumed gaussian, the normalized axial variation of the *n*th harmonic at low amplitude $\mathbb{F}_n(z)$ is then explicitly given as

$$(4.1\text{-}7) \qquad \mathbb{F}_n(z) = \left(1 - \frac{z}{F} - j\frac{z}{\mathbb{R}_n}\right)^{-1}$$

where $\mathbb{R}_n = 0.5k_n a_n^2$ represents the Rayleigh length at f_n and a_n is the characteristic radius of the gaussian profile of the *n*th harmonic at the aperture, ie, the amplitude of $\phi_n(z=0)$ at $r=a_n$ is smaller by a factor $e(\cong 2.718)$ than its maximum value at $r=0$.

The existence of an analytical solution for $\mathbb{F}_n(z)$ significantly reduces the numerical computation in the proposed propagation model since it is not required to calculate the complicated integration of Eq(4.1-6). The possibility of applying the gaussian approximation to the propagation model therefore makes it especially attractive

although is not essential.

B. Harmonic beam profile

In order to allow the one dimensional propagation model to account for the diffraction of harmonics either generated by nonlinear propagation or contained in the pulse at the source aperture, a knowledge of harmonic variation across the aperture is required. An empirical form for the characteristic radii of harmonics may be given in terms of κ as defined in Eq(4.1-1).

At the aperture (z=0), the value of κ is set to 0, if the shape of waveform is uniform across the surface of the aperture or the relative harmonic amplitude does not vary across the aperture. Alternatively κ may be set to a higher value, typically less than 0.5, when the relative harmonic amplitude across the aperture varies as may be the case when nonlinearly generated harmonics are also present.

As the beam propagates in the propagation model, the diffraction term (ie, $F_n(z)$), which is determined using linear diffraction theory with the initial aperture conditions including κ, may not be valid due to the radial beam profile changed as results of nonlinear harmonic generation and other effects leading to saturation. This is a fundamental problem in a one dimensional propagation model since it does not account for the alteration of radial beam profile.

This problem can be overcome to some extent by, on the basis of experiment, allowing κ to vary as a correction to the boundary condition during nonlinear propagation in order to correct the diffraction term, since radial harmonic beam profiles in front of the aperture ($z>0$) can be given as a function of κ using linear diffraction theory. In particular, for a focused gaussian field, the radial harmonic beam profile has been derived in Appendix A5 and at the focus the beam radius of each harmonic relative to that of the reference frequency of f_o is

$$\left.\frac{a_n}{a_o}\right|_{z=F} \propto \left(\frac{f_n}{f_o}\right)^{\kappa-1} \qquad (4.1\text{-}8)$$

This equation shows that the relative focal harmonic beam radius decreases as κ is reduced and, in particular cases, it varies as $(f_n/f_o)^{-1}$ for $\kappa=0$ and $(f_n/f_o)^{-0.5}$ for $\kappa=0.5$. This indicates that diffraction becomes more important as κ decreases.

Some experimental work (Reilly and Parker 1989, Lucas and Muir 1983) and theoretical predictions (Du and Breazeale 1987) on continuous waves show that the focal beam widths of the harmonics generated during nonlinear propagation vary as $(f_n/f_o)^{-0.5}$, at least for the first few harmonics. From this evidence the value of κ may therefore be set to 0.5 when predicting focal fields, if nonlinearly generated harmonics are assumed to dominate at the focus. This

condition is imposed on the one dimensional model described by Bacon (1986). While this may apply to continuous wave sources such a condition cannot be imposed on pulsed sources since the harmonic content in a pulse is not necessarily nonlinearly generated. In pulsed fields, as used in lithotripsy, it is not in general possible to distinguish between the harmonics generated at the source which constitute the pulse and those generated by nonlinear propagation. The value of κ may therefore be expected to lie between 0 and 0.5, in this case, representing a mixture of piston generated harmonics for which $\kappa=0$ from linear diffraction considerations and nonlinearly generated harmonics for which $\kappa=0.5$ from experimental evidence.

One method of choosing the value of κ during propagation (in continuous wave fields) might be to monitor the value of the fundamental harmonic amplitude to provide an estimate of the amount of nonlinear harmonic generation as suggested by Bacon (1986). The value of κ could, for example, then be increased as the fundamental amplitude decays.

In the case of lithotripsy fields the waveform at the aperture in an electrohydraulic type of lithotripter is already distorted as a result of nonlinear propagation from the electrode (Appendix B3) and therefore the value of κ, even at $z=0$, is required to be higher than 0. In a piezoelectric type of lithotripter, on the other hand, the

field close to the sources behaves linearly, and hence κ changes slowly from 0 to higher values as an initially linear beam becomes more dominated by nonlinear harmonics.

In summary, the parameter κ can be physically identified as a control factor which determines changes in the importance of diffraction in the beam. It therefore provides a convenient way of introducing a variable amount of beam alteration during nonlinear propagation.

C. Attenuation and dispersion

For a small amplitude signal in plane wave field, the variation of the attenuation coefficient of most media with frequency may be modeled by a power law relation (Hill 1978, Lyons and Parker 1988) over wide frequency ranges. The power law expression for the attenuation coefficient α at the frequency f is

$$\alpha = \alpha_o \left(\frac{f}{f_o} \right)^b \tag{4.1-9}$$

where α_o is the attenuation coefficient at the reference frequency f_o, and b is a constant to be either measured or estimated which depends upon the characteristics of a particular medium. The value of b is 2 for water and unity or slightly more for most biological tissues and fluids (Duck 1991, Sehgal and Greenleaf 1982).

This power law expression is appropriate for weak

attenuation in which $\alpha/k \ll 1$ where k is wavenumber. For strong attenuation which often occurs in a dispersive medium such as biological tissue (Wells 1977), α is replaced with a complex attenuation coefficient ξ defined by (Kinsler et al 1982, Rudenko and Soluyan 1977).

$$\xi = \alpha - j\delta \qquad (4.1\text{-}10)$$

where δ is a dispersion coefficient related to the phase change of harmonics due to dispersion phenomena in the medium and is determined by

$$\delta = -2\pi f \left(\frac{1}{c} - \frac{1}{c_o} \right) \qquad (4.1\text{-}11)$$

where c_o and c are the propagation speeds at the zero frequency and frequency of f, respectively. The value of δ becomes zero when values of propagation speed for all harmonics remain constant (ie, no dispersion).

The attenuation and dispersion coefficients can be related to each other by the principle of causality, so that only one input parameter is required to describe both effects. If the attenuation is known, the complimentary dispersion may be analytically calculated using the Kramers-Kronig integral of frequency integrated from zero to infinity. (Morfey 1991, Blackstock 1985).

A nearly local form of the approximate relationship between the attenuation and dispersion coefficients is derived on

the basis of the non-local Kramers-Kronig integral under the conditions that there are no rapid variations in the propagation speed and attenuation coefficient with frequency, such as those associated with a sharp resonance over the frequency range of interest (O'Donnell et al 1981). If the attenuation coefficient of a medium is known, the dispersion can be estimated from the following phase speed equation given as a function of the attenuation coefficient.

$$(4.1\text{-}12) \qquad \frac{1}{c} - \frac{1}{c_o} \cong \frac{1}{c} - \frac{1}{c(f_o)} = -\frac{1}{\pi^2} \int_{f_o}^{f} \frac{\alpha}{f^2} df$$

where $c(f_o)$ is the propagation speed at a convenient reference (not zero) frequency of f_o. The magnitude of dispersion $\Delta c (=c-c_o)$ is usually small compared to c_o, ie, $\Delta c \ll c_o$ and therefore $\Delta c (\cong c-c(f_o))$ may be approximated to

$$(4.1\text{-}13) \qquad \Delta c = \frac{c(f_o)^2}{\pi^2} \int_{f_o}^{f} \frac{\alpha}{f^2} df$$

O'Donnell et al (1978) demonstrate that this dispersion equation accurately predicts the ultrasonic dispersion in solutions of haemoglobin from the results of attenuation measurement. Goodsitt et al (1982) also show that the use of the attenuation-dispersion relationship results in a good representation of signals travelling through dispersive media.

Combining the equations from (4.1-9) to (4.1-12), the frequency dependent complex attenuation coefficient ξ_n at the frequency of f_n can be given as

i) for b=1

$$\xi_n = \alpha_o \left(\frac{f_n}{f_o} \right) \left[1 - j \frac{2}{\pi} \ln \left(\frac{f_n}{f_o} \right) \right] \qquad (4.1\text{-}14)$$

ii) for b≠1

$$\xi_n = \alpha_o \left(\frac{f_n}{f_o} \right)^b \left[1 - j \frac{2\left\{ 1 - \left(\frac{f_n}{f_o} \right)^{1-b} \right\}}{\pi (b-1)} \right] \qquad (4.1\text{-}15)$$

It should be noted that, at b=2 (eg, in water) where no dispersion is expected, Eq(4.1-15) still predicts a finite value of δ_n (even if relatively small). This is because the Kramers-Kronig relation used in the derivation of the equation does not depend on the specific mechanisms responsible for the attenuation and dispersion but hinges only on the properties of causality and linearity. Therefore the derived attenuation-dispersion relationship establishes that a system, which exhibits attenuation, must exhibit dispersion. Nevertheless the use of Eq(4.1-15) is expected to produce reasonable results for the value of b near the unity which is the case of a dispersive medium such as biological tissue.

An example of the relationship between attenuation and

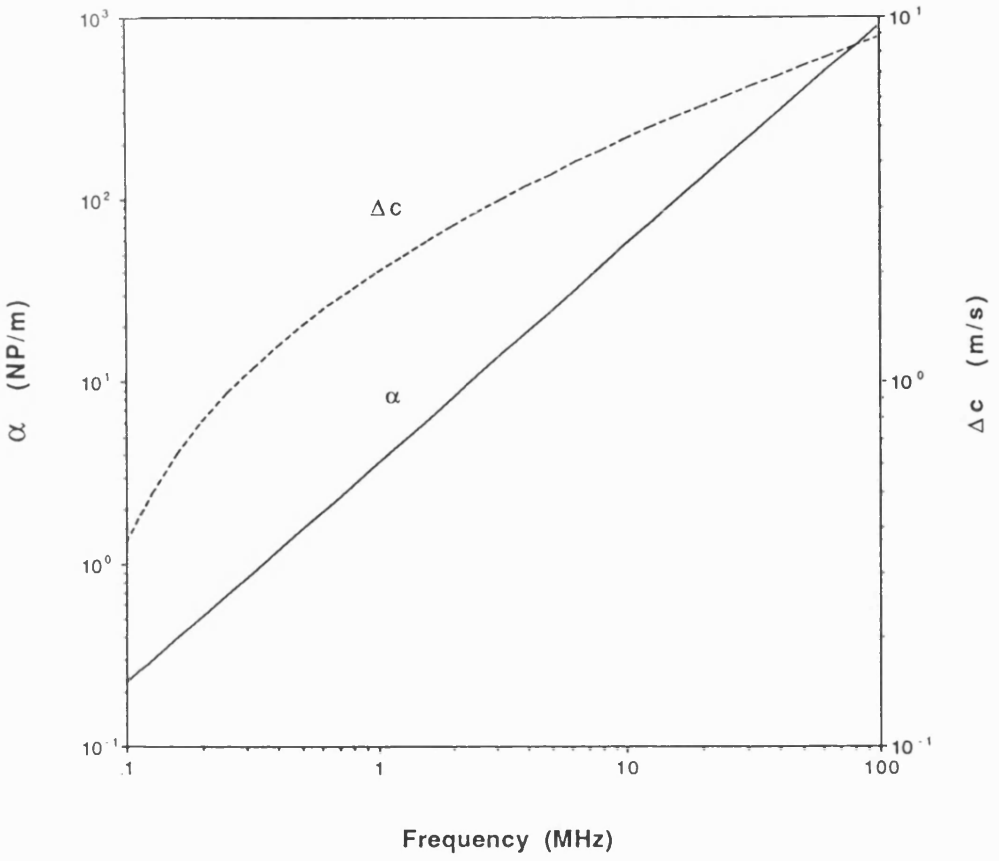

[Fig 4.1-1] Small signal attenuation coefficient (α in Np/m) of liver against frequency (in MHz) fitted using a power law relation (α_o=3.57Np/m at 1MHz, b=1.2; solid curve) and the predicted dispersion (Δc in m/s; dotted curve)

dispersion is illustrated in Fig 4.1-1 for beef liver tissue. The dispersion (Δc; dotted curve) is calculated for the attenuation coefficient (α; solid line) using Eq(4.1-13) and Eq(4.1-15) where $c(f_o) \cong c_o$ (=1570m/s). The attenuation curve is fitted to experimental data ranging from 1MHz to 10MHz (Jongen et al 1986) and extrapolated to the extended frequency range of 0.1MHz to 100MHz, typical working frequency region in lithotripsy. The constants for the best fit are α=3.57Np/m at 1MHz and b=1.2.

It is shown that the dispersion estimated in the liver (including most soft tissues), below 1MHz at which a typical clinical lithotripter operates, is very small, ie, $\Delta c \leq 2$m/s. It is therefore expected that the dispersive effects, such as distortion in the ultrasonic pulse shape, are correspondingly negligible. It is should be pointed out that, since there is no experimental data on biological tissue below 1MHz, further experimental work is required.

4.2 Numerical implementation

4.2.1 Propagation equation

A suitable propagation equation, which considers the effects of nonlinear propagation, diffraction, attenuation and dispersion, can be formed by combining the individual factors derived earlier. This equation, which is ideally

suited to numerical solution and appropriate to lithotripsy fields, is

$$(4.2\text{-}1)\qquad \frac{\partial \phi_n}{\partial z} = \frac{j\beta\epsilon k_n}{4}\left(\sum_{i=1}^{n-1} \phi_i \phi_{n-i} + 2 \sum_{i=n+1}^{\infty} \phi_i \bar{\phi}_{i-n} + 2\phi_o \phi_n \right)$$

$$- \xi_n \phi_n + \frac{\partial \mathbb{F}_n / \partial z}{\mathbb{F}_n} \phi_n$$

where $\phi_n(z)$ denotes the nth complex coefficient in the Fourier series of the time domain solution of $p(z,\tau)$, $\phi_o(z)$ represents the DC component of $p(z,\tau)$, n is an integer increasing from 0 to infinity which identifies the nth spectral component (eg, $f_n = n\Delta f$), $\epsilon = p_o/(\rho_o c_o^2)$ represents an acoustic mach number, k_n is the wavenumber of the nth spectral component, and $\mathbb{F}_n(z)$ is the complex axial profile of the nth harmonic at low amplitude determined from linear diffraction theory which includes the assumptions made concerning the value of κ. The $\phi_n(z)$ and $\mathbb{F}(z)$ here have been abbreviated by dropping '(z)'.

The first term on the right hand side of Eq(4.2-1) represents nonlinear interaction between harmonics during propagation, and the second and third terms represent the dissipation and diffraction, respectively. The full solution (ie, the pressure time waveform $p(z,\tau)$) is obtained by adding up the solution of each harmonic component (ϕ_n) using Eq(4.1-5). It is noted that the propagation equation Eq(4.2-1) provides the correct linear field prediction where κ is constant and $\beta=0$.

The nonlinear term shows, as expected, that nonlinear effects are proportional to the nonlinear parameter (β), acoustic mach number (ϵ) and wavenumber (k_n). The first sum in the nonlinear term is associated with the contribution of lower harmonics to the *n*th harmonic whereas the second infinite sum corresponds to the contribution of higher harmonics to the *n*th harmonic. The third term represents the contribution of the zero frequency (ie, DC component) to the *n*th harmonic. All contributions bring out the energy transfer process in both directions, depleting and accreting the energy of harmonics, depending on the actual sign of each individual coefficient. The bracketed nonlinear interaction term can be alternatively expressed in the form of a self convolution of $\varnothing_n$, ie, $\varnothing_n * \varnothing_n$.

4.2.2 Implementation

The *n*th complex Fourier coefficient $\varnothing_n$ separated into real and imaginary parts is given by $A_n - jB_n$. Replacement of $\varnothing_n$ by $A_n - jB_n$ in Eq(4.2-1) results in a coupled set of ordinary nonlinear differential equations which can be numerically computed.

A 4th order Runge-Kutta method is used for the integration of the differential equation system of Eq(4.2-1). Since the 4th order Runge-Kutta method is an explicit technique, the stability condition must be taken into consideration in order that a stable integration can be guaranteed (see

Section 4.2.3 for more detail). The computation process can involve some numerical errors which may cause serious problems if not properly controlled. The sources of errors are related to harmonic truncation, polynomial truncation, and numerical rounding and are listed below.

i) The harmonic truncation error arises from the fact that the infinite series in the nonlinear term of Eq(4.2-1), in practice, is truncated at a finite value due to computing limitation. Computation time is proportional to the square of the maximum harmonic number (N) retained in the calculation. When N=128, for instance, the running time for gaussian fields implemented on a PC (Macintosh II) using a Z-Basic compiler is 100 seconds per step. When transferred to a Vax 6310 mini-computer using a C compiler the same algorithm takes 1.5 seconds per step enabling more harmonics to be included. The harmonic truncation will be dealt with in more detail in Section 4.2.4 and 4.3.

ii) The 4th order local error in each step is due to a polynomial truncation when the Runge-Kutta technique is derived. The step size (Δz) should be controlled to maintain this error within certain bounds. Of course, the local error can be reduced by choosing other higher order techniques.

iii) The rounding error varies with computer capability related to the number precision used. It is not easy to

estimate this type of error but, in general, more computation and lower precision gives rise to larger rounding errors. This is normally negligible when double precision is used in most computers.

The key to controlling these errors is to maximize harmonic number (N) and minimize step size (Δz). The value of N should be properly selected to meet the conditions that the amplitude of harmonics beyond N is negligible and computing time reasonable. The step size (Δz) has to be controlled to maintain stability. It is also noted that the use of a large step size in the radial direction (Δr) for the calculation of $F_n(z)$ using Eq(4.1-6) can give rise to errors in the location of the axial maxima and minima.

4.2.3 Stability

For stable numerical calculation of Eq(4.2-1), the step size (Δz) must be small to meet a slow variation of ϕ_n, ie, $|\Delta\phi_n/\Delta z| \ll |\phi_n k_n|$ (Korpel 1980). This indicates that the value of Δz is frequency dependent and should be reduced as n increases. Therefore the more harmonics included, the more stiff the differential equation system of Eq(4.2-1) is.

A stability index may be given in terms of the eigenvalues of Jacobian matrix **J**(N X N) when the differential equation system is rewritten in a matrix form. The matrix form of Eq(4.2-1) is

$$(4.2\text{-}2) \qquad \left[\frac{\partial \phi_n}{\partial z} \right] = \left[\mathbf{J} \right] \left[\phi_n \right]$$

where the element $a(n,i)$ of $\mathbf{J}$ is given by

$$a(n,i) = \frac{j\beta\epsilon k_n}{4} \phi_{n-i} \qquad \text{for } n>i$$

$$= \frac{j\beta\epsilon k_n}{2} \phi_o - \xi_n + \frac{\partial \mathbb{F}_n / \partial z}{\mathbb{F}} \qquad \text{for } n=i$$

$$= \frac{j\beta\epsilon k_n}{2} \bar{\phi}_{i-n} \qquad \text{for } n<i$$

where n, i = 0,1,2, ..., N.

A system of differential equations is termed stiff, if the complex eigenvalues (Λ_i) of the matrix $\mathbf{J}$ have quite different negative real parts. A measure of the stiffness (S^F) of system is given by the quotient of the moduli of the largest and smallest real part of eigenvalues (Schwarz 1989), ie, $S^F = max(|\mathcal{R}e(\Lambda_i)|)/min(|\mathcal{R}e(\Lambda_i)|)$. The numerical computation becomes less stable, as S^F increases.

The absolute stability condition requires that the product $\Delta z \cdot \Lambda_i$ (for i=0,1,2,...,N) be located in a complex stability region which depends on numerical techniques used. In practice, the size of stability region is given by the stability interval (S^I) comprising the real negative maximum value. The condition for stability is $\Delta z \cdot max(\mathcal{R}e^-(\Lambda_i)) \subset S^I$ where $max(\mathcal{R}e^-(\Lambda_i))$ represents a value of the negative real part of Λ_i which has the greatest

magnitude. The stability interval for the 4th order Runge-Kutta method used here is S^I = (-2.78,0) (Schwarz 1989).

When N becomes large, however, it is required a huge amount of computation to obtain the eigenvalues of the matrix. According to the property of matrix, in practice, the value of $max(\mathcal{R}e^-(\Lambda_i))$ can be related to $max(\mathcal{R}e^-(a(n,i)))$ which is the value of the greatest magnitude of the negative real part of $a(n,i)$. In the particular case of Eq(4.2-2), the value of $max(\mathcal{R}e^-(a(n,i)))$ occurs when both the values of n and i are N. Therefore the criteria for stability here may be given as $\tilde{a}(\Delta z \cdot \mathcal{R}e(a(N,N))) \geq -2.78$ where $\tilde{a}$ is an empirical factor which compensates for the error due to the approximation of $max(\mathcal{R}e^-(a(n,i)))$ to $max(\mathcal{R}e^-(\Lambda_i))$ and therefore defined by $\tilde{a} = max(\mathcal{R}e^-(\Lambda_i))/\mathcal{R}e(a(N,N))$. For stable computing, the value of $\tilde{a}$ is required to be bigger than 2.

4.2.4 Reduction of harmonic truncation error

The error due to harmonic truncation is serious when nonlinear effects are significant. Unless sufficient harmonics are retained in the calculation, the amplitudes of higher harmonics grow too rapidly. This occurs because the energy flow from lower to higher harmonics stops at the last harmonic, as a result of which the last harmonic will start to grow abnormally, and begins to affect the preceding harmonics. Attenuation which increases with

frequency acts to reduce this problem. A simple guide to the harmonic number (N) which needs to be retained in any calculation for an initially monochromatic wave is given by the value of the acoustic Reynolds number (Gol'dberg 1956) representing the ratio of the nonlinearity to absorptive effects (Bacon 1986).

Few techniques have been discussed to minimize the harmonic truncation error (Neighbor and Bjørnø 1988, Fenlon 1971). In this study, the harmonic truncation is reduced by artificially increasing the attenuation at high values of frequency (Christopher et al 1990). This is achieved by adding up a frequency dependent small quantity 'ε_n' to the exponent 'b' of the power law expression for attenuation coefficient (Eq(4.1-9)):

$$b = b + \varepsilon_n \qquad (4.2\text{-}3)$$

where $\varepsilon_n = \bar{\varepsilon}(n-n_c)/(N-n_c)$ for $n>n_c$, $\bar{\varepsilon}$ is a small constant $(0\leq\bar{\varepsilon}<1)$ and n_c $(1\leq n_c<N)$ is a harmonic number beyond which harmonics are assumed to be contaminated due to the harmonic truncation error.

The extra exponent ε_n plays a role in limiting the unreasonably rapid growth of higher harmonics. This excess attenuation is not required in a medium with a high attenuation such as castor oil, whereas, when a nearly lossless medium such as water is taken into account, the excess attenuation needs to be increased by increasing $\bar{\varepsilon}$

and decreasing n_c. The value of ε_n should be chosen to be compatible with minimizing the harmonic truncation error and as small as possible to minimize the uncertainty in predicted values due to the use of ε_n.

4.3 Harmonic truncation effects

For a given harmonic number (N) retained in calculation, the harmonic truncation error increases with p_o and β in the same way as nonlinear effects, and the error is accumulated as the calculation progresses. The influence of harmonic truncation is accelerated in focused fields and is noticeable around the focus since focusing enhances nonlinear effects.

The amount of harmonic truncation can be estimated for a plane wave field. While a direct estimation of harmonic truncation may not be possible for a focused field, its effects can be examined by varying either the harmonic number (N) or excess attenuation (ε_n).

4.3.1 Plane wave field

For plane waves in lossless media, Eq(4.2-1) is simplified to the following equation in terms of a unitless parameter $\sigma(=z\beta\epsilon k_o)$ which is the distance normalized to the shock formation distance $(1/\beta\epsilon k_o)$ of the fundamental $f_o(=\Delta f)$

$$(4.3\text{-}1) \qquad \frac{\partial \phi_n}{\partial \sigma} = j\frac{n}{4}\left(\sum_{i=1}^{n-1} \phi_i \phi_{n-i} + 2\sum_{i=n+1}^{\infty} \phi_i \bar{\phi}_{i-n} + 2\phi_o \phi_n\right)$$

This equation shows that the DC value (ϕ_o) propagates in a nonlinear plane wave field and remains constant since $\partial \phi_o / \partial \sigma = 0$. Substituting $\phi_n = \mathbb{A}_n - j\mathbb{B}_n$ into Eq(4.3-1) gives a pair of coupled differential equations for $\mathbb{A}_n$ and $\mathbb{B}_n$. For a monochromatic wave, $\mathbb{B}_n = 1$ for n=1 and $\mathbb{A}_n = \mathbb{B}_n = 0$ otherwise and therefore the coupled equations for an initially monochromatic wave are reduced to a single equation:

$$(4.3\text{-}2) \qquad \frac{\partial \mathbb{B}_n}{\partial \sigma} = \frac{n}{4}\left(\sum_{i=1}^{n-1} \mathbb{B}_i \mathbb{B}_{n-i} - 2\sum_{i=n+1}^{N} \mathbb{B}_i \mathbb{B}_{i-n} + \mathbb{Q}_n\right)$$

where $\mathbb{Q}_n = \sum_{i=N+1}^{\infty} \mathbb{B}_i \mathbb{B}_{i-n}$ represents the amount of local harmonic truncation for a cut-off above the largest harmonic number (N) retained in the computation when calculating a new value of $\mathbb{B}_n$. The reduction from a pair to single differential equation implies that there is no phase shift between the harmonics generated during nonlinear propagation in the plane wave field.

For a continuous wave field, the amplitudes of the higher harmonics generated during nonlinear propagation may be smaller than those of lower ones and, particularly, it can be reasonably assumed that these amplitudes vary with the inverse of harmonic number (Baker 1989, Bacon 1986). The mathematical expression for this condition is

$$(4.3\text{-}3) \qquad \mathbb{B}_n \cong N\,\mathbb{B}_N \frac{1}{n} \qquad \text{for } n>N$$

Substituting this relationship into Eq(4.3-2) the infinite series $\mathbb{Q}_n$ can be given in terms of a finite series:

$$(4.3\text{-}4) \qquad \mathbb{Q}_n \cong N\,\mathbb{B}_N \left(\sum_{i=N+1}^{N+n} \mathbb{B}_{i-n} \frac{1}{i} + N\,\mathbb{B}_N \frac{1}{n} \sum_{i=N+1}^{N+n} \frac{1}{i} \right)$$

The accuracy of Eq(4.3-4) relies on the condition on harmonic variation assumed for n>N. A relative amount of local harmonic truncation ($\mathbb{H}_n$), when predicting a new value of $\mathbb{B}_n$, may then be given as

$$(4.3\text{-}5) \qquad \mathbb{H}_n = \frac{\mathbb{Q}_n}{\left(\sum_{i=1}^{n-1} \mathbb{B}_i \mathbb{B}_{n-i} - 2 \sum_{i=n+1}^{N} \mathbb{B}_i \mathbb{B}_{i-n} + \mathbb{Q}_n \right)}$$

The differential equation Eq(4.3-2) has been numerically integrated using a 4th order Runge-Kutta technique on a PC (Macintosh II). The calculation was performed with N=32 at values of σ from 0 to 5 for an initially sine wave. The calculated wave distortions and harmonic variations with increasing σ are shown in Fig 4.3-1 where figure a and b are the predictions when including $\mathbb{Q}_n$ defined by Eq(4.3-4) and when not including $\mathbb{Q}_n$ in the calculation, respectively.

When $\mathbb{Q}_n$ is included in the calculation, the characteristic nonlinear distortion and excess attenuation in the shock front of the calculated waveforms (Fig 4.3-1a upper graph)

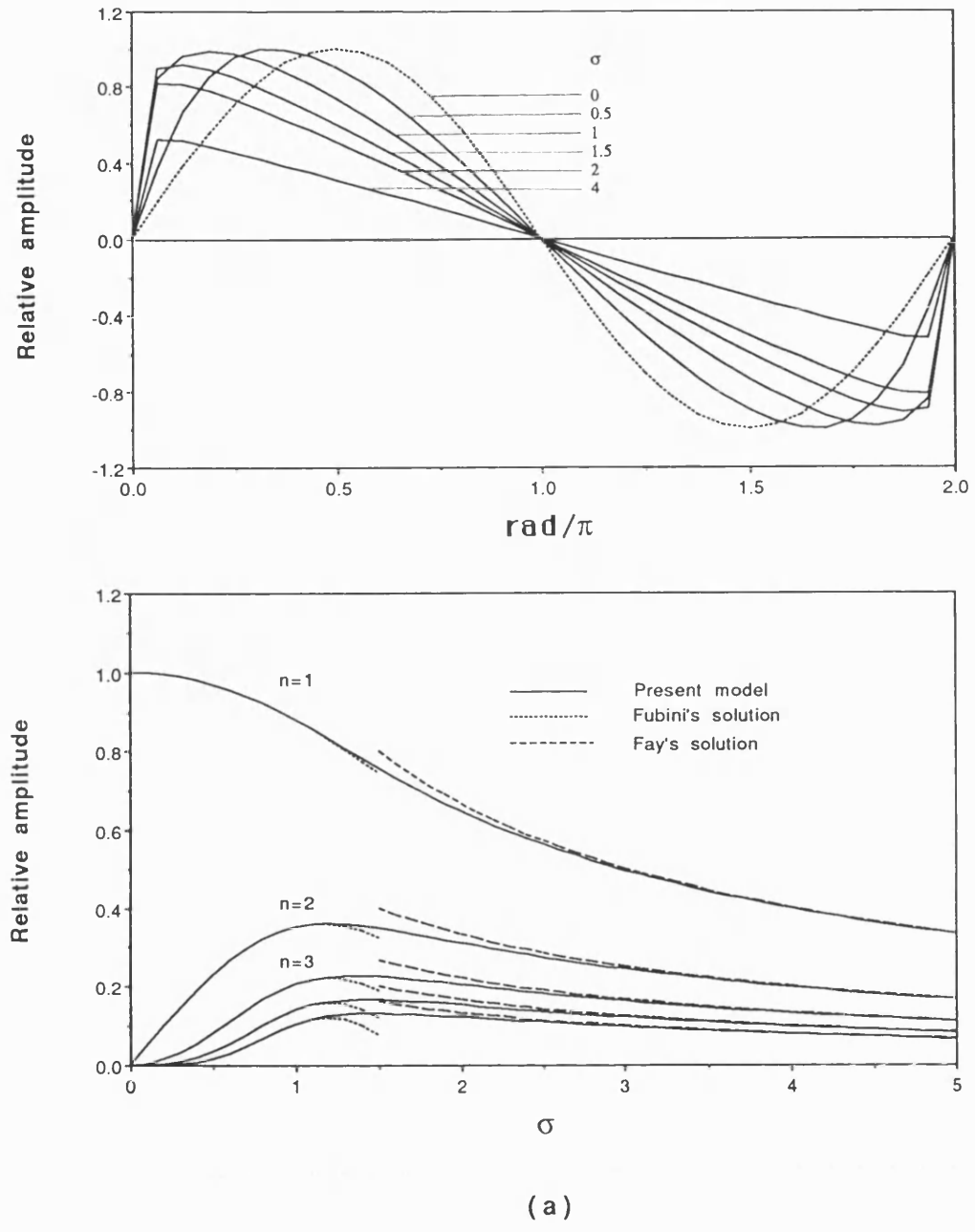

(a)

[Fig 4.3-1] Variations of waveforms (upper) and first five harmonic amplitudes (lower) as a function of σ calculated for an initially sinusoidal plane wave in a lossless medium (N=32). **(a)** Predictions including $\mathbb{Q}_n$ defined by Eq(4.3-4); in lower plot, dotted curves: Fubini solution ($0 \le \sigma \le 1.5$), dashed curves: Fay solution ($1.5 \le \sigma \le 5$) and solid curves: present model ($0 \le \sigma \le 5$). - continued in **(b)** -

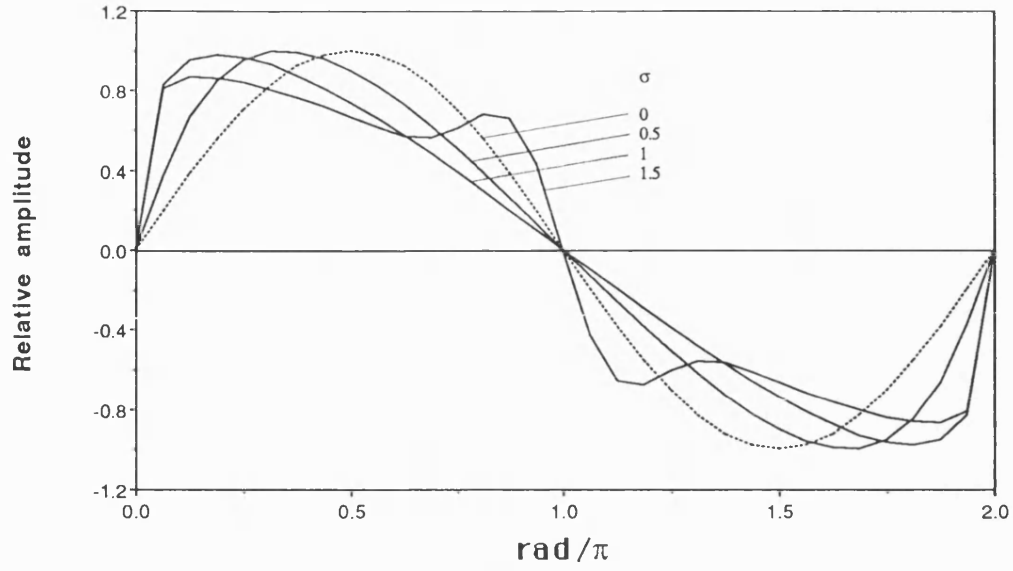

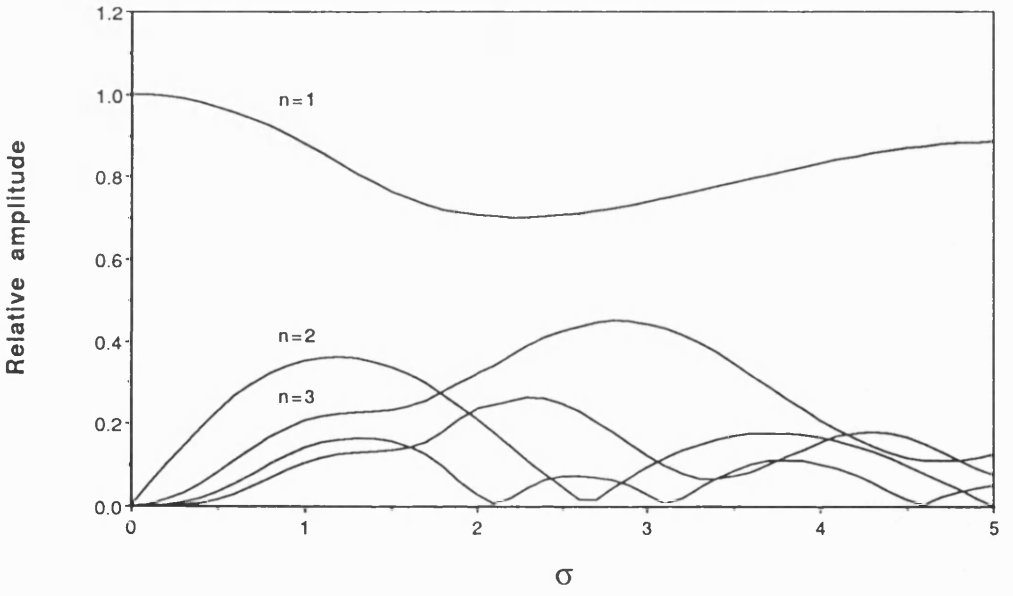

(b)

- continued -

[Fig 4.3-1] **(b)** Predictions without including Q_n

occur with increasing σ in its whole range. An excellent agreement is obtained between the prediction including $\mathbb{Q}$ and well known analytical solutions. The calculated harmonic variations along σ from the fundamental to 4th harmonic (Fig 4.3-1a lower graph) are shown to fit very closely with the Fubini (for $\sigma \leq 1$) and Fay solutions (for $\sigma > 3$) as well as to connect the two analytical solutions in the region of $1 < \sigma < 3$ where these solutions are not applicable.

Waveforms and harmonic variations calculated without including $\mathbb{Q}_n$ (Fig 4.3-1b) are shown to have a good fit to those calculated including $\mathbb{Q}_n$ for $\sigma \leq 1$, but not for $\sigma > 1$. This indicates that the model, when $\mathbb{Q}_n$ is omitted, breaks down for $\sigma > 1$, ie, the harmonic truncation error on nonlinear propagation is significant beyond the shock formation distance ($1/\beta \epsilon k_o$).

The variation of the relative local harmonic truncation ($\mathbb{H}_n$) for the first few harmonics is illustrated in Fig 4.3-2 along σ. As expected, $\mathbb{H}_n$ increases with harmonic number. There is a rapid increase in $\mathbb{H}_n$ as σ approaches a value between 1 and 1.5 for the harmonics, while $\mathbb{H}_n$ steadily increases with σ for the fundamental. It should be pointed out that the total, rather than the local, harmonic truncation error is accumulated as the wave propagates.

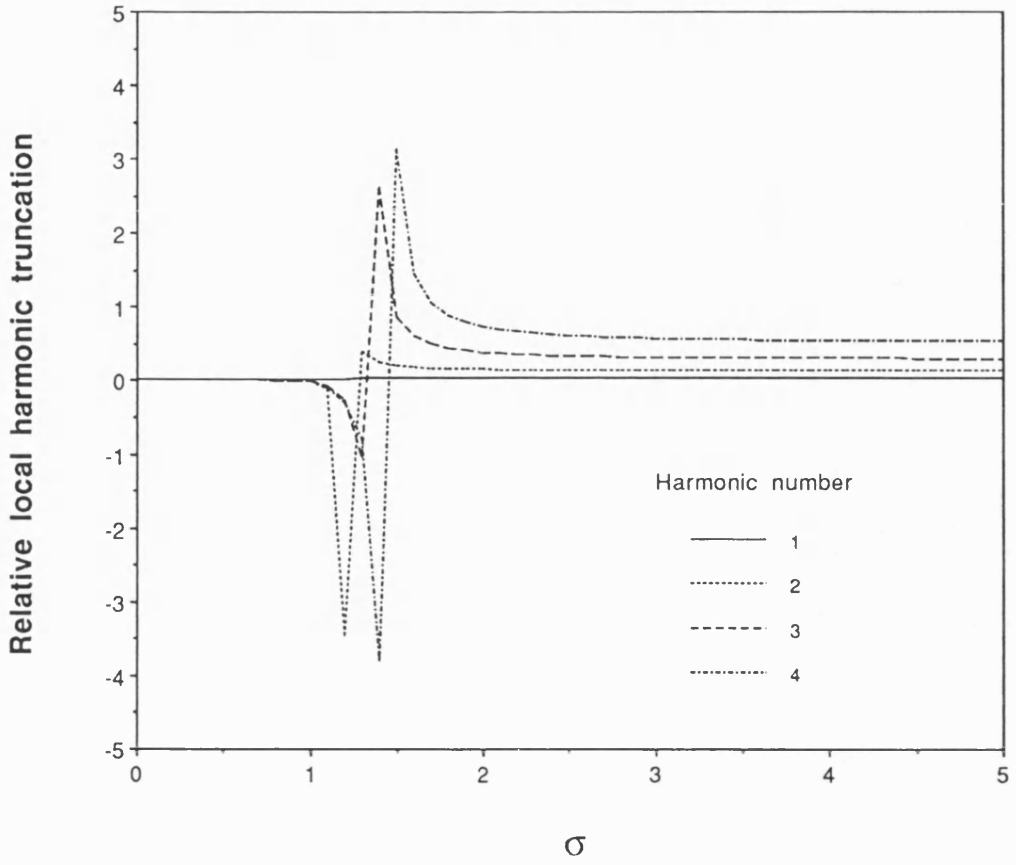

[Fig 4.3-2] Variation of the relative amount of local harmonic truncation (H_n) defined by Eq(4.3-5) of the first four harmonics as a function of σ for nonlinear propagation of an initially sinusoidal plane wave in a lossless medium.

4.3.2 Focused field

For focused fields, the approximation of Q_n is complicated because no simple extrapolation in amplitude and phase for harmonics higher than the truncation harmonic is available due to the combined effects of diffraction and nonlinear propagation. The harmonic truncation effects, however, can be examined by altering the harmonic number (N) and excess attenuation (ε_n) in the calculation.

The beam geometry of the focused field considered here is identical to that of the Dornier HM3 lithotripter shown in Fig 5.2-1 (F=115mm and a_o=30mm). As for the plane wave case, a sine wave of 0.15MHz was considered at the aperture and this wave propagates through initially water (55mm) and then castor oil (α=10.9Np/m at 1MHz, b=2, ρ_o=950kg/m^3 and β=7). The aperture peak pressure of p_o=5MPa is assumed which is sufficient to produce nonlinear propagation.

A. Influence of truncation harmonic number

Fig 4.3-3a shows full shocked waveforms calculated at the focus using Eq(4.1-7) and Eq(4.2-1) for N=64, 128, and 256 (ε_n=0). The waveform calculated with N=64 shows a noticeable oscillation at the shock front which results in overshooting the peak pressure. For N=128 the predicted waveform is stable at the shock front but underestimated in the peak amplitude compared to the case of N=256 where the harmonic truncation error is expected to be negligible.

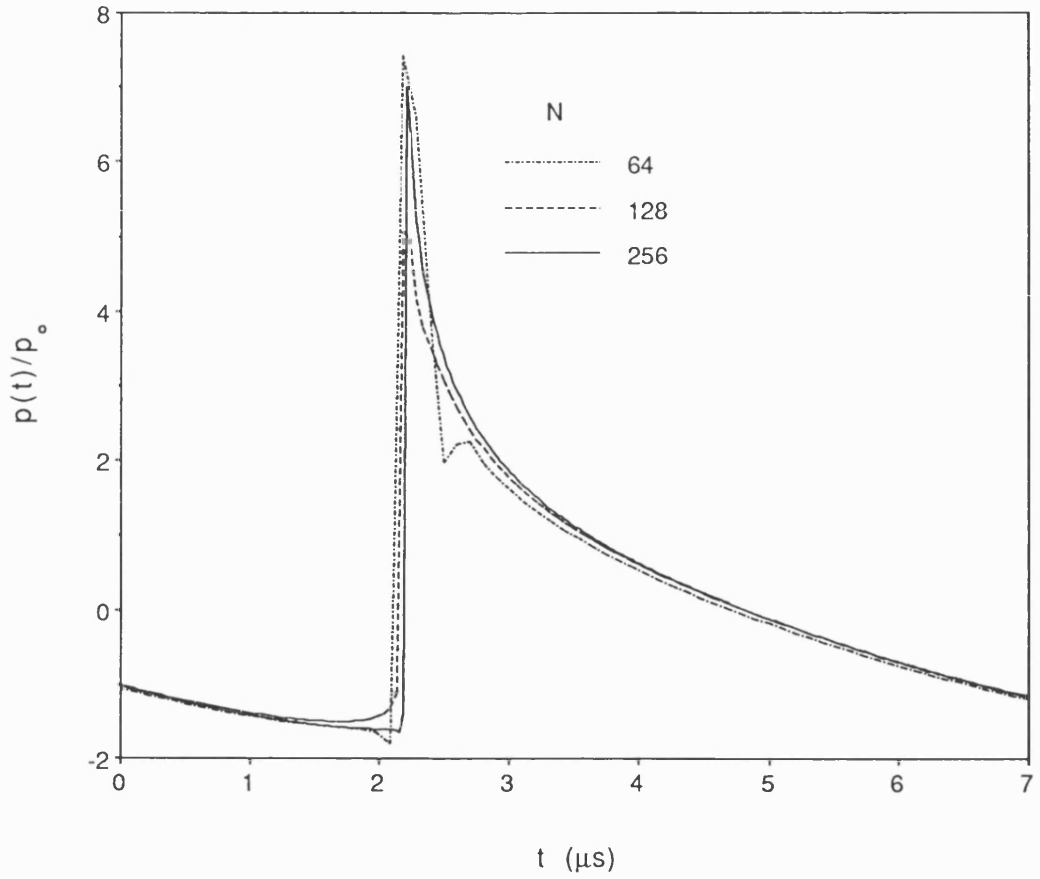

(a)

[Fig 4.3-3] Predictions at the focus of a 0.15MHz focused ultrasound (F=115mm, a_o=30mm and p_o=5MPa) propagating in water (55mm) and then castor oil. **(a)** Waveform; dot-dashed curve: N=64, dashed curve: N=128 and solid curve: N=256.

- continued in (b) -

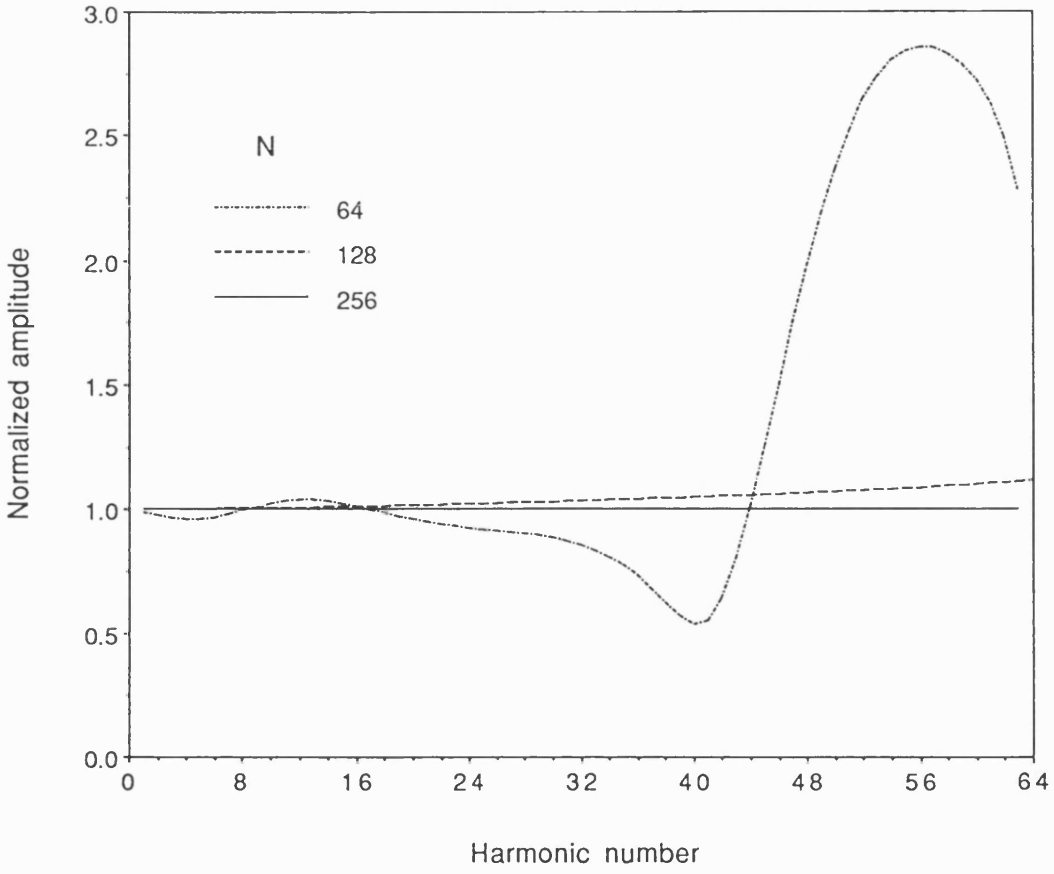

(b)

- continued -

[Fig 4.3-3] **(b)** Harmonic amplitudes normalized to those predicted at N=256; dot-dashed curve: N=64, dashed curve: N=128 and solid curve: N=256. - continued in (c) -

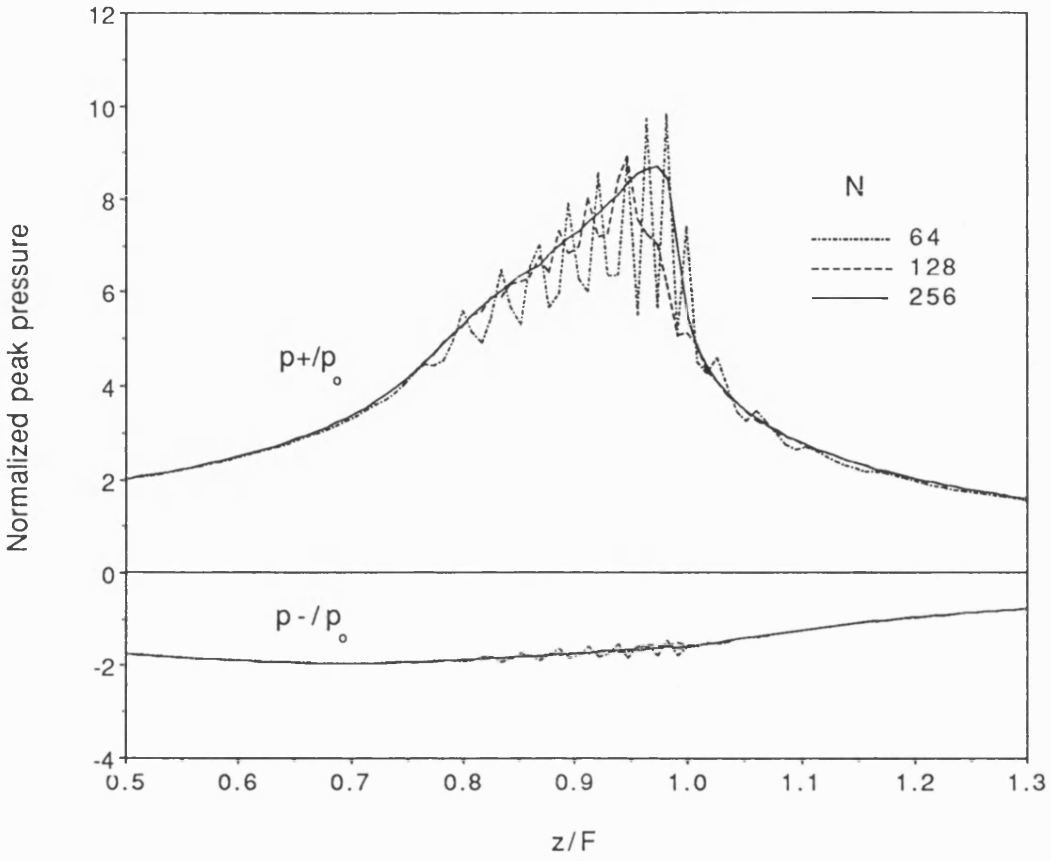

(c)

- continued -

[Fig 4.3-3] **(c)** Axial variation of p_+ and p_- normalized to p_o(=5MPa); dot-dashed curve: N=64, dashed curve: N=128 and solid curve: N=256.

Effects due to the accumulated harmonic truncation error are more clearly demonstrated in the frequency spectrum of each predicted waveform shown in Fig 4.3-3b where the harmonic amplitudes for N=64 and 128 are normalized to those for N=256. For N=64, amplitudes of the higher harmonics beyond the 45th harmonic become significantly overestimated (and in part underestimated in the lower harmonics). This large deviation almost disappear as N is increased to 128.

Harmonic truncation effects have also been examined in relation to the axial variation of temporal peak pressures (p_+, p-) and they are illustrated in Fig 4.3-3c for N=64, 128 and 256. It is shown that the harmonic truncation error is associated with the oscillation of the axial variation of peak pressures and has significant effects in the prediction of p_+ but not in p-. The amplitude of the axial oscillation in p_+ increases close to the focus and is reduced as N is increased.

B. Influence of excess attenuation

Effects of varying the value of ε_n have been examined for the same beam geometry and boundary conditions (N=128). The inclusion of ε_n in the calculation is applied from 30mm before the focus where harmonic truncation is expected to be significant. The value of ε_n used here is specified by $\bar{\varepsilon}$=0.1, 0.15, 0.2 and n_c=1 for all cases.

Fig 4.3-4 shows the harmonic amplitudes predicted for the different values of $\bar{\varepsilon}$ and normalized to those calculated for N=256 and $\bar{\varepsilon}$=0. It clearly illustrates that, when $\bar{\varepsilon}$=0, the amplitude of higher harmonics grows rapidly and this over-estimation is reduced with increasing $\bar{\varepsilon}$. When $\bar{\varepsilon}$ is increased to be bigger than 0.15, however, the amplitude of higher harmonics becomes underestimated. It is of interest to note that the use of ε_n results in slight increase in amplitudes of lower harmonics (for $n \leq N/2$). The best prediction (including the prediction of waveforms and peak pressures) is obtained at the value of $\bar{\varepsilon}$=0.15.

It is of importance to note that the use of ε_n makes the numerical model more stable since it substitutes a mechanism for energy loss in the higher harmonics which has been lost by limiting the number of harmonics in the calculation. The use of ε_n, therefore, has some physical justification.

4.3.3 Summary

The amount of harmonic truncation has been reasonably estimated for a plane wave case with an initially sinusoidal wave. The propagation model including the approximated harmonic truncation term ($\mathbb{Q}_n$) has shown excellent agreement with well known analytical (Fubini and Fay) solutions. It is found that the error due to the harmonic truncation ($\mathbb{H}_n$) is larger for higher harmonics and

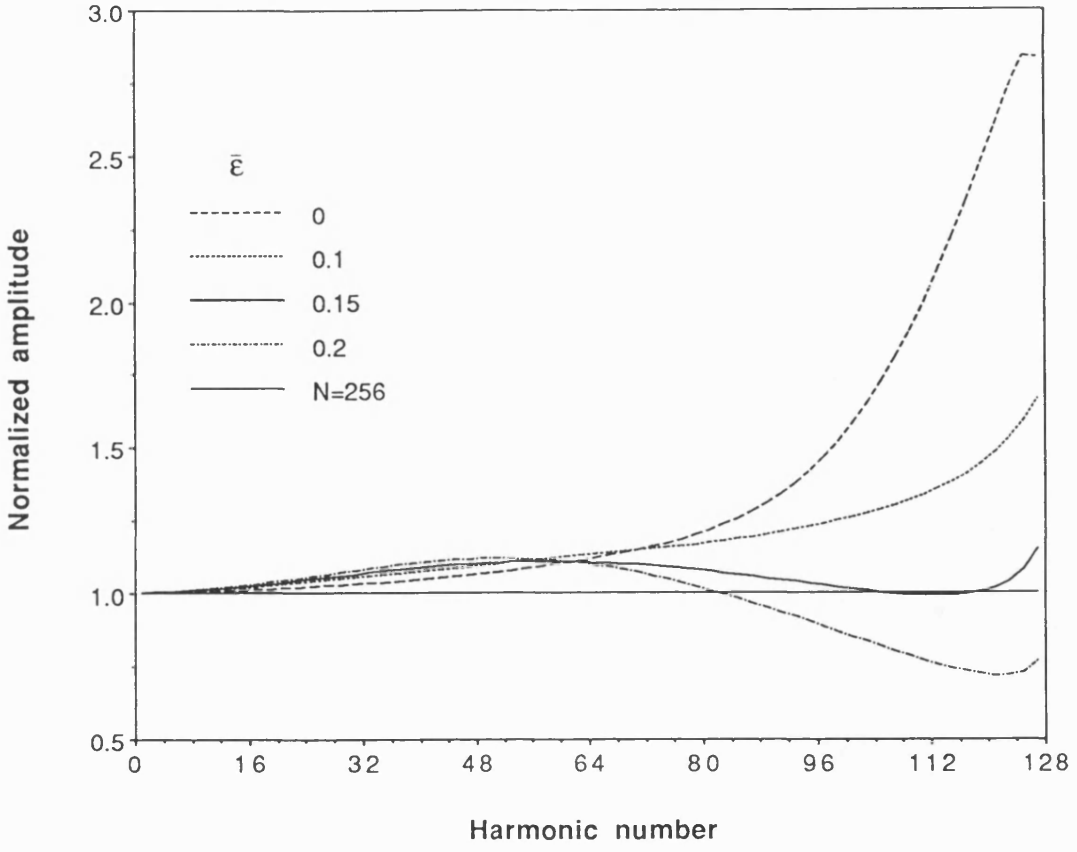

[Fig 4.3-4] Harmonic amplitudes predicted at the focus of a 0.15MHz focused ultrasound (F=115mm, a_o=30mm and p_o=5MPa), propagating in water (55mm) and then castor oil, for different values of $\bar{\varepsilon}$=0, 0.1, 0.15, and 0.2 (N=128, n_c=1) and normalized to those calculated for N=256 ($\bar{\varepsilon}$=0).

decreases with increasing the maximum harmonic number (N) retained in the calculation.

Although it is complicated to estimate the error due to the harmonic truncation for focused fields, its effects have been identified at different values of N. It has been shown that the harmonic truncation causes rapid oscillations at the shock front of predicted waveforms which result in spatial oscillations of peak pressures. The use of a properly selected excess attenuation exponent (ε_n) prevents rapid growth in higher harmonics resulting from the harmonic truncation and is therefore expected to improve the numerical stability and accuracy of the model.

4.4 Verification of the model

The proposed propagation model will now be compared with existing models and experimental measurements to validate the approximations used.

4.4.1 Small amplitude field

The axial variation of small amplitude pressures in front of a focused piston source (ie, K(r)=1) in water is illustrated in Fig 4.4-1 using Eq(4.1-6) and Eq(4.2-1) for β=0. The solid line is the calculated axial variation of normalized pressure amplitude and the points represent the

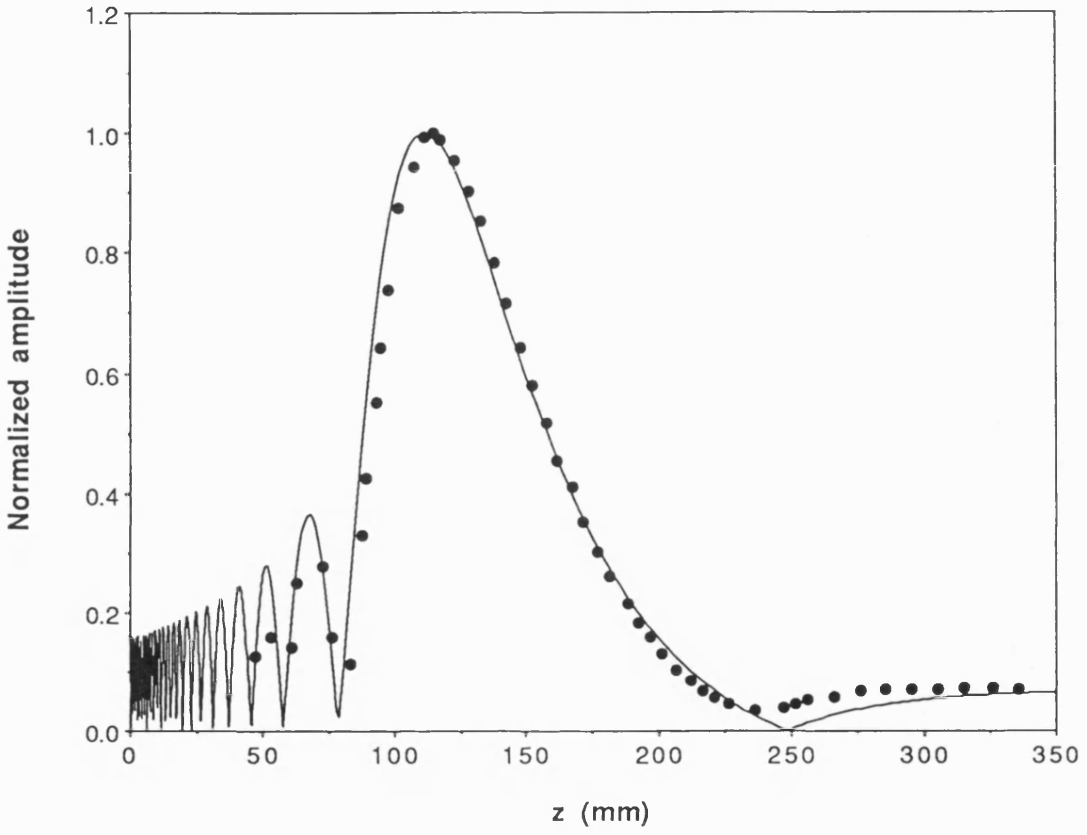

[Fig 4.4-1] Normalized linear pressure amplitude along the beam axis of a 2.08MHz focused piston transducer operated in water (F=120mm and a_o=18.56mm); solid line: predicted by present model (β=0) and data point: measured by Humphrey et al (1986).

measurement made by Humphrey et al (1986). The boundary conditions used in the calculation are F=120mm, a_o=18.56mm and f_o=2.08MHz. The acoustic parameters of water are c_o=1500m/s, ρ_o=1000 kg/m^3, β=3.5, α=0.025Np/m at 1MHz, and b=2. It is apparent that the theory and measurement are in excellent agreement.

4.4.2 Nonlinear parabolic model

A. Continuous wave field

The predictions of the proposed model have been compared with those made using a one dimensional model (Bacon 1986) and three dimensional model (Baker 1989) as well as measurements given by Bacon and Baker (1989). These studies have considered the field of a 3.5MHz focused transducer where F=38.7mm, p_o=1.17MPa and linear gain (G_{lin})=2.93.

Fig 4.4-2a shows the pressure waveform measured at the focus in water (solid line) and the waveforms predicted using Bacon's one dimensional model (dotted line) and Baker's three dimensional model (dot-dash line). The waveforms calculated using the present parabolic gaussian model are given in Fig 4.4-2b (for N=256, κ=0 and 0.5). The acoustic parameters of water used in the calculation are the same as given in Section 4.4.1. It can be seen that there is close agreement between Bacon's model (Fig 4.4-2a dotted line) and that for the present model with κ=0.5 (Fig 4.4-2b dotted line). As discussed in Section 4.1.2, with

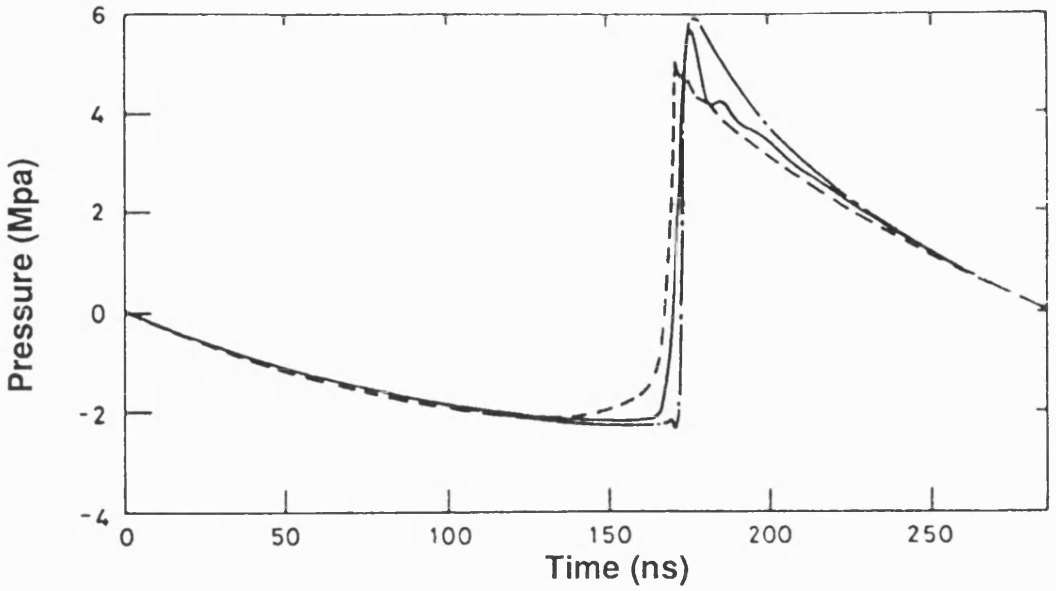

(a)

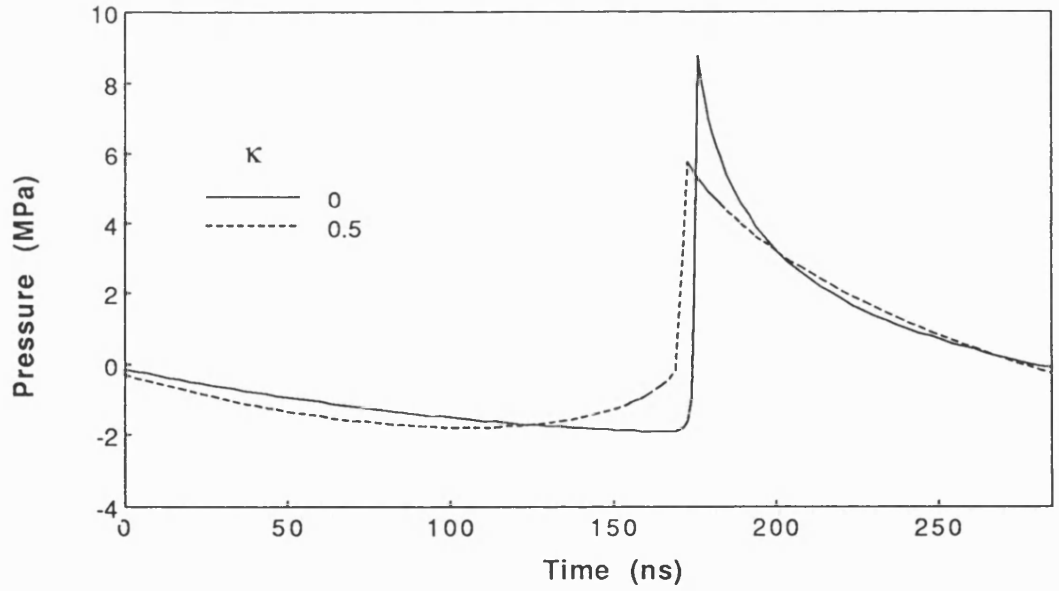

(b)

[Fig 4.4-2] Pressure waveforms at the focus of a 3.5MHz focused transducer (F=38.7mm and G_{lin}=2.93) in water. **(a)** Solid curve: measured, dot-dashed: Baker's prediction and dotted: Bacon's prediction (Bacon and Baker 1989). **(b)** Prediction of present model (N=256); solid curve: κ=0 and dotted: κ=0.5.

this value of κ the present model gives, as expected, similar results as Bacon's model.

Interestingly, at a reduced value of κ of 0 the waveform (Fig 4.4-2b solid line) takes on a sharper leading edge (although the slope of the leading edge remains similar) which is closer to the waveforms measured (Fig 4.4-2a solid line) and predicted using Baker's model (Fig 4.4-2a dot-dashed line). This suggests that diffraction may be more important than is estimated by Bacon's model and that the beam may not be dominated by nonlinearly generated harmonics for at least part of its propagation close to the source. Alternatively, the effect could be attributed to the use of a gaussian model to describe a piston beam in Bacon's model.

The best fit with the measured peak positive pressure is obtained when κ=0.45. These results indicate that the assumption that nonlinear generated harmonics dominate may be moderated by allowing for some proportion of linear diffraction behaviour. Precise comparison of the models is difficult since the number of harmonics used in the published results (Bacon and Baker, 1989) are not given. Peak values of compression may be expected to be sensitive to the choice of this parameter below certain values.

B. Pulsed field

The present model has also been compared in a pulsed field

with measurements and Baker's three dimensional model. The pulsed field was generated by a circular piston source with a focusing lens operating in water. The boundary conditions of the field include a_o=19mm, F=440mm and the aperture pulse with a centre frequency of 2MHz with p_o=0.15MPa (Baker and Humphrey 1989). The measured aperture pressure waveform used in the calculation is illustrated in Figure 1a of Baker and Humphrey (1989) where 0.333MHz was taken as the pulse repetition frequency (ie, Δf).

Fig 4.4-3a shows the pressure waveforms measured in water at the focus (solid line) and predicted by the Baker's model (N=199, dotted line). Waveforms calculated by the present model for κ=0 (solid line) and 0.5 (dotted line) are plotted in Fig 4.4-3b (N=384). The best agreement in terms of peak positive pressure between the present and Baker's model is obtained at the value of κ=0.4. Discrepancies between the absolute values of the peak pressures may not be significant since the two models have used different numbers of harmonics. Indeed, in Baker's model, this value varies during propagation so that precise comparison is technically difficult. It is noted, nevertheless, that the waveforms are in reasonable agreement.

4.4.3 Nonparabolic model

The present model has also been compared with the three dimensional nonlinear model developed by Christopher et al

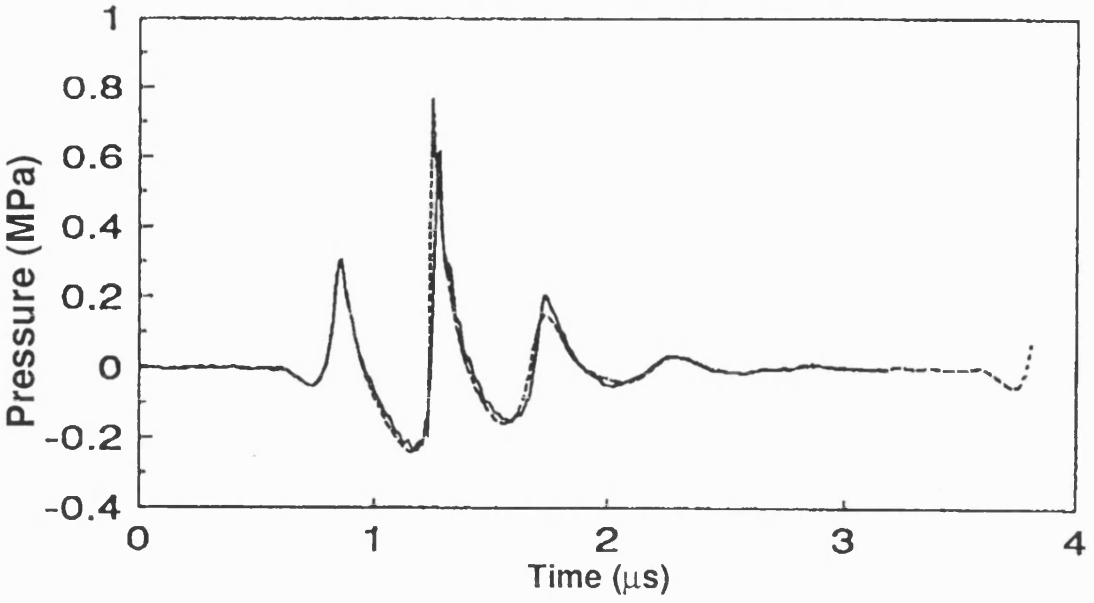

(a)

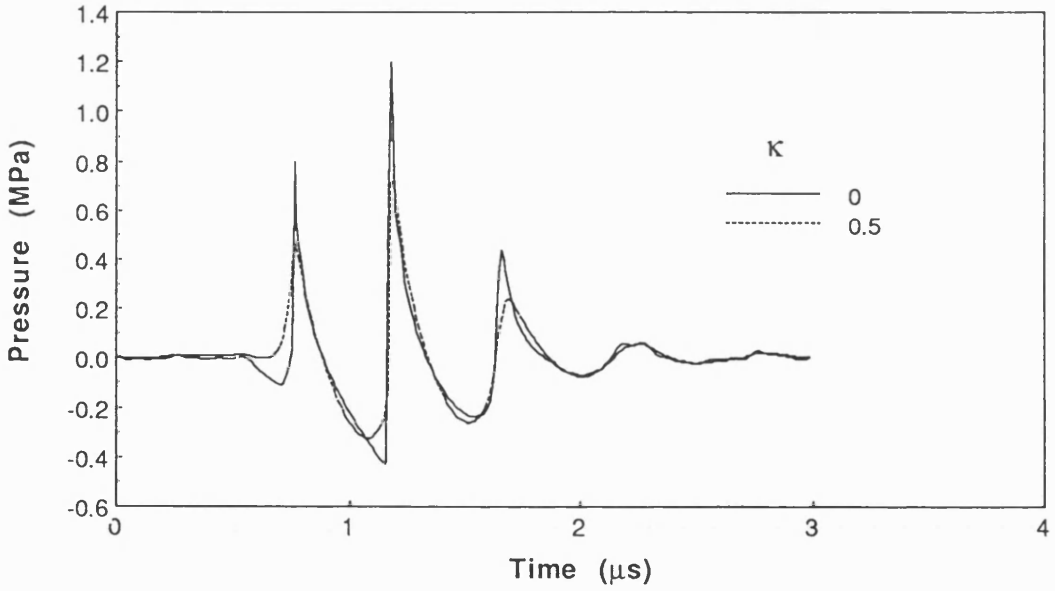

(b)

[Fig 4.4-3] Pressure waveforms at the focus of a focused pulsed transducer (F=440mm and a_o=19mm) in water. **(a)** Solid curve: measured and dotted: Baker's prediction (Baker and Humphrey 1989). **(b)** Prediction of present model (N=384); solid curve: κ=0 and dotted: κ=0.5.

(1990) which does not require a parabolic approximation. A focused piston field showing significant nonlinear effects is chosen to simulate the two models. The piston transducer is driven at 3MHz in water with p_o=0.3MPa, and its geometry is specified by F=100mm and a_o=10mm.

Axial variation of amplitude for the first four harmonics and pressure waveforms at the focus (z=F) calculated using Christopher's model (N=50) and the present model (κ=0.5, N=64) are compared in Fig 4.4-4. The axial variation of harmonics between the two models shown in Fig 4.4-4a (upper graph) and Fig 4.4-4b (upper graph) is in good agreement in general. An apparent difference is that the position of the last axial minimum moves away from the source as the harmonic number increases in Christopher's model (Fig 4.4-4a upper graph), whereas the position of all harmonics coincides with that of the fundamental in the prediction of the present model (Fig 4.4-4b upper graph). This is due to the fact that the position at the nth harmonic depends on $k_n a_n^2$ and the use of κ=0.5 results in this parameter being constant for all harmonics. If a lower value of κ is used this will not occur.

It is of interest to note that the nonlinear effects is likely weakened by the number of axial zeros or minima of near field oscillations in pressure. Accordingly the generation of higher harmonics is less significant before the last axial minimum and the main build up of nonlinear

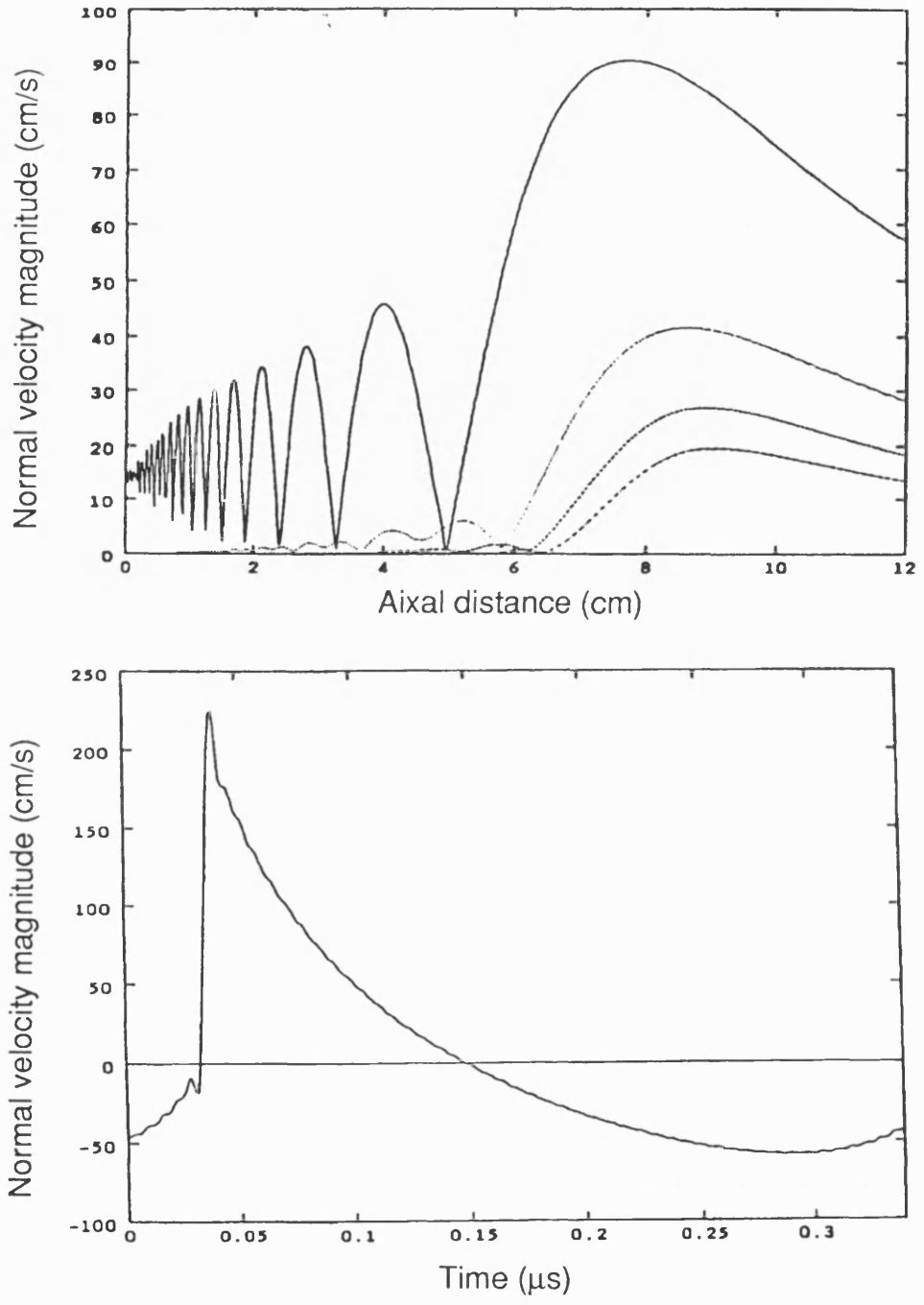

(a)

[Fig 4.4-4] Axial amplitude variation of the first four harmonics (upper) and focal waveform (lower) for a focusing piston source of 3MHz in water (F=100mm and a_o=10mm). **(a)** Prediction of Christopher et al (1990) - continued in (b) -

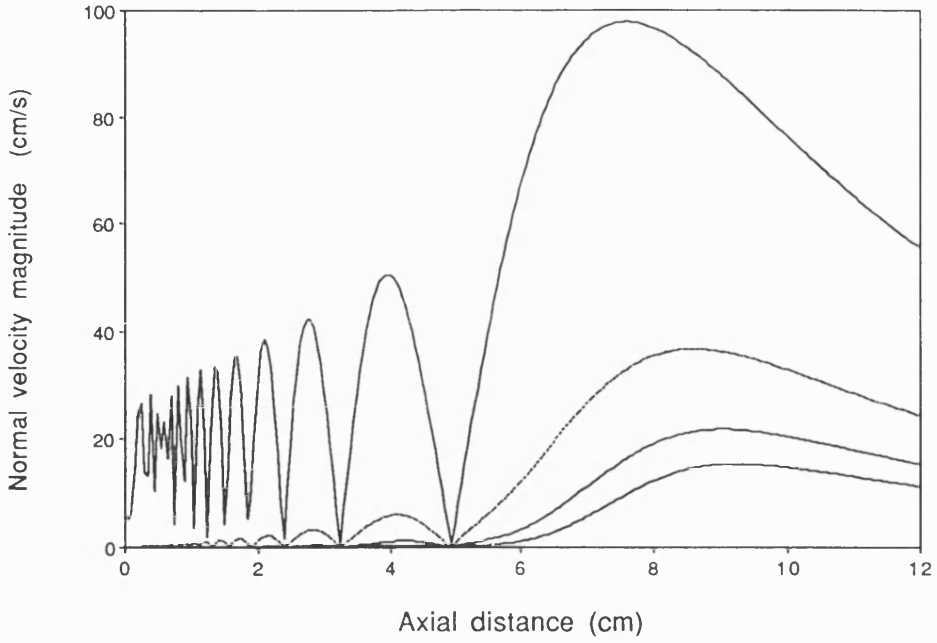

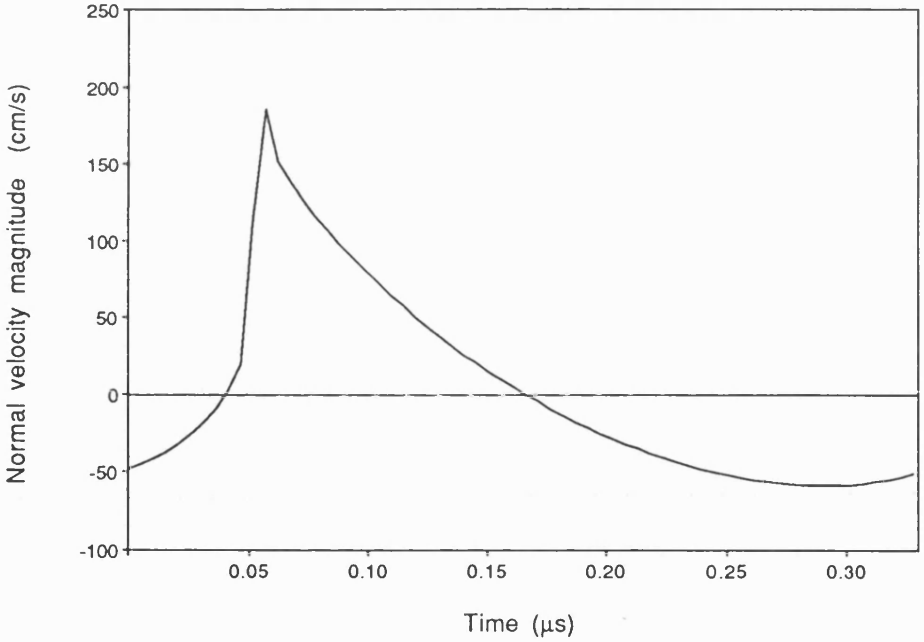

- continued -

[Fig 4.4-4] **(b)** Prediction of present model (N=64 and κ=0.5).

distortion does not take place until after the last axial minimum. The prediction in the present case shows that the initial propagation of the beam before the last axial minimum is not dominated by nonlinearly generated harmonics and the value of κ in the calculation is expected to be less than 0.5.

The pressure waveforms calculated using the two models are given in Fig 4.4-4a (lower graph) and 4.4-4b (lower graph) and they are shown to be in reasonable agreement. The value of the positive peak pressure (p_+) predicted by the present model with κ=0.5 is shown to be lower than that of Christopher's model but this value can be increased by selecting the value of κ smaller than 0.5. Good agreement in the negative peak (p-) between the two models is shown and this is attributed to the fact that the precise value of κ has little influence on p-.

The validation of the present nonparabolic model is important since it shows that the technique can be applied to the fields of a large aperture source like a piezoelectric type lithotripter to which the parabolic approximation can not be made.

4.4.4 Summary

The proposed one dimensional model has been shown to be in good agreement with experimental measurements and predictions of existing models. This is encouraging since

the present model allows an enormous reduction in computing time; typically by a factor of several orders. From comparisons with Christopher's (nonparabolic) model, the model may be expected to provide reasonable predictions for nonparabolic sources and takes some account of radial beam broadening in nonlinear fields

CHAPTER 5. MODEL PREDICTIONS FOR LITHOTRIPSY FIELDS

5.1 Introduction

The objective of this chapter is to obtain theoretical predictions of acoustical parameters in the field of a clinical lithotripter using the numerical model developed in Chapter 4.

Detailed consideration is given to the acoustic fields generated by electrohydraulic (EH) lithotripters (Dornier HM3), because these have been available for the longest time period and most reported pressure measurements have been obtained from these machines. This type of lithotripters, in common with certain electromagnetic (EM) shock wave sources, have relatively small aperture angles where the matched gaussian and parabolic approximations are reasonable as demonstrated in Appendix B4 and hence computing time is greatly reduced. It is also reasonable to consider that EH sources provide a relatively severe test for the present model because the measured pressure waveform appears shocked at most positions in the field in contrast to EM and piezoelectric (PE) sources where the shocks, if formed, occur close to the focus. Additionally, although sparse, more data is available on the EH type of lithotripters compared to the other types, which makes it

more useful at present to test the model on the EH lithotripters.

While the model can be adapted to contain the full non-parabolic diffraction term (Eq(4.1-6)) and provides good agreement with other models (including Christopher's) in which the parabolic approximation is not made (Section 4.4.3) a practical problem with numerical implementation in wide aperture sources remains to be overcome. The problem is associated with the extremely small step size required in the near field close to the source aperture because of the rapid oscillation of higher harmonics. This problem is not a property of the present model but associated with all frequency domain approaches to linear diffraction of pulsed sources particularly in large aperture sources with non-gaussian shading functions.

The problem is typically overcome in many published studies by simply ignoring these oscillations; this is done implicitly by limiting the step size and the number of harmonics in the calculation. For example, the harmonic amplitudes predicted by the three dimensional model (Baker and Humphrey 1989, Figure 4) show no oscillations in the near field close to the aperture of a piston source directly as a result of the step size limitation. While this may be an acceptable approximation for continuous wave or small bandwidth pulses it is unclear how important this problem is in large aperture lithotripsy sources where a

wide range of frequencies is to be considered. For this reason pressure waveforms calculated for the case of certain wide aperture sources are not presented although general predictions unrelated to the precise pressure waveform are given.

The model prediction has been carried out for a standard aperture waveform of a heavily damped sine pulse, while the prediction has also been made with a measured aperture waveform (Section 5.4) for the comparison between theory and experiment. The prediction is concerned initially with the field at a fixed source output setting of the electrohydraulic lithotripter (Section 5.3) and then the theoretical model has been used to investigate the behaviour of acoustic fields and saturation effects as the lithotripsy source power increases (Section 5.5), since many of the clinical and experimental studies often involve examining the biological response at different source output settings.

5.2 Boundary conditions

Consideration of the boundary conditions associated with the three main types of lithotripsy sources (EH, EM and PE) in a suitable form for use with the propagation model are given in Appendix B3. In this section the specific boundary conditions for the electrohydraulic lithotripter (Dornier

HM3) taken to obtain predictions are detailed below.

5.2.1 Beam Geometry

Fig 5.2-1 shows the beam geometry typical of clinical lithotripters in which the beam propagates first in water and then tissue. The water-tissue interface at the skin occurs at a position before the focus where kidney stones or gall stones are assumed to be located. For the Dornier HM3 lithotripter considered here, the focal distance (F) is 115mm and the depth of tissue to the stone (d) is fixed at 60mm which is typical of the clinical situation for kidney stone treatment where the stone is situated in the renal pelvis. A matched gaussian shading function is used with a characteristic aperture radius (a_o) of 30mm.

5.2.2 Aperture waveform

A heavily damped sinusoidal pulse, as a standard aperture waveform which represents characteristically the measured waveform (shown in Fig 5.4-1a), has been used to propagate at lithotripsy pressure levels. Fig 5.2-2 shows the damped sine pulse with an asymmetry ratio of 9 which is used in calculation. This waveform was obtained from Eq(B3-6) (Appendix B3) with values of $\tilde{a}$=1.52, t_c=1.5μs, and f_o=0.15MHz. It should, however, be noted that the rise time of leading edge of the positive pressure half cycle of this waveform is not as short as that for the measured waveform. This discrepancy in using this standard pulse is assumed to

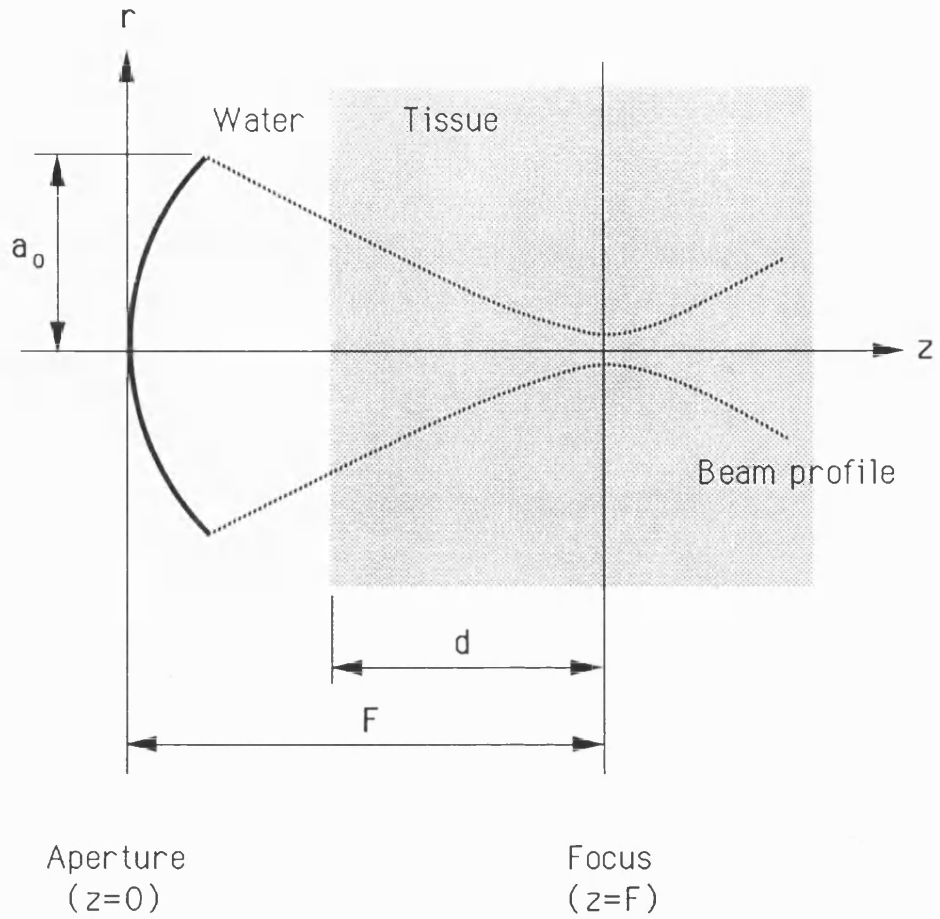

[Fig 5.2-1] The beam geometry of a focused field for lithotripsy. A pulse propagates initially through water and then tissue represented by the shaded area. a_o is the characteristic beam radius at the aperture, F is the focal distance and d represents the depth of tissue to the focus.

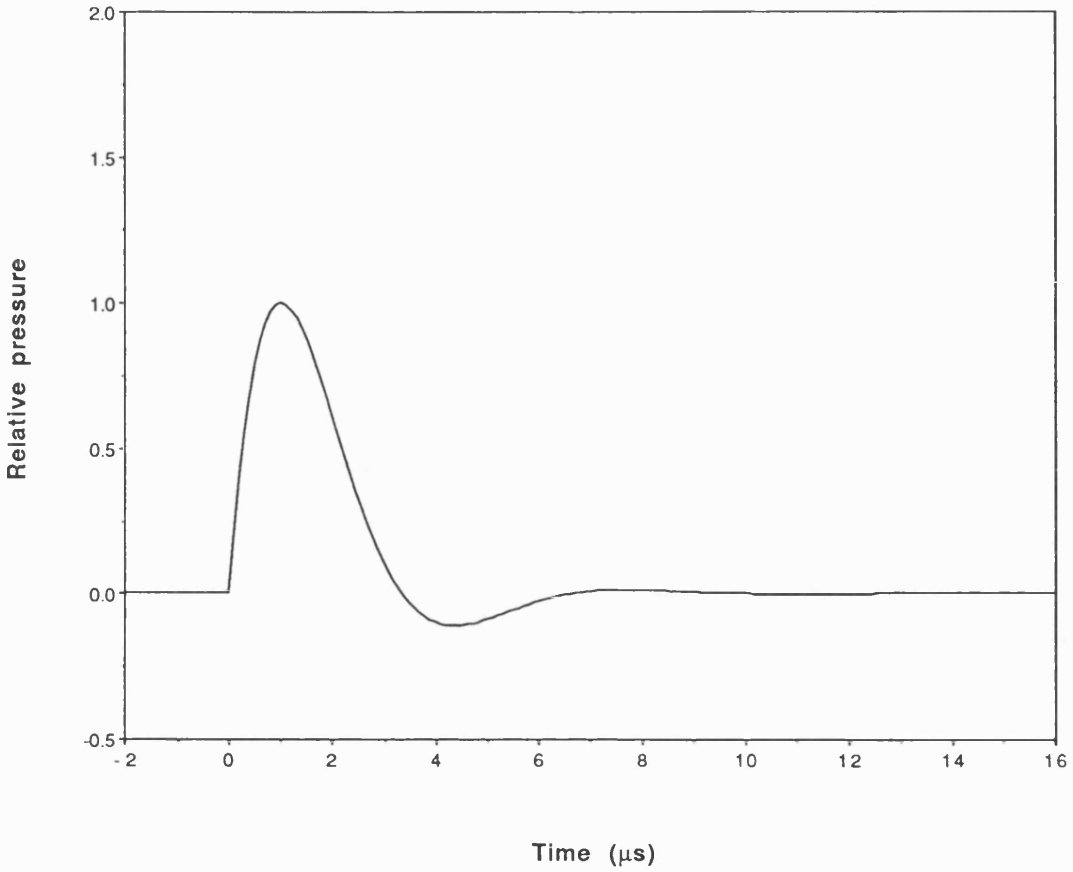

[Fig 5.2-2] A normalized heavily damped sinusoidal waveform defined by Eq(B3-6) where ã=1.52, t_c=1.5μs and f_o=0.15MHz.

be small since the model predicts that the discontinuity forms within a relatively short distance from the aperture.

In representing the pulse by a Fourier series, the repetition frequency (Δf), ie, the first frequency in the model was set to 0.05MHz which is a third of the centre frequency (f_o=0.15MHz). The Δf represents the reciprocal length of the time domain waveform analyzed, ie, the pulse repeats outside the chosen interval. This repetition frequency has to be controlled in order that the pulse does not interact with successive pulses and the extra delay of the edge wave is well located in the pulse length. The span of the edge wave from the shock front will be a minimum around the focus since all waves are coincident there. The time interval between pulses can be increased by choosing a lower frequency for the first component but this increases the number of harmonic components required to gain the same degree of accuracy in frequency domain spectrum.

It is of interest to note that the damped sine pulse has a finite DC component (ϕ_o). Measured aperture waveforms also appear to have a finite DC component although it is unclear at present if this represents a net fluid flow across the aperture (at the beam axis) or is simply a measurement artifact resulting from differences in the low and high frequency response of the hydrophone. The fact that the propagation equation Eq(4.2-1) retains the DC component (ϕ_o) in the nonlinear term was unexpected. The

interpretation of this term is not straightforward and requires further analysis. It presumably indicates that nonlinear effects are influenced by the DC component of a pulse whereas it is clear that linear diffraction is unable to propagate a DC term. The DC term is therefore, in practice, lost in the first step of the model which is equivalent to stating that although an asymmetric aperture waveform is used, within a short distance positive and negative half cycle area will be equal as required for zero net fluid motion. In plane waves, however, the DC term remains throughout propagation and contributes to changes in the harmonic content of signal.

5.2.3 Medium

The numerical calculation has been carried out to predict the field in water and at depth in tissue. For the tissue case, numerical calculations were performed including and without including dispersion, so that the dispersion effect could be examined and related to its influence on the value of peak pressures. The acoustic parameters for water used in the calculation are ρ_o=1000kg/m^3, c_o=1500m/s, β=3.5, α_o=0.025Np/m at 1MHz, and b=2, and the values for tissue taken from liver are ρ_o=1100kg/m^3, c_o=1570m/s, β=4.8, α_o=7Np/m at 1MHz, and b=1.17 (Goss et al 1979).

5.2.4 Other numerical considerations

The harmonic number (N) retained in the calculation was set

to 512 unless stated, ie, the frequency components beyond 25.6MHz were truncated. The value of $\bar{\varepsilon}$ at z=F was 0.5 for water and 0.3 for liver when the aperture peak pressure (p_{o+}) is 5MPa, these values were decreased on either sides of the focus. The value of n_c was set to 1 at z=F, and increased on either sides of the focus. The calculations were carried out on the Vax 6310, taking 24 seconds per step at N=512. The step size (Δz) was in the order of 0.5mm and decreased as approaching the focus. Unless specified, the value of κ was set to 0 representing a source in which the radial profiles of all the harmonics were identical.

5.3 Predicted fields

This section describes the acoustic fields calculated in water and tissue for the damped sinusoidal aperture pulse with peak pressures of p_{o+}=5MPa and p_{o-}=0.55MPa.

5.3.1 Pressure waveform

Pressure waveforms predicted at several positions along the beam axis of the (Dornier HM3) lithotripter for propagation in initially water (for z/F<0.48) and then liver are plotted in Fig 5.3-1. This figure clearly illustrates the progressive nonlinear wave distortion and focusing effects which the model predicts. For propagation in water for z/F>0.48 the predicted waveforms are similar to those in

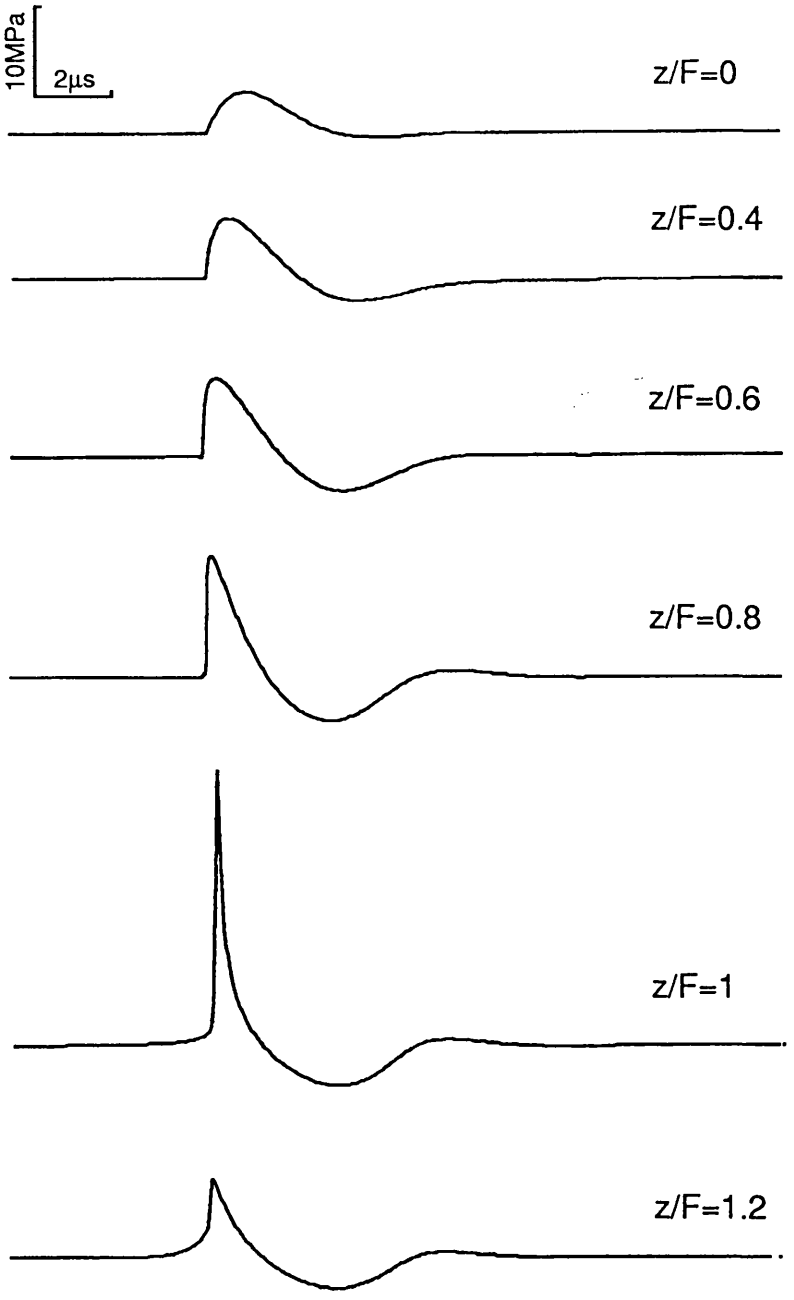

[Fig 5.3-1] Pressure waveforms predicted at several positions along the beam axis of the electrohydraulic lithotripter for an damped sine aperture pulse (p_o+=5MPa, p_o-=-0.55MPa) that propagates through water into liver tissue 60mm before the focus.

liver but, as approaching the focus, increasingly different. Pressure waveforms calculated at the beam focus shown in Fig 5.3-2 where figure a is for propagation in water and figure b in liver tissue. The pressure in the figure is normalized to the temporal peak pressure (p_+) and time is in units of μs. The dotted waveform in tissue represents the prediction without considering dispersion.

The calculated waveforms show the characteristic features of measured waveforms (see Fig 1.2-1 or Fig 5.4-2ac) including a steep rise time and slower negative pressure variation. It is noted that the duration of the positive half cycle of the calculated waveform in water is characteristically narrower than that in tissue. The asymmetry ratio of the water waveform is about 15 compared with 10 for the tissue. The waveform predicted in tissue is not much altered when the phase changes resulting from dispersion are omitted from the calculation, although there is some increase in positive peak pressures. These changes are considered in more detail in Section 5.3.4.

5.3.2 Axial variation

Axial variation of temporal positive and negative peak pressures (p_+, p_-) normalized to the aperture peak (p_{o+}) is plotted in Fig 5.3-3 where figure a is for propagation in water and figure b in tissue. In tissue propagation dispersion has been included in the calculation. The dotted curves in both the figures represent linear propagation

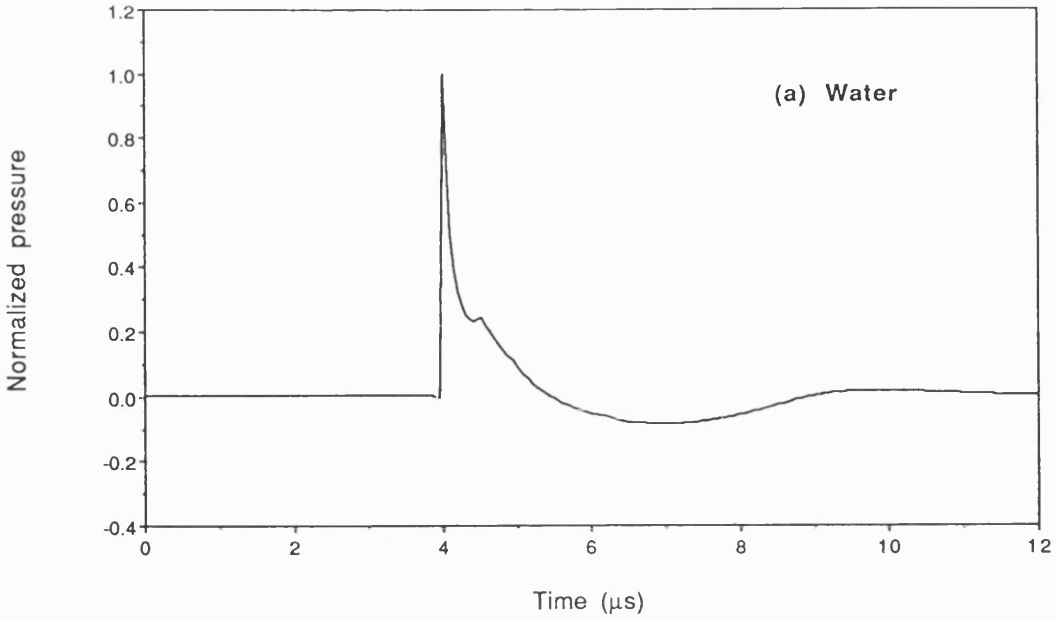

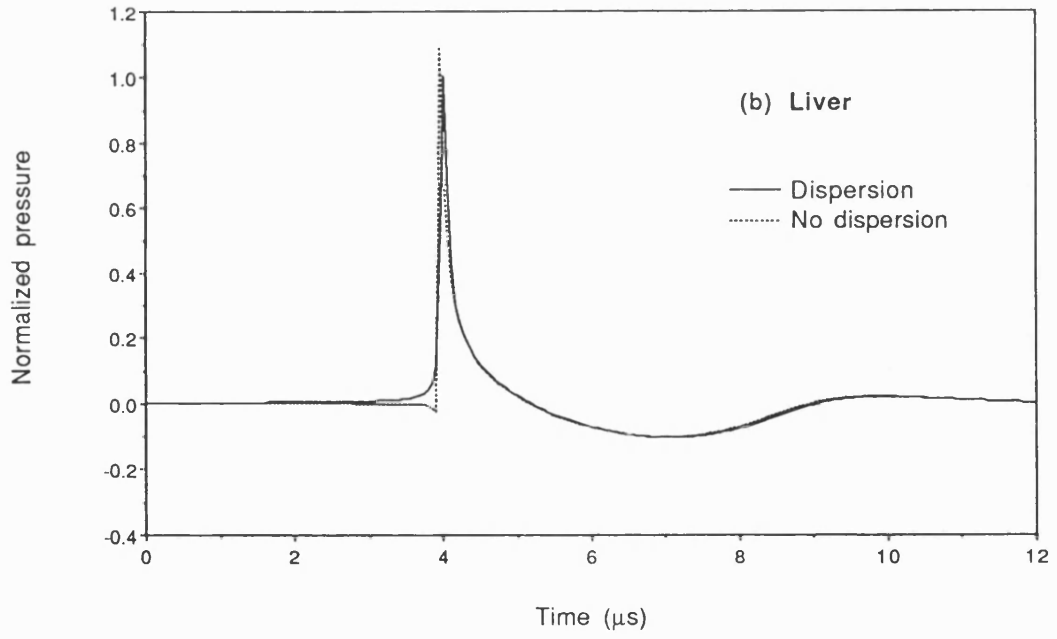

[Fig 5.3-2] Normalized pressure waveforms predicted at the focus of a Dornier HM3 lithotripter in **(a)** water and **(b)** liver. In (b); solid curve: including dispersion and dotted curve: omitting dispersion (normalized to the peak pressure calculated including dispersion).

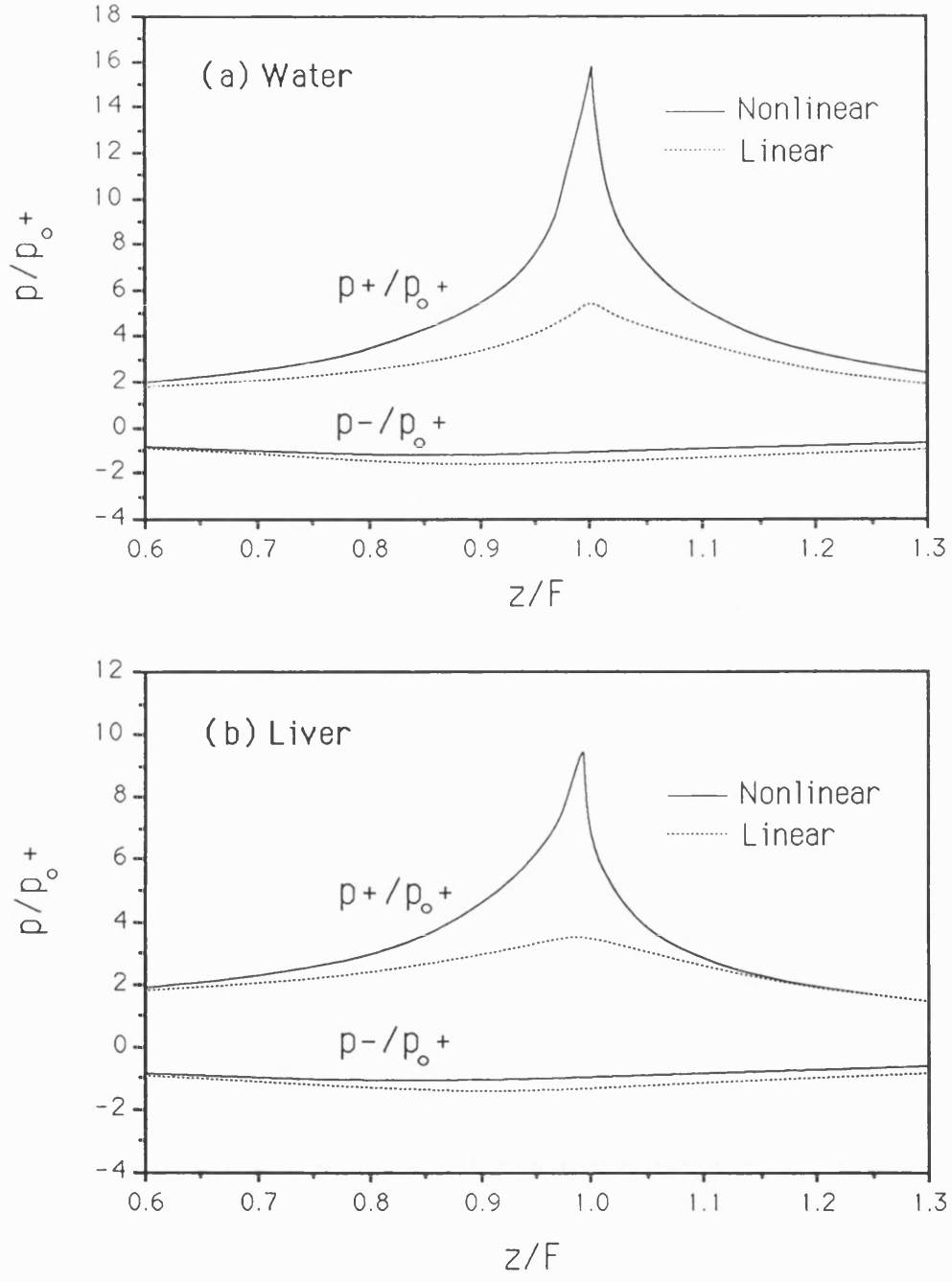

[Fig 5.3-3] Axial variation of predicted peak pressures (p_+, p_-) normalized to the aperture peak pressure (p_{o+}) in propagation of **(a)** water and **(b)** liver. In liver case dispersion is included in the calculation. Dotted curves: linear propagation and solid curves: nonlinear propagation.

calculated by setting the nonlinearity parameter β to zero in the propagation model.

As expected, the axial variation of temporal peak pressures varies smoothly since diffractive effects leading to near field oscillations are not present in a gaussian beam. The value of p_+ increases relatively slowly toward the beam focus defined as the position at which the axial maximum in p_+ occurs. It is then followed by a rapid fall in p_+, which is attributed to the excess absorption in higher harmonics generated during nonlinear propagation overrides the other effects increasing pressure. Some sharp changes in p_+ are noted around the focus. The axial variation in p- is, in contrast, shown to be nearly flat without a rapid change. The position of the beam focus does not coincide with the geometric focus (z=F) but is shown to lie slightly nearer to the source than that predicted by linear diffraction theory. It should be noted that the axial maximum of p- occurs in advance of the beam focus.

The relative importance of nonlinear propagation compared to linear propagation on temporal peak pressures can be examined using the nonlinear gain parameter 'Γ' defined as the ratio of the peak pressure predicted in the nonlinear field to that of linear propagation ($\Gamma=p/p_{lin}$). According to Fig 5.3-3 the axial variation in Γ_+ ($=p_+/p_{lin_+}$) is above unity and reaches its maximum value at the focus, whereas the axial value of Γ_- ($=p_-/p_{lin_-}$) is less than one with a

smoother variation. This illustrates the principal property of nonlinear propagation in a focused acoustic field. The nonlinear effect results in the energy flow from lower to higher harmonics. At the same time diffraction results in the harmonic beams more tightly focused and phase shifted with respect to each other gives rise to increase the asymmetry ratio of waveform. These accumulated and combined processes lead to p_+ and p- being respectively increased and reduced above the values linearly predicted.

The nonlinear effects combined with diffraction give a focal depth shorter than that predicted by linear diffraction theory alone. The focal depth (D_{-3dB}) is defined here as the distance along the beam axis in which the value of p_+ is more than -3dB (70%) of its maximum at the beam focus. It is noted, from Fig 5.3-3, that D_{-3dB} in water (5mm) is shorter than that in tissue (7mm) and this indicates that the axial variation of p_+ in water around the beam focus is much more rapidly changing than in tissue.

5.3.3 Acoustic pressure

The values of p_+ and p- predicted at the beam focus in water and tissue are presented in Table 5.3-1. The values of pressure gains ($G_+=p_+/p_{o+}$, $G_-=p_-/p_{o-}$) and nonlinear gains (Γ_+, Γ_-) are also listed in the table, which provide a measure of the focusing efficiency of the field.

As already noted, the values of Γ_+ are greater than unity and Γ_- less than unity. The value of Γ_+ in water is greater than that in tissue. This indicates that nonlinear propagation, as expected, has a much larger effect on p_+ when propagation is in water. It is shown that the values of Γ_- vary only slightly for propagation in either water or tissue and are similar at around 0.7.

[Table 5.3-1] Predicted values of peak pressures (p_+, p_-) and pressure gains (G_+, G_-) and nonlinear gains (Γ_+, Γ_-) at the beam focus of the Dornier HM3 for a damped sinusoidal pulse propagating from the aperture through water into either water or liver tissue 60mm before the focus.

Medium	p_+(MPa)	p_-(MPa)	G_+	G_-	Γ_+	Γ_-
water	79.77	-5.35	15.95	9.64	3.05	0.69
tissue	47.00	-4.92	9.40	8.83	2.72	0.71
	(53.45)	(-4.83)	(10.69)	(8.70)	(2.92)	(0.70)

+ Note that values for propagation in tissue are obtained with dispersion and those shown in parentheses are calculated without including dispersion.

5.3.4 Dispersion effects

According to Table 5.3-1, when dispersion is omitted in the calculation for tissue case, p_+ is found to increase by 13.7% and p_- to decrease by 1.9%, so that the asymmetry

ratio ($|p_+/p_-|$) is increased to 11.1 from 9.6. This indicates that dispersion acts to oppose the nonlinear and diffraction effects which, in contrast, act to increase the value of p_+ and asymmetry ratio of calculated waveforms. The difference in the axial variation of temporal peak pressures calculated when and when not including dispersion is shown to be noticeable only around the beam focus and maximum deviation occurs at the focus.

5.3.5 Summary

The proposed theoretical model predicts a value of p_+ higher and p_- lower than those expected from the linear propagation. The axial variation of p_+ increases relatively slowly before the focus and then falls off rapidly. The focal depth is predicted to be smaller than that calculated from linear propagation. These features caused by nonlinear effects provide some clinical advantages. The enhanced pressure gain at the focus allows high pressures to be achieved in small focal volumes as required for stone fragmentation. The rapid fall off in p_+ beyond the beam focus reduces acoustic exposure to surrounding tissue.

5.4 Comparison between prediction and measurement

Theoretical predictions of axial peak pressures and pressure waveforms are compared in this section with

measurements made on an experimental electrohydraulic lithotripter (Coleman et al 1989) using a Marconi bi-laminar PVdF membrane hydrophone with a sensitive element diameter of 0.5mm. Previously published pressure waveforms from the Dornier HM3 (Coleman et al 1987a) are also compared with these predictions.

Theoretical predictions were carried out in water using the nonlinear model with the boundary conditions including the aperture waveform (p_{o+}=10MPa) measured on the experimental EH lithotripter operated at 20kV (shown in Fig 5.4-1a) and gaussian shading function with a_o=30mm. The values of κ were measured at both the aperture and focus and they were approximately 0.1 at z=0 and 0.4 at z=F. The value of κ was assumed to change smoothly. The first Fourier frequency (Δf) of waveforms was set to 0.05MHz and the harmonic number (N) was increased from 512 (at z=0) to 1000 at (z=F). The excess attenuation (ε_n) was increased by changing from $\bar{\varepsilon}$=0.05 (at z=0) to 0.4 (at z=F).

5.4.1 Pressure waveforms

Fig 5.4-1 shows the aperture waveform of the experimental lithotripter operated at a 20 kV discharge (figure a) and pressure waveforms predicted in water at several positions along the beam axis (figure b). For the purpose of comparison with measurements, waveforms predicted at the three distinct positions of before (z/F=.5), after (z/F=1.3) and at the focus (z/F=1) have been taken into

account and those measured and predicted at the three positions are displayed in Fig 5.4-2.

The agreement between predicted waveforms (Fig 5.4-2b) and those measured on the experimental lithotripter (Fig 5.4-2a) is quite reasonable considering the approximations involved. In particular, the model successfully predicts the narrowing of the positive pressure half cycle near the beam focus. Waveforms from the Dornier HM3 lithotripter (Fig 5.4-2a) show a lower zero crossing frequency than on the experimental lithotripter and agreement with theory could no doubt be improved by using the aperture waveform measured on this device rather than the experimental lithotripter. Apart from this difference there is good agreement between the general shape of the predicted and measured waveforms.

5.4.2 Axial peak pressures

Positive peak pressures obtained from repeated measurements at positions along the beam axis are shown in Fig 5.4-3a and 5.4-3b for the source operated at 20 kV and 10 kV, respectively. Solid lines indicate the theoretical predictions based on the boundary conditions specified above (for a discharge potential of 20 kV). Changes in boundary conditions for the discharge potential of 10kV include the use of a measured aperture pressure waveform with p_o+=5MPa and the value of κ was increased from 0.05 (at z=0) to 0.3 (at z=F). The numerical constants remain

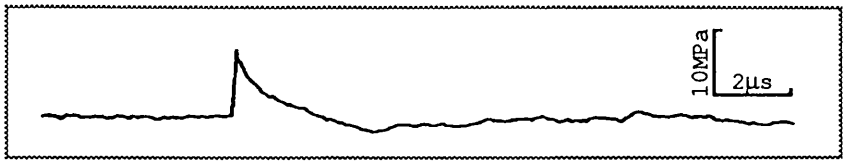

(a) Measured waveform (z/F=0)

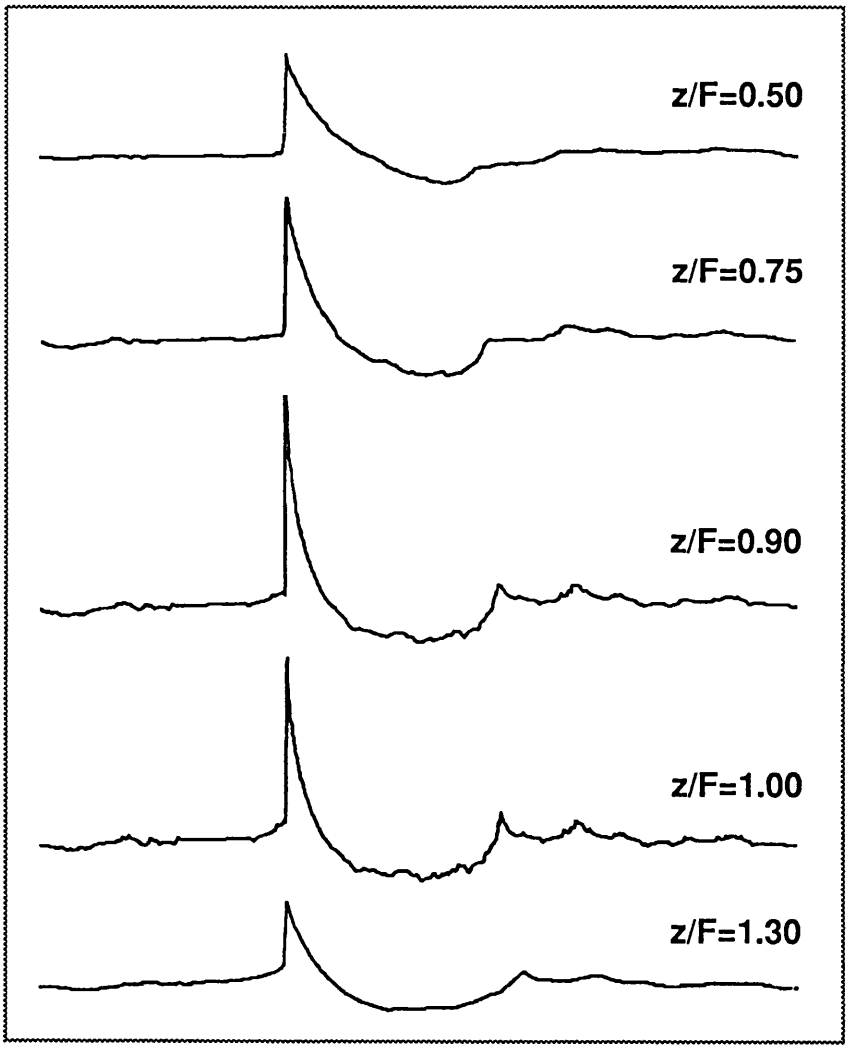

(b) Predicted waveforms

[Fig 5.4-1] **(a)** Aperture pressure waveform (p_o+=10MPa) measured on the experimental electrohydraulic lithotripter operated at 20kV discharge potential and **(b)** pressure waveforms predicted in water at several positions along the beam axis of the lithotripter.

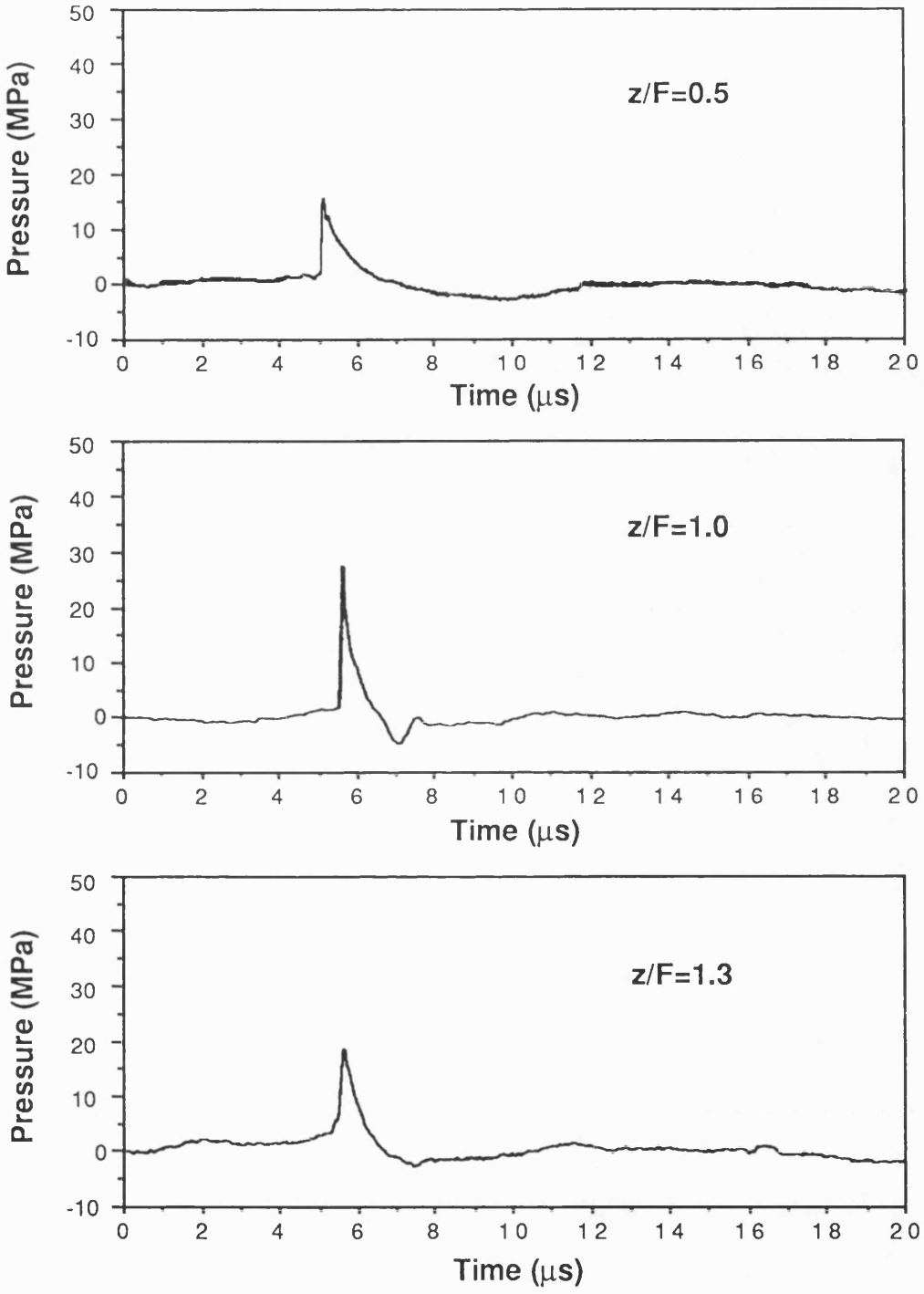

[Fig 5.4-2] **(a)** Pressure waveforms measured in water using a bi-laminar PVdF membrane hydrophone at the positions of z/F=0.5, 1.0 and 1.3 of the experimental electrohydraulic lithotripter operated at 20kV. - continued in (b) -

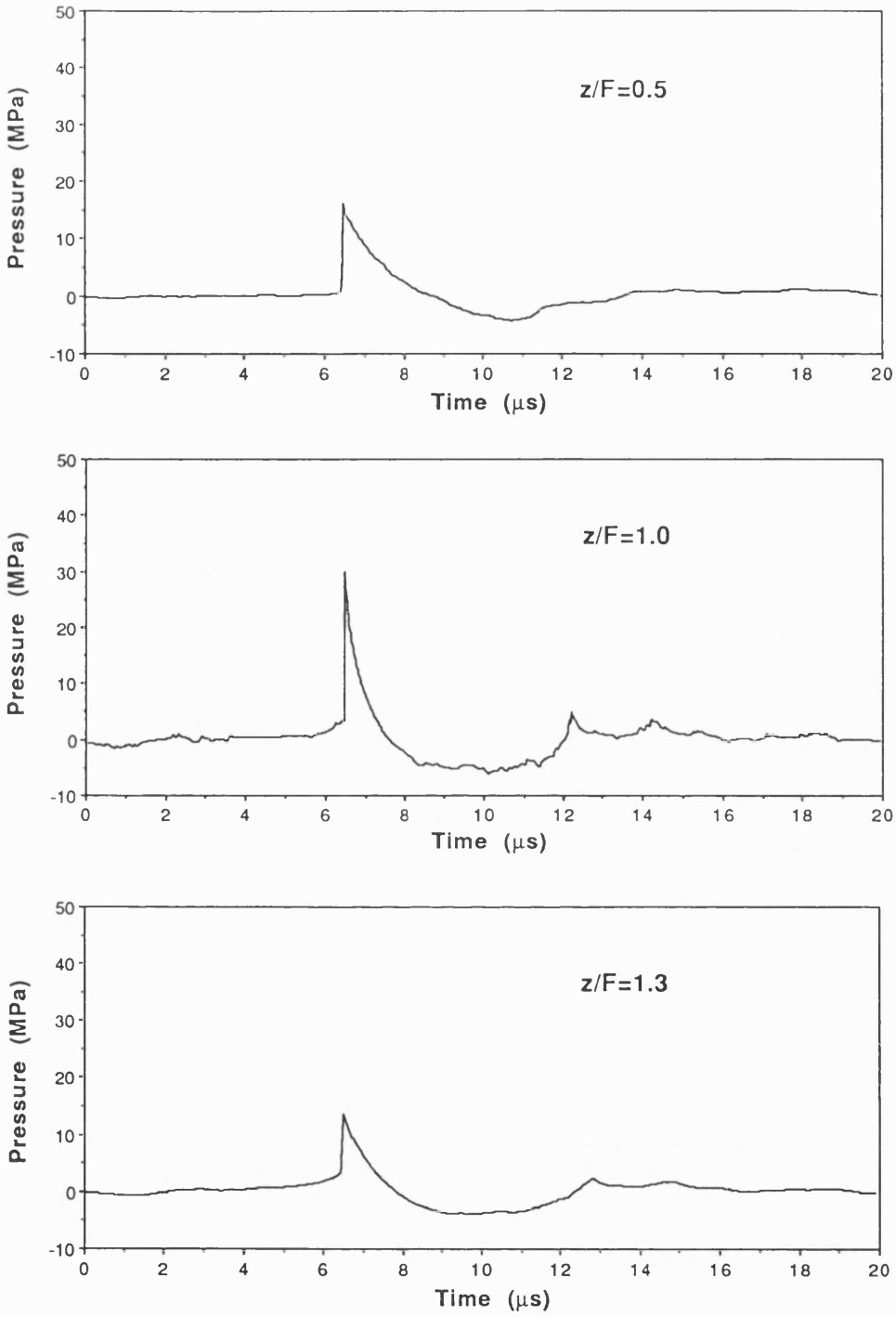

- continued -

[Fig 5.4-2] **(b)** Pressure waveforms predicted in water using the present nonlinear propagation model at the positions of z/F=0.5, 1.0 and 1.3 of the experimental electrohydraulic lithotripter operated at 20kV. - continued in (c) -

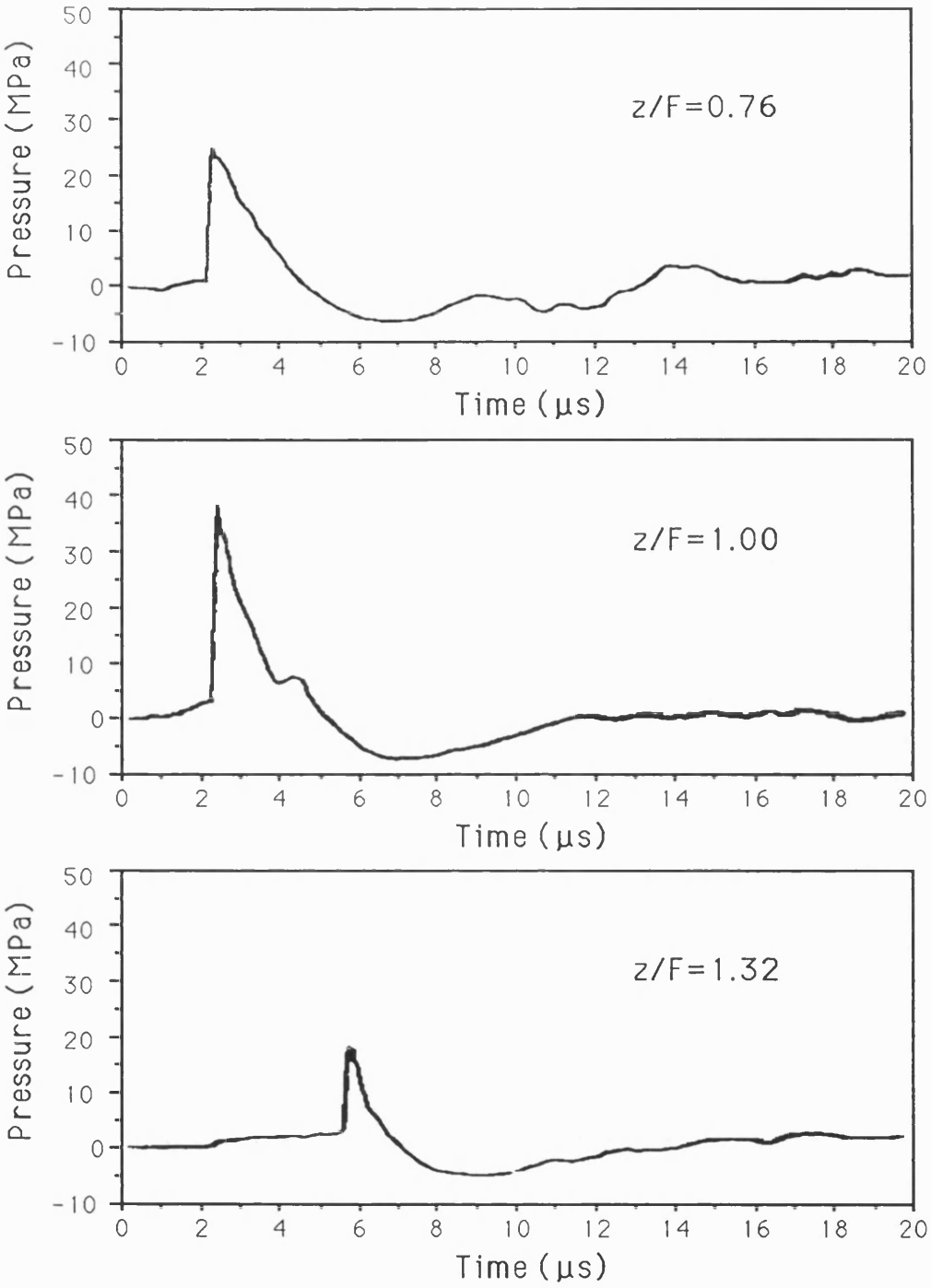

- continued -

[Fig 5.4-2] **(c)** Pressure waveforms measured in water using a bi-laminar PVdF membrane hydrophone at the positions of z/F=0.76, 1.0 and 1.32 of the Dornier HM3 electrohydraulic lithotripter operated at 20kV (Coleman et al 1987a).

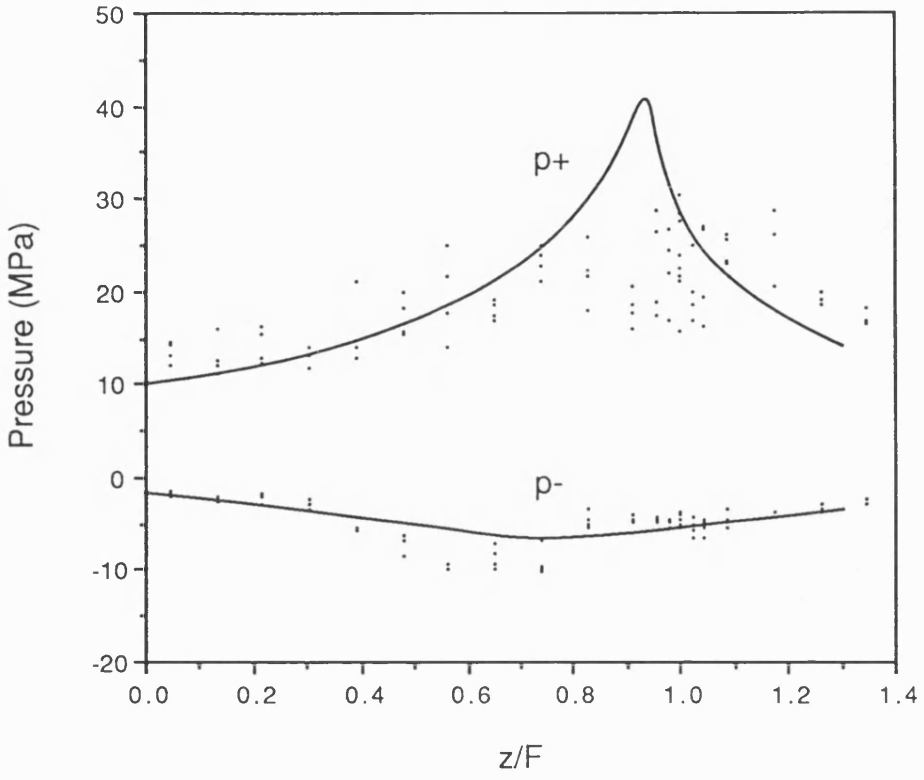

[Fig 5.4-3] **(a)** Axial variation of peak pressures (p_+, p_- in MPa) measured (dots) and predicted (solid curves) for the experimental electrohydraulic lithotripter operated at the discharge potential of 20kV. - continued in (b) -

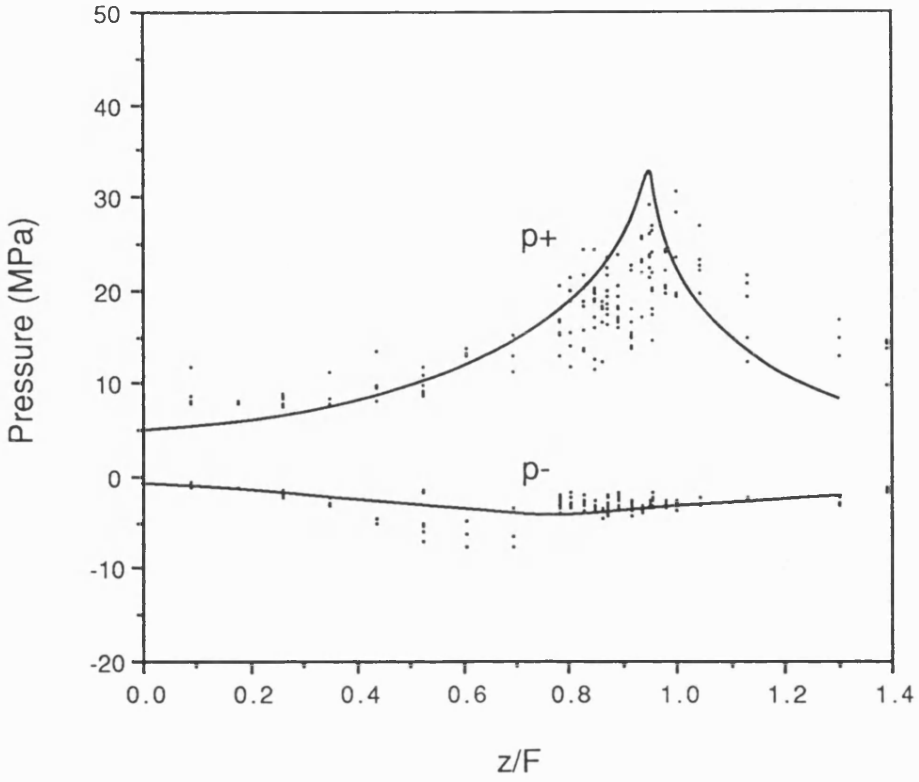

- continued -

[Fig 5.4-3] **(b)** Axial variation of peak pressures (p_+, p_- in MPa) measured (dots) and predicted (solid curves) for the experimental electrohydraulic lithotripter operated at the discharge potential of 10kV.

the same as for the case of 20kV.

Theoretical axial variations of p_+ and p- for both discharge potentials follow the experimental values reasonably well up to the position of the beam focus after which they show a rather more rapid decay in p_+ than is measured. The predicted pressure gain at the beam focus (G_+=4.1 for 20kV and G_+=6.5 for 10kV) corresponds to the maximum measured value for the 10KV and is higher than that measured for the 20KV. The positions of the spatial peak values of p_+ and p- correspond reasonably well with both the measured and calculated position of p- being well in advance of that of p_+. A doubling of the aperture value of peak pressure p_{o+} from 5MPa to 10 MPa does not result in a corresponding doubling of p_+ at the focus as a result of increased attenuation of the higher frequencies generated during propagation. At the higher output setting the experimental values of p_+ are even lower than those predicted near the beam focus.

5.4.3 Discrepancy between prediction and measurement

Part of the discrepancy is attributed to incomplete characterization of the source (eg, shading function and κ) and measurement errors, including hydrophone bandwidth limitations, most of which result in underestimated pressures due to degradation of the recorded shock front.

As discussed in Section 2.6 most sources of systematic

error in hydrophone measurements of the peak pressure (p_+) in lithotripsy fields act to generate underestimates of its true value. These sources of systematic errors include hydrophone calibration uncertainties, nonlinearity of hydrophone response, possible misalignment (directional response) and spatial averaging over the sensitive element. While some effects including resonance overshoot may partially compensate for these systematic errors it is more than likely that the recorded pressure represents an underestimate of at least 10% from these effects. There is also another, more subtle source of systematic error in the measured values of p_+. This is related to shock-to-shock instability in the position of the acoustic field. The maximum value of p_+ will be recorded only when the beam axis coincides with the hydrophone position. A measured value of p_+, therefore, is more likely to be less than that of p_+ on the axis.

The measured random uncertainty in p_+ is about 20% (Coleman and Saunders, 1989) in repeated readings of p_+ and about half this can be attributed to shifts in the field position. Combining these systematic errors suggests that the measured mean values in p_+ is likely to be at least 20% lower than the true values. The predicted values are shown within the random error of measurements. Significant reduction of such systematic sources of error is probably not yet technically possible.

5.5 Alteration of source output: Predicted

Acoustic fields generated at different source output settings are examined using the theoretical model. Other conditions are unchanged except that castor oil is taken here as a tissue equivalent medium instead of liver. Acoustic parameters of castor oil are ρ_o=950kg/m^3, c_o=1500m/s, β=7, α_o=10.9Np/m at 1MHz, and b=2 (Duck 1990). The use of castor oil has some clear merits in that the numerical model runs without the need to employ an excess attenuation (ε_n) to reduce harmonic truncation error. It is because castor oil has a relatively higher attenuation coefficient than most tissue at high frequencies due to the squared dependence of the attenuation coefficient with frequency. The fact that it may not be the most suitable or stable tissue equivalent is not considered of interest here since any medium providing significant attenuation would serve to allow the model to be examined without requiring the excess attenuation of higher harmonics.

5.5.1 Source output setting

The source output power can be set by altering either the voltage or capacitance in the driving circuit. Alteration of the capacitance results in changes not only in the amount of the stored electric energy but also the discharge circuit resonant frequency, and hence the rate at which the electric energy is supplied to the transducer. In practice,

the output setting on commercial lithotripters is typically related to the voltage used to charge the capacitor in the discharge circuit.

Assuming that the energy distribution (ie, aperture shading function) and pressure waveform across the aperture surface remain the same at different source outputs, the aperture peak pressure (p_{o+}) may vary linearly with voltage applied to the generator driving circuit, since it varies to a first approximation of the square root of source energy (Coleman et al 1991b). It will be assumed for the sake of argument, therefore, that the alteration in source output is directly related to the aperture pressure in the calculation. The range of source powers considered here are given in terms of p_{o+} varying from 1MPa to 7MPa.

5.5.2 Predicted waveform

Pressure waveforms predicted at the position of the focus for a variety of p_{o+} values are shown in Fig 5.5-1 where changes in their shock fronts are clearly illustrated. The rise time (t_r) decreases with p_{o+} for $p_{o+} \leq 3$MPa and remains constant for $p_{o+} > 3$MPa. This is attributed to the fact that the shock front of the waveform is fully formed at the focus when p_{o+} reaches a certain pressure, p_s (=3MPa here) which may be called a shock formation aperture pressure (p_s). The source output setting at a given beam geometry, therefore, determines whether or not the front of the waveform at the focus is fully shocked. The duration of the

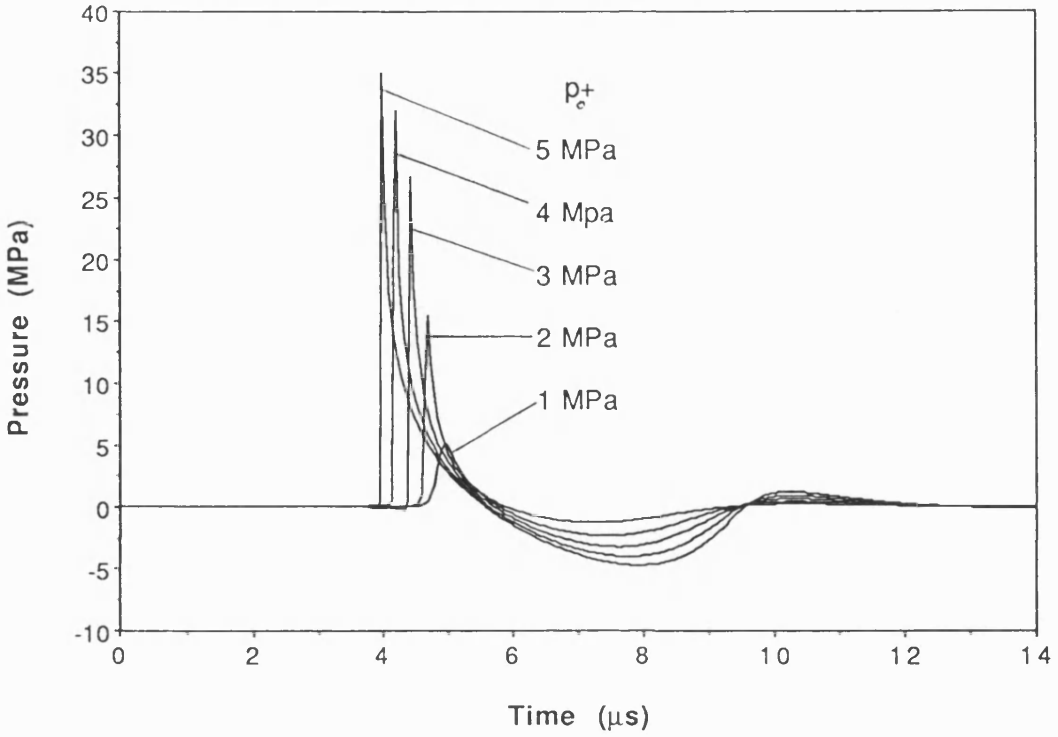

[Fig 5.5-1] Pressure waveforms predicted in castor oil at the focus of the Dornier HM3 lithotripter with an aperture peak pressure (p_{o+}) ranging from 1 to 5MPa.

positive half cycle (t_+) of predicted waveforms is noted to be approximately proportional to p_{o+} since the more intense shock front has a faster propagation speed. The duration of the negative half cycle (t-), on the other hand, is not sensitive to p_{o+}.

5.5.3 Axial variation

Each curve shown in Fig 5.5-2 represents an axial plot of p_+ (figure a) and p- (figure b) normalized to p_{o+}. Approaching the beam focus, values of the axial pressure gain (p_+/p_{o+}) with increasing p_{o+} are shifted up for $p_{o+} \leq 3$MPa but decreased for $p_{o+} > 3$MPa. The rapid fall off in p_+ beyond the beam focus becomes more significant when $p_{o+} > 3$MPa. The position of the beam focus does not appear to alter significantly in the whole range of p_{o+} from 1MPa to 7MPa. The axial negative pressures gain (p_-/p_{o+}) slightly decreases with increasing p_{o+} but is not particularly sensitive to changes in the aperture pressure.

Changes in focal depth (D_{-3dB}) with p_{o+} are illustrated in Fig 5.5-3 where the two lines represent the position of the -3dB pressure either side of the beam focus. The focal depth is obtained from the vertical separation of the two curves at a given value of p_{o+}. Fig 5.5-3 shows that D_{-3dB} narrows with increasing p_{o+} for $p_{o+} \leq 3$MPa, indicating that the beam becomes more tightly focused. On the other hand, D_{-3dB} becomes broader with increasing p_{o+} for $p_{o+} > 3$MPa. This can be attributed to excess absorption caused by shock

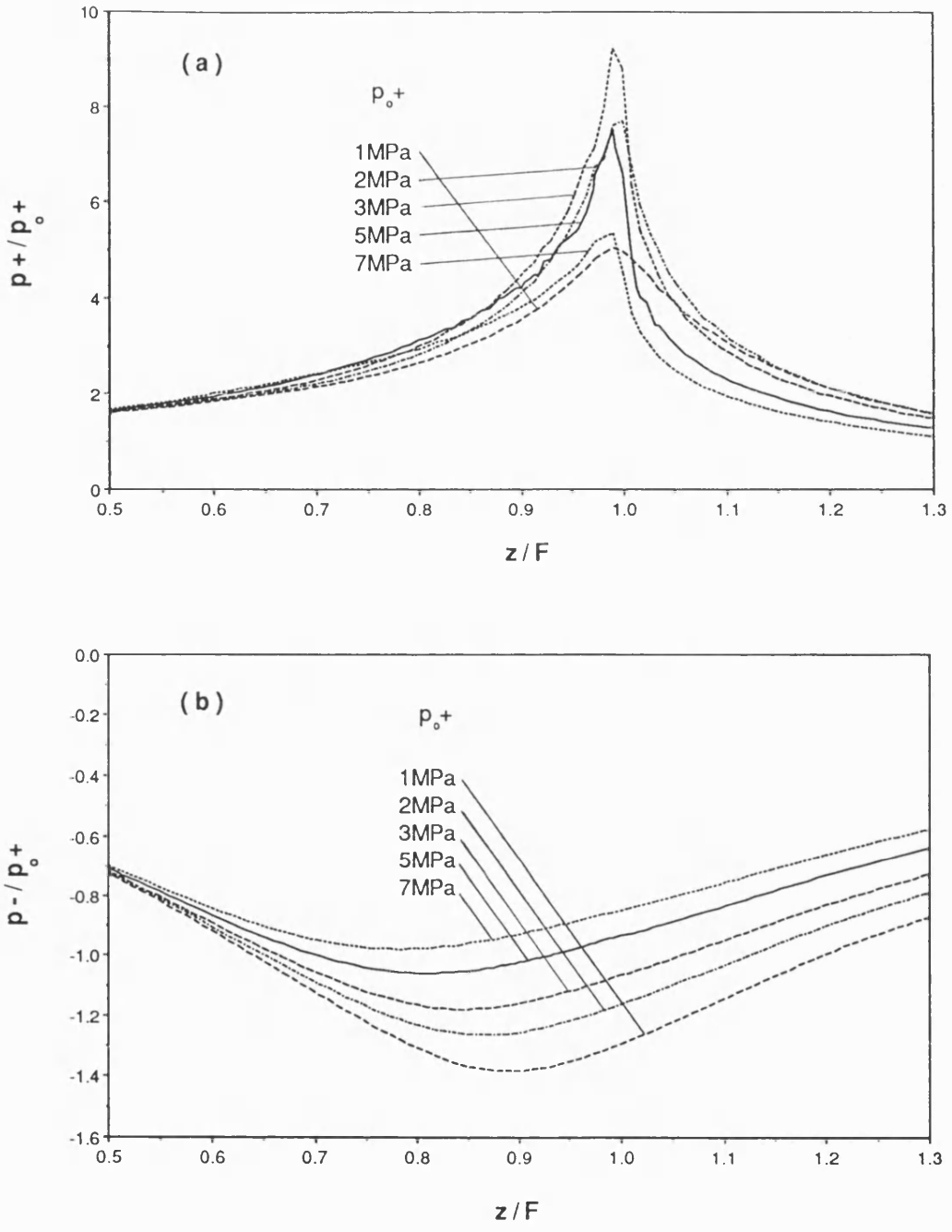

[Fig 5.5-2] Axial variation of **(a)** the positive peak pressure (p_+) normalized to the aperture peak pressure (p_{o+}) and **(b)** the negative peak pressure (p_-) normalized to p_{o+} which are predicted in castor oil for the Dornier HM3 lithotripter with p_{o+}=1,2,3,5 and 7MPa.

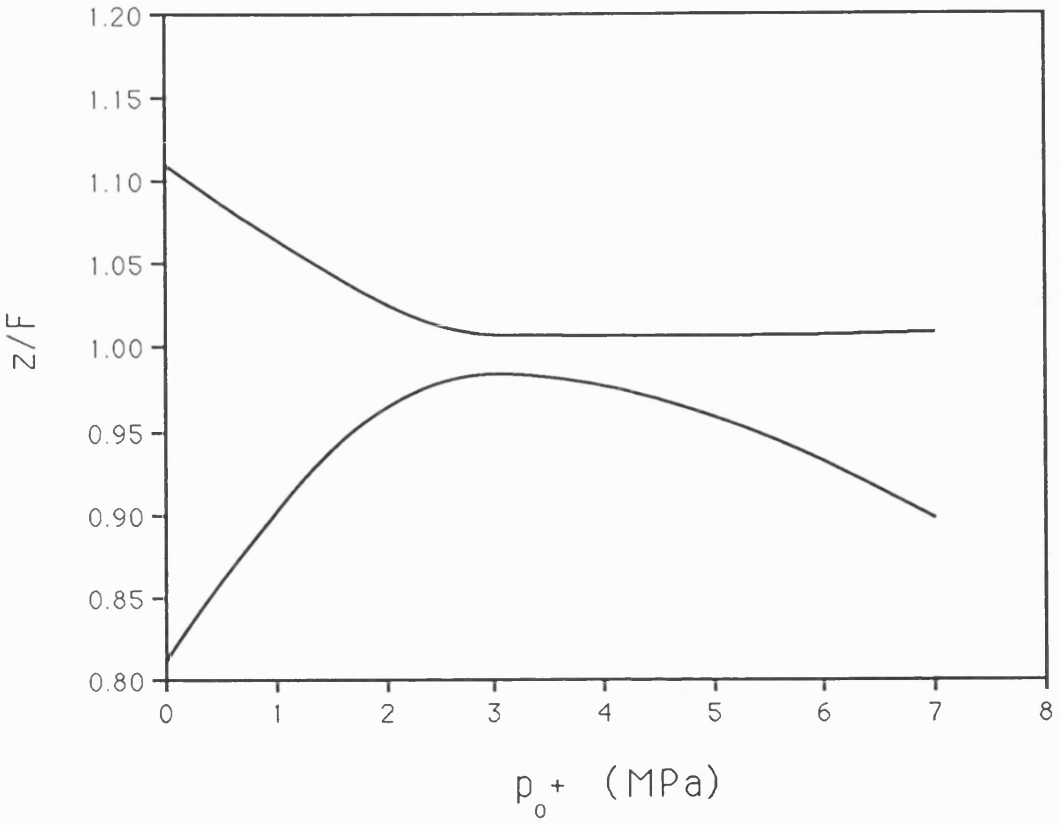

[Fig 5.5-3] Variation of the axial position (z/F) of -3dB focal pressure for the Dornier HM3 lithotripter as a function of aperture peak pressure (p_{o+}). The value of -3dB focal depth is determined by the distance between the lower and upper curves.

formation as predicted by the model. The changes in focal depth as the source output is turned up are likely expected to be similar to the changes in the beam width at the focus. The value of focal depth is, of course, constant regardless of p_{o+} when the amplitude of p_{o+} is infinitesimal, ie, linear pressure level.

5.5.4 Acoustic pressure

The behaviour of predicted temporal peak pressures (p+, p-) at the beam focus while increasing the value of the aperture pressure (p_{o+}) is illustrated in Fig 5.5-4. The dotted lines labeled p_{lin+} and p_{lin-} indicate the focal peak pressures expected for linear propagation. This linear model obviously breaks down for p_{o+} above a certain limit. The solid curves in Fig 5.5-4 indicate predictions made using the present nonlinear model. It is shown that the values of both p+ and p- vary nonlinearly with p_{o+} and three characteristically different regions are identified: linear ($p_{o+} \leq 0.05$MPa), pre-shock ($0.05\text{MPa} < p_{o+} \leq 3\text{MPa}$) and shock region ($p_{o+} > 3$MPa). The transition between the three regions is indicated in Fig 5.5-4 by the vertical broken lines.

In the linear region the value of p_{o+} is infinitesimal, and the values of both p+ and p- vary linearly with p_{o+}. When p_{o+} is increased to be finite in the pre-shock region, p+ increases more rapidly than that predicted by linear propagation and p- starts to saturate. In the shock region

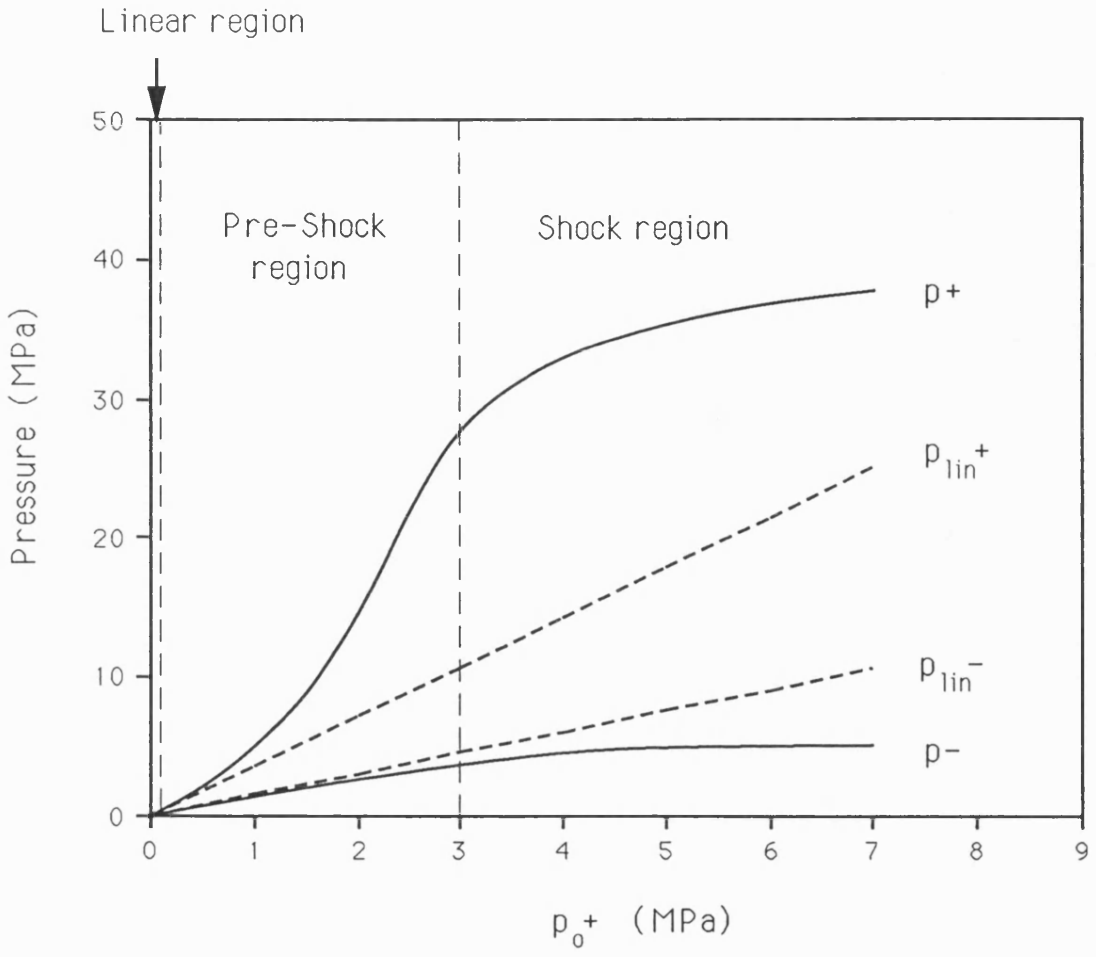

[Fig 5.5-4] A plot of focal peak pressures (p_+, p-) against aperture peak pressure for the Dornier HM3 lithotripter; dashed lines: linear propagation and solid line: nonlinear propagation. The two vertical broken lines indicate transitions from the linear to pre-shock regions and from the pre-shock to shock regions.

the rate of increase of p_+ becomes less than that predicted by linear propagation while p- remains almost constant.

In the pre-shock region nonlinear propagation leads to a flow of energy from lower to higher harmonics. This enhances the focusing over that predicted by linear diffraction. The features shown in the shock region are attributed to the attenuation increases at the fully formed shock front and this results in a reduction in p_+. On the other hand, the value of p- associated with the lower frequency part of the waveform, is not sensitive because changes in lower harmonics are balanced by two opposite mechanisms, ie, nonlinearity and focusing.

Associated with the behavior of p_+ with increasing p_{o+} in the different regions are changes in the focal gain (G_+) and rise time (t_r). In the pre-shock region, as p_{o+} is turned up, G_+ increases and t_r decreases, while, as p_{o+} increases in the shock region, G_+ decreases but t_r remains constant.

5.5.5 Summary

Acoustic fields generated by an electrohydraulic lithotripter have been examined at different source output settings given in terms of aperture peak pressures using the present theoretical model. Three regions are identified as the source output is increased, each with a different relationship between the peak positive pressures at the

focus and aperture. These are characterized as linear, pre-shock and shock regions which are associated with the amount of distortion in pressure waveforms due to nonlinear and diffraction effects as well as attenuation.

5.6 Alteration of source output: Observed

Regions in which the different types of lithotripters operate have been examined using the relationships between measured focal pressures (p_+) and source output settings. Fig 5.6-1 shows the variation of p_+ measured in water at the foci of the three different types of clinical lithotripters: Dornier HM3 (EH), Stortz Modulith SL-10 (EM) and Piezolith 2200 (PE), while increasing their source outputs. The pressure in the figure is normalized to the value of the pressure measured at the maximum output setting of each lithotripter. Since the method and range of the source output setting is different for the lithotripters, ie, EH (10kV-25kV), PE (1-4) and EM (1-9), for the sake of comparison, the full range of each lithotripter setting is fitted equivalently to that of the Stortz lithotripter, ie, minimum setting to 1 and maximum to 9.

If the aperture peak pressure (p_{o+}) is assumed to have linear relationship with the source output, the plot of p_+ against the source output setting shown in Fig 5.6-1

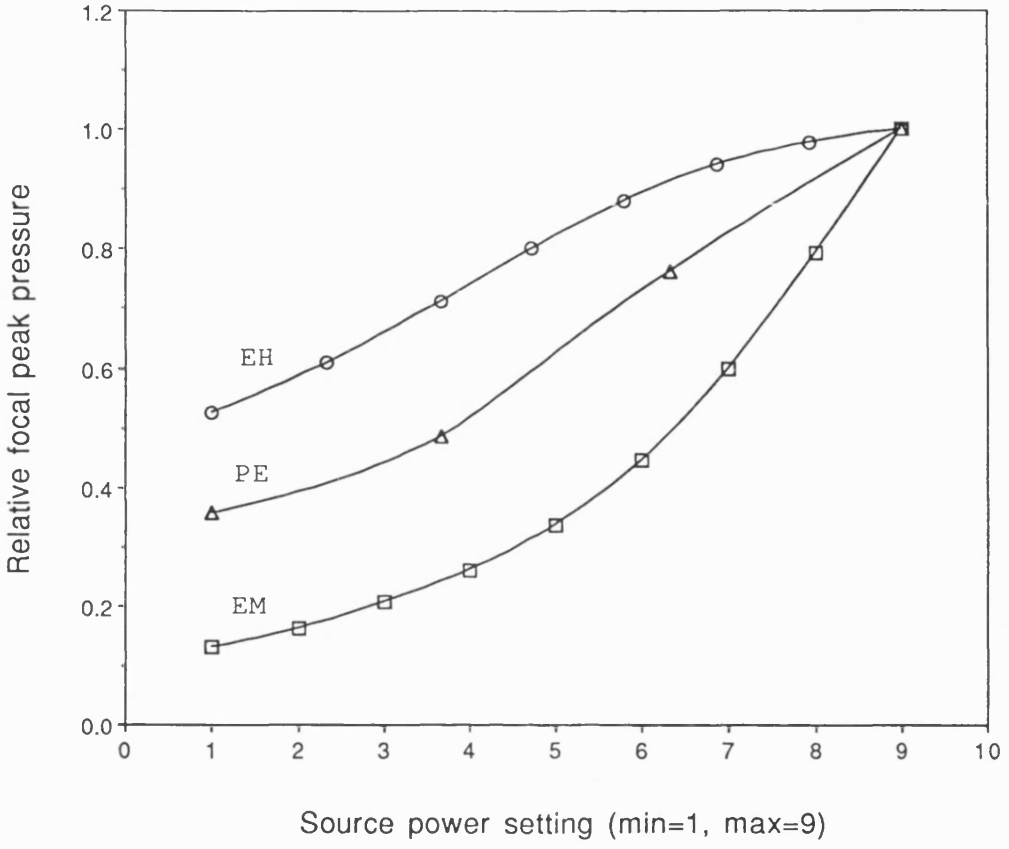

[Fig 5.6-1] Variation of peak positive pressure measured at the beam focus as a function of source output setting for the three different types of clinical lithotripters: EH; Dornier HM3, PE: Piezolith 2300 and EM: Stortz Modulith SL-10. The focal peak pressures are normalized to the peak pressure measured at the maximum output settings. The source output setting of each lithotripter is equivalently fitted between minimum 1 and maximum 9.

represents the relationship between the focal and aperture peak pressures of each lithotripter. This relationship can characteristically be compared with the theoretical predictions illustrated in Fig 5.5-4.

The beam behaviour in the EH lithotripter is seen to be associated with the shock region. This indicates that the Dornier HM3 lithotripter can not be turned down below the shock region. The lowest setting (10kV) of the source will correspond to the value of p_{o+} greater than the shock formation aperture pressure (p_s) beyond which shocks are formed at the focus. At a discharge voltage lower than 10kV, the necessary electric discharge would be inhibited. The EM and PE lithotripters are shown to operate mainly in the pre-shock region and partially in the shock region. Changes in the rise time with the source output power of the three different types of lithotripters displayed in Fig 5.6-2 supports this classification.

Measurements made by Coleman and Saunders (1989) have also shown that, as the source output increases, the focal pressure gain increases and the rise time decreases in the current commercial PE and EM lithotripters which are the characteristics of fields in the pre-shock region, whereas the gain falls and the rise time remains constant in the EH lithotripter which are the characteristics of fields in the shock region. For instance, the rise time measured in a PE lithotripter (EDAP LT-01), is reduced from 300ns to 100ns

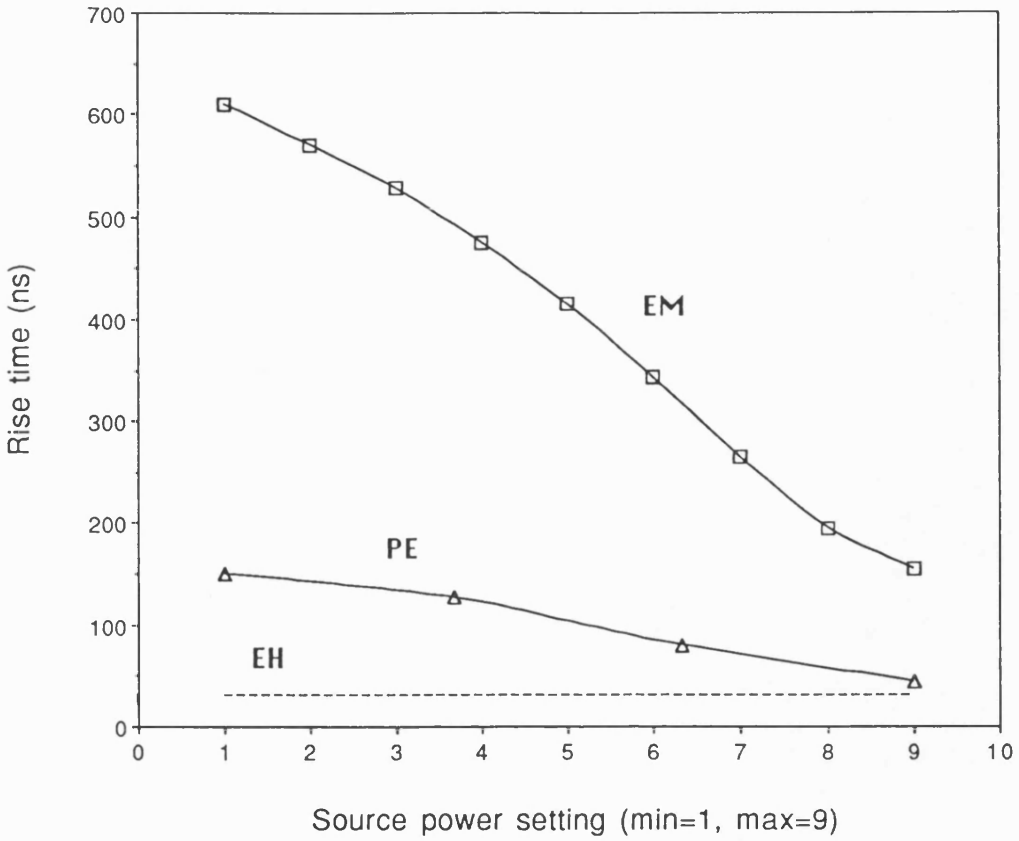

[Fig 5.6-2] Variation of the rise time of the waveforms measured at the foci of the three different types of clinical lithotripters as a function of source output setting (EH: Dornier HM3, PE: Piezolith 2300 and EM: Stortz Modulith SL-10). The source output setting of each lithotripter is equivalently fitted between minimum 1 and maximum 9.

when the output setting of the generator increases from 10% to 50%.

5.7 Discussion

An illustration of how the proposed one dimensional model might be used in lithotripsy fields and comparison between predictions and measurements have been presented for the case of an electrohydraulic lithotripter (Dornier HM3) radiating into water. It is also shown how the model might be used to allow prediction of *in situ* pressure by examining propagation in an attenuating medium (eg, liver). Although harmonic truncation and beam broadening impose the most severe test of the model, particularly, for shock pulse propagation through a nearly lossless medium like water, the relative simplicity of the model allows a variety of effects to be examined relatively quickly and provides estimates of the lithotripsy field, which are reasonable considering the lack of detailed characterization of the source.

In practice it may be possible to avoid the requirements for accurate predictions of pressures in water by carrying out measurements in water with a well characterized attenuator between the hydrophone and source (Preston et al 1991). These pressures could be more simply and accurately predicted and be related to predictions at depth in tissue

by means of the present model. The additional advantages of this approach in high amplitude pulsed ultrasonic fields are that hydrophones would be operated at pressures closer to those at which they are calibrated and would be less subject to physical damage.

It should be pointed out that the theoretical consideration and measurement used in this chapter have been performed for single pulse propagation. However the clinical extracorporeal shock wave lithotripsy uses a series of pulses, so that the gas bubbles generated by preceding pulses influence the propagation of succeeding pulses. The positive peak pressure, for example, is expected to be reduced by the shock front interaction with gas bubbles. The cavitation effects in clinical lithotripsy fields will be considered in detail in Chapter 6.

CHAPTER 6. CAVITATION EFFECTS IN LITHOTRIPSY FIELDS

6.1 Introduction

The propagation equations considered so far have assumed propagation of a single pulse in an ideal medium with sufficiently high tensile strength where cavitation effects can be ignored. In clinical extracorporeal shock wave lithotripsy, however, a series of pulses are used, and cavitation bubbles generated by preceding pulses may alter the acoustic properties of the medium. Unless the bubbles are completely dissolved, succeeding pulses will interact with the bubbles and hence the propagation will be altered.

It has been reported that stronger damping of the acoustic waves takes place in the liquid containing air bubbles and qualitative changes in the structure of waveform have been observed (Dontsov et al 1988). This is attributed to a significant change in the acoustic properties of the medium containing even small numbers of bubbles (Silberman 1957, Urick 1975) with most notably a large increase in high attenuation and dispersion (Prosperetti 1984b). In lithotripsy fields it is indicated that energy transfer from shock pulses to cavitation bubbles does indeed take place (Brümmer et al 1989b).

This chapter predicts the features of cavitation activity induced by clinical ESWL fields using a simple nonlinear bubble dynamics model and describes the effects of these bubbles on shock pulse propagation. As in Chapter 5, the analysis is carried out for an electrohydraulic source as used in the Dornier HM3 lithotripter, although it could be applied equally well to any other lithotripsy source.

6.2 Nonlinear bubble dynamics

The response of bubble clouds to high amplitude pulsed ultrasonic fields is complicated and no analytical theory has been reported. The theoretical analysis is simplified here by considering the behaviour of a single free (ie, spherical) bubble exposed to the acoustic fields. The Gilmore model has been chosen since it is particularly well suited to the conditions of high pressure where the compressibility of a liquid plays an important role (Vokurka 1986) and can be implemented on a super computer with reasonable running time. The diffusion of gas in and out of the bubble has also been taken into account since this critically influences the bubble radius (Church 1989).

6.2.1 Gilmore model

The fundamental assumptions of the Gilmore model include that the bubble is initially at equilibrium in an infinite

liquid and it retains its spherical shape throughout the motion, the radius of the bubble is much smaller than the wavelength of an applied field, and that the motion of the liquid surrounding the bubble is isentropic. Note that the Gilmore model does not consider diffusion. The Gilmore model for the radial motion of a spherical bubble with the initial equilibrium radius of R_o is given by the following nonlinear differential equation under the condition that the centre of the bubble is the origin of the coordinate system.

$$(6.2\text{-}1) \qquad \frac{dU}{dt} = \frac{1}{R\left(1-\frac{U}{C}\right)}\left[H\left(1+\frac{U}{C}\right)-\frac{3}{2}\left(1-\frac{U}{3C}\right)U^2\right] + \frac{1}{C}\frac{dH}{dt}$$

where U=dR/dt, R is the instantaneous bubble radius, t is a time variable, C is the speed of sound at the bubble wall and H is the enthalpy of liquid at the bubble interface.

Both C and H are determined from a pressure density relationship of liquid, ie, $C^2 = dp/d\rho$ where p and ρ are the time varying pressure and density, respectively, and H $= \int_{P_\infty(t)}^{P(R)} dp/\rho$ where P(R) is the pressure at the bubble wall given by $P(R) = P_g - 2\frac{\phi}{R} - 4\mu\frac{U}{R}$ provided that the vapour pressure inside the bubble is assumed to be negligible where P_g is the pressure of gas within the bubble, ϕ is the surface tension, μ is the coefficient of shear viscosity, and $P_\infty(t)$ is the pressure at infinity given by $P_\infty(t) = p(t)+P_o$ where p(t) is the acoustic pressure of liquid and

P_o is the steady ambient pressure of the surrounding liquid.

A modified Tait pressure density equation of state obtained using an experimental isentropic compressibility law for liquid is given by $p(t)=\mathcal{A}(\rho(t)/\rho_o)^m-\mathcal{B}$ where m is a power index in the Tait equation, and $\mathcal{A}$ and $\mathcal{B}$ are constants. Following Lastman and Wentzell (1981), m=7, $\mathcal{A}=c_o^2\rho_o/mP_o$ and $\mathcal{B}=\mathcal{A}-1$. If the Tait equation is used, the enthalpy and sound speed at the bubble interface are then calculated by

$$C = \sqrt{c_o^2 + (m-1)H} \qquad (6.2\text{-}2)$$

$$H = \frac{m}{m-1}\frac{\mathcal{A}^{1/m}}{\rho_o}\left[\left(P(R)+\mathcal{B}\right)^{(m-1)/m} - \left(P_\infty(t)+\mathcal{B}\right)^{(m-1)/m}\right]$$

where c_o is the small signal sound speed in the liquid, ρ_o is the equilibrium density of the liquid.

The use of the Tait equation may introduce considerable error into calculation when the pressure in the liquid exceeds 10^4MPa. The error may be reduced by the use of a different state equation, for example, the Van der Waals equation at high pressure, but more computing time would be required. In lithotripsy fields, the Tait equation can reasonably be retained since high pressure exists for a relatively short time.

The pressure distribution in the liquid surrounding the

bubble can be calculated, according to the method described by Akulichev (1971):

$$(6.2\text{-}3) \qquad P(r,t) = \mathcal{A}\left[\frac{2}{m+1} + \frac{m-1}{m+1}\left(1+\frac{m+1}{rc_o^2}\Omega\right)^{1/2}\right]^{2m/(m-1)} - \mathcal{B}$$

where r is the distance from the centre of the bubble and Ω is a variant of the bubble motion at the bubble surface defined by $\Omega=R(H+U^2/2)$.

6.2.2 Diffusion

The gas diffusion has been taken into account using a zero order solution to the diffusion equation given by Eller and Flynn (1965) and the instantaneous mol number of gas inside the bubble (M) is calculated by

$$(6.2\text{-}4) \qquad M = M_o - 4\sqrt{\pi\mathcal{D}} \int_o^q Q(q')/\sqrt{q-q'}\, dq'$$

where M_o is the initial mol number of gas inside the bubble, $\mathcal{D}$ is the diffusion constant of the gas in the liquid, the parameter q is defined by $q = \int_o^t R^4(t')dt'$ and $Q(q) = \mathcal{C}_s(P_g/P_o)-\mathcal{C}_i$ represents the difference between the gas concentrations at the bubble wall and far from the bubble, where $\mathcal{C}_s$ and $\mathcal{C}_i$ are the saturation and dissolved gas concentration, respectively, in the liquid far from the bubble, $P_g = (P_o+2\phi/R_o)(R_o/R)^{3\eta}(M/M_o)(R_{oi}/R_o)^{3(\eta-1)}$ where η is the polytropic exponent of the gas and R_{oi} is the time varying equilibrium bubble radius.

The diffusion equation Eq(6.2-4) is coupled to the equation of bubble motion Eq(6.2-1) through P_g which is a function of M. The use of the zero order solution Eq(6.2-4) for gas flow may be justified from the fact that its contribution to the total flow is far greater than that due to all of the higher order terms combined for short time (Crum and Hansen 1982, Eller and Flynn 1965) and higher-order terms require a considerable increase in computing time.

6.3 Bubble response to shock pulse

The motion of a spherical air bubble in water in response to a single pulse generated by an electrohydraulic lithotripter (Dornier HM3) has been simulated using the Gilmore single bubble model described in Section 6.2. The 5th order Runge-Kutta method has been used to solve the equations from (6.2-1) to (6.2-4) simultaneously and the source code has been implemented on a Cray X-MP/28 super computer using a C-compiler. With step size optimization the program takes about one hour to run for the examples considered here. The parameters predicted by the model are the time variation of bubble radius (R(t)) and the pressure at the bubble wall (P(R,t)), which are known to be useful in describing the behaviour of the bubble motion. Other parameters like temperature are not concerned here although they can be obtained from the model.

6.3.1 Boundary conditions

In the electrohydraulic lithotripter, unlike other types of shock wave sources, multiple shock pulses are emitted due to successive collapses and rebounds of a plasma bubble generated in the water close to the electrode tips as a result of the electrical discharge (Appendix B2). Only the first two shock pulses are shown to be significant and these two are considered here and identified as 'primary' and 'secondary' shock pulses, respectively. Assuming that both the primary and secondary shock pulses are characteristically identical, a simplified mathematical expression for these waveforms is expressed by

$$(6.3\text{-}1) \quad p(t) = \tilde{a}p_o(1-\exp(-t/t_e))\exp(-t/t_c)\cos(2\pi f_o t+\pi/3)$$

where $\tilde{a}$ is a constant to make the maximum value of $p(t)$ equal to p_o, t_e is a time constant to determine the rise time of waveform, t_c is the decay time constant of waveform, and f_o denotes the reference frequency chosen from the duration of the negative half cycle (t-) of measured waveform, ie, $f_o=1/(2t\text{-})$ (Church 1989).

A typical waveform constructed using Eq(6.3-1) for the focal field of the electrohydraulic lithotripter is shown in Fig 6.3-1. The values of parameters used to construct these waveforms are $t_c=1.25\mu s$ and $f_o=0.0833MHz$ (ie, $t\text{-}=6\mu s$) for the primary shock pulse to give a pulse with an

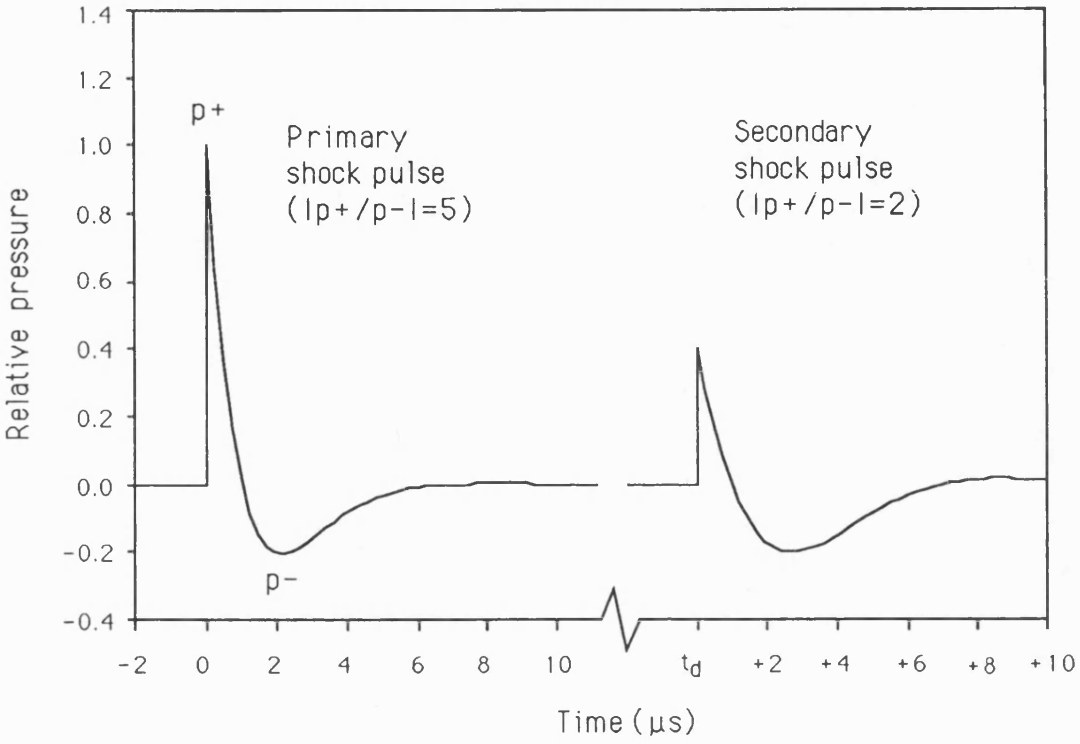

[Fig 6.3-1] A typical focal pressure waveform of an electrohydraulic lithotripter (Dornier HM3) which is defined by Eq(6.3-1), normalized to the temporal peak pressure (p_+) of the primary shock pulse. The value of p_+ of the secondary pulse is 40% of the primary. The t_d denotes the time delay between the primary and secondary shock pulses.

asymmetry ratio of 5, and for the secondary pulse t_c=2.38μs and f_o=0.0833MHz to fit a measured asymmetry ratio of 2. The rise time is set here to zero (ie, t_e=0) since it is very small (≤30ns) and noted not to be sensitive to the bubble response (Church 1989). The peak positive pressure (p_+) of the secondary shock pulse is typically 40% of that of the primary and they are separated by about 3ms (=t_d) depending on the discharge strength.

The response of a pre-existing bubble in water to the primary shock pulse is calculated with p_+=50MPa corresponding to a 25KV source output setting. The initial bubble radius R_o is set to 3μm which is typical of an air bubble in tap water (Keller 1972) although, as will be seen, the value of R_o is not critical. The response of the bubble to the secondary shock pulse is calculated with p_+=20MPa and with an initial bubble radius which is the bubble radius following the primary shock.

The values of the physical constants which have been selected for the case of oxygen gas dissolved in water (at T_o=293K) are A=321428571(Pa), c_o=1500(m/s), ρ_o=1000(kg/m^3), P_o=10^5(Pa), D=2.42E-9(m^2/s), ϕ=7.25E-2(N/m), η=γ=1.4, μ=0.001(kg/m/s), C_s=6.03(mol/m^3) and C_i/C_s=0.9 which is approximately the physiological value of gas concentration (Church 1990). The initial conditions (at t=0) are U=0, P(R)=P_o, P_∞=P_o, C=c_o and H=0.

6.3.2 Dynamic features of a bubble response

The calculated time variation of the bubble radius (R(t)) and pressure at the bubble wall (P(R,t)) in response to the primary and secondary shock pulses (Fig 6.3-1) are illustrated in Fig 6.3-2. The plots of R(t) show that the bubble collapses as soon as the shock front is encountered and then proceeds to grow rapidly to a very large size as the tensile part of shock pulse is encountered (Fig 6.3-2a). The initial rapid growth is then followed by a relatively long period (t_q), where little change in radius occurs. At the end of this period, the bubble collapses violently and, if it is not fragmented, continues to oscillate with a period of about 25μs and 45μs for the primary and secondary shock pulses, respectively.

A large amount of gas flows into the bubble during the expansion phase for a considerable time of t_q when the gas pressure within the bubble is low. This diffusion effect is found to reduce the violence of the primary collapse and to prolong the subsequent ringing when compared to R(t) calculated without the diffusion. For the primary shock pulse, the initially 3μm bubble grows to a final radius of about 55μm. This is taken as the initial bubble radius to be encountered by the secondary shock pulse.

The pressure at the bubble wall (P(R,t)) consists of the initial peak which occurs when the bubble encounters the shock wave (at t=0) followed by an acoustically quiet

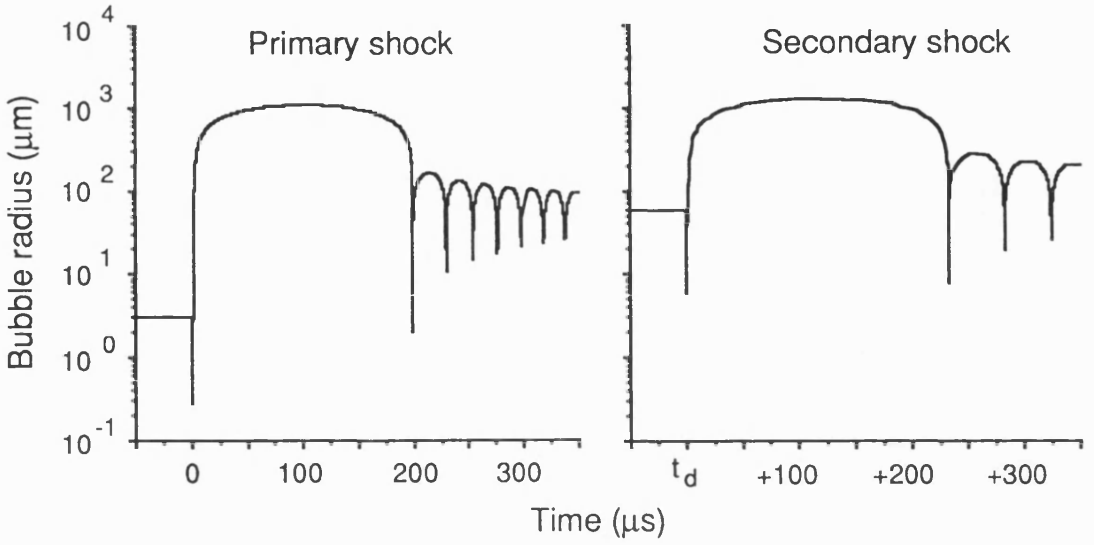

(a) Radial bubble movement

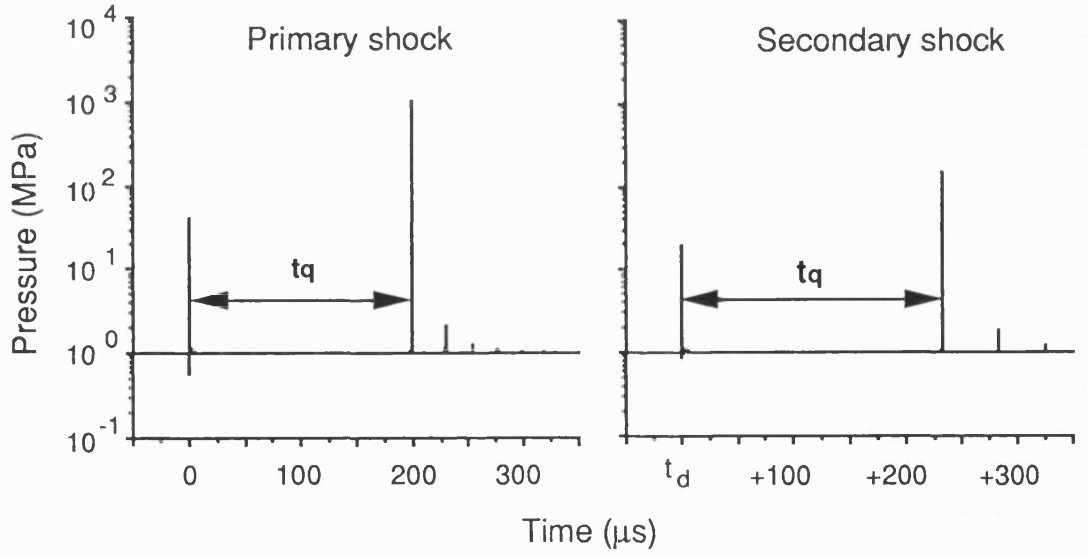

(b) Pressure at the bubble wall

[Fig 6.3-2] Predicted bubble responses to the primary (p_+=50MPa, p_-=10MPa) and secondary shock pulses (p+=20MPa, p_-=10MPa). **(a)** Time history of bubble radius and **(b)** pressure at the bubble wall. (t_d: time delay between the primary and secondary pulses, and t_q: acoustically quiet time period)

period (t_q) where any noticeable acoustic output is not shown, and then the second burst and subsequent heavily damped acoustic emissions (Fig 6.3-2b). The amplitude of the initial peak is a factor of about ten lower than that of the second. The pressure amplitude of the emission from the bubble in response to the secondary shock pulse is expected to be smaller than that from the bubble in response to the primary shock pulse.

Fig 6.3-2 indicates that R(t) and P(R,t) have similar forms for the primary and secondary shock pulses, except that diffusion is less significant in the bubble response to the secondary shock pulse than to the primary. Values of t_q in the bubble responses to both the primary and secondary shock pulses are similar and estimated to be about 200μs. It is of interest to note that any bubble response beyond 10μs takes place in the absence of a driving field, since the entire duration of the shock pulse is about 10μs.

The bubble model used here does not account for bubble fragmentation, although in practice the violence, particularly, of the second bubble collapse may well result in its fragmentation. While the bubble fragmentation has occurred due to the primary shock pulse, the bubble population encountered by the secondary pulse is still expected to have a larger initial radius than that encountered by the primary pulse and the bubble radius would be between 16μm and 38μm (Flynn and Church 1984)

rather than of 55μm predicted by the model.

6.3.3 Effects of shock strength

The behaviour of the bubble response has been examined using the model when the source output setting is altered. The primary shock pulse is assumed to have p_+ in the range from 20MPa to 60MPa corresponding to the discharge potential of 15kV and 25kV, respectively, in the electrohydraulic (Dornier HM3) lithotripter. It is assumed that the shape and asymmetry of shock pulses do not change during the alteration of the source output.

The calculated results show that the bubble responses are similar but that t_q increases with shock strength. The predicted variation of t_q against p_+ of the primary shock pulse for two different initial bubble radii (R_o=3μm and 55μm) are illustrated in Fig 6.3-3. The value of t_q is seen to increase almost linearly with p_+ and is weakly dependent on R_o. A roughly twenty fold increase in R_o (from 3μm to 55μm) will lead to an increase in t_q of less than 50%.

Another useful prediction of the model is that bubbles, regardless of their initial radii, tend to grow to about the same size as p_+ becomes large as shown in Church (1989). At p_+=50MPa, for example, all bubbles with R_o ranging from 1μm to 10μm grow to 55μm. This implies that bubble radii will tend to be equalized in the lithotripsy field following the primary shock pulse. Even if bubble

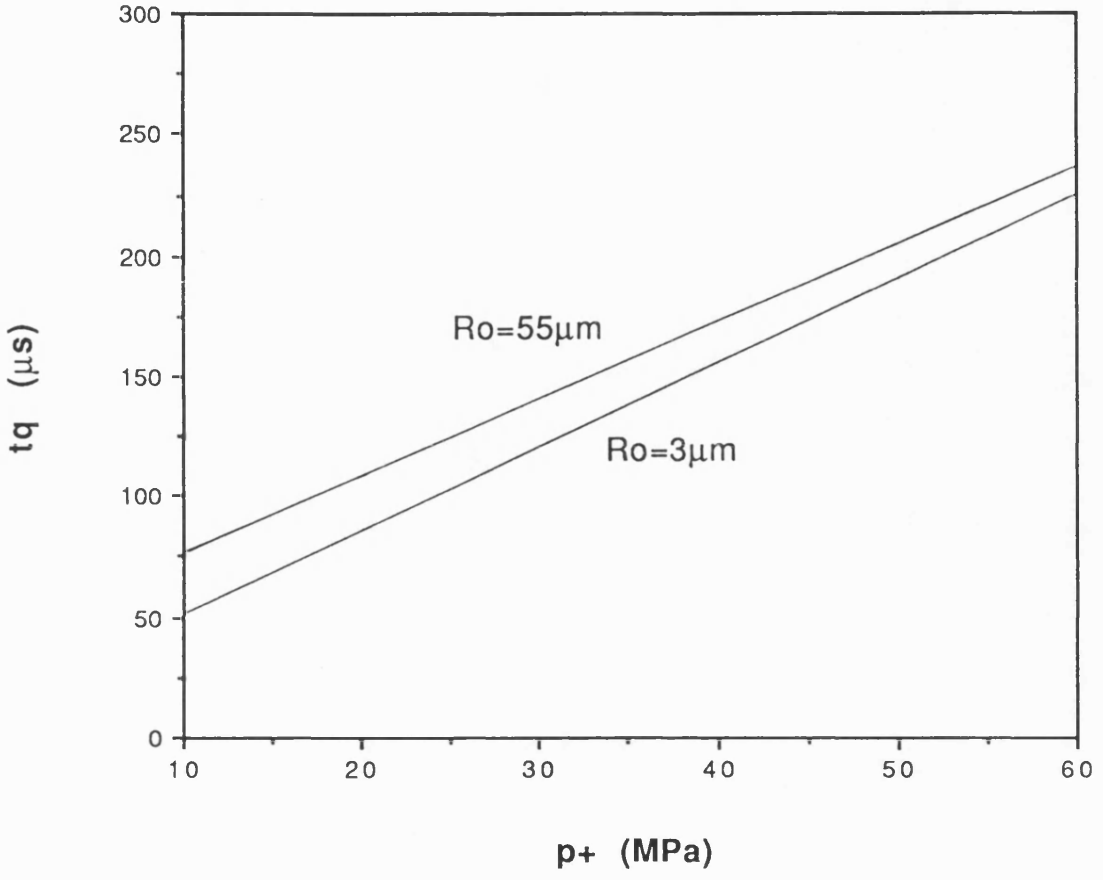

[Fig 6.3-3] Variation of the acoustically quiet period (t_q in μs) predicted for R_o=3μm and 55μm against the peak pressure (p_+ in MPa) of the primary shock pulse.

fragmentation occurs, after the primary shock pulse hits bubbles, the bubble cloud is likely to be more uniform than before it hits. It is therefore expected that the response of bubbles in the cloud to the secondary shock pulse will be more coherent.

6.4 Agreement between prediction and detection

Although the predicted response of a single bubble may provide some qualitative basis on cavitation activity for a bubble cloud in lithotripsy fields, in practice, more than one bubble with a wide variation in R_o are activated. These bubbles interact with each other and, as they collapse, their shapes are more likely to be asymmetrical. The acoustic emission from the bubbles in such a cloud is therefore expected to be incoherent, ie, detectable as white noise (Cramer and Lauterborn 1982). Predictions from the single bubble model indicate that the initial emission occurs for all bubbles at t=0 independent of their initial radii and therefore the emitted signal from the first collapse may be more coherent than that from the second or subsequent collapses. The acoustic signal emitted from the bubble cloud encountered by the secondary shock pulse is expected to be more coherent since the bubble radii may be equalized following the primary shock pulse appearance as noted in Section 6.3.

Coleman et al (1992a) describe the first use of a passive focused hydrophone to detect the acoustic emission from bubbles activated by the lithotripsy field in order to examine some of theoretical predictions. Aspects of this work, which have a bearing on the single bubble model predictions discussed above, are considered in this section.

6.4.1 Detection of cavitation activity

A passive focused hydrophone is positioned with its axis of symmetry perpendicular to that of the electrohydraulic lithotripter and directed to the beam focus of the lithotripter (see Fig 6.4-1). Acoustic emissions resulting from cavitation activity at the focus of the lithotripter (F_2) have been identified as signals well above the noise level at the 1MHz resonance of the hydrophone. No particular care was taken to control or monitor the condition of the tap water used throughout this experiment. Tap water contains sufficient particulate impurities to act as nucleation sites for cavitation and may therefore be expected to support cavitation relatively well.

The 1MHz signal registered by the hydrophone over a 10ms period (time base 1ms/div) with a lithotripter output setting of 20kV is shown in Fig 6.4-2a. The reference pulse corresponds to the moment of the electrical discharge through the electrode. It is then followed by an acoustical signal burst (first acoustic signal) after a delay

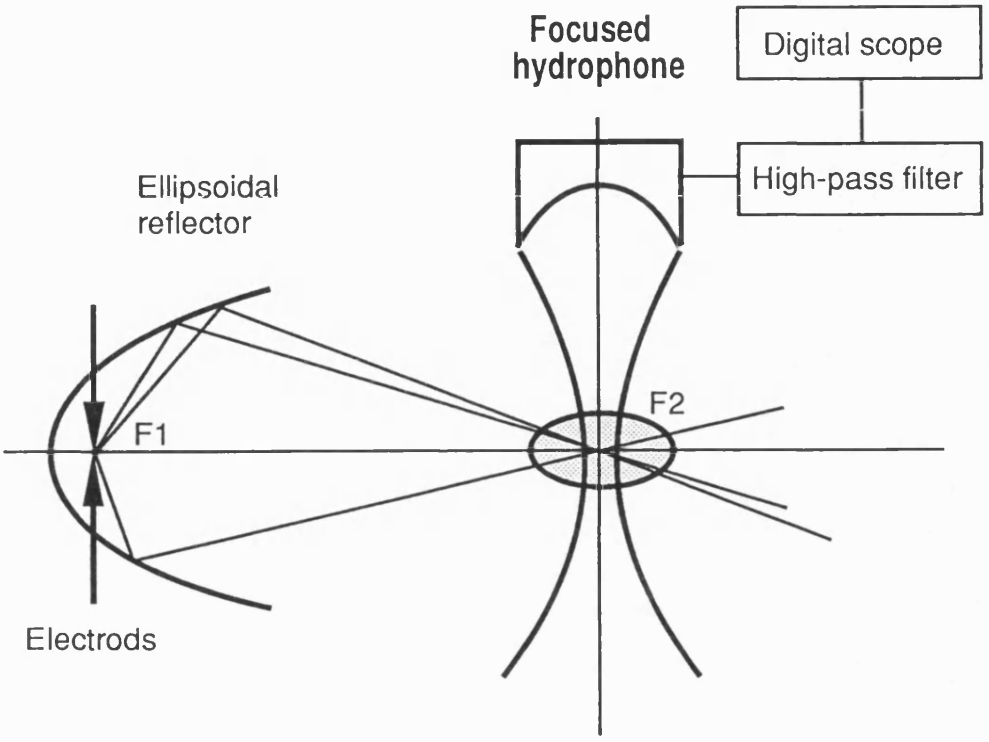

[Fig 6.4-1] Experimental set-up for acoustic measurements showing relative positions of the electrohydraulic shock wave source (Dornier HM3 lithotripter) and focused hydrophone. The focus of the hydrophone is chosen to coincide with the focus of the shock wave source (F_2). A high pass filter eliminates a relatively large amplitude signal at the radial resonance of the hydrophone (18KHz).

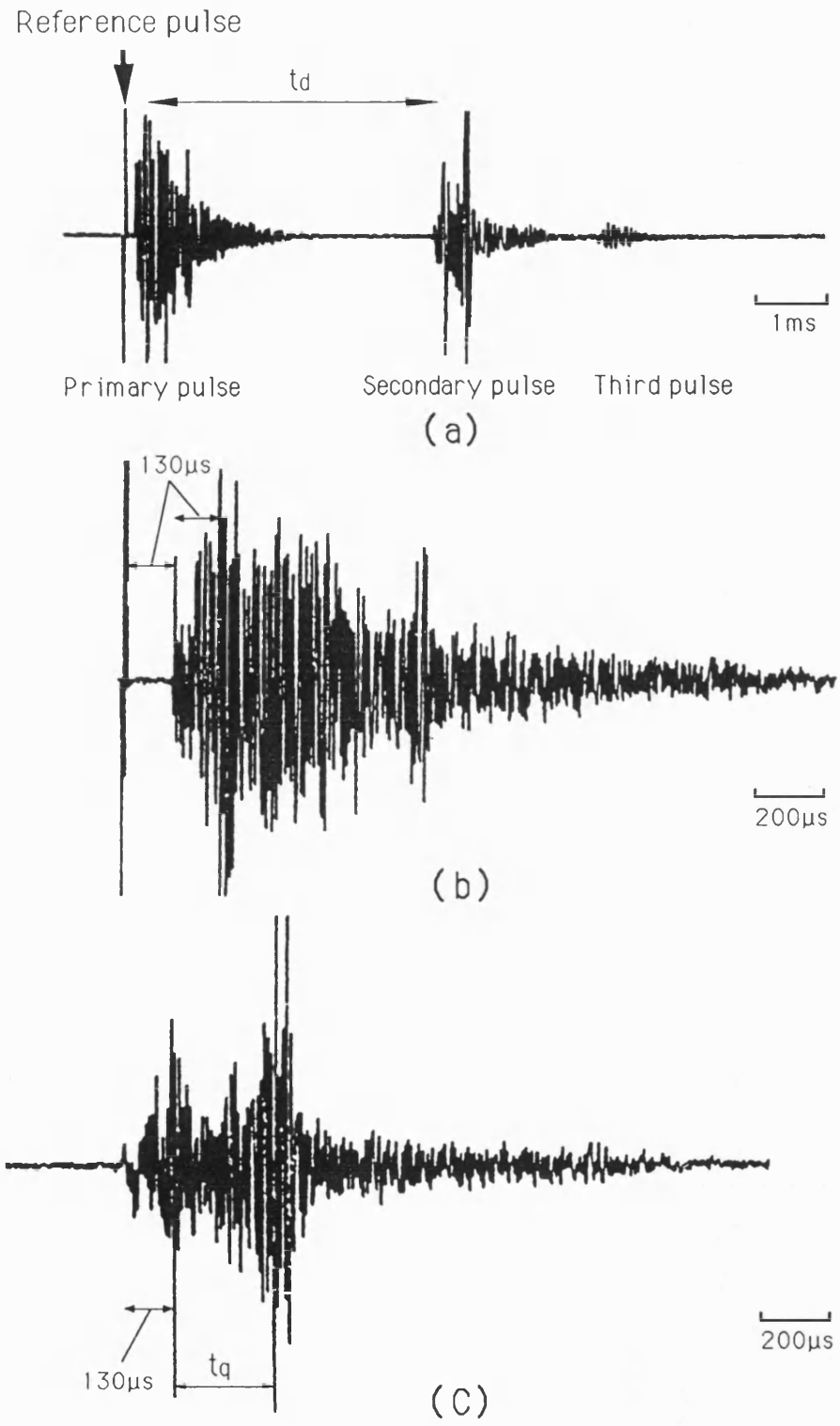

[Fig 6.4-2] Signal traces representing 1MHz sound. **(a)** Over a 10ms period (1ms/div.) detected from a region around the beam focus of the electrohydraulic shock wave source. Over a 2ms period (200μs/div.) **(b)** due to the primary shock pulse and **(c)** due to the secondary shock pulse.

associated with propagation time of the primary shock pulse plus the subsequent cavitation emission. The amplitude of the acoustic signal falls roughly exponentially with a time constant of about 1ms, and within this period there are various fluctuations in amplitude which do not appear to be particularly reproducible features. A second signal burst associated with the secondary shock pulse follows about 3.9ms (=t_d) after the primary shock pulse. The amplitude of this secondary signal dies away, again roughly exponentially with a 1ms time constant. It is followed, 2ms later, by a signal burst of significantly smaller amplitude associated with the arrival at the focus of a third shock pulse emitted by the lithotripter source.

The acoustic traces are expanded to the time base of 200μs/div to gain better resolution of the time delay between the reference pulse on the left of each trace and the onset of signal burst and these are shown in the figure b and c of Fig 6.4-2 for the first and second cavitation signals, respectively. In the first cavitation signal (Fig 6.4-2b), the first small signal above the noise level occurs 130μs after the reference pulse which represents the arrival time at the hydrophone of the edge wave generated from the aperture of the ellipsoidal reflector. The first noticeable peak occurs about 260μs after the reference pulse. This is attributed to the source of the signal originating from F_2 since this delay corresponds to the time of 180μs for the primary shock pulse traveling 276mm

from the electrode (F_1) to F_2 plus an additional delay of 80μs for which the cavitation signal originating at F_2 propagates 120mm to the detector. In the second signal (Fig 6.4-2c), as for the signal associated with the primary shock pulse, a small initial spike attributed to the arrival at the hydrophone of the edge wave is followed by the main peak originating at F_2 with the same time delay. A small intermediate peak is followed by a large amplitude pulse which occurs 400μs after the edge wave.

6.4.2 Comparison between theory and detection

A. Structure and timing

It is suggested that the duration between the two main peaks of the detected signal ($\bar{t}_q$) reflects the acoustical quiet time period (t_q) predicted by the single bubble model. In Fig 6.4-2 the value of $\bar{t}_q$ for the signal trace associated with the secondary shock pulse is shown to be 270μs and this is of the same order of magnitude as the calculated value of t_q (see Fig 6.3-2). The smaller delay measured for the secondary shock pulse compared to that for the primary may result from the smaller amplitude of the secondary pulse. The value of $\bar{t}_q$ measured from the second cavitation signal appears to be more reproducible than that from the first one. This is taken to imply, as noted in Section 6.3, that the bubble radii may be equalized following the primary shock pulse and therefore the acoustic signal emitted from the bubble cloud encountered

by the secondary shock pulse will be more coherent.

B. Signal variation with shock strength

The time interval between the two main peaks ($\bar{t}_q$) was examined at a different output setting of the Dornier HM3 lithotripter over the range 15kV to 25kV. Since, as noted above, the detected cavitation signal for the secondary shock pulse appears to be more reproducible and has more clearly identifiable peaks than that for the primary, the value of $\bar{t}_q$ obtained from the signal burst following secondary shock pulses has been used to compare with theoretical predictions.

The value of $\bar{t}_q$ measured from the plot of the detected time history of 1MHz amplitude signal has been plotted together with error bars in Fig 6.4-3 as a function of the lithotripter source output setting converted into the peak pressure (p_+) of secondary shock pulse. It is shown that the value of $\bar{t}_q$ increases with the lithotripter source output. The solid lines in the figure represent the theoretical prediction of t_q for different pressures of p_+ of the secondary shock pulse. The conversion of the source output settings to pressures is estimated from 40% of the primary shock amplitudes measured at the focus at different discharge potential settings (Coleman and Saunders 1989). Although values of estimated p_+ are subject to large errors (about ±25%) since they were not directly measured, Fig 6.4-3 does illustrate that the measured value of $\bar{t}_q$

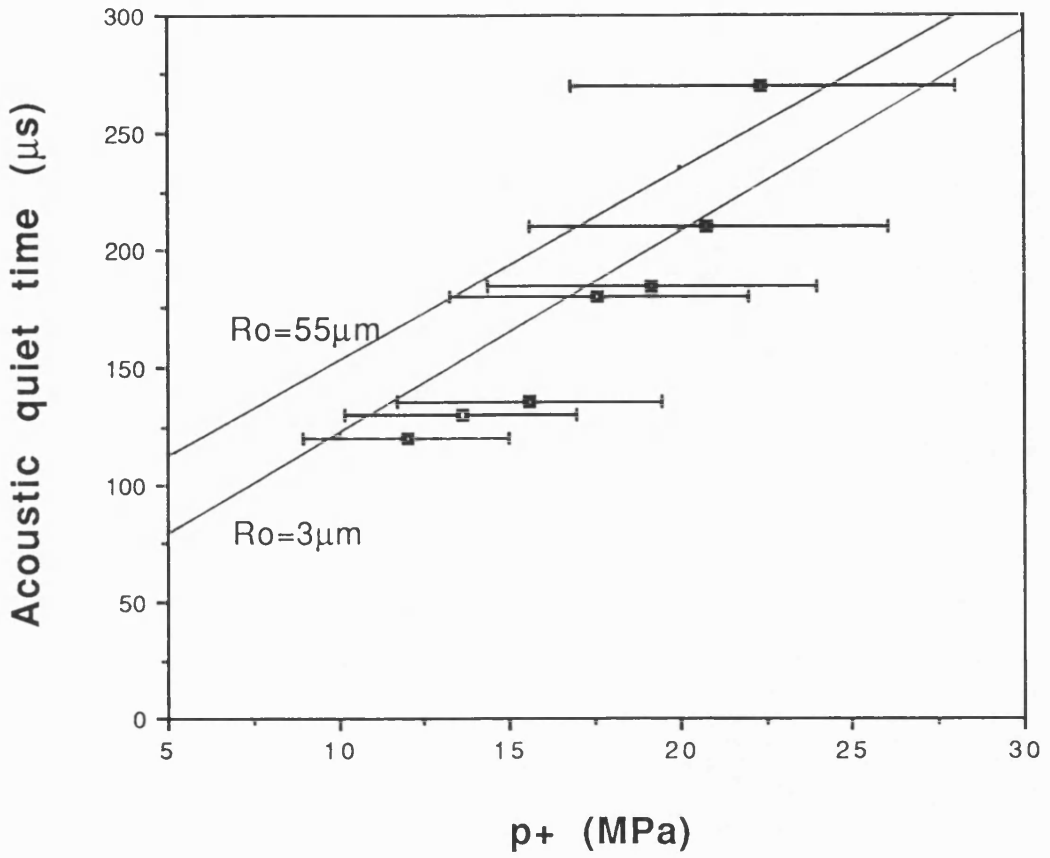

[Fig 6.4-3] Variation of the acoustically quiet time period (t_q; solid lines) predicted for R_o=3μm and 55μm and time delay ($\bar{t}_q$; dots with error bars) between the main peaks in detected acoustic signals associated with the secondary shock pulse as a function of shock pulse strength (p_+).

increases in much the same way as t_q predicted by the theory for the wide range of initial bubble radii.

6.4.3 Summary

Transient cavitation activity induced by the high amplitude pulsed ultrasound for lithotripsy has been detected using a passive focused hydrophone. Detected signals show some agreement in structure and timing with those predicted from a Gilmore single bubble model. This represents the first independent confirmation that the bubble model can be usefully applied in high amplitude pulsed fields used in clinical extracorporeal shock wave lithotripsy. Careful use of the bubble model may therefore allow some quantitative data on the cavitation activity.

6.5 Bubble dissolution

Bubbles generated by lithotripsy fields decrease in their radii and dissolve quickly with time. When the time delay between preceding and succeeding lithotripsy pulses is large enough for the bubbles to dissolve, there will be no interaction between the bubbles and succeeding pulses. If a lithotripsy source is pulsed rapidly, however, the successive pulses may interact via the cavitation generated. The limitation of pulse repetition rate is therefore an important feature of clinical lithotripsy.

Technically the pulses can be applied at rates of 10Hz making treatment time as short as 5 minutes instead of an hour. At such high pulsing rates, the tissue damage is found to be unacceptably high and stone fragmentation appears to be reduced (Delius and Brendel 1989), and these would understandably be associated with the interaction between the pulses and cavitation bubbles.

The bubble dissolution time (or life time) can be estimated from the following differential equation describing the change in an instantaneous equilibrium radius (R_{oi}) under the conditions that the liquid contains free gas bubbles and is acoustically unstirred (Epstein and Plesset 1950).

$$(6.5\text{-}1) \qquad \frac{dR_{oi}}{dt} = \frac{\mathcal{D}\mathcal{G}T_o\mathcal{C}_s}{P_oR_{oi}}\left(\frac{\mathcal{C}_i/\mathcal{C}_s - 1}{1 + 4\phi/3P_oR_{oi}}\right)\left(1+\frac{R_{oi}}{\sqrt{\pi\mathcal{D}t}}\right)$$

where $R_{oi}(t)$ is the time varying equilibrium bubble radius, $\mathcal{D}$ is the diffusion constant between the gas and liquid, $\mathcal{G}$ is the universal gas constant (8.315 J/mol K), T_o is the Kelvin temperature, P_o is the static pressure in the liquid, $\mathcal{C}_s$ and $\mathcal{C}_i$ are respectively the saturated and dissolved gas concentrations in the liquid.

The rate of disappearance depends not only on the initial bubble radius R_o (ie, R_{oi} at t=0) but also on the dissolved gas concentration ($\mathcal{C}_i$). Large bubbles disappear much more slowly than small ones and the dissolution time at high gas concentration is much longer than that at low

concentration. In contrast, bubbles may grow large and rise to the surface, when the liquid is supersaturated and the condition of bubble size and surface tension is above the threshold for bubbles to grow. For instance, the threshold for air bubbles in water (ϕ=7.25E-2N/m, T_o=293K), is illustrated in Fig 6.5-1 in which the bubbles grow only in the upper-right region while they shrink in the lower-left region unless there is a mechanism for stabilization. The threshold curve will be shifted up as ϕ increases, *vice versa*, as ϕ decreases.

Examples of bubble dissolution are illustrated in Fig 6.5-2 for a 90% air saturated water (ie, $\mathcal{C}_i/\mathcal{C}_s$=0.9) by solving Eq(6.5-1) with a 5th order Runge-Kutta method. The initial bubble radius (R_o) is in the range of 10μm to 70μm, where R_o represents a final equilibrium radius of the bubble activated by a preceding lithotripsy pulse. Numerical constants used in the calculation are the same as Section 6.3.

Fig 6.5-2 shows that the calculated bubble radius rapidly decreases once it begins to dissolve. If the dissolution delay time ($t_{5\%}$) denotes a time at which 5% reduction in bubble radius occurs, the value of $t_{5\%}$ increases from 0.2s to 1s as R_o is increased from 16μm to 38μm. The bubble life time ($t_{95\%}$), defined as the time required for the bubble to be virtually dissolved, increases from 4s to 20s as R_o is increased from 16μm to 38μm. The two solid curves in Fig

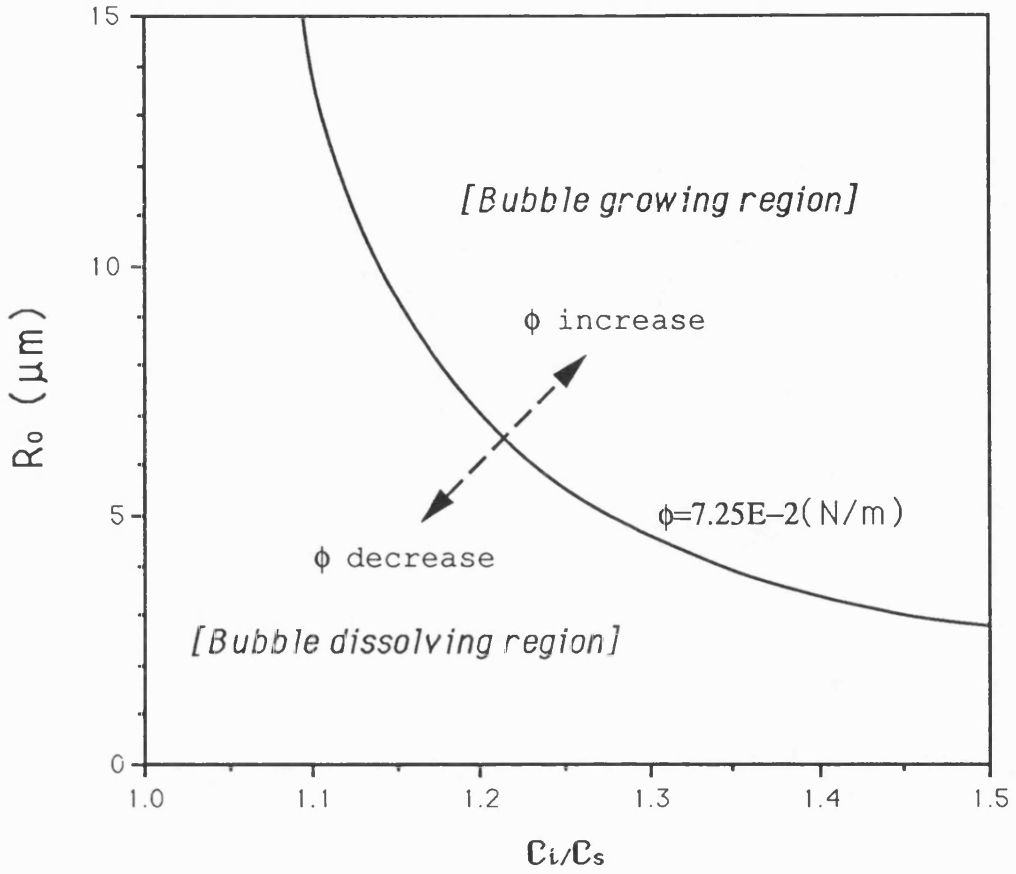

[Fig 6.5-1] Stability curve for air bubbles in water (ϕ=7.25E-2N/m and T_o=293K). If an air bubble lies above the curve, it will grow by diffusion at zero acoustic pressure while, if the bubble lies below the curve, it will dissolve. The curve will move in the directions indicated by the arrows when other gases (ie, different values of ϕ) are considered.

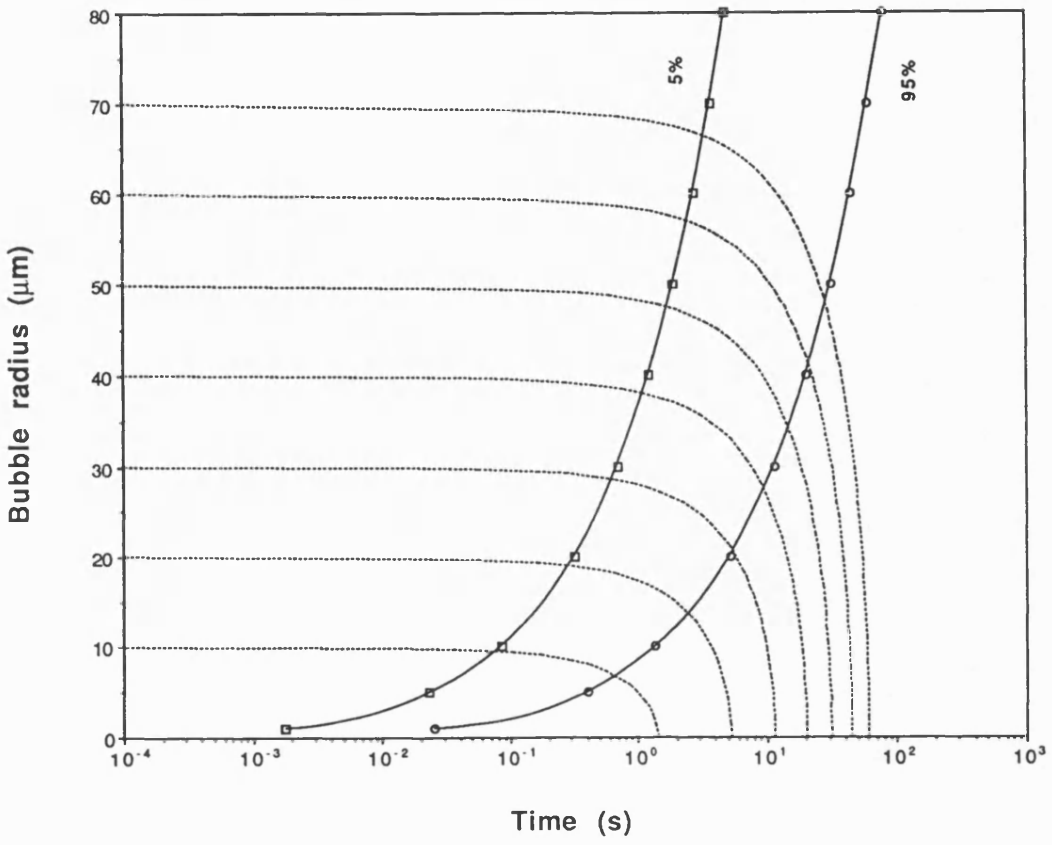

[Fig 6.5-2] Dissolution curves of air bubbles in (90% air saturated) water for the initial bubble radius of R_o ranging from 10μm to 70μm (dotted curves). Two solid curves represent the time for 5% and 95% reduction in the radius of bubbles from their initial value of R_o.

6.5-2 representing $t_{5\%}$ and $t_{95\%}$ indicate that the main bubble dissolution occurs between $t_{5\%}$ and $t_{95\%}$.

The bubble with a radius around 40μm starts to dissolve in about 1s which corresponds to a typical pulse repetition frequency in clinical extracorporeal shock wave lithotripsy. Accordingly many bubbles distributed in the range of between 16μm and 55μm, following a preceding shock pulse, will still be present when a succeeding pulse propagates through the medium. It is therefore required that, for the prediction of *in situ* lithotripsy fields, the propagation model account for effects of the bubble interaction with shock pulses.

6.6 Acoustical properties of bubbly fluid

Gas bubbles contained in a fluid influence significantly the acoustic characteristics of the fluid. When the bubble size is small compared to the wavelength (λ) of an applied acoustic field, the presence of bubbles substantially alters the compressibility (or bulk modulus) of the fluid. As the bubble size increases and becomes comparable to λ, the bubble increasingly represents a scattering discontinuity rather than a change in the bulk propagation parameters of gas bubble-fluid mixture (Morse and Ingard 1968).

6.6.1 Sound speed

A mathematical expression of a small signal sound speed in a mixture of gas bubbles in fluid is given by the following equation under the assumptions that spherical bubbles are evenly distributed in the fluid and the bubble radius is uniform and much less than a driving acoustic wavelength (Prosperetti 1984b).

$$(6.6\text{-}1) \qquad \bar{c}^2 = \left(\frac{\upsilon^2}{c_G^2} + \frac{(1-\upsilon)^2}{c_L^2} + \frac{3\upsilon(1-\upsilon)}{(2\pi R_o)^2 (f_r^2 - f^2 + j\zeta f/\pi)} \right)^{-1}$$

where υ is the fraction of the volume occupied by bubbles in a unit volume of the mixture, $\bar{c}$ is the complex sound speed of the mixture, c_G and c_L are infinitesimal sound speeds in gas inside the bubble and liquid, respectively, ζ is the effective damping coefficient which is associated with energy losses resulting from viscous, radiation and thermal dampings (refer to Eq (29) of Prosperetti (1984a)), and f_r is the resonance frequency of the bubble which can be obtained from Eq(34) of Prosperetti (1984a):

$$(6.6\text{-}2) \qquad f_r^2 = \frac{P_\infty}{\rho_L (2\pi R_o)^2} \left(3\eta + (3\eta - 1) \frac{2\phi}{R_o P_\infty} \right)$$

where P_∞ is the static pressure of the fluid at a large distance from the bubble, ρ_L is the density of liquid, and η is the polytropic exponent of the gas inside the bubble.

It should be pointed out that, since Eq(6.6-1) is valid for

all bubbles with the same size and in this case the damping coefficient ζ in Eq(6.6-1) is rapidly decreased when approaching the bubble resonance frequency, the prediction of $\bar{c}$ obtained from the equation will show sudden changes and give unrealistic values near the bubble resonance. When a wide distribution of bubble size is taken into account, although the propagation equation includes a complicated integral over the bubble distribution (see Anderson and Hampton (1980)), such a sudden change in the predicted value of $\bar{c}$ will be moderated. For a reasonably narrow range of bubble radii, in practice, a simple and more realistic approach has been suggested by Carstensen and Foldy (1947) in which an experimentally obtained ζ which is larger than calculated was used.

6.6.2 Attenuation and dispersion

As treated in Section 4.1, the complex wave damping coefficient in a gas bubble-liquid mixture can be written as $\bar{\xi}=\bar{\alpha}-j\bar{\delta}$ where $\bar{\alpha}$ and $\bar{\delta}$ represent the wave attenuation and dispersion in the mixture, respectively. The $\bar{\alpha}$ and $\bar{\delta}$ can be derived by relating $\bar{\xi}$ to the complex speed of sound $\bar{c}$, ie, $\bar{\xi}=-j2\pi f/\bar{c}$ (Rudenko and Soluyan 1977). Accordingly $\bar{\alpha}$ and $\bar{\delta}$ at the frequency of f_n in the mixture are given as

$$\bar{\alpha}_n = 2\pi f_n \, \mathcal{I}m(1/\bar{c}_n) \tag{6.6-3}$$

$$\bar{\delta}_n = 2\pi f_n \, \mathcal{R}e(1/\bar{c}_n)$$

where $\bar{c}_n$ is the complex speed of sound in the mixture at

the frequency of f_n.

Examples of sound attenuation and dispersion calculated using the equations from (6.6-1) to (6.6-3) are illustrated in Fig 6.6-1 for water containing air bubbles. The values of parameters used in the calculation are c_G=340m/s, c_L=1500m/s, υ=0.001% to 0.01% and R_o=16μm to 55μm.

Calculated attenuation coefficients of bubbly water are displayed in Fig 6.6-1a as a function of frequency and are compared with that of distilled (or, bubble free) water. The two solid curves in the figure represent predictions for R_o=16μm and 55μm at υ=0.01%, the dotted curve for R_o=55μm at υ=0.001%, and the dotted straight line is the attenuation coefficient for distilled water. It is shown that the attenuation coefficient in the mixture is increased with increasing υ but is decreased with increasing R_o. A sharp change in attenuation coefficient at frequencies near the bubble resonance indicates the rapid change in compressibility of the bubbly mixture. It is likely that the bubbly water acts as a low pass filter with a cut off frequency determined by the resonance frequency of bubble, ie, its size. A plot of the resonant frequency f_r calculated using Eq(6.6-2) for air bubbles in water is given in Fig 6.6-1c as a function of bubble size.

The predicted speed of sound in bubbly water (given by $2\pi f/\bar{\delta}$) is illustrated in Fig 6.6-1b where the two solid

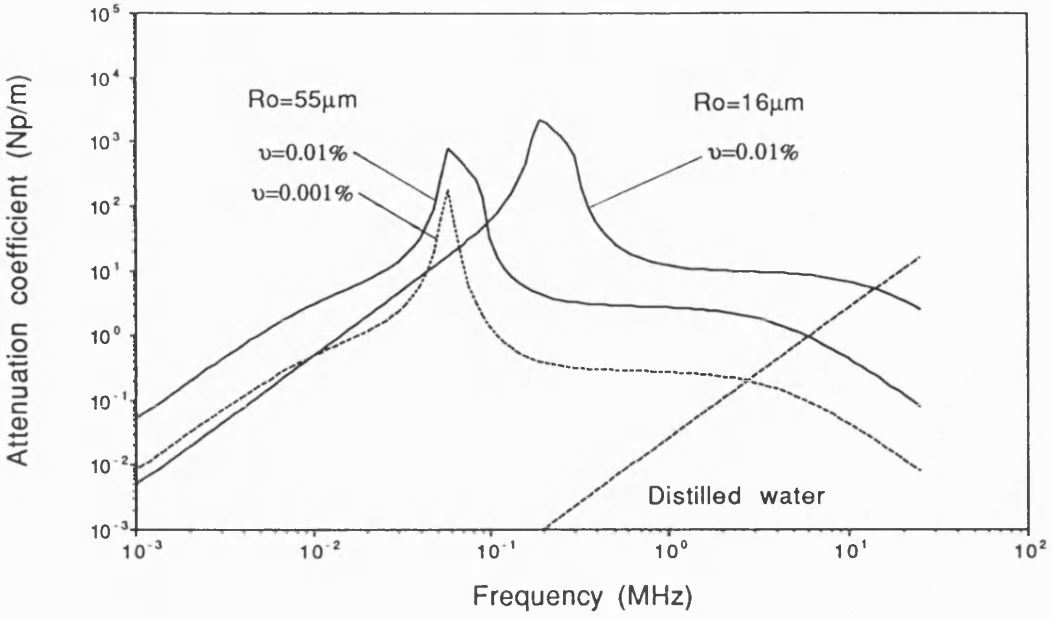

(a)

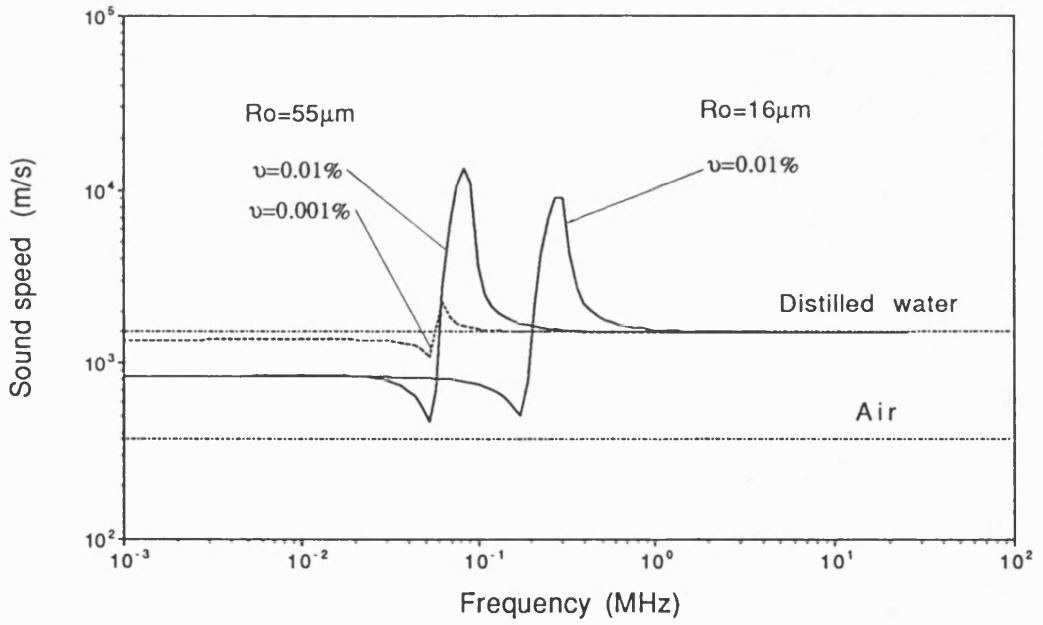

(b)

[Fig 6.6-1] **(a)** Predicted attenuation and **(b)** speed of sound in water containing air bubbles as a function of frequency at low amplitude field. - continued in (c) -

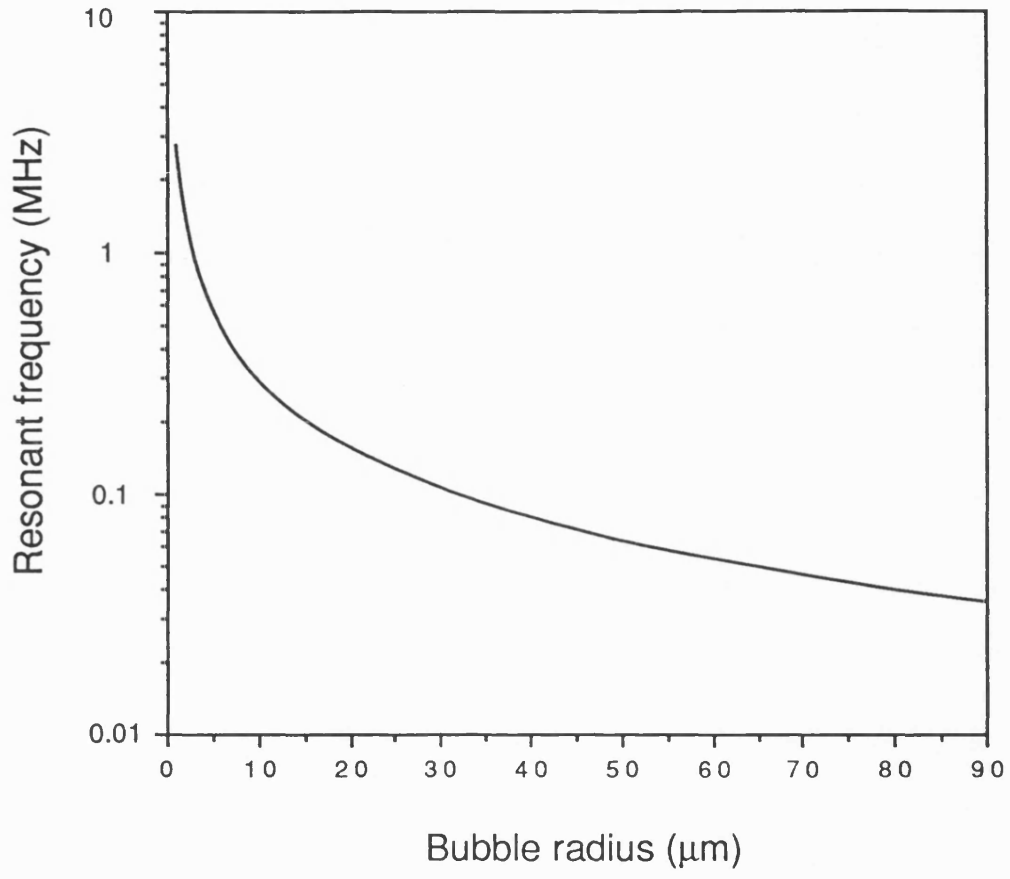

(c)

- continued -

[Fig 6.6-1] **(c)** Predicted resonant frequency as a function of bubble radius.

curves represent the predictions for R_o=16μm and 55μm at υ=0.01%, and the dotted curve for R_o=55μm at υ=0.001%. The speeds of sound for distilled water (c_L=1500m/s) and air (c_G=340m/s) are also displayed by the horizontal broken lines. The predicted speed of sound in the bubbly water is shown to increase with not only υ but also R_o. At frequencies near the bubble resonance, a sharp increase in sound speed occurs. The speed of sound in bubbly water is less than that in distilled water when far below the bubble resonance frequency but approaches that in distilled water when far beyond the bubble resonance. This implies that the mixture is more compressible than distilled water below the bubble resonance but less compressible above the resonance. The wide variation of the speed of sound with frequency indicates that the air bubble-water mixture is highly dispersive.

It should be noted that, as indicated above, since the theory has been derived for the uniform bubble size in liquid, the predicted attenuation and speed of sound in the mixture are seen to be unrealistic near the bubble resonance. For instance, at given values of R_o=55μm and υ=0.01%, the theory predicts the attenuation coefficient near the bubble resonance to be several orders of magnitude bigger than that of distilled water and the speed of sound to reach up to about 6 times bigger than that in distilled water. Nevertheless an important consideration from the values shown in Fig 6.6-1 is that, even if few air bubbles

are contained in water, the mixture will be highly dispersive and attenuating.

Comparison of theory and experiment is difficult since it is necessary to produce bubbles within a reasonably narrow range of diameters and to measure their bubble size. Nevertheless some of classical experimental measurements (Silberman 1957) have shown satisfactory agreement (Prosperetti 1984b) particularly in the range of frequency not close to the bubble resonance.

6.7 Shock pulse propagation in bubbly liquid

When cavitation occurs in a lithotripsy field, it is expected that the increased attenuation results in the decrease of power reaching the focus and the significant dispersion acts to defocus the field. The influence of gas bubbles contained in liquid on lithotripsy pulse propagation is considered here using the propagation model under the assumption that the attenuation and dispersion of gas bubble-liquid mixture do not influence nonlinearity and diffraction. A typical pulse predicted in distilled water at the focus of the lithotripter, has been repropagated in the linear plane wave field through water containing air bubbles in order to obtain the marginal alteration due to the presence of bubbles in water, although the prediction does not account for more complicated effects such as

nonlinear propagation in bubbly media indicated by Wu and Zhu (1991) and Asada and Watanabe (1990).

In the calculation, bubbly water was assumed to be in the region 30mm before and 20mm after the focus of an electrohydraulic lithotripter. This is justified by high speed photographic evidence (Riedlinger 1990) suggesting that a bubble cloud extending 50mm in the axial direction around the focus is formed in water as a result of exposure to the electrohydraulic lithotripter. Attenuation and dispersion coefficients in the bubbly water have been estimated using the equations from (6.6-1) to (6.6-3). The primary shock pulse shown in Fig 6.3-1 was taken as a typical waveform predicted at the focus in bubble free water. The Fourier repetition frequency (Δf) of waveform was set to 0.025MHz which was even lower than the resonant frequency of bubbles considered here and the harmonic number (N) retained in the calculation was 512.

6.7.1 Effects of void fraction

As indicated in Section 6.6, the sound attenuation and dispersion in bubbly mixture increase with void volume fraction (υ) and this effect on shock pulse propagation has been examined here. Assuming that R_o is 55μm, predicted waveforms for various values of υ of air bubbles in water (ranging from 0.001% to 0.1%) are shown in Fig 6.7-1a where the pressure is normalized to that predicted in distilled water. This figure shows that the predicted waveforms in

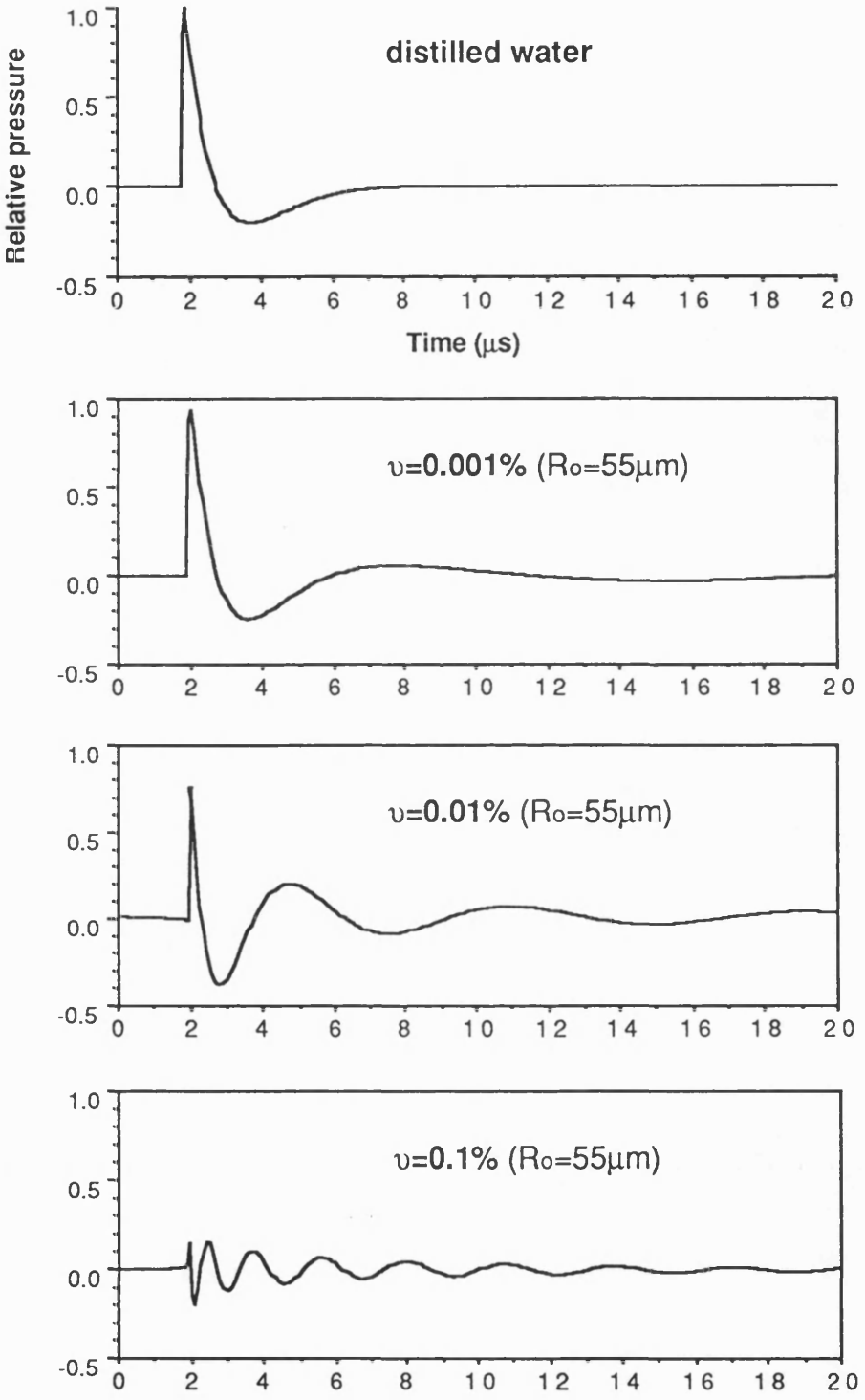

[Fig 6.7-1] **(a)** Predicted waveform for shock pulse propagation in water containing air bubbles of υ=0.001%, 0.01% and 0.1% at R_o=55μm, normalized to the peak pressure predicted in distilled water. - continued in (b) and (c) -

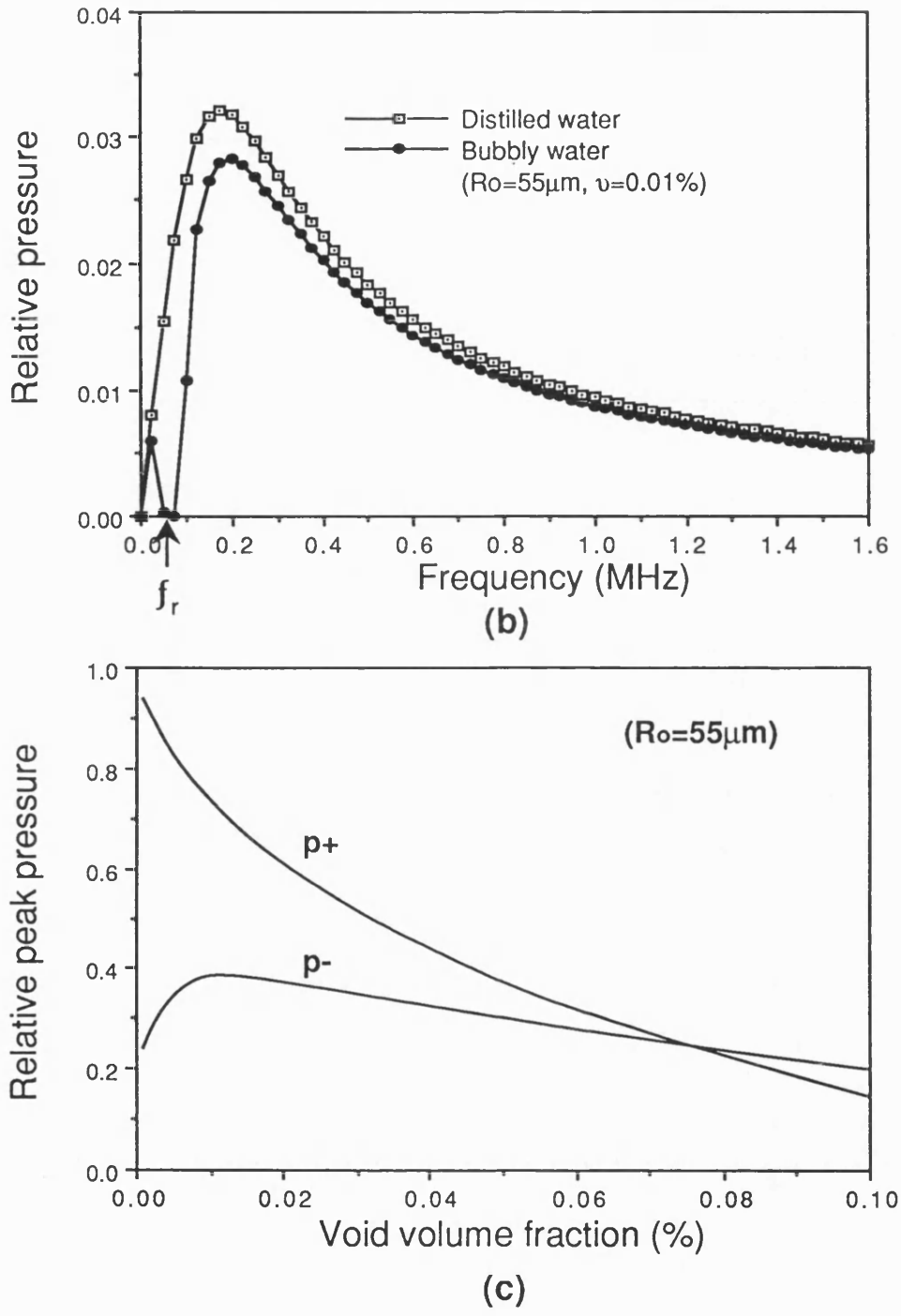

[Fig 6.7-1] **(b)** Comparison between the harmonic amplitudes predicted in distilled water and bubbly water of υ=0.01% and R_o=55μm (f_r: the resonance frequency of bubble). **(c)** Variation of the peak pressures (p_+, p-) predicted in bubbly water as a function of void volume fraction at R_o=55μm.

bubbly water are not significantly different from that in distilled water unless υ>0.001%. The extent of deviation of predicted waveform in bubbly water from that in distilled water increases with υ.

Since the energy of acoustic waves is most severely attenuated around the bubble resonant frequency (f_r), it is expected that the frequency components around f_r are missing. This is demonstrated in Fig 6.7-1b by comparing the frequency spectrum of a predicted waveform in distilled water to that in bubbly water of υ=0.01%. It shows clearly that for propagation in bubbly water the amplitude of frequency near the bubble resonant frequency (f_r=0.06MHz) is almost zero.

It is of interest to note that the predicted waveform, in particular, for the case of υ=0.1%, shows oscillations of about 2μs period which last for more than 20μs, while a single major heavily damped oscillation of much longer period but shorter duration is shown in the waveform in distilled water. This lengthened oscillation duration may be attributed to the sudden and significant drop in phase speed before the resonant frequency as shown in Fig 6.6-1b and the change in attenuation (see Fig 6.6-1a). The degree of the oscillations increases with υ at a given bubble radius, since changes in phase speed and attenuation are larger for higher values of υ.

The attenuation and dispersion effects of the bubbly mixture on shock pulse propagation are more obviously demonstrated in Fig 6.6-1c which shows changes of the peak pressures (p_+, p_-) of predicted waveform as a function of υ, normalized to those predicted in distilled water. The value of p_+, as expected, decreases with υ. On the other hand, the magnitude of p_- is initially increased with υ to the maximum value of 0.4 at υ=0.01% and then slowly decreased (* note that, unless specified, the value of p_- in this section indicates $|p_-|$). Interestingly, when υ>0.075%, p_- is bigger than p_+. It is noted that the predicted value of p_+ in bubbly water are always far less than that in distilled water, while p_- is greater and reaches a maximum which is twice than in distilled water.

The initial increase in p_- indicates that dispersion which increases p_- is more significant than attenuation and the following slow decrease in p_- reflects the fact that dispersion becomes relatively weak compared with attenuation. In practice, however, p_- is likely to be limited by cavitation so that such an increase in p_- may not be observed. In addition the predicted increase in p_- may be smaller when nonlinear propagation is considered since the value of nonlinear parameter (β) is more likely to increase (Wu and Zhu 1991, and Asada and Watanabe 1990).

6.7.2 Effects of bubble size

The bubble size determines the resonant frequency at which

most severe attenuation and dispersion in bubbly media occur. The bubble size effect on shock wave propagation has been examined for a constant volume fraction of 0.01% while the bubble size varies from R_o=16μm to 55μm which are the estimated lower and upper limits following a single lithotripsy pulse.

Predicted waveforms for R_o=16μm, 30μm and 55μm are given in Fig 6.7-2a. The pressure in the figure is normalized to that predicted in distilled water. The predicted waveform in bubbly water is seen to change significantly as R_o decreases and at R_o=16μm little coherent signal is transmitted through the bubbly water. The large extent of changes in waveforms with R_o is attributed to the different position of peak attenuation and dispersion (ie, bubble resonance frequency) increases inversely with R_o.

The variation of peak pressures (p_+, p-) of predicted waveforms is shown in Fig 6.7-2b as a function of R_o. The value of p_+, as expected, increases with R_o and begins to saturate from $R_o \cong 30\mu m$ and does not exceed 0.8 for $R_o \leq 70\mu m$. The p- behaves in the similar way as p_+ for $R_o < 20\mu m$. After p- reaches its maximum value of 0.39 around R_o=30μm, however it weakly declines as R_o is increased. Since, as already indicated in Section 6.7.1, p- is limited by cavitation and nonlinear effects likely increased in bubbly water are not included here, the true value of p- will be smaller than that shown in the Fig 6.7-2b.

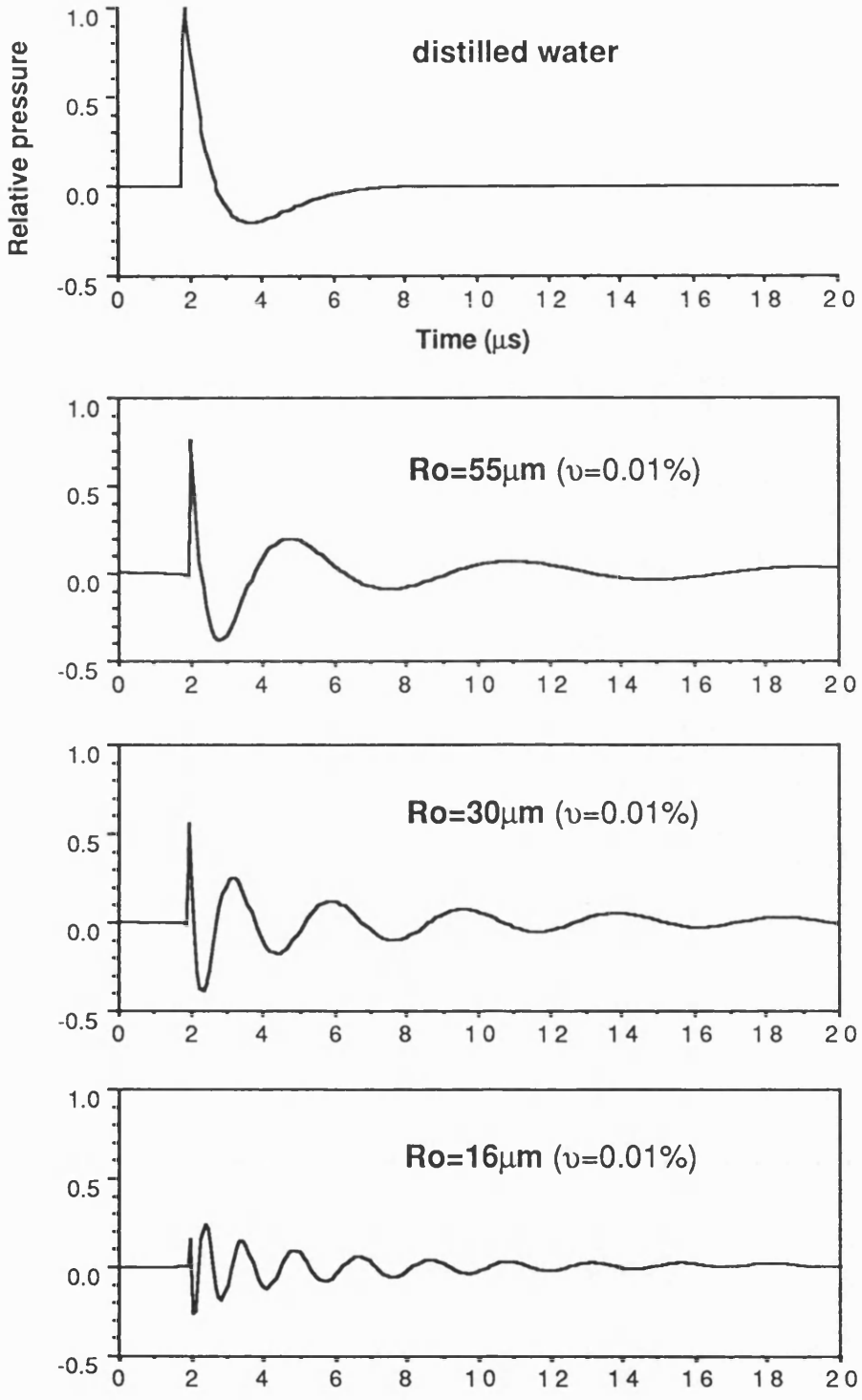

[Fig 6.7-2] **(a)** Predicted waveforms for shock pulse propagation in water containing air bubbles of R_o=55μm, 30μm and 16μm at υ=0.01%, normalized to the peak pressure predicted in distilled water. - continued in (b) -

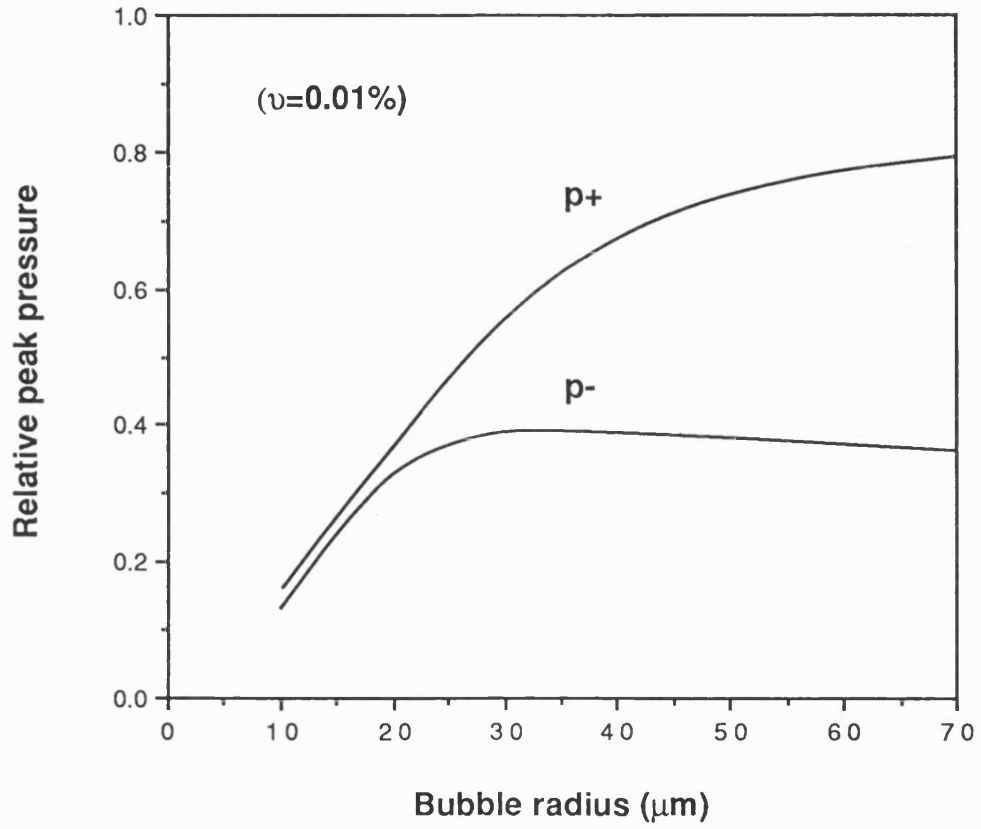

[Fig 6.7-2] **(b)** Variation of the peak pressures (p_+, p_-) predicted in water containing air bubbles at υ=0.01% as a function of bubble radius (R_o).

6.7.3 Summary

Propagation of shock pulses in water containing air bubbles results in reduction of p_+ and increase in the magnitude of p- compared to the predictions in distilled (bubble free) water. The predicted value of p_+ decreases as υ is increased or R_o is decreased. Although the magnitude of p- is predicted in bubbly water to be about twice as high as in distilled water, such an increase in practice is limited by cavitation and nonlinear effects increased in the gas bubble-liquid mixture. While tissue damage at high pulsing rates may simply reflect an increase in the energy supplied to the bubbles it may also be related to the change in pressure waveform making cavitation more likely.

6.8 Experimental and clinical observation

It is found clinically that, as the pulse repetition frequency (PRF) increases, the efficiency of stone fragmentation is reduced while the tissue damage increases (Delius and Brendel 1989). It is possible to speculate that this result from an increase in cavitation activity with increasing PRF. Tissue damage due to cavitation may increase in advance of the focus as more energy is transferred to pre-existing bubbles, and stone fragmentation decreases as the shock pulse arriving at the

focus becomes attenuated by cavitation. These speculations should obviously be experimentally tested.

Coleman and Saunders (1989) have measured changes of p_+ with the alteration of PRF setting on the EDAP LT-01 lithotripter and shown that p_+ decreases with increasing PRF. These measured values of p_+ against PRF are plotted in Fig 6.8-1 where for PRF>10Hz p_+ is seen to be reduced to about 40% of its single shot value (ie, for PRF≅0). This variation of p_+ with PRF can be interpreted from the consideration of the dissolution time for bubbles activated by preceding shock pulses with PRF (Section 6.5) and the predictions of lithotripsy pulse propagation in the air bubble-water mixture (Section 6.7).

When PRF>10Hz, according to the bubble dissolution time curve shown in Fig 6.5-2, the value of υ (for R_o>3μm) does not change and therefore the acoustic properties of the bubbly mixture remain constant. This indicates that predicted value of p_+ will be constant, regardless of further increasing PRF (provided that this does not alter the bubble size distribution). On the other hand, if PRF<0.1Hz (for R_o≤30μm), most bubbles are dissolved and hence the shock pulse seems to propagate in a bubble free water, which may correspond the condition of the single shot shown in Fig 6.8-1. For 0.1Hz≤PRF≤10Hz, there exists a transient region where bubbles dissolve and so values of υ and R_o decrease. In this region the value of p_+ is expected

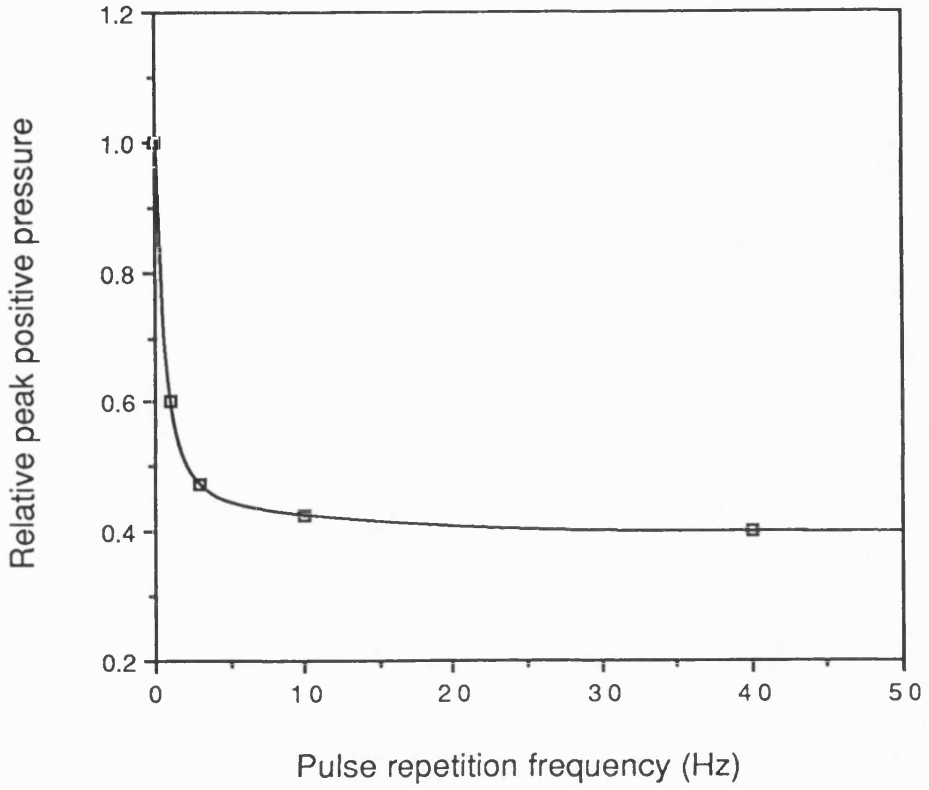

[Fig 6.8-1] Variation of the peak pressure measured at the focus of the EDAP LT-01 lithotripter as a function of pulse repetition frequency (PRF), normalized to that of a single shot (ie, PRF≅0).

to decrease as PRF increases.

Effects of υ on shock pulse propagation has been investigated with standard platter blocks (phantom stones) as well as L1210 cells in different oxygen concentrations (Brümmer et al 1989a). The phantom stones and L1210 cell suspension in a polyethylene pipette positioned at the focus of an experimental lithotripter (Dornier XL1) in normal water (containing oxygen 9mg/1ℓ) and partially degassed water (containing oxygen 4mg/ℓ) are exposed to 125 shock pulses.

In tap water a wide distribution of the impacts and a flat crater is seen. In contrast, in partially degassed water a more concentrated focus resulted in a deeper crater and in a more distinct destruction of the opposite side of the shock wave entry. The percentage of intact cells, after the shock treatment, in the partially degassed water is significantly lower than in tap water.

These experimental results are attributed to an increased number of cavitation bubbles in the water path between the source and the focus due to higher gas content and a consequent reduction in p_+ at the focus due to increased attenuation. Reduced p_+ leads to diminished shear forces and less cavitation around the focus, and this may explain the decreased cell damage and stone fragmentation under higher oxygen content.

6.9 Discussion

Cavitation is a likely mechanism leading to biological effects in medical use of high amplitude pulsed acoustic fields. Consideration of some of the theoretical aspects of cavitation induced in high amplitude pulsed fields have been shown to provide a means of extracting quantitative information from measurements with a cavitation detector. In particular, it is shown that by timing the acoustic emission from cavitation, some estimation of the strength of the driving acoustic field and bubble radius can be obtained.

Propagation of high amplitude ultrasound in water containing air bubbles has been examined using the propagation model by considering the sound attenuation and dispersion in the air bubble-water mixture estimated at given uniform bubble size and void fraction. Despite the relatively crude nature of the theoretical models considered in this chapter it has been possible to make some useful predictions which appear to be borne out in clinical practice. Most importantly the relation between the pulse repetition frequency and transmitted pressure amplitude is predicted, considering that bubbles remaining from one pulse interact with succeeding pulses. This feature of lithotripsy fields is also observed experimentally. In addition, a mechanism can be proposed by which tissue damage is enhanced at high pulse repetition

rates.

An alternative evolution of an acoustic field in bubbly liquid may be possible using the Korteweg-de Vries (KdV) Burgers equation (Kuznetsov et al 1977). Correlating the KdV equation with a diffraction operator is straightforward and results in a propagation equation for a focused field in gas-liquid mixture. This work is not included here since the third time derivative term of the KdV Burgers equation requires a very small step size to maintain the numerical stability and therefore a large volume of computation compared to the present propagation model.

CHAPTER 7. CONCLUSIONS

This chapter summarizes the contribution of this thesis to the examination of the theoretical aspects of the high amplitude pulsed ultrasound used in clinical lithotripsy. The main predictions of the theory are listed and those areas where some agreement between theory and experiment have been obtained are indicated. Suggestions for the extension of the theory and further experimental work are also given.

7.1 Propagation model

7.1.1 Advantage of proposed approach

The main part of the work presented in this thesis relates to a proposed one dimensional nonlinear propagation model. The model draws on the advantages in computational speed of the one dimensional model developed by Bacon (1986) but departs from this model in its development.

Bacon's approach is formally derived from the KZK equation using a gaussian beam in which the beam is assumed to be dominated by nonlinearly generated harmonics. The beam profile is constrained, on the basis of the theoretical

development and experimental evidence, to follow a $(1/n)^{0.5}$ dependence at the source and focus - 'n' represents the harmonic number.

The primary motivation of the proposed model is to avoid constraining the harmonics present at the source to follow the same focusing behaviour as those generated subsequently by nonlinear effects. This approach is necessary if wide bandwidth pulsed fields are to be correctly modeled since at least some harmonics will focus with a 1/n dependence. This also supplies the model with some flexibility. It can, for example, model the linear field of a pulsed piston source (in which all harmonics follow a 1/n dependence at the focus) which cannot be done with the constrained model. This allows a direct comparison of linear and nonlinear parameters (including p_+ and p_-) using the same model.

More importantly, the present method provides a natural way of introducing beam broadening effects into the one dimensional model by the control of a parameter κ. The parameter κ is related to radial harmonic beam profiles and therefore allows off axis information obtained experimentally to be introduced to the one dimensional model.

The model proposed here is not based on the KZK equation and is justified on the basis that it incorporates the

appropriate form for each effect which is considered to act over a small step (Δz). This approach allows the form of, for example, the diffraction term to be chosen as desired so that either parabolic or non-parabolic forms can be used. While such an approach for introducing diffraction has not been rigorously derived, use of a higher order approximation in the diffraction term will not lead to any loss of accuracy over the KZK approach in which all terms are approximated to second order and both models assume diffraction and nonlinear effects to be treated separately.

7.1.2 Numerical implementation

Particular requirements for the numerical implementation of the propagation model in the high amplitude pulsed focused fields employed in extracorporeal shock wave lithotripsy have been considered in detail. The stability of the 4th order Runge-Kutta technique used in the model is examined and a condition imposed on the step size such that any net change in axial step size will produce only small changes in the diffraction, attenuation and nonlinear terms. Problems related to truncation of the infinite series which appears in the propagation equation have also been closely examined and it is shown that they can be reduced by artificially removing energy from higher harmonics without significant effects on predicted pressure waveforms.

7.1.3 Further work

A. Radial profile of harmonics

The one dimensional model relies on some information on the off axis values being provided from experiments either as boundary conditions or as conditions which are allowed to vary as the beam propagates. There is little information, however, on the relationship between harmonics generated by the source and those generated nonlinearly in pulsed fields. This information is required to allow κ to be set correctly.

B. Large aperture field

Piezoelectric and some electromagnetic types of lithotripsy sources typically have large apertures with the shading functions which vary slowly and have sharp cutoffs at the limit of aperture (Appendix B3). Such sources will generate large edge waves and significant and rapid nearfield oscillations which require large amounts of computing time in order to correctly model. It may be that a time domain solution is more appropriate for modeling the linear field immediately in front of these sources and then the present frequency domain model can be used to propagate in the remaining region where the oscillations are less rapid and nonlinear effects more important.

C. Attenuation and dispersion

Dispersion is rather simply introduced to the propagation model by altering the real attenuation term to a complex term. The explicit relationship between the attenuation and dispersion used in the model has been derived on the basis of Kramers-Kronig relation. It has been identified the lack of experimental data on tissue attenuation below 0.5MHz as being of considerable importance in lithotripsy fields where pulses typically have centre frequencies of 0.15MHz.

D. Experimental data in lithotripsy

It has been difficult to apply the proposed propagation model in anything other than a general way to lithotripsy fields because of the lack of measurements on their real sources. The first step in confirming any proposed model will be to obtain precise data about the acoustic field close to the source aperture. In this way the model can be used beneficially to estimate *in situ* pressures which are proving technically difficult to measure.

The work presented in this thesis on comparison of theory and experiment is restricted by the extreme sensitivity in p_+ values to measurement and calculation errors. Away from the shock front, it seems likely that pressures including p_- may be better approximated and it may prove more fruitful to examine the theoretical model.

7.2 Cavitation fields

7.2.1 Bubble response to lithotripsy fields

A well known nonlinear bubble dynamic model (called Gilmore model) including diffusion effects has been taken in this study since the model has already been used by Church (1989) to obtain interesting predictions about the quantity of cavitation that may be generated during lithotripsy. By implementing this bubble model it has been possible to extend these predictions for the case of a real electrohydraulic lithotripter which generates a series of two or three pulses at about 3ms intervals following a single discharge. This analysis has allowed the results of cavitation experiments on this type of lithotripters to be interpreted in a novel way and also allows quantitative prediction of the bubble radius to be obtained from measurements of the acoustic 'quiet' time during the acoustic emission from the bubbles excited in response to lithotripsy pulses.

Detailed consideration of gas diffusion between the fluid and bubble makes it possible to examine the effects of increasing the partial pressure of gas in the fluid on the violence of cavitational activity in the fields. Preliminary experimental evidence (Coleman et al 1991c) suggests that the damaging effects of lithotripsy on

brittle materials are reduced when the partial pressure of dissolved gas is high.

7.2.2 Cavitation effects on clinical lithotripsy fields

Clinical features of lithotripsy treatment appear to be closely related to cavitational activity and a propagation model alone appears inadequate in describing many of the interesting features of lithotripsy fields. Simple considerations outlined in this thesis concerning the bubble dissolution time and the sound attenuation in a bubbly fluid allow some interpretation of the observed fall in measured pressure as the lithotripsy pulse repetition frequency increases and the consequent decrease in stone fragmentation efficiency and increase in tissue damage. While the correct use of the theoretical models presented in this thesis requires more accurate information on the properties of a gas bubble-liquid mixture, it is shown, by considering a range of parameters such as a bubble size and void fraction, that experimental measurements of increased attenuation with increasing the pulse repetition frequency can be reasonably well matched by the predictions.

7.2.3 Further work

A. Degree of cavitation

The Gilmore model incorporated with a diffusion model could

now be usefully applied to consider the influence of factors including viscosity, gas content and temperature on cavitational activity in lithotripsy fields. This would provide valuable evidence of dose effects in extracorporeal shock wave lithotripsy where it is experimentally observed, for example, that immobilizing cells in highly viscous gel reduces cell damage.

B. Shock pulse propagation in cavitation fields

It is critical to understand how cavitation may act to attenuate lithotripsy pulses if the propagation model is to be used with any confidence to predict *in situ* pressures. While it is unlikely that a comprehensive model can be developed in which both propagation and cavitation effects are combined, it would be useful to place limits on the accuracy of the propagation model predictions by considering the attenuation and dispersion due to cavitation.

The observed 10MPa upper limit on the negative peak pressure measured in water in lithotripsy fields may, perhaps, be explained by loss of energy to cavitation in the negative half cycle during propagation. Since negative pressure appears to hold the key to the clinical effects of stone fragmentation and tissue damage in lithotripsy fields an analysis of this limit might prove interesting and useful.

7.3 Concluding statements

As the medical use of the high amplitude pulsed ultrasound increases and a variety of equipment becomes available, the efficiency, performance and safety of the procedures should be critically examined. An important aspect of this evaluation is to develop a reasonable theoretical model which can provide estimates of *in situ* exposure (or dose) parameters and allows important aspects of lithotripsy fields, including in particular their ability to generate acoustic cavitation, to be modeled to some extent.

While more complex, typically three dimensional, propagation models will be developed to run on super computers, the relatively simple one dimensional approach has been shown in this thesis to allow prediction of the clinically important features of the high amplitude pulsed acoustic field used in extracorporeal shock wave lithotripsy. The considerable difficulties in modeling acoustic cavitation in this field suggest that, in many cases, more precise propagation models are unnecessary at present since the predicted field will be significantly affected by cavitation.

APPENDIX A. SMALL AMPLITUDE FIELD OF A FOCUSING RADIATOR

A1 Aperture field

For an acoustic source driven to radiate either monochromatic or polychromatic waves (Fig A1-1), a general expression of non-uniform pressure field at the aperture (z=0) can be written as

$$(A1\text{-}1) \quad p(z=0,x,y,t) = p_o\, K(x,y,t) * g(t+t_a(x,y))$$

where p_o is the reference pressure at the aperture (eg, spatial temporal peak), $K(x,y,t)$ is the aperture shading function ($0 \le K(x,y,t) \le 1$), $g(t)$ is the normalized pressure time history at the origin of the aperture, $t_a(x,y)$ is the time delay of waves across the aperture, and the symbol * denotes convolution.

The time delay $t_a(x,y)$ establishes the plane of wavefront at the aperture (z=0) to ensure that the beam will be either converged or diverged. If $t_a(x,y)$ is constant, the field in front of the aperture will be a plane wave. For a field spherically converging with the focal distance of F (ie, curvature radius of the aperture wavefront plane) the plane equation of the wavefront at the aperture (ie, $t_a(x,y)$) is given from geometric considerations as

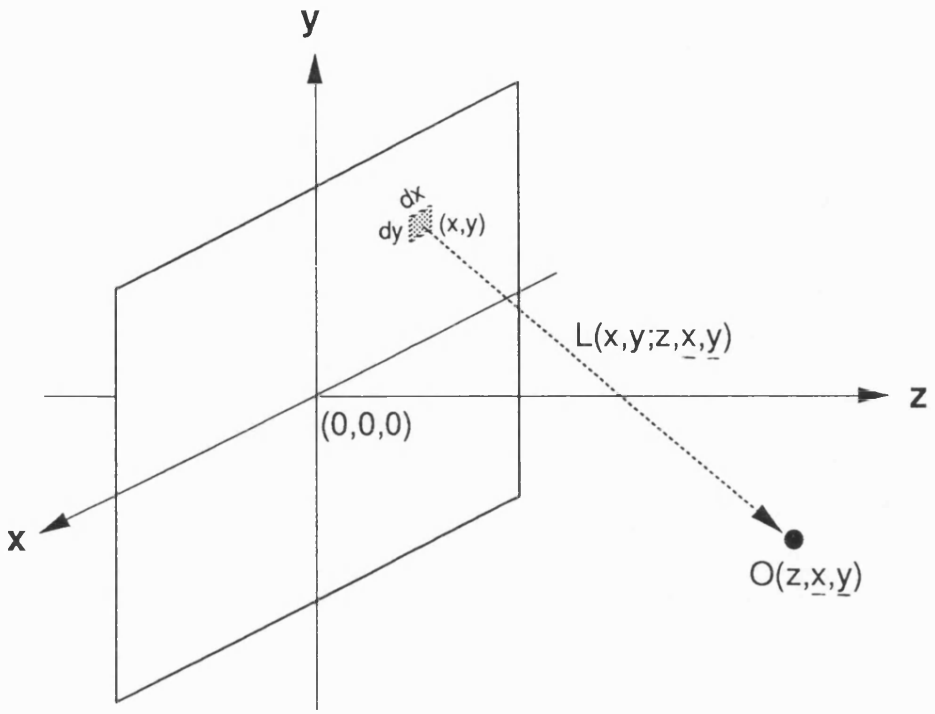

[A1-1] The geometry of an arbitrary baffled acoustic source of any shape and with non-uniform complex pressure distribution. The O(z,x,y) is an object point at which the acoustic field will be calculated and L(x,y;z,x,y) is the scalar distance between the coordinate of (x,y) at the surface of the aperture and O(z,x,y). The shaded area specified by dx and dy represents a differential area for integration.

(A1-2) $$t_a(x,y) = \frac{1}{c_o}\left(\sqrt{x^2+y^2+F^2} - F\right)$$

where c_o is the small signal speed of sound.

A2 Linear diffraction theory

For an infinitesimal acoustic signal in a lossless medium, the diffractive field in front of the aperture (z>0) can be evaluated by superimposing the pressure potentials due to all constituent point sources of the aperture plane being considered as simple sources (Huygen's principle). The pressure field at an object point $O(z,\underline{x},\underline{y})$ (see Fig A1-1) which is given as the sum of the diverging spherical waves emerging from the aperture is

(A2-1) $$p(z,\underline{x},\underline{y},t) = \frac{p_o}{2\pi c_o}\iint dxdy\,\frac{K(x,y,t)}{L(x,y;z,\underline{x},\underline{y})} * \frac{\partial}{\partial t} g(t+t_a(x,y)-L(x,y;z,\underline{x},\underline{y})/c_o)$$

where $L(x,y;z,\underline{x},\underline{y})$ is the scalar distance between a position of (x,y) at the aperture and $O(z,\underline{x},\underline{y})$. The dimension of the differential area (dx·dy) at the surface of the aperture should be small compared to the wavelength in order to ensure that it can be treated as a simple source.

Changing variable t by a retarded time parameter $\tau(=t-z/c_o)$ gives

$$(A2\text{-}2)\quad p(z,\underline{x},\underline{y},\tau) = \frac{p_o}{2\pi c_o}\iint dxdy\,\frac{K(x,y,\tau)}{L(x,y;z,\underline{x},\underline{y})} * \frac{\partial}{\partial\tau} g(\tau-\tau_d(x,y;z,\underline{x},\underline{y}))$$

where $\tau_d(x,y;z,\underline{x},\underline{y})$ represents a retarded time delay at $(O(z,\underline{x},\underline{y}))$ and is given by $L(x,y;z,\underline{x},\underline{y})/c_o - t_a(x,y) - z/c_o$.

This equation is a weighted integral of the normal pressure gradient on the aperture surface, which characterizes a linear pressure field in front of the aperture ($z>0$) with a non-uniform aperture pressure field. The Eq(A2-2) becomes the well known Rayleigh-Sommerfeld Integral (Goodman 1968) when the shading function does not depend on time (ie, $K(x,y,\tau)=K(x,y)$) and hence the convolution in the equation disappears.

A3 Focusing circular radiator

Special attention is paid to the case of focusing circular radiators which are used in most medical ultrasonic machines including extracorporeal shock wave lithotripters. In particular the axial response of the circular radiator is attractive since the information on axis is often most valuable, also lead to reasonable estimation on the off axis response and its analysis is greatly simplified because of its radial symmetry.

Consider a focusing circular radiator with aperture radius of 'a' and focal distance of 'F', and assume the aperture is mounted in an infinite rigid plane wall (ie, baffled) and hence the shading function can be set to zero for $|r| \geq a$. The axial response of the circular radiator in a lossless medium, according to Eq(A2-2), will then be simplified to a line integral:

$$(A3\text{-}1) \qquad p(z,\tau) = \frac{p_o}{c_o} \int_0^a r dr \frac{K(r,\tau)}{L(r;z)} * \frac{\partial}{\partial \tau} g(\tau - \tau_d(r;z))$$

where $\tau_d(r;z) = L(r;z)/c_o - t_a(r) - z/c_o$, $L(r;z) = \sqrt{r^2+z^2}$ and $t_a(r) = (\sqrt{r^2+F^2} - F)/c_o$.

The retarded time at the focus $\tau_d(r,z=F)$, in particular, becomes zero. This indicates that all waves converging from the aperture plane are in phase at the focus. Accordingly the integral Eq(A3-1) at z=F is further simplified to

$$(A3\text{-}2) \qquad p(F,\tau) = \frac{p_o}{c_o} \int_0^a r dr \frac{K(r,\tau)}{L(r;F)} * \frac{\partial}{\partial \tau} g(\tau)$$

The solution of this integral can be derived using a decomposition approach through which the solution for polychromatic waves can be obtained by superimposing monochromatic solutions. The decomposition approach begins to define the Fourier series of a pressure field in time domain by (Champeney 1985)

$$(A3\text{-}3) \quad p(z,\tau) = \frac{1}{2} p_o \sum_{n=-\infty}^{\infty} \phi_n(z) \exp(j2\pi f_n \tau)$$

where the subscript 'n' is an integer increasing from negative to positive infinity and identifies the frequency $f_n (=n\Delta f)$ in which Δf is an incremental frequency and $\phi_n(z)$ denotes the *n*th complex coefficient in the Fourier series of $p(z,\tau)$.

Combining the two equations (A3-2) and (A3-3), the Fourier coefficient $\phi_n(z=F)$ is derived as

$$(A3\text{-}4) \quad \phi_n(z=F) = jk_n \left[\int_0^a r dr \, K_n(r) \left(r^2 + F^2 \right)^{-0.5} \right] \phi_n(z=0)$$

where $\phi_n(z=0)$ represents the *n*th Fourier coefficient of $g(\tau)$ and $K_n(r)$ is the shading function at the frequency f_n.

For the simplest case of $K_n(r)=1$ (the uniform distribution at the aperture), Eq(A3-4) is more concisely given as

$$(A3\text{-}5) \quad \phi_n(z=F) = jk_n \left(\sqrt{a^2 + F^2} - F \right) \phi_n(z=0)$$

The factor "jk_n" in the equation implies that the waveform at the focus is given by the time derivative of $g(\tau)$ and the value of the bracket accounts for the geometric contribution to focal gain. The full time domain solution at the focus ($p(z=F,\tau)$) is then obtained using Eq(A3-3) with the calculated value of $\phi_n(z=F)$.

A4 Focused gaussian field

The gaussian field is of special interest since an analytical solution can be derived if the parabolic approximation is used (Novikov et al 1987). Consider a circular focusing source radiating a monochromatic wave of f_o with the gaussian radial profile which has the characteristic radius of a_o, then the complex pressure field at the aperture $\phi_o(z=0,r)$ takes the form (Lucas and Muir 1983):

$$(A4\text{-}1) \qquad \phi_o(z=0,r) = p_o \exp\left[-\left(\frac{r}{a_o}\right)^2\left(1 - j\frac{R_o}{F}\right)\right]$$

where F is the focal distance, a_o is the radius at which the amplitude of $\phi_o(z=0,r)$ is smaller by a factor of e($\cong$2.718) than its maximum value at r=0, and $R_o=0.5k_oa_o^2$ represents the Rayleigh length.

The small amplitude response in front of the gaussian source (z>0) can be analytically evaluated by solving the parabolic integral Eq(3.4-1). With the aid of the Hankel transformation, Eq(3.4-1) is transformed into a first order ordinary differential equation which can be easily solved. The solution satisfying the aperture condition specified by Eq(A4-1) is then inversely transformed to obtain the following desired solution:

$$(A4\text{-}2)\quad \phi_o(z,r) = p_o \mathbb{F}_o(z) \exp\left[-\mathbb{F}_o(z)\left(\frac{r}{a_o}\right)^2\left(1 - j\frac{\mathbb{R}_o}{F}\right)\right]$$

where $\mathbb{F}_o(z) = \left(1-\frac{z}{F}-j\frac{z}{\mathbb{R}_o}\right)^{-1}$ represents the normalized axial variation at low amplitude.

Examples of the focused gaussian fields on axis are illustrated in Fig A4-1 using Eq(A4-2) for f_o=0.15MHz, 0.3MHz and 0.45MHz with the boundary conditions of a_o=30mm and F=115mm which are likely to be the equivalent beam geometry of the Dornier HM3 lithotripter. The figure shows that the near field gaussian fields have no near field maxima and minima characteristics of the Fresnel field of the circular source. It is noted that the axial peak increases with frequency and the position of peak approaches the geometric focus (z=F) with increasing frequency.

A5 Radial profile of harmonics

When there exists a number of source generated frequency components at the aperture (eg, pulsed field), it is of great value to be aware of how the beam of each frequency component varies at the given aperture condition. Suppose a_o is the characteristic aperture radius at the reference (or centre) frequency f_o, then the characteristic aperture radius a_n at the frequency $f_n(=n\Delta f)$ may be written as

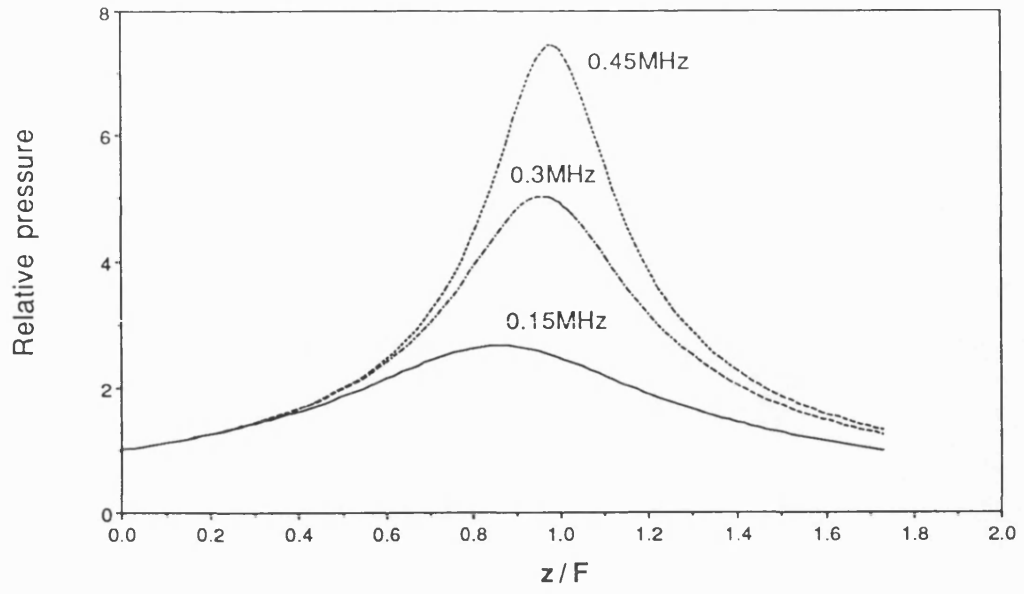

(a)

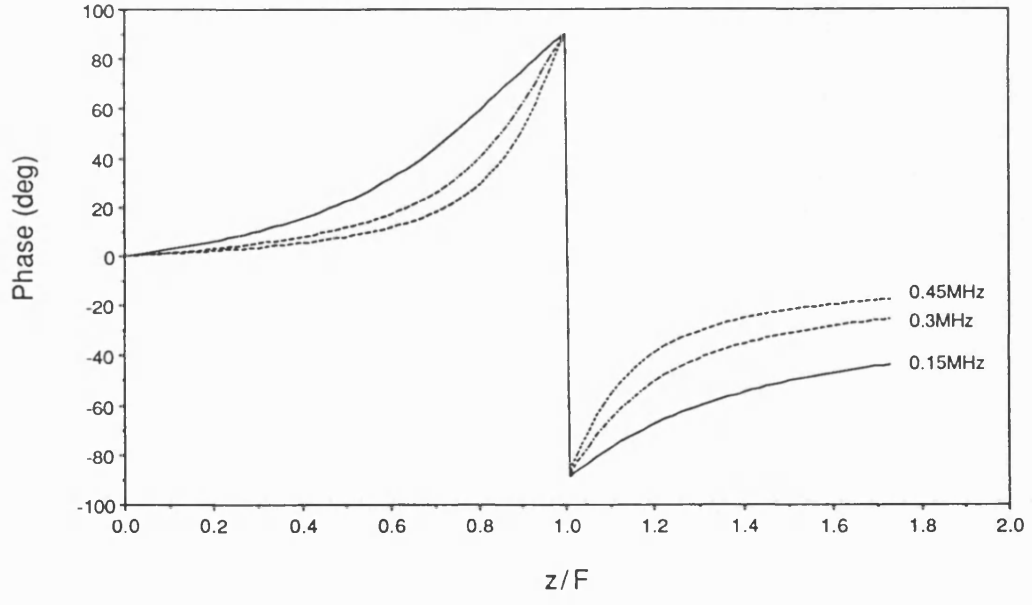

(b)

[Fig A4-1] Axial variations of **(a)** the pressure amplitudes normalized to the aperture pressure and **(b)** phases, for the focused ultrasound of 0.15MHz, 0.3MHz and 0.45 MHz of a gaussian radiator (a_o=30mm, F=115mm)

$$(A5\text{-}1) \qquad a_n = a_o \left(\frac{f_n}{f_o} \right)^{-\kappa}$$

where κ is a positive constant.

The variation of the characteristic radius of the frequency component f_n along the axis ($\bar{a}_n(z)$) can be given in the term of $\mathbb{F}_n(z)$ as

$$(A5\text{-}2) \qquad \bar{a}_n(z) = \frac{a_n}{|\mathbb{F}_n(z)|}$$

Substituting $\mathbb{F}_n(z)$ taken from Eq(A4-2) into Eq(A5-2), for a gaussian beam profile, $\bar{a}_n(z)$ can be written as

$$(A5\text{-}3) \qquad \bar{a}_n(z) = a_n \left[\left(\frac{z}{\mathbb{R}_n} \right)^2 + \left(1 - \frac{z}{F} \right)^2 \right]^{0.5}$$

where $\mathbb{R}_n = 0.5 k_n a_n^2$ represents the Rayleigh distance at the frequency of f_n.

The variation of the harmonic beam width normalized to the fundamental one (ie, $\bar{a}_n(z)/\bar{a}_o(z)$) is illustrated in Fig A5-1 for the first four harmonics at values of κ=0, 0.3, 0.5 and 0.8 (f_o=Δf=0.15MHz, a_o=30mm and F=115mm). The figure shows that, as the focus is approached, the relative harmonic beam width becomes narrower for $0 \le \kappa < 0.5$ and wider for $\kappa > 0.5$, while it remains constant for κ=0.5. The focal harmonic beam width is equal to the fundamental for κ=1 and wider than the fundamental for $\kappa > 1$. These situations may

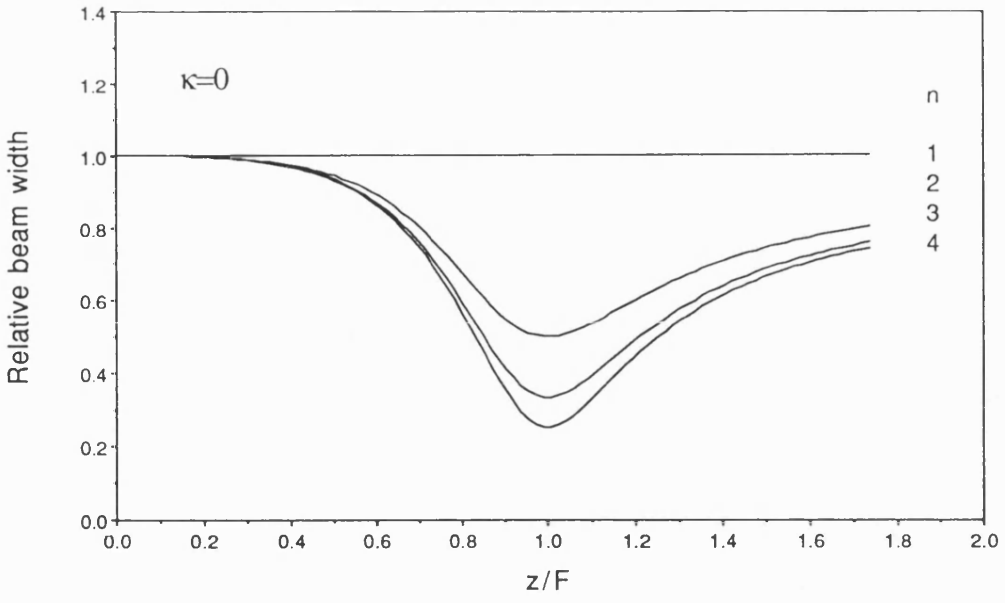

(a)

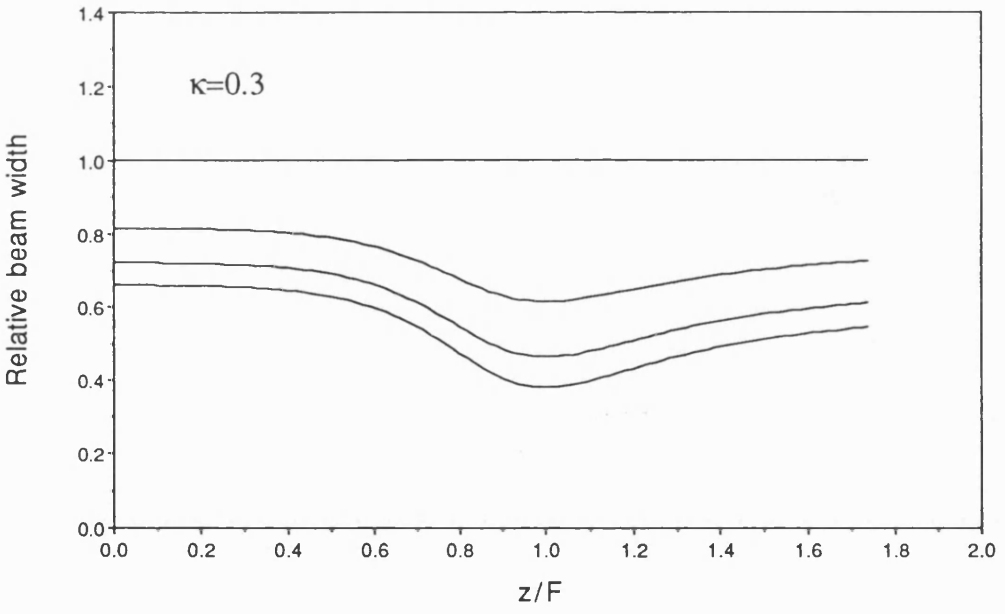

(b)

[Fig A5-1] Axial variations of the beam widths of the first four harmonics normalized to those of the fundamental (0.15MHz) for a focused gaussian field (a_o=30mm, F=115mm) at different values of κ. **(a)** κ=0, **(b)** κ=0.3.

- continued in (c) and (d) -

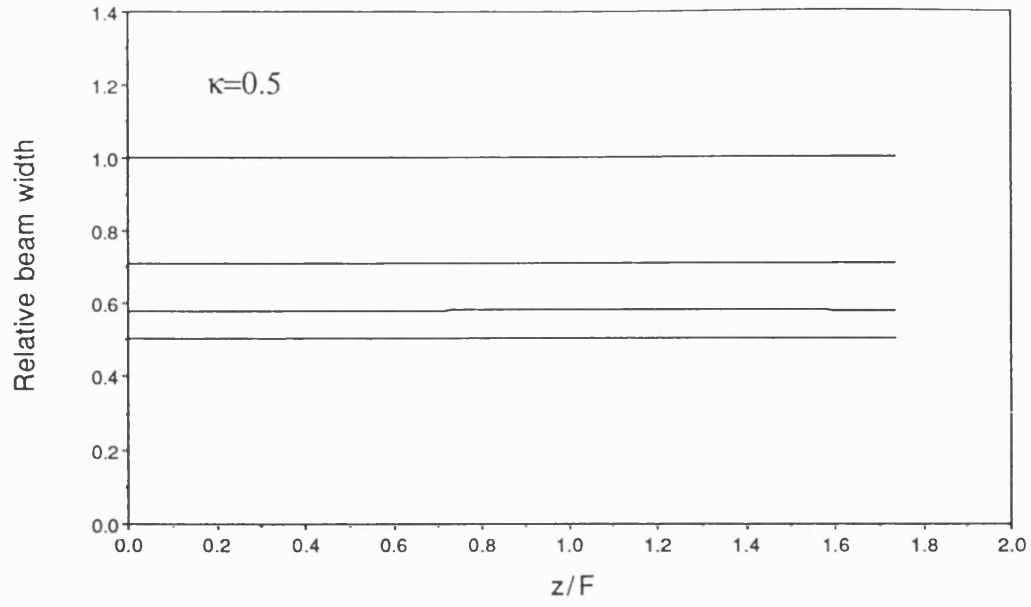

(c)

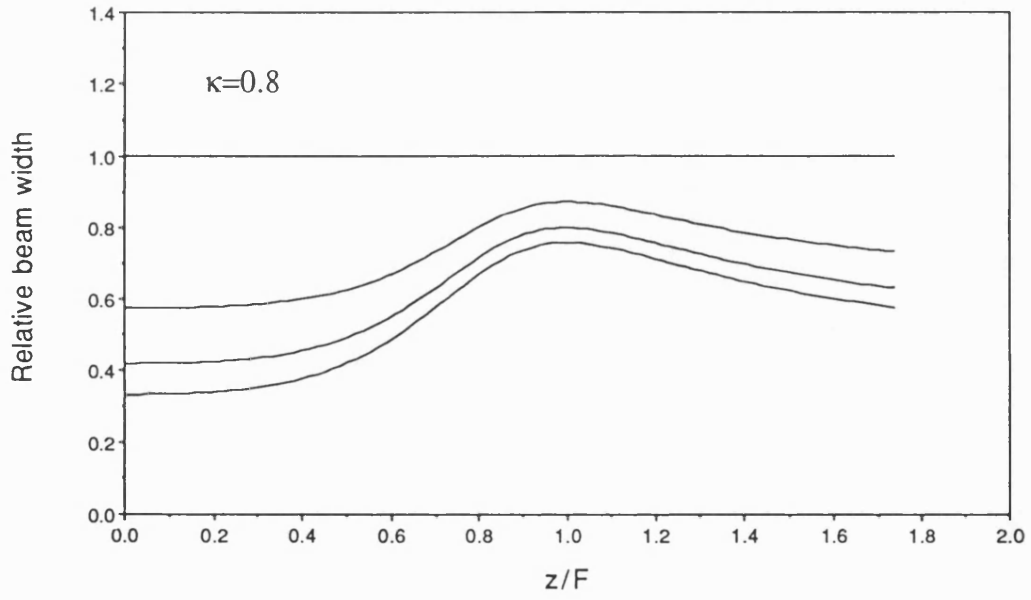

(d)

- continued -

[Fig A5-1] **(c)** κ=0.5 and **(d)** κ=0.8.

not be physically realistic and therefore the value of κ is expected to range between 0 and 1.

It is of interest to point out that Eq(A5-3) predicts that the relative harmonic beam radius at the focus varies with $n^{\kappa-1}$ where 'n' denotes the harmonic number (ie, $n=f_n/\Delta f$). When $\kappa=0$, the focal harmonic beam width of harmonics is proportional to n^{-1}. If $\kappa=0.5$, the harmonic beam width at the focus varies as $n^{-0.5}$ which is the variation predicted by Du and Breazeale (1987) and observed by Reilly and Parker (1989) for the fields where harmonics are generated by nonlinear propagation.

APPENDIX B. LITHOTRIPSY SOURCES: BOUNDARY CONDITIONS

B1 Introduction

While the proposed propagation model (Eq(4.2-1)) has been verified against existing models for well characterized acoustic sources (Section 4.4), it is useful to examine how it might be applied in the case of the high amplitude pulsed acoustic sources used in ESWL, since this application is the primary motivation for the development of the proposed model. It is therefore important to consider the characteristics of the sources used in clinical ESWL since these form the basis for defining the boundary conditions to be used in the model.

The beam geometry and boundary conditions, including the pressure waveform and shading function at the position of the accessible source aperture, may determine the applicability of approximations used in the theoretical model. By identifying the approximations which are appropriate in each case it is possible to avoid the excessive computations required by more general all encompassing models. For instance, in sources with small apertures angle it is appropriate to utilize the parabolic approximation and in sources which produce a gaussian shading function further simplification is possible.

Little experimental data on the aperture fields of real lithotripsy (shock wave) sources has been published so far and, in the lack of this data, the best approach presently available is to determine the boundary conditions on the basis of a semi-empirical approach. While this is unsatisfactory for allowing precise verification of the theoretical model, it provides an illustration of how the model might be applied to real lithotripsy sources. It also allows some of the general properties of the different types of lithotripsy sources to be modeled.

B2 Lithotripsy sources

Three essentially different types of sources are used in current clinical lithotripters: electrohydraulic (EH), piezoelectric (PE) and electromagnetic (EM) types. Fig B2-1 illustrates the modes of shock wave generation and focusing for the three different types of sources. In each case a large amplitude electrical impulse is applied to each transducer and the transducer emits a typically heavily damped sinusoidal pressure pulse.

B2.1 Electrohydraulic source

A pair of opposing metal electrodes are connected in series with a driving circuit. The electrodes are surrounded by a

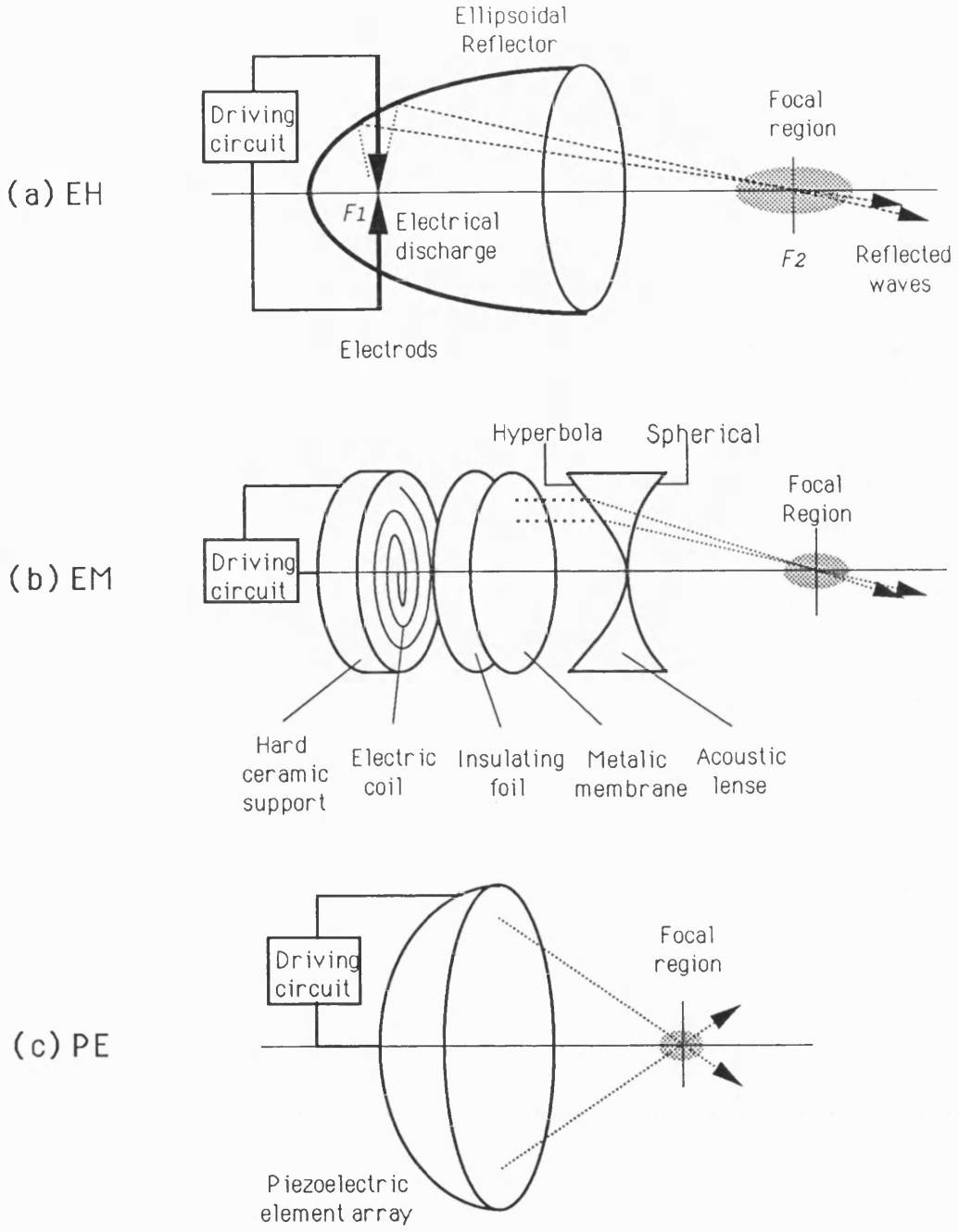

[Fig B2-1] A simplified configuration and focusing geometry of shock wave sources used in clinical lithotripters. **(a)** Electrohydraulic type (EH), **(b)** electromagnetic type (EM) and **(c)** piezoelectric type (PE).

Faraday-like cage which electrically isolates the electric discharge. The electrode gap is located at the first focus (F_1) of a rotationally symmetrical ellipsoidal metal reflector and immersed in water (Fig B2-1a).

The capacitor of the driving circuit, charged to a high voltage normally in the range of 13kV to 28kV, is discharged through the water between the electrodes. The temperature of water near the electrodes rises very rapidly reaching several thousand K. The resulting heated gas (plasma) then expands at supersonic speed before collapsing. The compressive part of the primary acoustic pulse is produced during the rapid expansion stage of the plasma bubble, and it is followed by a long tail of decaying pressure which goes negative. The secondary pulse is emitted during rebounding of the bubble about 500μs after the voltage discharge and it is much weaker than the primary (Hunter et al 1986ab). About 90% of the energy of the pressure waves emitted from the electrode gap is reflected to the second focus (F_2) of the ellipsoidal reflector, while the unfocused part remains spherically diverging.

Hydrophone measurements show successive shocked pulses of diminishing amplitude and asymmetry emitted at intervals of the order of ms. There are three distinctive pulses shown in the pressure time history measured at the second focus (Reichenberger 1988, Hunter 1987). The first one which has

a small pressure value is contributed by the unreflected acoustic waves emitted during the electric discharge. The second pulse is made of focused waves and the value of the peak pressure reaches up to 100MPa. The third one results from the secondary pulse during the rebound of the bubble at the spark channel. The measured value of the peak pressure of the second pulse is found to fluctuate by approximately 25%-45% and this is attributed to the inherent variability of the electrical discharge (Coleman et al 1987a).

B2.2 Electromagnetic source

A flat spirally wound coil is fixed on a rigid support and an insulating foil is placed to prevent electrical breakdown between the flat solenoid and a metallic membrane surrounded by water (Fig B2-1b).

When the capacitor is discharged, a strong electric current pulse flows through the flat coil. The magnetic field in the metal membrane then changes and this induces an eddy current in the metal membrane. Two magnetic fields between the coil and metal membrane influence each other and the metal membrane is repelled from the coil. This movement of the membrane results in acoustic disturbances which set up plane waves (Eisenmenger 1964). These plane waves are focused typically by a bi-concave acoustic lens placed in front of the metal membrane. The field generated by the electromagnetic source is highly reproducible and stable.

The shot to shot variation in temporal peak positive pressure measured at the focus, for example, has been reported to be about 1% (Reichenberger and Naser 1986).

B2.3 Piezoelectric source

Several thousand piezoelectric crystals, such as barium-titanate or lead-zirconate-titanate, are mounted inside the surface of a partial spherical dish filled with water (Fig B2-1c). A high voltage is applied simultaneously to all piezoelectric elements by the discharge of the capacitor, and the subsequent deformation of the elements induces acoustic pulses into the adjacent water. The pulse generated from the piezo-elements are directed to the centre of the spherical dish and no additional focusing device is needed.

The impedance of the electrical network and the time function of the drive voltage step are required to be matched to the electro-acoustical characteristics of the piezo-elements, so that a small amplitude of tensile pressure of the pulse with few cycle oscillations can be obtained (Reichenberger 1988). The wave energy released over the generator area is limited by the tolerance of piezoelectric material. In general this is lower than the other types of sources, accordingly the dimension of piezoelectric element array is required to be large to obtain the same energy at the focus as the other types. For the limited tolerance of the crystals, the pressure

waveform near the aperture has relatively long rise time. The shock to shock variation has been observed stable (about 1%).

B3 Aperture field

The lithotripsy sources are acoustically equivalent to circular focusing radiators and the pressure fields at the aperture (z=0) can be expressed as (Appendix A1)

$$(B3\text{-}1) \quad p(z=0,r,t) = p_o\, K(r,t) * g(t+t_a(r))$$

where p_o is the spatial temporal peak pressure at the aperture, $K(r,t)$ is the aperture shading function ($0 \le K(r,t) \le 1$), $g(t)$ is the normalized pressure waveform at the centre of the aperture ($r=0$), and $t_a(r) = (\sqrt{r^2+F^2} - F)/c_o$ representing the time delay of $g(t)$ across the aperture.

The shape of $g(t)$ depends on the values of driving circuit parameters such as inductance and capacitance (Davros et al 1991), and $K(r,t)$ varies with the type of focusing devices used. Typical $g(t)$ and $K(r,t)$ of clinical lithotripsy sources are specified in this section.

B3.1 Aperture shading function

The convolution between $K(r,t)$ and $g(t+t_a(r))$ accounts for the shape of aperture waveforms varying with r and can be

more conveniently treated in frequency domain. The fourier coefficient of p(z=0,r,t) is given as

(B3-2) $\varnothing_n(z=0,r) = p_o \, \mathbb{K}_n(r) \, \varnothing_n(z=0)$

where $\varnothing_n$ is the *n*th complex fourier coefficient defined by A3-3 and $\mathbb{K}_n(r)$ is the shading function at the *n*th frequency component.

In practice, it is reasonable to assume that the shape of the shading function of each harmonic is the same and, under the condition, if K(r) denotes the shading function at the reference frequency f_o, then $\mathbb{K}_n(r)=K(r_n)$ where $r_n=ra_o/a_n$, a_o and a_n are the characteristic aperture radii of the spectral components of f_o and f_n, respectively.

An analytical form of K(r) may be estimated in a straightforward way on the basis of geometric ray theory. A number of rays emitted from the sources are drawn in Fig B3-1 to illustrate the focusing geometry of the three different types of reflectors and the ray density variations at their aperture (z=0) of the three different types of reflectors. Assuming that K(r) is proportional to the ray density distribution across the aperture surface, K(r) derived for each source on the base of the geometric consideration is as following:

i) for ellipsoidal reflector (Müller 1987)

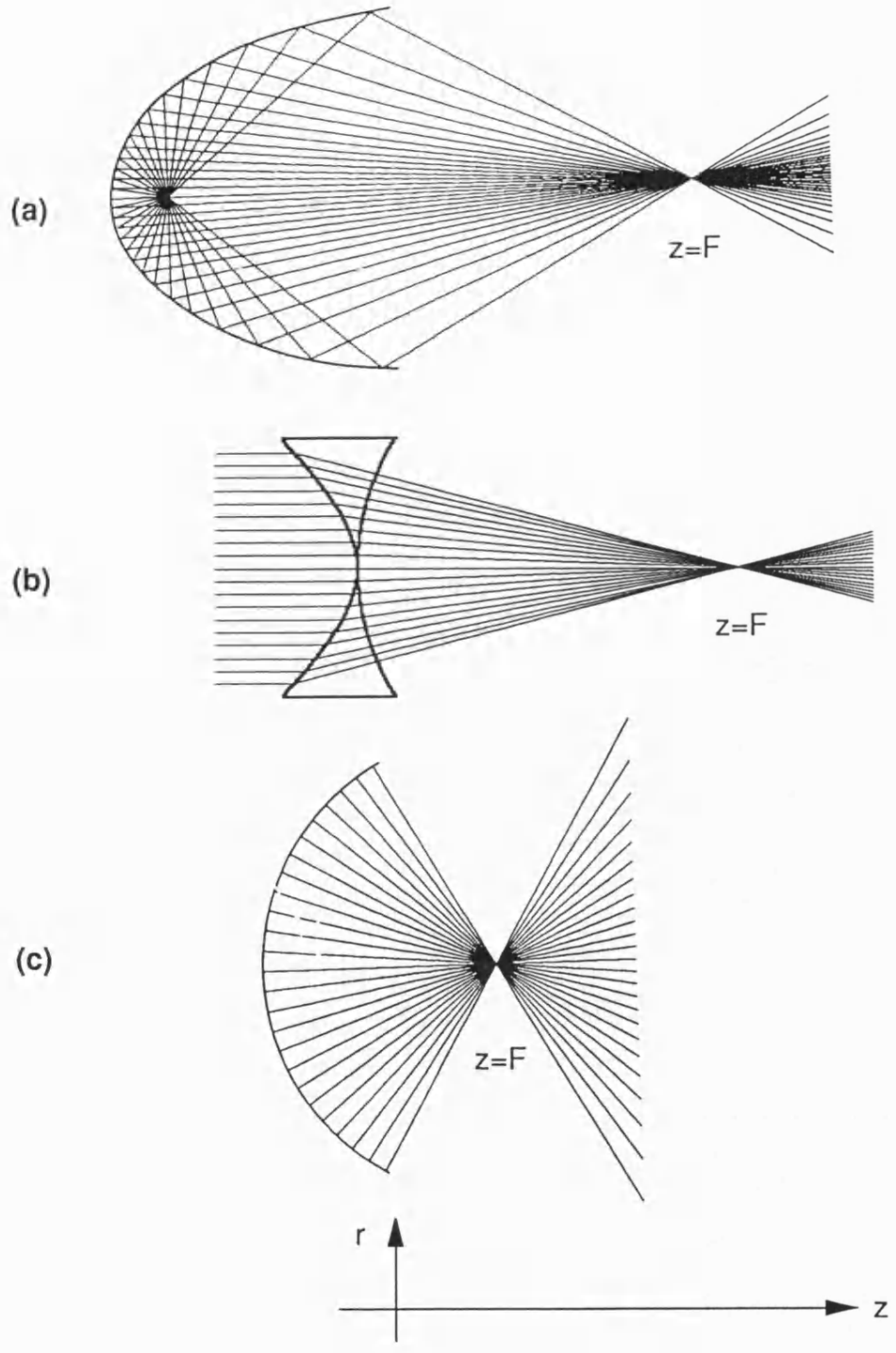

[Fig B3-1] Focusing system of extracorporeal shock wave lithotripsy sources. **(a)** Ellipsoidal reflector, **(b)** acoustic lens and **(c)** spherical shell.

$$(B3\text{-}3) \qquad K(r) = \frac{\cos(\theta(r))(1-e)^2}{1 + e^2 - 2e\cos(\theta(r))}$$

where $\theta(r) = \tan^{-1}(r/F)$, e is the eccentricity of the ellipse

ii) for acoustic focusing lens

$$(B3\text{-}4) \qquad K(r) = k_1(r)\, k_2(r)$$

where $k_1(r)$ represents the ray density at the aperture for the lens resulting from refraction alone and $k_2(r)$ is a correction for reflection at the lens which becomes large away from the beam axis due to increasing oblique incidence. The expressions for $k_1(r)$ and $k_2(r)$ are not given here due to their complexity, although they can be simply derived.

iii) for spherical reflector

$$(B3\text{-}5) \qquad K(r) = \cos(\tan^{-1}(r/F))$$

These analytical K(r) are depicted in Fig B3-2 as a function of the radius normalized to the characteristic aperture radius a_o defined as the radius at which the value of K(r) is smaller by a factor of e(≅2.7183) than its maximum value at r=0. The values of F and a_o for the sources used in Fig B3-2 are listed in Table B3-1 where EH, PE and EM represent the ellipsoidal reflector, spherical reflector and focusing lens, respectively. The values of

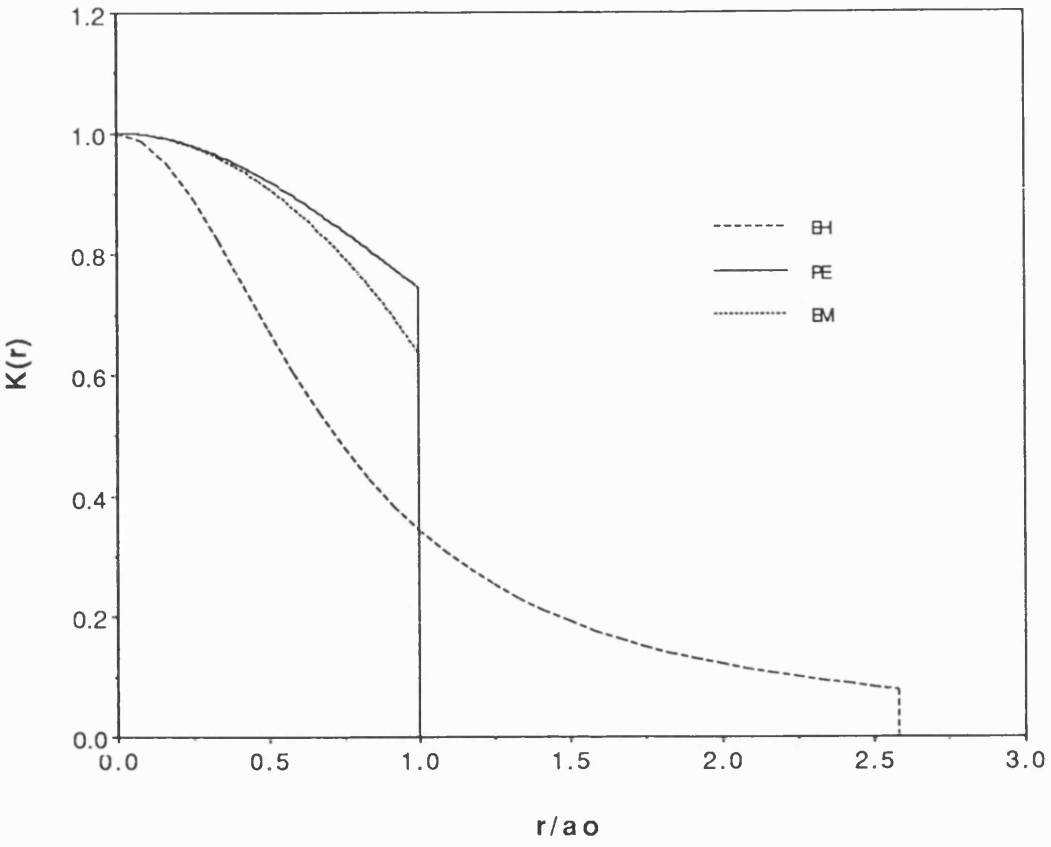

[Fig B3-2] Aperture shading function (K(r)) estimated on the basis of geometric acoustics. EH (dashed line): Dornier HM3 (a_o=30mm, F=115mm), PE (solid line): Piezolith 2200/3300 (a_o=250mm, F=238mm), and EM (dotted): Seimens Lithostar (a_o=53mm, F=110mm).

geometric parameters are taken from the Dornier HM3 lithotripter (e=0.83) for EH, Piezolith 2200/3300 for PE and Siemens Lithostar for EM. Note that the value of the characteristic aperture radius (a_o=30mm) in EH is different from the physical aperture radius (a=77mm), while they are the same in the other types of sources. The K(r) for the ellipsoidal reflector has been shown to be in reasonable agreement with the measured for the Dornier HM3 lithotripter (Coleman et al 1989) while, for the other types of sources, the experimental data is not available.

[Table B3-1] Geometric characteristics of lithotripsy sources. Aperture angle θ_o is given by $\tan^{-1}(a_o/F)$ where F and a_o are the focal distance and characteristic radius of the aperture, respectively. (EH: Dornier HM3, PE: Piezolith 2200/3300 and EM: Siemens Lithostar)

Source	F(mm)	a_o(mm)	θ_o(deg)
EH	115	30	15
EM	110	53	26
PE	238	250	46

B3.2 Aperture waveform

The aperture waveforms (g(t)) shown in Fig B3-3 represent characteristic features in different types of lithotripsy sources rather than those precisely measured, since the

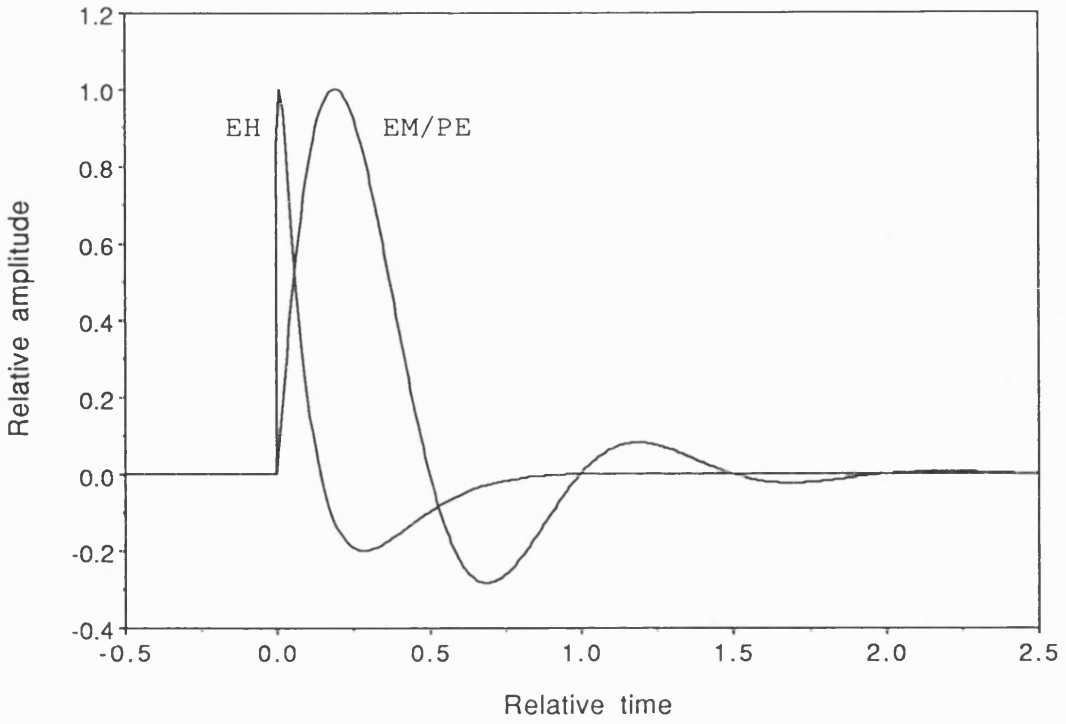

[Fig B3-3] Characteristic aperture pressure waveforms of acoustic sources used in extracorporeal shock wave lithotripsy. The time is normalized to the period of the centre frequency component. EH: electrohydraulic type of sources and EM/PE: electromagnetic and piezoelectric types of sources.

measured g(t) has not yet been reported except for an electrohydraulic type lithotripter (Coleman et al 1989).

In the EH lithotripter g(t) has distinct properties compared with those of the other types of lithotripters, which results from plasma bubble dynamics at the electrode gap. The waveform is already significantly distorted whereas most distortion occurs during nonlinear propagation beyond the aperture (z>0) in the other types of sources. In addition, damped oscillations are not generally observed following the initial half cycle because the cavitation bubble expansion phase at the electrodes lasts for as long as 1 ms.

The g(t) for EM and PE lithotripters is expected to be a heavily damped sinusoidal pulse with a relatively large rise time from the consideration of their source characteristics. A waveform measured near the aperture in a prototype of the EM lithotripter (Eisenmenger 1964) looks similar to a damped sine pulse. Until precise measurements are made, therefore, the damped sine pulse may be reasonably assumed to represent a true aperture waveform.

The mathematical expression of the damped sine pulse is

$$(B3\text{-}6) \quad g(t) = \tilde{a} \exp(-t/t_c) \sin(2\pi f_o t)$$

where $\tilde{a}$ is a constant chosen to give the temporal peak of g(t) to be one, which is given by $\tilde{a} = 1/g(t')$ where $t' =$

$\tan^{-1}(2\pi f_o t_c)/2\pi f_o$, t_c is the time constant of the exponential damping in the pulse, and f_o represents the centre frequency of waveform.

The g(t) for EM/PE sources shown in Fig B3-3 are obtained using t_c=2.65μs and ã=1.73. The value of f_o varies with source type and is expected to be in the range of 0.1 to 0.4MHz from the consideration of the waveforms measured at the foci of the different types of lithotripsy sources (Coleman and Saunders 1989).

B4 Applicability of approximations

When boundary conditions are such that it is possible to employ parabolic and gaussian approximations, $F_n(z)$ in the proposed propagation model is analytically solved (Section 4.1.2). This allows enormous computing efficiency and it is therefore of interest to examine the possibility of applying these approximations before proceeding to predict fields using the model.

B4.1 Parabolic approximation

The use of the parabolic approximation is restricted by the aperture angle. Fig B4-1 illustrates the effects of the parabolic approximation on axial variation of a 0.6MHz sinusoidal wave produced by a circular focusing radiator

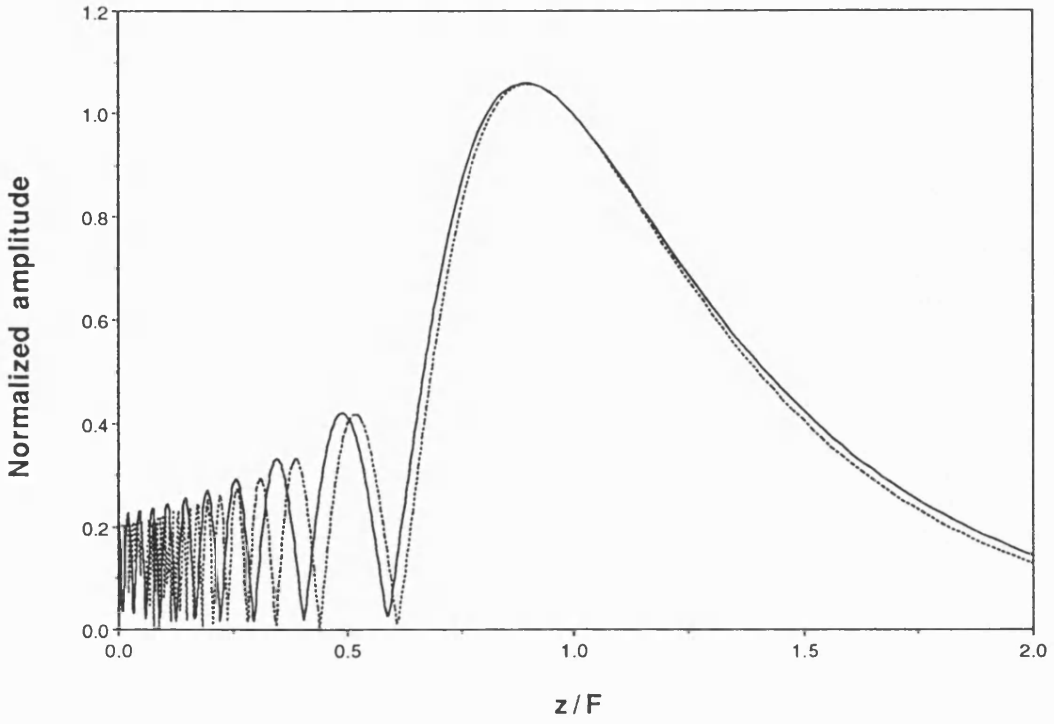

[Fig B4-1] Axial amplitude variation of pressure for a 0.6MHz focused piston source (θ_o=15°) at low amplitude, normalized to that at the focus (z=F). Solid line: Rayleigh integral and dotted line: Parabolic integral.

($K(r)=1$, $\theta_o=15^\circ$). The solid curve in the figure represents an exact solution calculated using the Rayleigh Integral (Eq(A3-1)) and the dotted curve is obtained using the parabolic integral (Eq(3.4-1)). It is shown that the error due to the parabolic approximation for the given source conditions is relatively small around the focus and increases as approaching the source.

For the circular focusing source with $K(r)=1$, the parabolic integral and Rayleigh integral can be analytically solved at the focus in frequency domain and, therefore, the error due to the parabolic approximation at $z=F$ can be analytically given. The *n*th harmonic fourier coefficient at the focus are given as follows:

i) for the parabolic integral (Lucas and Muir 1983)

$$\text{(B4-1)} \qquad \phi_n(z=F) = jk_n \frac{a_o^2}{2F} \phi_n(z=0)$$

ii) for the Rayleigh integral (Eq(A3-5))

$$\text{(B4-2)} \qquad \phi_n(z=F) = jk_n \left(\sqrt{a_o^2 + F^2} - F \right) \phi_n(z=0)$$

Anticipating the equations (A3-3), (B4-1) and (B4-2), the percentage error due to the parabolic approximation (E_{pa}) in predicting focal pressures at low amplitude is given as

$$\text{(B4-3)} \qquad E_{pa}(\%) = \left(\frac{\tan^2(\theta_o)}{2(\sqrt{\tan^2(\theta_o) + 1} - 1)} - 1 \right) \text{X } 100$$

This equation indicates that the error due to the parabolic approximation at the focus depends on θ_o only. The variation of E_{pa} with θ_o is illustrated in Fig B4-2 and the corresponding values of E_{pa} for the three different types of lithotripsy sources specified in Table B3-1 are indicated. The error E_{pa} for the EH (2.2%) and EM (5.5%) sources is small while it is significantly high for the PE (22.5%). This suggests that, although the value of E_{pa} may provide a lower limit in the error due to the parabolic approximation in predicting an axial field at low amplitude, the parabolic approximation used in the propagation model will be relatively accurately applied for the prediction of the focal fields of the EH or EM sources. For the PE source with large aperture angle, however, the nonparabolic diffraction term Eq(4.1-6) is required to be calculated.

B4.2 Gaussian shading function approximation

Linear diffraction theory predicts the waveform at the focus to be the time derivative of the aperture waveform g(t) while the shading function K(r) influences the amplitude. Therefore, although K(r) may not have gaussian form, there exists a matched gaussian form of K(r) which gives the same linear gain (G_{lin}) at the focus.

The standard form of a gaussian function is

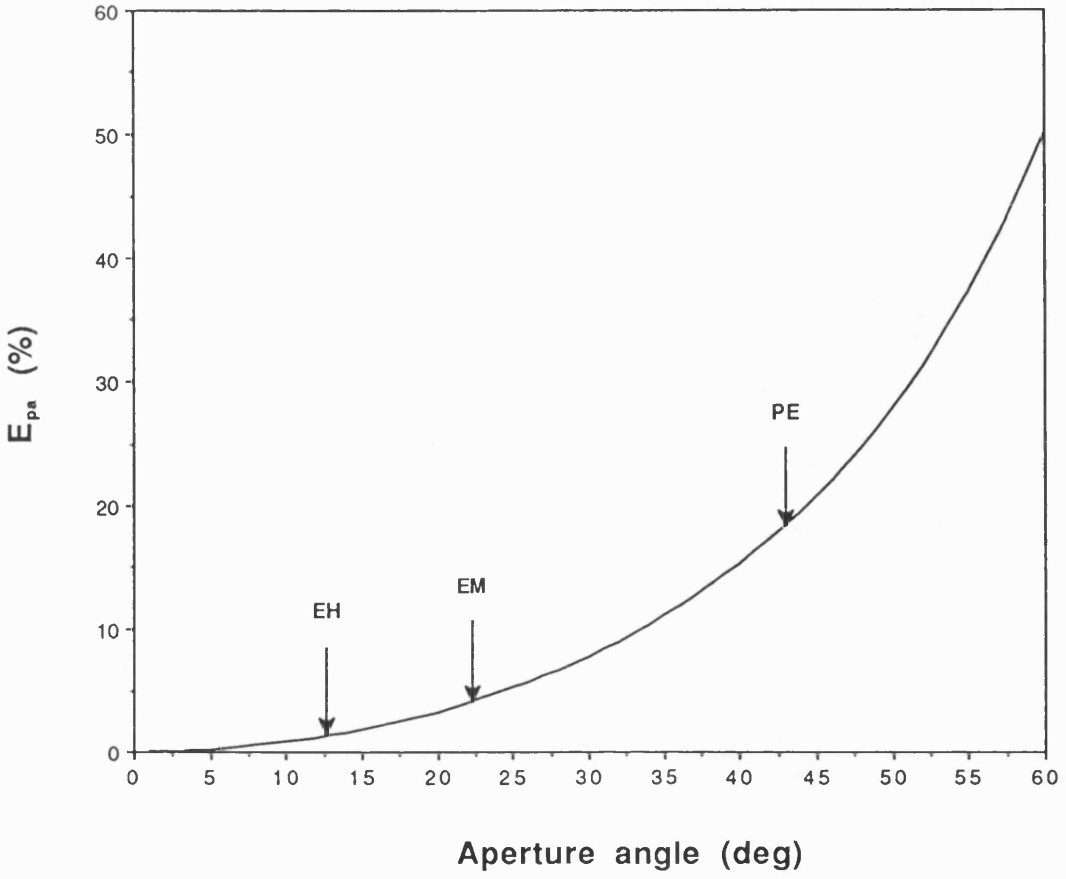

[Fig B4-2] A plot of error (E_{pa} in %) in predicted pressure amplitude at the focus due to the parabolic approximation as a function of aperture angle (θ_o). EH: Dornier HM3 (θ_o=15°), EM: Siemens Lithostar (θ_o=26°) and PE: Piezolith 2200/3300 (θ_o=46°).

(B4-4) $$K(r) = \exp\left[-\left(\frac{r}{a_o} \right)^2 \right]$$

Since the linear gain of the gaussian source is $k_o a_o^2/2F$, a_o for a non-gaussian source with G_{lin} can be given by

(B4-5) $$a_o = \sqrt{\frac{2FG_{lin}}{k_o}}$$

When K(r)=1, (ie, uniform aperture distribution of a perfect piston source), the value of a_o is equal to the physical aperture radius of a. If K(r) deviates from unity, the value of a_o relative to a will be changed. For different lithotripsy sources, the values of a_o/a are listed below:

a_o/a	= 1.00	for perfect piston source
	= 0.82	for PE type source
	= 0.79	for EM type source
	= 0.41	for EH type source

The axial variations in amplitude for the different types of sources, ie, the different values of a_o/a ranging from 0.41 to 1 as specified above, have been illustrated in Fig B4-3 at G_{lin}=10 using the Rayleigh integral (Eq(A3-1)). The figure shows that the near field oscillation is noticeable for the sources with values of a_o/a near to 1. At the smallest value of a_o/a=0.41 (ie, EH type of lithotripsy source), the near field oscillation in amplitude is not significant and is well fitted to that of the gaussian source which has a smooth axial variation in both amplitude

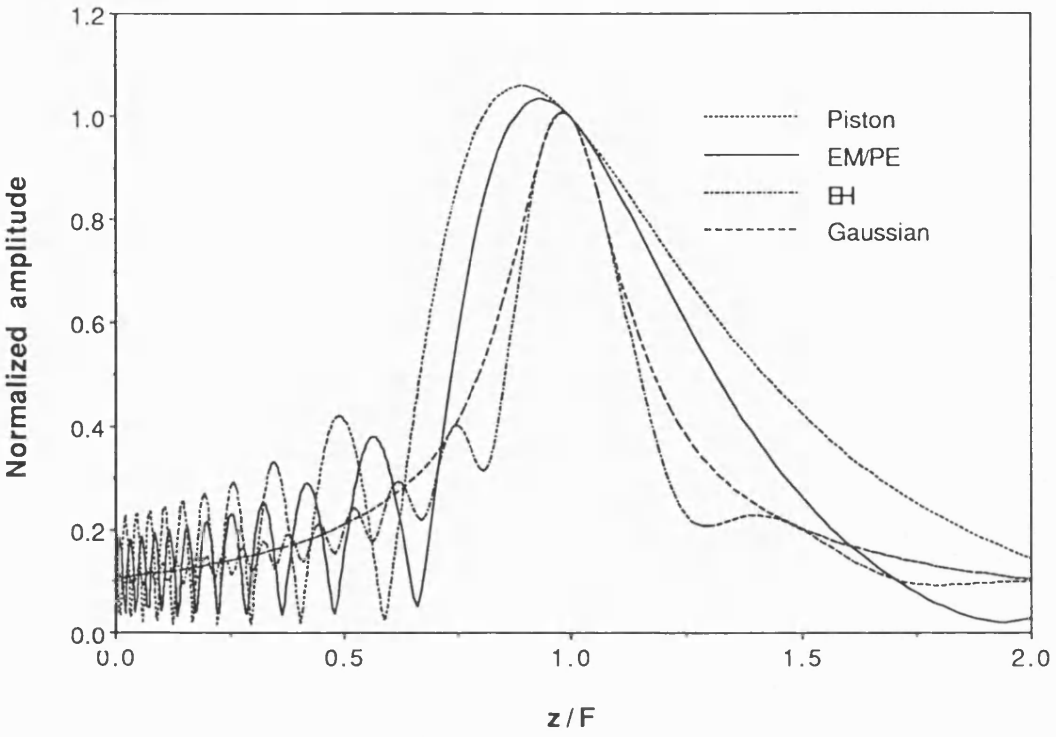

[Fig B4-3] Axial amplitude variation for different types of focused transducers (ie, Piston source, EM/PE types of lithotripters, EH type lithotripter and Gaussian source) with the linear focal gain of 10 at low amplitude, predicted using the Rayleigh integral (Eq(A3-1)), and normalized to the pressure at the focus (z=F).

and phase. This is because K(r) for the EH source decreases away from the centre of the aperture in a similar pattern to gaussian. The degree of difference between the gaussian source and the PE and EM sources lies somewhere between the piston and EH sources.

As consequence, the predicted axial response at low amplitude with a matched gaussian form of K(r) is relatively accurate at small values of a_o/a (eg, ≤ 0.5) even in the nearfield, and therefore the error due to the gaussian approximation to the true shading function would be small for the EH source and lies between the EH and piston sources for PE and EM sources.

B4.3 Summary

The gaussian shading function approximation is attractive when it is combined with the parabolic approximation because it results in an analytical solution in the diffraction term of the proposed propagation model and this allows the propagation model to significantly reduce computing efforts. The linear theory indicates that the parabolic and gaussian approximation may be used, within an accuracy in the order of 10% or less, to predict the focal fields of EH and EM types of shock wave sources. For the PE type with large aperture, however, the error is unacceptably large (more than 20%). This is an important feature because most clinical lithotripters fall in either EH or EM types and the propagation model highlights the

quick prediction for these types of lithotripsy sources. Indeed, the model can also predict the field in which such approximations may not be applicable, although it requires relatively considerable computing efforts.

B5 Boundary condition effects

Some interesting features of predicted waveforms which result from the choice of boundary conditions, including the precise form of the shading function (K(r)) and aperture waveform (g(t)), are illustrated quite effectively using linear diffraction theory. The boundary conditions considered here are taken from the case of the EH source used in the Dornier HM3 lithotripter where experimental data is available.

Unlike other types of sources, in the EH source with the ellipsoidal reflector, there are two distinct contributions to the fields, due to first waves outgoing from the spark gap of the electrode and secondly waves reflected by the ellipse. The contribution from the outgoing waves is a minor one, which is from the consideration of geometric acoustics less than 10% of energy generated by the spark, and so only reflected contributions are considered here.

A series of calculations using the Rayleigh integral (Eq(A3-1)) has been carried out for the following three

different cases of boundary conditions:

case 1. analytical g(t) with analytical K(r)

case 2. analytical g(t) with measured K(r)

case 3. measured g(t) with measured K(r)

where the measured and analytical (fitted pulsed exponential) g(t) and measured K(r) used here in the calculation are taken from Coleman et al (1989) and the analytical K(r) is defined by Eq(B3-3). The influence of K(r) on predicted fields is analyzed from the difference between case 1 and 2, and the effects of g(t) are examined from comparison between case 2 and 3.

Examples of the normalized waveforms calculated for case 1 at different positions through the focus are shown in Fig B5-1 where figure a is the prediction before the focus (z/F=0.82), figure b near the focus (z/F=0.98) and figure c beyond the focus (z/F=1.2). In these waveforms it is possible to identify the focused wave and edge wave components. The focused and edge wave contributions are clearly distinguished before the focus while the edge wave overtakes the focused one beyond the focus.

The effects of the three different boundary conditions on the field have been examined at z/F=0.82 where the edge wave is clearly shown. Fig B5-2 shows calculated waveforms along the waveform measured in water for a Dornier HM3 lithotripter using a needle hydrophone (Coleman et al 1989)

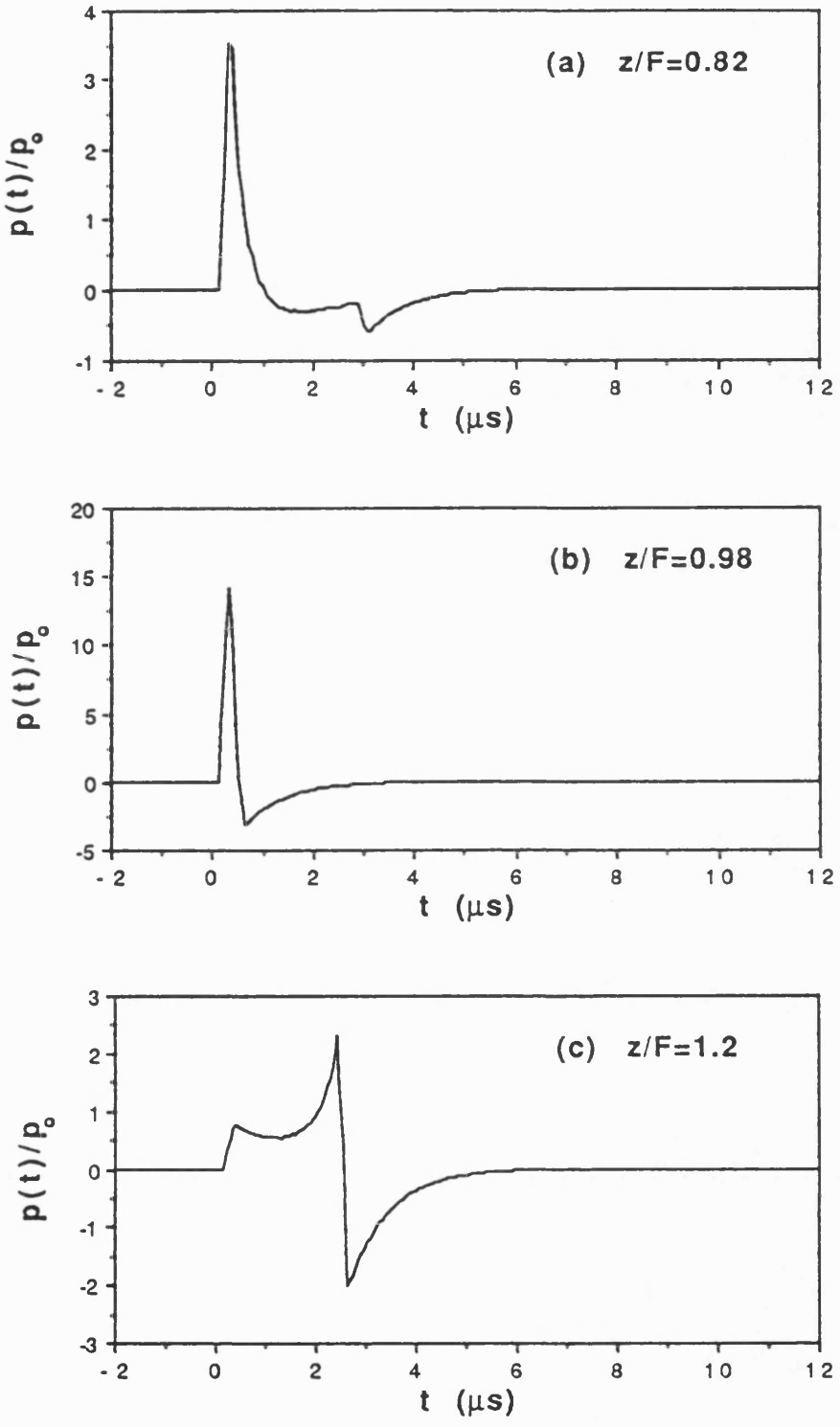

[Fig B5-1] Pressure waveforms calculated for a Dornier HM3 using Rayleigh integral with analytical aperture waveform and shading function at **(a)** z/F=0.82, **(b)** z/F=0.98, and **(c)** z/F=1.2, normalized to aperture peak pressure (p_o)

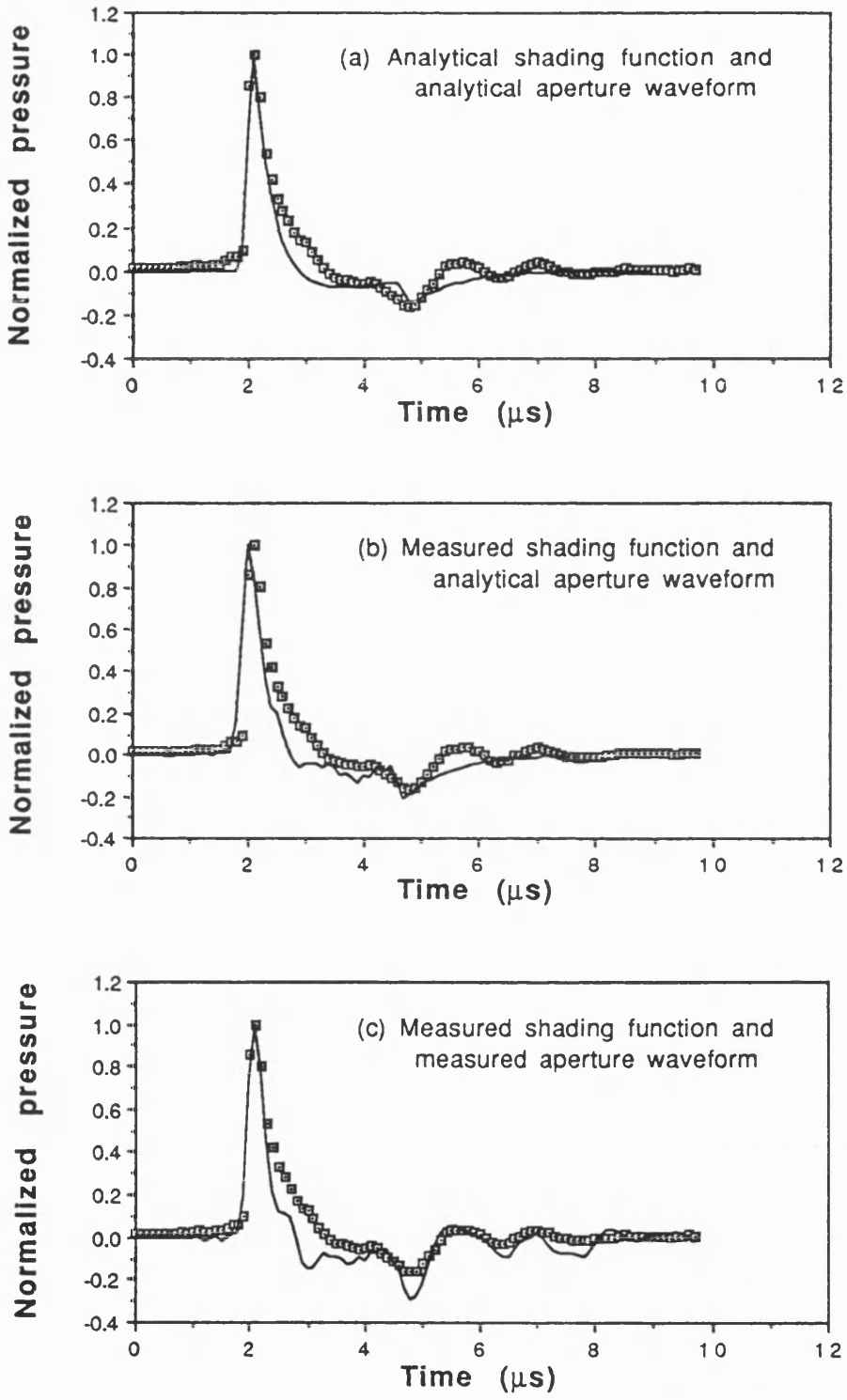

[Fig B5-2] Relative pressure waveforms at the position of z/F=0.82 of a Dornier HM3 lithotripter. Square dots: measured, solid curves: predicted for the different boundary conditions using Rayleigh integral.

where figure a is the prediction for case 1, figure b for case 2, and figure c for case 3.

Fig B5-2b shows that the inclusion of the measured K(r) in the calculation leads to a slight inflection on the decaying portion of the positive pressure half cycle and results in a slight broadening of this cycle. There is close agreement between the calculated and measured oscillations following the negative peak when the measured g(t) is used in calculation (Fig B5-2c). The best agreement between experiment and theory, as expected, has been obtained using the measured K(r) and g(t).

It is noted that in all cases the duration of positive half cycle (t_+) of calculated waveforms is shown to be smaller than that of the measured. This may be attributed to the fact that calculations do not account for attenuation and nonlinearity which can cause increase in t_+ (Section 5.5). Negative half cycles of the predicted waveforms are more sensitive to the boundary conditions than the positive half cycles, which is mainly due to edge wave effects. This property may be beneficially used to achieve desirable negative pressure fields by altering source conditions, for example, Lewin et al (1990) has reduced the negative peak pressure (p_-) at the focus by adjusting source conditions.

In summary, while the detailed structure of pressure waveforms around the focus can be obtained using the

measured boundary conditions, the main features are well represented by the appropriate analytical forms of these measured conditions. This may justify the use of some approximated boundary conditions such as an idealized shading function and analytical input waveform in the prediction of the general properties of acoustic fields around the focus using the proposed propagation model.

REFERENCES

Aanonsen S.I. (1983). Numerical computation of the nearfield of a finite amplitude sound beam, Report 73 of Dept. of Math., Univ. of Bergen, Bergen, Norway.

AIUM/NEMA. (1989). Acoustic output and labeling standard for diagnostic ultrasound equipment. National Electrical Manufacturers Association, Washington DC 20037 USA.

Akulichev V.A. (1971). Pulsations of cavitation voids. In: Rozenberg L.D. ed. High intensity ultrasonic fields, New York: Plenum Press.

Anderson A.L. and Hampton L.D. (1980). Acoustics of gas-bearing sediments: I. Background. J. Acoust. Soc. Am., 67, 1865-1889.

Apfel R.E. and Holland C.K. (1991). Gauging the likelihood of cavitation from short-pulse low-duty cycle diagnostic ultrasound. Ultrasound in Med. & Biol., 17(2), 179-185.

Apfel R.E. (1981). Acoustic cavitation. In: Edmonds, P. ed. Methods of experimental physics: Volume 19, p355. New York: Acad. Press.

Asada T. and Watanabe Y. (1990). Experiments of parametric amplification using nonlinear vibration of bubble under water. In: Hamilton M.F. and Blackstock D.T. eds. Frontiers of Nonlinear Acoustics; Proceedings of 12th ISNA, pp.485-490. London: Elsevier Science Publishers Ltd.

Bacon D.R. and Baker A.C. (1989). Comparison of two theoretical models for predicting non-linear propagation in medical ultrasound fields. Phys. Med. Biol., 34(11), 1633-1643.

Bacon D.R. (1989). Prediction of *in situ* exposure to ultrasound: an improved method. Ultrasound Med.& Biol., 15(4), 355-361.

Bacon D.R. (1986). Finite amplitude propagation in acoustic beams. PhD thesis, University of Bath, England.

Bacon D.R. (1984). Finite amplitude distortion of the pulsed fields used in diagnostic ultrasound. Ultrasound Med. & Biol., 10, 189-195.

Baker A.C. (1989). Finite amplitude propagation of focused ultrasonic waves in water. PhD thesis, University of Bath, Bath, England.

Baker A.C. and Humphrey V.F. (1989). The nonlinear propagation in pulsed ultrasonic fields. Proceedings of Ultrasonic International 89, pp.691-696.

Baker A.C., Anastasiadis K. and Humphrey V.F. (1987). Nonlinear propagation in focused field: Experimental and theory. Ultrasonic International 1987.

Bakhvalov N.S., Zhileikin Ya.M. and Rudenko O.V. (1978). Operating characteristics of high power acoustic radiators. Sov. Phys. Acoust., 24, 68-70.

Baumgartner B.R., Dickey K.W., Ambrose S.S., Walton K.N., Nelson R.C. and Bernadino M.E. (1987). Kidney changes after ESWL: appearance on MR imaging. Radiology, 163, 531.

Berens M.E., Welander C.E., Griffin A.S. and McCullough D.L. (1989). Effect of acoustic shock waves on clonogenic growth and drug sensitivity of human tumour cells *in vitro*. J. Urol., 142, 1090-1094.

Beyer R.T. (1974). Nonlinear acoustics. Written for the Naval Ship Systems Command Department of the Navy, US Government printing Office: 1975 O-596-215.

Blackstock D.T. (1985). Generalized Burgers equation for plane waves. J. Acoust. Soc. Am., 77(6), 2050-2053.

Blackstock D.T. (1969). History of nonlinear acoustics and a survey of Burgers' and related equations. In: Muir, T.G. ed. Nonlinear acoustics. Proceedings of a conference held at Applied Research Laboratories. The University of Texas at Austin, Nov. 1969, pp1-27.

Blackstock D.T. (1964). Thermoviscous attenuation of plane, periodic, finite amplitude sound waves. J. Acoust. Soc. Am., 36, 534-542.

Bräuner T., Brümmer F. and Hülser D.F. (1989). Histopathology of shock wave treated tumour cell suspensions and multicell spheroids. Ultrasound in Med. & Biol., 15(5), 451-460.

Brümmer F., Brenner J., Bräuner T. and Hülser D.F. (1989a). Effect of shock waves on suspended and immobilised L1210 cells. Ultrasound in Med. & Biol., 15(3), 229-239.

Brümmer F., Staudenraus J., Nesper M., Suhr D., Eisenmenger W., and Hülser D.F. (1989b). Biological effects and physical characterization of shock waves generated by an XL-1 experimental lithotripter. Ultrasonics International 89 Conference Proceedings, pp.1130-1135.

Carstensen E.L., Campbell D.S, Hoffman D., Child S.Z. and Aymé-Bellegarda E.J. (1990). Killing of drosophila larvae by the fields of an eletrohydraulic lithotripter. Ultrasound in Med. & Biol., 16(7), 687-698.

Carstensen E.L. and Foldy L.L. (1947). Propagation of sound through a liquid containing bubbles. J. Acoust. Soc. Am., 19(3), 481-501.

Champeney D.C. (1985). Fourier transforms in physics. Bristol: Adam Hilger Ltd.

Chaussy C.G. and Fuchs G.J. (1989). Current state and future developments of noninvasive treatment of human urinary stones with extracorporeal shock wave lithotripsy. J. Urology, 141, 782-789.

Chaussy C.G. (1988). ESWL: Past, Present, and Future. J. Endourol.,

2(2), 97-105.

Chaussy C.G. ed. (1986). Extracorporeal shock wave lithotripsy. 2nd ed. Basel, Switzerland: Karger.

Chaussy C.G., Brendel W. and Schmiedt E. (1980). Extracorporeally induced destruction of kidney stones by shock waves, Lancet, 13, 1265-1268.

Christopher P.T. and Parker K.J. and Phillips R.A. (1990). Nonlinear acoustic field propagation. Submitted to: 1990 IBM Supercomputing Competition.

Church C.C. (1989). A theoretical study of cavitation generated by an extracorporeal shock wave lithotripter. J. Acoust. Soc. Am., 86(1), 215-227.

Coleman A.J., Choi M.J. and Saunders J.E. and Leighton T.G. (1992a). Acoustic emission and sonoluminescence due to cavitation at the beam focus of an electrohydraulic shock wave lithotripter. Ultrasound in Med. & Biol., 18(3), 267-287.

Coleman A.J., Saunders J.E. and Choi M.J. (1992b). The physical properties and biological effects of the high amplitude pulsed ultrasound fields used in extracorporeal shock wave lithotripsy. Ultrasonics. (Submitted)

Coleman A.J., Choi M.J. and Saunders J.E. (1991a). Theoretical predictions of the acoustic pressure generated by a shock wave lithotripter. Ultrasound in Med. & Biol., 17(3), 245-255.

Coleman A.J., Choi M.J. and Saunders J.E. (1991b). Analysis of output of a shock wave lithotripter. In: Paumgartner G., Sauerbruch T., Sackmann M. and Burhenne H.J. eds. Lithotripsy and related techniques for gallstone treatment, Chapter I. Chicago: Mosby Year Book Inc.

Coleman A.J., Montgomery B.S., Saunders J.E., Choi M.J. and Whitlock M.

(1991c). Malvern water as an inhibitor of Trebor Imperial mint fragmentation during shock wave lithotripsy: experimental results and clinical implications. (to appear in BMJ).

Coleman A.J. and Saunders J.E. (1989). A survey of the acoustic output of commercial extracorporeal shock wave lithotripters. Ultrasound in Med. & Biol., 15(3), 213-227.

Coleman A.J., Saunders J.E. and Choi M.J. (1989). An experimental shock wave generator for lithotripsy studies. Physics in Med. & Biol., 34(11), 1733-1742.

Coleman A.J., Saunders J.E., Preston R.C. and Bacon D.R. (1987a). Pressure waveforms generated by a Dornier extracorporeal shock-wave lithotripter. Ultrasound in Med. & Biol., 13, 651-657.

Coleman A.J., Saunders J.E., Crum L.A. and Dyson M. (1987b). Acoustic cavitation generated by an extracorporeal shockwave lithotripter. Ultrasound in Med. & Biol., 13(2), 69-76.

Coleman A.J., Saunders J.E. and Palfrey E.L.H. (1987c). The destruction of renal calculi by external shock waves: practical operation and initial results with the Dornier lithotripter. J. Medical Eng. & Tech., 11, 4-10.

Cramer E. and Lauterborn W. (1982). Acoustic cavitation noise spectra. Applied Scientific Research, 38, 209-214.

Crum L.A. and Fowlkes J.B. (1986). Acoustic cavitation generated by micro second pulses of ultrasound. Nature, 391, 52-54.

Crum L.A. and Hansen G.M. (1982). Generalized equations for rectified diffusion. J. Acoust. Soc. Am., 72, 1586-1592.

Crum L.A. (1982). Acoustic cavitation. Proceedings of the 1982 IEEE Ultrasonics Symposium, IEEE. New York, 1982, pp. 1-11.

Davros W.J., Garra B.S. and Zeman R.K. (1991). Gallstone lithotripsy: Relevant physical principles and technical issues. Radiology, 178, 397-408.

Delius M. and Gambihler S. (1991). Effect of shock waves on gallstones and materials. In: Paumgartner G., Sauerbruch T. Sackmann M. and Burhenne H.J. eds. Lithotripsy and related techniques for gallstone treatment, pp.27-33. Chicago: Mosby Year Book Inc.

Delius M., Denk R., Berding C., Liebich H.-G., Jordan M. and Brendel W. (1990). Biological effects of shock waves: cavitation by shock waves in piglet liver. Ultrasound in Med. & Biol., 16(5), 467-472.

Delius M., Miller A., Vogel A. and Brendel W. (1989). Shock waves and cavitation. In: Ferrucci J.T., Delius M., Burhenne H.J. eds. Biliary Lithotripsy, pp.23-30. Chicago: Year Book Medical Pub. Inc.

Delius M. and Brendel W. (1989). Mechanisms of action in extracorporeal shock wave lithotripsy: Experimental studies. In: Ferrucci J.T., Delius M. and Burhenne H.J. eds. Biliary lithotripsy, pp.31-42. Chicago: Year Book Medical Pub. Inc.

Delius M., Brendel W. and Heine G. (1988a). A Mechanism of gallstone destruction by extracorporeal shock waves. Naturwissenschaften, 75, 200-201.

Delius M., Enders G., Brendel W. (1988b). Passage of stone fragments from canine gall-bladders. Surgery Gynecology Obstetrics, 166, 241-244.

Delius M., Enders G., Heine G., Stark J., Remberger K. and Brendel W. (1987). Biological effects of shock waves: lung haemorrhage by shock waves in dogs - Pressure dependence. Ultrasound in Med. & Biol., 13, 61-67.

Dontsov V.E., Kuznetsov V.V., Markov P.G. and Nakoryakov V.E. (1988). Evolution of a pressure wave of moderate intensity in a liquid containing gas bubbles. Sov. Phys. Acoust. 33(6), 605-607.

Drach G.W., Dretler S., Fair W., Finlayson B., Gillenwater J., Griffith D., Lingeman J. and Newman D. (1986). Report of the United States cooperative study of extracorporeal shock wave lithotripsy. J. Urol., 135, 1127-1133.

Du G. and Breazeale M.A. (1987). Theoretical description of a focused gaussian ultrasonic beam in a nonlinear medium. J. Acoust. Soc. Am., 81(1), 51-57.

Duck F.A. and Martin K. (1991). Trends in diagnostic ultrasound exposure. Phys. Med. Biol., 36(11), 1423-1432.

Duck F.A. (1990). Physical properties of tissue; A comprehensive reference book. London: Academic Press Ltd.

Duck F.A. (1987). The measurement of exposure to ultrasound and its application to estimates of ultrasound 'dose'. Phys. Med. Biol., 32(3), 303-325.

Duck F.A., Starritt H.C. and Hawkins A.J. (1986). A survey of the output of diagnostic ultrasound equipment. In: Evans J.A. ed. Physics in medical ultrasound, Chapter 6. London: The Institute of Physical Science in Medicine, Report No 47.

Duck F.A., Starritt H.C., Aindow J.D., Perkins M.A. and Hawkins A.J. (1985). The British Journal of Radiology, 58, 989-1001.

Dyer R.B., Karstaedt N., McCullough D., Zagoria R.J., Harrison L.H., Wolfman N.T. and Appel B. (1990). MRI evaluation of immediate and intermediate change in kidneys treated with extracorporeal shock wave lithotripsy. J. Litho. and Stone Disease, 2(4), 302-308.

Eisenberger F., Fuchs G., Miller K. et al. (1985). Extracorporeal shock wave lithotripsy and endourology: an ideal combination for the treatment of kidney stones. World J. Urol., 3, 41.

Eisenmenger, W. (1988). Methoden der stosswellenerzengung und -messung, Biomed. Tech., 33, 1-5.

Eisenmenger, W. (1964). Experimental determination of shock front thickness from the acoustic spectrum of shock waves with shock pressures between 10 and 100 atm generated with electromagnetic means in liquids. Acustica, 14, 184.

Eller A. and Flynn H.G. (1965). Rectified diffusion during nonlinear pulsations of cavitation bubbles. J. Acoust. Soc. Am., 37(3), 493-503.

Epstein P.S. and Plesset M.S. (1950). On the stability of gas bubbles in liquid-gas solutions. J. Chem. Phys., 18(11), 1505-1509.

Escartin P., Calvo C., Ramos J., Avello F., Taboada M., Escartin Munoz-Ortiz P. and Abreu L. (1989). Extracorporeal shock wave biliary lithotripsy: Short-and long term experience in 100 cases. Doenier User Letter, 5th Issue, pp.8-15.

Fenlon F.H. (1971). A recursive procedure for computing the nonlinear spectral interactions of progressive finite-amplitude wave in nondispersive fluids. J. Acoust. Soc. Am., 50(5), 1299-1312.

Filipczyński L. and Piechocki M. (1990). Estimation of the temperature increase in the focus of a lithotripter for the case of high rate administration, Ultrasound Med. & Biol., 16(2), 149-156.

Flynn H.G. and Church C.C. (1984). A mechanism for the generation of cavitation maxima by pulsed ultrasound. J. Acoust. Soc. Am., 76, 505-512.

Gambihler S., Delius M. and Brendel W. (1990). Biological effects of shock waves: Cell disruption, viability, and proliferation of L1210 cells exposed to shock waves in vitro. Ultrasound Med. & Biol., 16(6), 587-594.

Geise R.A., Hobbie R.K., Lee T.S. and Thompson W.M. (1990). Erosion of

thin films by shock waves from an extracorporeal lithotripter. J. Litho. and Stone Disease, 2, 289-301.

Goetz A.E., Konigsberger R., Gamarra F., Naegele M., Lumper W., Conzen P.F., Lissner J. and Brendel W. (1988). Shock wave induced collapse of tumour microcirculation.: intravital microscopy and magnetic resonance imaging (MRI). Eur. Surg. Res., 20(suppl. 1), 118-119.

Gol'dberg Z.A. (1956). On the propagation of plane waves of finite amplitude. Sov. Physics. Acoust. 3, 346.

Goodman J.W. (1968). Introduction to Fourier optics. San Francisco: McGraw-Hill Book Company.

Goodsitt M.M., Madsen E.L. and Zagzebski J.A. (1982). Field patterns of pulsed, focused, ultrasonic radiators in attenuating and nonattenuating in media. J. Acoust. Soc. Am., 71, 318-329.

Goss S.A., Frizzell L.A. and Dunn F. (1979). Ultrasonic absorption and attenuation in mammalian tissues. Ultrasound Med. & Biol., 5, 181-186.

Granz B., Holzapfel R. and Kohler G. (1989). Measurement of shock waves in the focus of a lithotripter. IEEE. 1989 Ultrasonics Symp., pp.991-994.

Griffith D.P. and Gleeson M.J. (1990). Gallstones: advantages and disadvantages of five treatment alternatives. J. Litho. and Stone disease, 2(3), 184-198.

Hamilton M.F., Tjøtta J.N. and Tjøtta S. (1985). Nonlinear effects in the farfield of a directive sound source. J. Acoust. Soc. Am., 78(1) 202-216.

Harris G.R. (1991) Lithotripsy pulse measurement error due to non-ideal hydrophone and amplifier frequency response. IEEE 1990 Ultrasonics Symposium, pp.1393-1398.

Hart T.S. and Hamilton M.F. (1988). Nonlinear effects in focused sound beams. J. Acoust. Soc. Am., 84(4), 1488-1496.

Hartman C., Cox C.A., Brewer L., Child S.Z., Cox C.F. and Carstensen E.L. (1990a). Effects of lithotripsy fields on development of chick embryos. Ultrasound in Med. & Biol., 16(6), 581-585.

Hartman C., Child S.Z., Mayer R., Schenk E. and Carstensen E.L. (1990b). Lung damage from exposure to the fields of an electrohydraulic lithotripter. Ultrasound in Med. & Biol., 16(7), 675-679.

Heinrich R., Schreckenberg A., Natterer G., Benz H., Mager H.J. and Zierden E. (1989). Preliminary experiences with extracorporeal shock wave lithotripsy of gallbladder stones in 260 patients. Dornier User Letter, 5th Issue, 4-7.

Hepp W. (1988). Zertrümmerungswirkung von stosswellen auf Nieren - und gallenstein. Biomed. Tech., 33, 15-16.

Hill C.R. and ter Haar G.R. (1989). Ultrasound. In: Suess M.J. and Benwell-Morison D.A. eds. Nonionizing radiation protection. 2nd ed., pp.245-291. Copenhagen: WHO regional publication, European series, No 25.

Hill C.R. (1978). Ultrasonic attenuation and scattering by tissues. In: de Vlieger M., Holmes J.M. and Kossoff E. et al. eds. Handbook of clinical ultrasound, pp.91-98. New York: Wildy.

Hofmann A.F. (1991). Organic solvents for contact dissolution of cholesterol gall stones. In: Paumgartner G., Sauerbruch T., Sackmann M., Burhenne H.J. eds. Lithotripsy and related techniques for gallstone treatment, pp129-136. Chicago: Mosby Year Book.

Holmer N.-G., Almquist L.-O., Hertz T.G., Holm A., Lindstedt E., Persson H.W. and Hertz C.H. (1991). On the mechanism of kidney stone disintegration by acoustic shock waves. Ultrasound in Med. & Biol., 17(5), 479-489.

Holmes R.P., Yeaman L.I., Li W.-J., Hart L.J., Wallen C.A., Woodruff R.D. and McCullough D.L. (1990). The combined effects of shock waves and cisplatin therapy on rat prostate tumours, J. Urol., 144, 159-163.

Humphrey V.F., Burgess M. and Sampson N. (1986). Harmonic generation due to non-linear propagation in a focused ultrasonic field. Proc. Inst. Acoust., 8(2), 47-54.

Hunter H.P.T. (1987). The physics and geometry pertinent to ESWL, In; Riehle R.A. Jr ed. Principles of extracorporeal shock wave lithotripsy, pp13-27. New York: Churchill Livingstone.

Hunter H.P.T., Finlayson B., Hirko R.J., Voreck W.C., Walker R., Walck S. and Nasr M.E. (1986a). Measurement of shock wave pressures used for lithotripsy. J. of Urology, 136, 733-738.

Hunter H.P.T., Finlayson B., Newman R.C. et al. (1986b). Geometry of and pressures with ESWL. In; Gravenstein J.S. and Peter K. eds. Extracorporeal shock wave lithotripter for renal stone disease, Technical and Clinical Aspects, pp.19-28. Boston: Butterworth.

Jenkins A., Wilbert D. and Hohenfellner R. (1987). Clinical experience with the Siemens Lithostar. In: Coptcoat M.J., Miller R.A. and Wickham J.E.A. eds. Lithotripsy II, pp.109-119. London: B.D.I. Publishing.

Jocham D. (1987). Historical development of ESWL. In: Riehle R.A. and Newman R.C. eds. Principles of extracorporeal shock wave lithotripsy, Chapter I. New York: Churchill Livingstone.

Johnson H.F. (1987). An improved method for computing a discrete Hankel transform. Comp. Phys. Comm., 43, 181-202.

Jongen H.A.H., Thijssen J.M., van den Aarssen M. and Verhoef W.A. (1986). A general model for the absorption of ultrasound by biological tissues and experimental verification. J. Acoust. Soc. Am., 79(2), 535-540.

Kahnoski R.J., Lingeman J.E., Coury T.A., Steale R.E. and Mosbaugh P.G. (1986). Combined percutaneous and extracorporeal shock wave lithotripsy for staghorn calculi: an alternative to anatrophic nephrolithotomy. J. Urol., 135, 679-681.

Kambe K., Kuwahara M., Orikasa S. and Takayama K. (1988). Mechanism of fragmentation of urinary stones by underwater shock wave. Urol. Int.,43, 275-281.

Keller A. (1972). The influence of cavitation nucleus spectrum on cavitation inception, investigated with a scattered light counting method, Trans. ASME. J. Basic Eng., 94, 917-925.

Kinsler L.E., Frey A.R., Coppens A.B. and Sanders J.V. (1982). Fundamentals of acoustics. 2nd ed. New York: John Wiley & Sons.

Kirchberger S. (1991). The diffusion of two technologies for renal stone treatment across Europe. London: Stocking. King's Fund Centre.

Knapp P.M., Kulb T.B., Lingeman J.E., Newman D.M., Mertz J.H.O, Mosbaugh P.G. and Steele R.E. (1988). Extracorporeal shock wave lithotripsy induced perirenal haematoma. J. Urol., 139, 700-703.

Koch H. and Grünewald M. (1989). Disintegration mechanisms of weak acoustical shock waves. Ultrasonics international 89 conference proceedings, pp.1136-1141.

Korpel A. (1980). Frequency approach to nonlinear dispersive waves. J. Acoust. Soc. Am., 67(6), 1954-1958.

Kuznetsov V.E., Nakoryakov V.E., Pokusaev B.G. and Shreiber I.R. (1977). Propagation of disturbances in a gas-liquid mixture. Sov. Phys. Acoust., 23(2), 153.

Kuznetsov V.E. (1970). Equations of nonlinear acoustics.Sov. Physics - Acoustics, 16, 467-470.

Lastman G.L. and Wentzell R.A. (1981). Comparison of five models of spherical bubble response in an inviscid compressible liquid. J. Acoust. Soc. Am., 69(3), 638-642.

Lauterborn W. and Bolle H. (1975). Experimental investigation of cavitation bubble collapse in the neighborhood of a solid boundary. J. Fluid Mech., 72, 391.

Laudone V.P., Morgan T.R., Huryk R.F., Heston W.D. and Fair W.R. (1989). Cytotoxicity of high energy shock waves: methodological considerations. J. Urol., 141, 965-968.

Lewin P.A., Chapelon J.Y., Mestas J.L., Birer A. and Cathignol D. (1990). A novel method to control p+/p- ratio of the shock wave pulses used in the extracorporeal piezoelectric lithotripsy (EPL). Ultrasound in Med. & Biol., 16(5), 473-488.

Lewin P.A., Schafer M.E. (1991). Shock wave sensors. I. Requirements and design. J. Litho. and Stone Disease, 3, 3-17.

Lewin P.A., Schafer M.E. (1986). Ultrasonic probes in measurement practice. Med. Device & Diagn Ind., 8(5), 40-46.

Lingeman J.E., Evan A.P., Wood J.R. and Toth P.D. (1988). The bioeffects of shock waves and the risk of hypertension following ESWL. J. Urol., 139. Part 2, 291A. abstract 514.

Lucas B.G. and Muir T.G. (1983). Field of a finite-amplitude focusing source. J. Acoust. Soc. Am., 74(5), 1522-1528.

Lucas B.G. and Muir T.G. (1982). The field of a focusing source. J. Acoust. Soc. Am., 72(4), 1289-1296.

Lyons M.E. and Parker K.J. (1988). Absorption and attenuation in soft tissues II - experimental results. IEEE Trans. Ultra. Ferr. Freq. Cont., 35(4), 511-521.

Mays N, Challah S, Patel S, Palfrey E, Creeser R, Vadera P and Burney P. (1988). Clinical comparison of extracorporeal shock wave lithotripsy and percutaneous nephrolithotomy in treating renal calculi. BMJ., 297, 253-258.

McHugh D. (1986). IPSM survey of manufacturers data of diagnostic ultrasound equipment.In: Evans J.A. ed. Physics in medical ultrasound, Chapter 5. London: The Institute of Physical Science in Medicine, Report No 47.

McLachlan N.W., Meyers A.L. (1935). Spherical sound wave of finite amplitude, Phys. Soc., 47(4), 644-656.

Morfey C.L. (1991). Effect of dispersion on a plane ultrasonic pulse. 121st Meeting ASA. May. 1991, paper 7PA2.

Morse P.M. and Ingard K.U. (1968). Theoretical acoustics, pp418-427. New York: McGraw Hill.

Müller M. (1987). Stoβwellenfokussierung in wasser. PhD Thesis, RWTH (Rheinisch-Westfalischen Technischen Hochschule) Aachen.

Nasr M.E. (1986). The evoluation and dynamics of spark generated shock waves and their focussing by ellipsoidal reflectors in lithotripsy. PhD dessertation, University of Florida, Gainesville, FL, USA.

Neighbors T.H. and Bjørnø L. (1988). A study of the KZK equation. Rapport Nr.14. Laboratoriet For Industiel Akustik, Procesteknisk Institut, Danmarks Tekniske Højskole.

Neubrand M., Sauerbruch T., Stellaard F. and Paumgartner G. (1986). *In vitro* cholesterol gallstone dissolution after fragmentation with shock waves. Digestion, 34, 51-59.

Newman R.C. (1987). Clinical and experimental effects associated with ESWL. In: Riehle R.A. and Newman R.C. eds. Principles of extracorporeal

shock wave lithotripsy, pp.31-41. New York: Churchill Livingstone.

Novikov B.K., Rudenko O.V. and Timoshenko V.I. (1987). Nonlinear under water acoustics. Translated by Beyer R.T. Published for Acoust. Soc. Am. by the American Institute of Physics.

O'Donnell M., Jaynes E.T. and Miller J.G. (1981). Kramers-Kronig relationship between ultrasonic attenuation and phase velocity. J. Acoust. Soc. Am., 69(3), 696-701.

O'Donnell M., Jaynes E.T. and Miller J.G. (1978). General relationships between ultrasonic attenuation and dispersion. J. Acoust. Soc. Am., 63(6), 1935-1937.

Oosterhof G.O.N., Smits G.A.H.J., de Ruyter J.E., Schalken J.A. and Debruyne F.M.J. (1991). Effects of high energy shock waves combined with biological response modifiers in different human kidney cancer xenografts. Ultrasound in Med. & Biol., 17(4), 391-399.

Oosterhof G.O.N., Smits G.A.H.J., de Ruyter J.E., Schalken J.A. and Debruyne F.M.J. (1990). *in vivo* effects of high energy shock waves on urological tumours; an evaluation of treatment modalities. J. Urol., 144, 785-789.

Oosterhof G.O.N., Smits G.A.H.J., de Ruyter J.E., van Moorselaar R.J.A., Schalken J.A. and Debruyne F.M.J. (1989). The *in vitro* effect of electromagnetically generated shock waves (Lithostar) on the Dunning R3327-PAT-2 rat prostatic cancer cell-line. Urol. Res., 17, 13-19.

Plesset M.S. and Chapman R.B. (1971). Collapse of an initially spherical vapor cavity in the neighborhood of a solid boundary. J. Fluid Mech., 47, 283.

Preston R.C., Shaw A. and Zeqiri B. (1991). Prediction of *in situ* exposure to ultrasound: a proposed standard experimental method. Ultrasound in Med. & Biol., 17(4), 333-339.

Prosperetti A. (1984a). Bubble phenomena in sound fields: part one. Ultrasonics, 22, 69-77.

Prosperetti A. (1984b). Bubble phenomena in sound fields: part two. Ultrasonics, 22, 115-124.

Randazzo R.F., Chaussy C.G., Fuchs G.J., Bhuta S.M., Lovrekovich H., and de Kernion J.B. (1988). The *in vitro* and *in vivo* effects of extracorporeal shock waves on malignant cells.Urol. Res. 16, 419-426.

Reichenberger H. (1988). Lithotriper systems. Proceedings of the IEEE., 76(9), 1236-1246.

Reichenberger H. and Naser G. (1986). Electromagnetic acoustic source for the extracorporeal generation of shock waves in lithotripsy. Siemens Forschungs Und Entwicklungs Berichte, 15, 187-194.

Reilly C.R. and Parker K.J. (1989). Finite-amplitude effects on ultrasound beam patterns in attenuating media. J. Acoust. Soc. Am., 86(6), 2339-2348.

Riedlinger R. (1990). Cavitation in the field of a focused pulsed high power sources: photo documents and their relationship to biological effects. Proceedings of Workshop on biological effects and physical characterization of shock waves, Stuttgart, 18-19th April 1990.

Rotus S.N. ed. (1987). Stone disease, diagnosis and management. Orlando, FL: Grune & Stratton.

Rudenko O.V. and Soluyan S.I. (1977). Theoretical Foundations of nonlinear acoustics. Translated from Russian by Beyer R.T. New York: Consultants Bureau.

Russo P., Mies C., Huryk R., Heston W.D.W., Fair W.R. (1987). Histopathologic and ultrastructural correlates of tumor growth suppression by high energy shock waves. J. Urol., 137, 338-341.

Russo P., Stephenson R., Mies C., Huryk R., Heston W.D.W., Melamed R. and Fair W.R. (1986). High energy shock wave suppress tumor growth in vitro and in vivo. J. Urol., 135, 626-628.

Sass W., Bräunlich M., Dreyer H.-P., Matura E., Folberth W., Priesmeyer H.-G. and Seifert J. (1991). The mechanism of stone disintegration by shock waves. Ultrasound in Med. & Biol., 17(3), 239-243.

Sauerbruch T. and Paumgartner G. (1991). Gallbladder stones: management. The Lancet, 338, 1121-1124.

Schulze H., Hertle L., Graff J., Funke P.-J. and Senge T. (1986). Combined treatment of branched calculi by percutaneous nephrolithotomy and extracorporeal shock wave lithotripsy. J. Urol., 135, 1138-1141.

Schwarz H.R. (1989). Numerical Analysis: a comprehensive introduction. Chichester: John Wiley & Sons.

Sehgal C.M. and Greenleaf J.F. (1982). Ultrasonic absorption and dispersion in biological media: A postulated model. J. Acoust. Soc. Am., 72(6), 1711-1718.

Silberman E. (1957). Sound velocity and attenuation in bubbly mixtures measured in standing wave tubes. J. Acoustic. Soc. Am., 29, 925-933.

Smits G.A.H.J., Oosterhof G.O.N., de Ruyter J.E., Schalken J.A. and Debruyne F.M.J. (1991). Cytotoxic effects of high energy shock waves in different in vitro models: Influence of the experimental set-up. J. Urol., 145, 171-175.

Sutin A.M. (1978). Influence of nonlinear effects on the properties of acoustic focusing systems. Sov. Phys. Acoust., 24, 334-339.

Tjøtta J.N. and Tjøtta S. (1981). Nonlinear equation of acoustics, with application to parametric acoustic arrays. J. Acoust. Soc. Am., 69, 1644-1652.

Urick R.J. (1975). Principles of underwater sound. New York: McGraw-Hill.

Vakil N., Gracewski S.M. and Everbach E.C. (1991). Relationship of model stone properties to fragmentation mechanisms during lithotripsy. J. Litho. and Stone Disease, 3(4), 304-310.

Vokurka K. (1986). Comparison of Rayleigh's , Herring's, and Gilmore's models for gas bubbles. Acustica, 59, 214-219.

Webb D.R., Payne S.R. and Wickham J.E.A. (1986). Extracorporeal shock wave lithotripsy and percutaneous renal surgery. Comparisons, combinations and conclusions. Br. J. Urol., 58, 1-5.

Weiss N., Delius M., Gambihler S, Dirschedl P., Goetz A. and Brendel W. (1990). Influence of the shock wave application mode on the growth of A-Mel 3 and SSK2 tumours *in vivo*. Ultrasound in Med. & Biol., 16, 595-605.

Wells P.N.T. (1977). Biomedical ultrasonics, London: Academic press.

Whelan J.P. and Finlayson B. (1988). An experimental model for the systematic investigation of stone fracture by extracorporeal shock wave lithotripsy. J. Urol., 140, 395-399.

Whelan J.P., Gravenstein N., Welch J.L., Lampotang S., Newman R.C. and Finlayson B. (1988). Simulation of ventilatory-induced stone movement and its effect on stone fracture during extracorporeal shock wave lithotripsy. J. Urol., 140, 405-407.

Wilbert D.M., Strohmäier W.L., Flüchter S.H. and Bichler K.-H. (1990). Urinary proteins as parameters of renal functional changes after extracorporeal shock wave lithotripsy. Proceedings of Workshop on biological effects and physical characterization of shock waves, Stuttgart, 18-19th April 1990.

Williams A.R., Delius M, Miller D.L. and Schwarze W. (1989).

Investigation of cavitation in flowing media by lithotripter shock wave both *in vitro* and *in vivo*. Ultrasound in Med. & Biol., 15(1), 53-60.

Wu J. and Zhu Z. (1991). Measurements of the effective nonlinearity parameter B/A of water containing trapped cylindrical bubbles. J. Acoust. Soc. Am., 89(6), 2634-2639

Zabolotskaya E.A. and Khokhlov R.V. (1969). Quasi-plane waves in the nonlinear acoustics of confined beams Sov. Phys. Acoust., 14, 35-40.